# Production of Inhaler Grade Lactose by Crystallization

**A Thesis presented in partial fulfilment of the requirements for the degree of Doctor of Philosophy in Process Engineering at Massey University**

**Konrad Raimund Shaffer**

**2013**

## Abstract

This work focused on producing Inhaler grade lactose (IGL) directly by crystallization. IGL is a high purity lactose excipient meeting a range of precise particle size distribution specifications. The 50 percent particle size ($d_{50}$) on a volume basis desired for this work was in the range of 50 to 90 μm, and a span less than 1. IGL is commonly used as a drug carrier in dry particle inhalers. Typical industrial lactose crystallization produces lactose with a $d_{50}$ greater than 200 μm and a span of around 2. The large span has been attributed to successive nucleation events during the growth phase and growth rate dispersion. Costly additional processing is currently required to produce IGL, generally in the form of sieving and milling.

Initially the crystallization literature was reviewed with a specific focus on alternative methods for producing a narrow particle size distribution. From this, three methods were mathematically modelled for their ability to produce IGL. Crystallization in droplets literature and model predictions showed great potential for targeting a particle size distribution with a very low span directly from crystallization; however issues arose with scalability and potential contamination if not using a lactose or water carrier phase. Subsequent crystallization product stream processing via a hydrocyclone or inclined settler also showed the ability, in theory, to produce IGL; however both these methods were deemed as additional processing and a novel crystallization process was desired. This led to the development of the continuous settling crystallizer (CSC).

The CSC consists of a vertical column, where a pre-nucleated feed stream enters near the bottom of the column and flows out the top, all under laminar conditions. Inside the column only growth occurs as additional nucleation is limited by the chosen column conditions. The CSC incorporates the key elements revealed from the literature for achieving a narrow span of a single nucleation event and a method to counteract growth rate dispersion. Slow growing crystals travel further up the column than fast growing crystals before growing to the terminal particle settling diameter, opposing flow, and settling out from the column and into the product stream. For a particular fluid velocity, the crystals settle out into the product stream at the same final particle size. Under laminar flow conditions a parabolic profile occurs across the column radius and the CSC theoretical model developed predicted a product $d_{50}$ of 73 μm and a span of 0.47 for the chosen column conditions.

Lab scale experiments were then carried out for the CSC. The resulting product $d_{50}$ was in the desired range of 50 to 90 μm, but the span ranged from 1.4 to 1.5. Column channelling, an area of high flow and subsequent low flow elsewhere, was suspected as the cause of the experimental deviations. The theoretical model was modified to include channelling and predictions matched the experimental product results well. Due to the high level of control required for the CSC it is recommended that a batch process is designed to efficiently produce IGL; this would incorporate a single nucleation event and a hydrocyclone cut.

## Acknowledgements

I am a man of few words, so undoubtedly writing my PhD thesis has been one of my most daunting but worthwhile challenges to date, and as Clive Davies stated to me, I have 40 years ahead of me to hone my writing skills. The thesis and PhD work overall could not have been completed without the help of many people. I would like to thank:

My primary supervisor Tony Paterson; thank you for all your help and constant support, and also for the invites to dinners, play golf, and go fishing; I still haven't been able to go fishing with you yet, but hopefully one day!

My secondary supervisors Clive Davies and Gerald Hebbink; thank for your important contributions and in particular I would like to thank Clive for helping me improve my understanding of the written language.

DFE Pharma; all this work would not have been able to be carried out if it was not for their project funding and lactose provided, so I am very grateful. It was also fantastic being able to present at conferences and travel to The Netherlands to give yearly summaries to Gerald at DFE Pharma.

Laboratories, workshop and administration; huge thanks goes to all the technicians I hassled over the years while undertaking my experiments, in particular Anne-Marie Jackson, Bruce Collins, John Edwards, Anthony Wade, all the office ladies, and of course Clive Bardell, who adopted the greeting "oh no here's trouble".

A special thank you goes to Elyssa Barnaby, who joined me later on in my PhD journey, and has provided unlimited love and support. I would also like thank Eli who I have been friends with since undergraduate and also undertook a PhD at the same time as me.

My family; Dad, Mum, and my brother, thank you for all the love and support.

Finally, a thank you goes out to anyone that has helped me over the years but I have not named directly.

# Contents Page

## List of Figures

## List of Equations

## List of Tables

## Chapter 1 - Overview

The pharmaceutical industry and other industries rely on the use of crystallized lactose with a specific particle size distribution (PSD) for use in various products. Typical lactose crystallization processes result in a wide PSD, which is undesirable in the pharmaceutical industry.

A common use for lactose crystals, that requires a narrow PSD, is as a drug carrier in dry particle inhalers; this grade is termed inhaler grade lactose (IGL). Typical production methods for IGL involve batch crystallization with subsequent sieving, meeting a range of specific PSD targets, depending on the end consumer use. With reference to Figure 1 below, the differences between the PSDs of typical batch crystallized lactose and the desired IGL can be seen. In addition to the $d_{50}$ (µm) lying within the desired particle size range, the span, ($d_{90}$-$d_{10}$)/$d_{50}$, of IGL is less (narrow); $d_{50}$ is the 50% particle size, $d_{90}$ (µm) is the 90% particle size, and $d_{10}$ (µm) is the 10% particle size on a volume basis. Due to inefficiencies and the costly nature of current crystallization processes, new and improved methods to achieve a narrow PSD are needed.

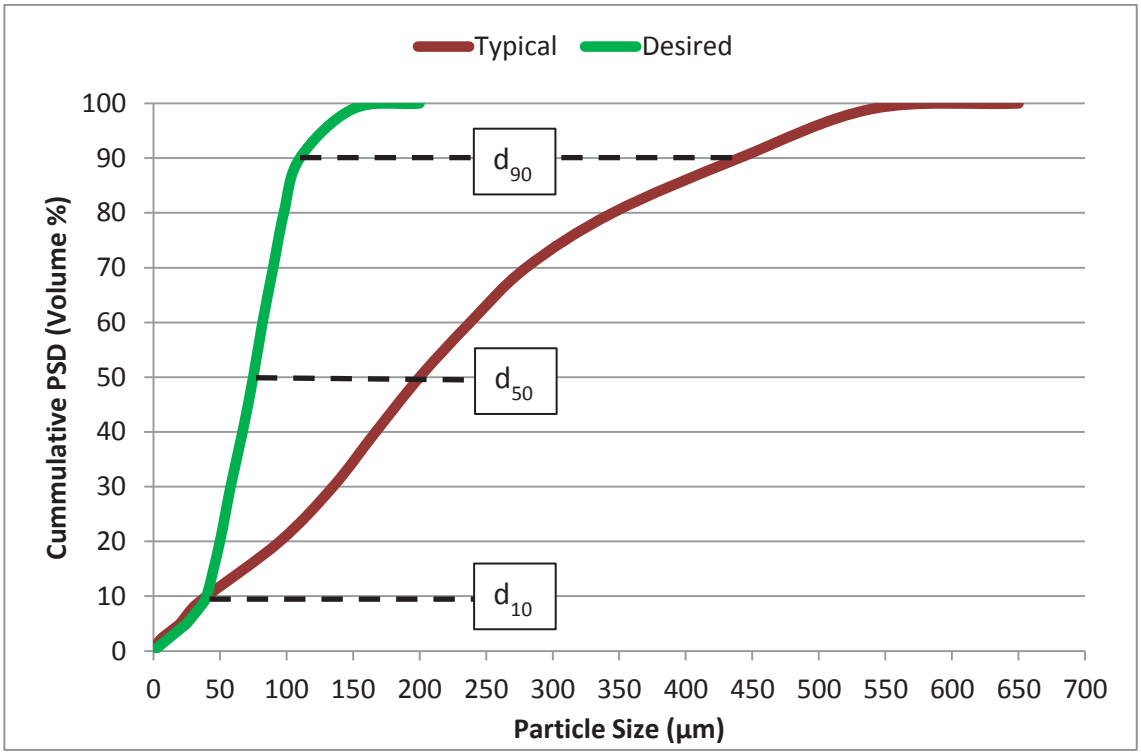


**Figure 1 Typical batch lactose crystallization particle size distribution (PSD), span ~2, and this works desired inhaler grade lactose PSD, span less than 1**

The primary objective of this study is to develop a reliable process capable of producing IGL directly by crystallization, ideally without further separation steps, such as sieving. This involves considering innovative new crystallization processes or modifying existing crystallization processes. The current desired crystallization target process parameters are:

- A narrow PSD, with a $d_{50}$ between 50 to 90 µm and a span less than 1; refer to Figure 1
- Reproducible; such that a consistent product can be produced
- Very low levels of contaminants; which is required for a pharmaceutical product

# Chapter 2 – Literature Review

## 2.1 Lactose Background

### *2.1.1 General Information*

The study of lactose has not been a recent pursuit and has in fact been occurring for many centuries. In 1633 Fabricio Bartoletti, a doctor of philosophy and medicine, first discovered the presence of lactose in milk (Roelfsema, Kuster, Heslinga, Pluim, & Verhage, 2002). Lactose is a carbohydrate which is primarily found in mammalian milk and has the highest concentration of all the carbohydrates in milk.

The primary industrial source of lactose is whey, a byproduct from the cheese making process. Milk is curdled by the addition of acid, resulting in curds and whey; the curds are then used to make cheese. Of the average 4.6 weight percent lactose contained in cow's milk, approximately 95% of this lactose leaves with the whey in cheese making (Butler, 1998). Most of this lactose can be recovered and utilised in other areas.

Initially, the main uses of lactose have been in the food and fine chemical industries. Although in recent years, its use and importance in the pharmaceutical industry have been increasing. This includes the use in drug formulation, and what this thesis is centred on, the use as a drug carrier in dry particle inhalers.

### *2.1.2 Lactose Properties*

Lactose is a milk sugar, $C_{12}H_{22}O_{11}$, with the scientific name 4-*O*-β-D-galactopyranosyl-α-D-glucopyranose (Dincer, 2000). Lactose's structure is a disaccharide sugar comprised of a galactose and glucose molecule.

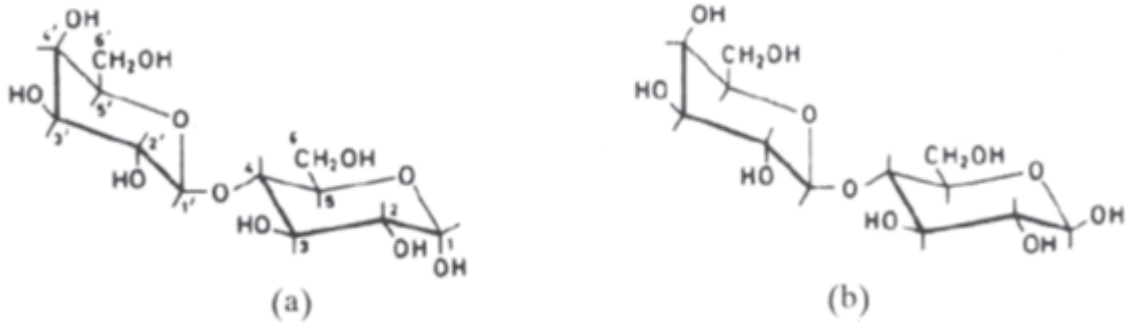


**Figure 2 Lactose molecular structure, showing the difference in α (a) and β (b) anomers; redrawn from Dincer (2000)**

Lactose exists in two main forms (Figure 2); these are the alpha (α) and beta (β) anomers. The α and β structures differ in the steric configuration of the OH and H group on the glucose carbon atom (C1). α-Lactose is the least soluble form and will crystallize out in water solutions

below temperatures of 93.5°C as the hydrated form $C_{12}H_{22}O_{11}{\cdot}H_2O$. α-Lactose monohydrate crystals are desired in the pharmaceutical industry (and other industries) as well as β-lactose. In commercial products, different anomers change factors such as drug release and flowability. Aqueous solutions of lactose contain an equilibrium ratio of α-lactose and β-lactose. When either form of crystallized lactose is dissolved in water a change in form takes place, until equilibrium is reached. The equilibrium concentrations of α-lactose and β-lactose (g lactose/ 100 g water), $C_{\alpha s}$ and $C_{\beta s}$ respectively, can be represented by the equilibrium constant, K (-).

$$K = \frac{C_{\beta s}}{C_{\alpha s}}$$

**Equation 1 Lactose β and α equilibrium ratio constant**

The effect of temperature on the equilibrium constant in the literature shows contradictions. One of the more widely accepted results is that *K* is inversely proportional to increasing temperature (Roetman & Buma, 1974), agreeing with and backing up earlier work of Gillis (1920). The studies stating otherwise (Hudson, 1904, 1908; Kendrew & Moelwyn-Hughes, 1940; Nickerson & Moore, 1974) have been shown to be incorrect due to false assumptions made in the calculation of *K*. Generally, *K* decreases from about 1.64 at 0°C to about 1.36 at 100°C (Gillis, 1920; Roetman & Buma, 1974).

The change from α-lactose to β-lactose can be studied through the determination of change in the optical rotation, known as mutarotation (Roetman & Buma, 1974). A study into the *in situ* and quantitative measurements of the mutarotation reaction in solid state lactose (Lefort, Caron, Willart, & Descamps, 2006), showed there was no transformation when starting from a crystalline state. For lactose in an amorphous state, mutarotation starts on heating and reaches an equilibrium slightly above the glass transition state, with a ratio of 1:1 for α and β anomers. This leads to the conclusion that the solid state energy profile is different than aqueous solutions.

There are many different forms of lactose, or polymorphs. A polymorph is a material which exhibits different crystal structures within a solid but has identical characteristics in a solution. Although there is a lot of debate on the different polymorphs for lactose (Kirk, Dann, & Blatchford, 2007), it is generally accepted that there are four main forms: α-lactose monohydrate (single hydrated form), β-lactose (three dehydrated form), stable anhydrous α-lactose and unstable hygroscopic anhydrous α-lactose. There are also α and β mixed forms that exist within crystals. Kirk *et al*, (2007) found that, with no prior knowledge of a lactose solution composition, it was possible to distinguish between the different polymorphs.

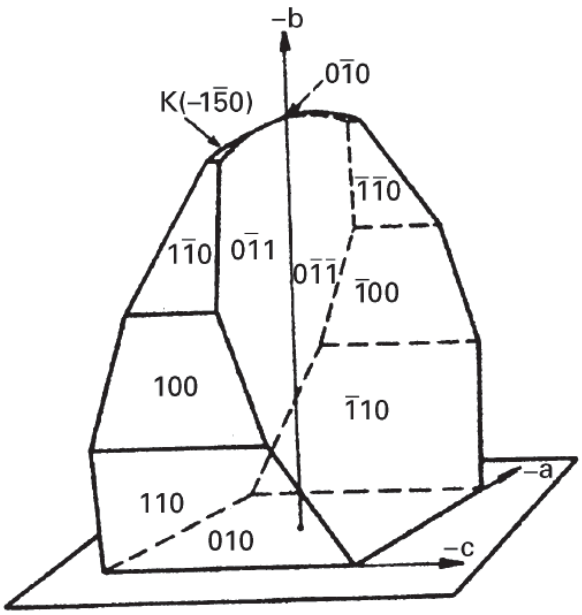


**Figure 3 Lactose tomahawk crystal structure, including the miller indices; redrawn from van Kreveld and Michaels (1965)**

The usual crystalline structure of α-lactose monohydrate, crystallized from water solution, has been found to be a tomahawk shape; as depicted in Figure 3. A table of lactose physical properties is given in the Appendix A.1.

## 2.2 Dry Particle Inhalers

The following section focuses on issues related to lactose particles produced for use as carriers for pulmonary drugs. The main example of this application is the dry particle inhaler (DPI), which is a commonly used type of asthma inhaler. Changing the particle characteristics can have a significant effect on drug formulation and Table 1 summarises these effects. Table 2 summarises the main methods used in particle formulation.

During blending of the lactose carrier particles and the required drug, certain interactions can occur. Figure 4 below illustrates the types of interactions that the active drug particles or fines can have with the surface of the lactose carrier particle. The fines are generally less than 5µm, whereas the lactose carrier particles are generally greater than 50 µm. In DPIs, once the static lactose carrier powder is aerosolised and dilated the attached fines then become detached, as illustrated in Figure 5. During the detachment of the fines, the larger lactose carrier particles hit the back of the throat, while the fine drug particles travel further down into the lower respiratory tract to be utilised by the body.

| Particle Characteristics | Effects on Formulation |
|---|---|
| Solid state: crystallinity, polymorphism, hygroscopicity, impurities, solubility, dissolution rate | Physical and chemical stability, bioavailability, toxicity |
| Particle size distribution, shape, porosity or density | Aerosolisation behaviour, in vitro and in vivo deposition profiles, bioavailability |
| Surface morphology, energetic and electrostatics | Powder handling, inhaler filling, dose metering, storage stability, shelf-life, dose-uniformity and consistency |
| Powder bulk density, agglomeration, cohesiveness, flow properties | Dose uniformity |
| Co-formulation or blending; composition or coating | Modified or extended release, toxicity |
| Formulation, dispersion media | Type of inhaler<br>Mode of administration |

**Table 1 Particulate properties and their effects on respiratory drug Delivery; reproduced from Chow, Tong, Chattopadhay, and Shekunov (2007)**

| Method | Typical Products Formed | Major Advantages and Disadvantages for Respiratory Drug Delivery | Challenges |
|---|---|---|---|
| Micronization and blending | Dense, irregularly shaped, crystalline particles | Established, proven | Cohesiveness, amorphous domains, poor powder dispersion due to electrostatic charges |
| Spray drying | Solid or low-density composite amorphous particles | Developed, simple | Thermal degradation, protein aggregation, solid-state instabilities |
| Spray freeze drying | Low-density composite amorphous particles with high specific surface area | Processing of heat sensitive compounds, dissolution rate enhancement | High processing cost, underdevelopment |
| Emulsion based | Solid composite particles, drug particles with narrow size distribution | Production of controlled release formulations, micro and nanosuspensions | Manufacturing complexity, slow production rate, large waste streams, residual solvent removal |
| Supercritical antisolvent | Low-powder density crystalline particles | Pure, stable, non-cohesive powders | Particle size control, material specific |

**Table 2 Comparison of different particle formation techniques; reproduced from Chow *et al., (2007)***

Typical lactose crystallization (see Section 2.3) from a concentrated whey solution utilizes large temperature controlled batch crystallizers. Maximising yield is the primary aim, and little span control occurs. Typical crystallization is unsuitable for direct use in respiratory drug delivery.

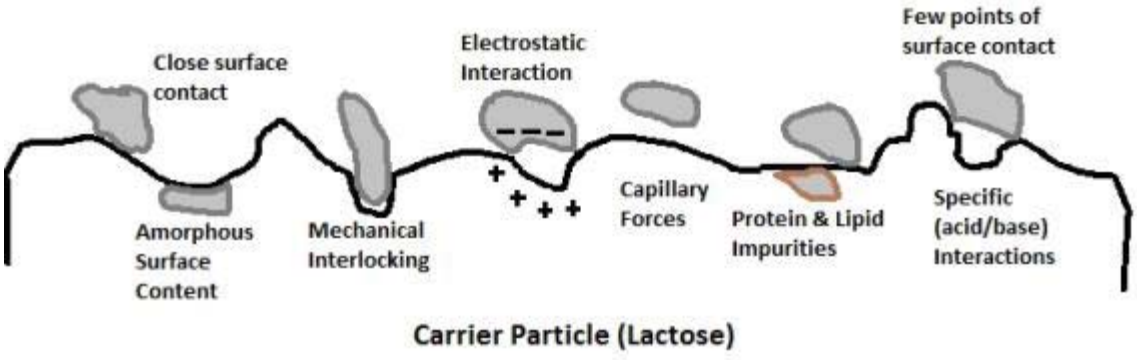


**Figure 4 Causes of various types of interactions between fines and carrier particles; redrawn from Hickey *et al.*, (2007)**

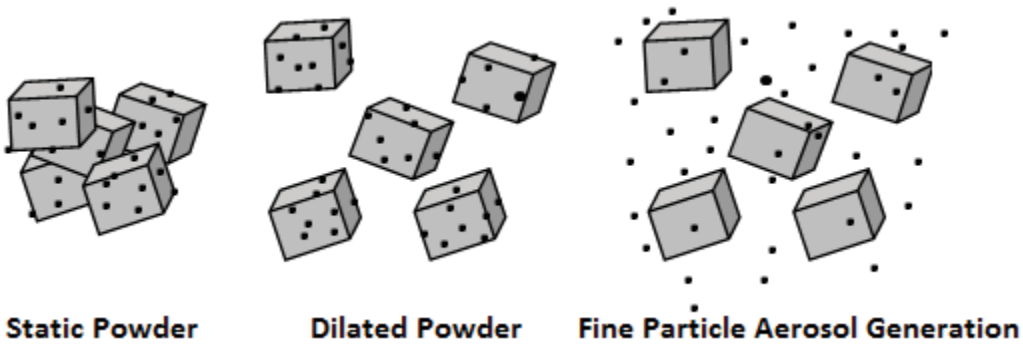


**Figure 5 Process occurring when aerosol is used, fines are detached once static powder is dilated and aerosolised; redrawn from Hickey *et al.*, (2007)**

The surface energy distribution is an important property of lactose crystals when considering its use as a drug carrier, as this affects how drugs bind to the crystal and also how it is released when ingested into the body (Thielmann, Burnett, & Heng, 2007). It was found that milled lactose crystals have a different energy distribution compared to untreated and recrystallized lactose, and this was attributed to amorphous regions on the surface caused by the milling process (Thielmann*, et al.*, 2007). Sieved lactose is generally used for DPIs; which can be understood when looking at scanning electron microscope (SEM) images of sieved and milled lactose particles.

SEM imaging of sieved lactose revealed (Hickey *et al.*, 2007):

- A uniform particle shape distribution
- Few particle aggregates
- A relatively narrow size distribution
- Few single particles under 10 µm
- Smooth irregularly shaped asymmetric cubic morphology with some nanocrevices

While SEM imaging of milled lactose revealed (Hickey*, et al.*, 2007):

- A non-uniform particle shape distribution
- Significantly more particle aggregates than sieved
- A relatively wide particle size distribution compared to sieved
- Many particles under 10 µm
- Irregular morphology, increased surface roughness compared to sieved, nanocrevices and surface fines

Sieving results in a uniform and narrow distribution of lactose crystals with fewer fines, which is a desired characteristic for DPIs, and why it is commonly used for producing inhaler grade lactose (IGL). A recent review article into IGL lactose characteristics and aerosol generation by Pilcer, Wauthoz, & Amighi (2012) covers the discussed aspects in this section in detail, and is useful additional reading.

## 2.3 Lactose Crystallization

Crystallization is a very important process to many industries, including the chemical, pharmaceutical and electronic industries. Lactose crystallization is especially important for use in food (infant milk powders) and drug formulation (dry particle inhalers). Understanding the crystallization process is important when trying to develop methods to produce a product with a narrow particle size distribution (PSD). There are aspects of the crystallization process which can cause a widening of the PSD, and these include: successive nucleation events under batch conditions, and differential growth rates of these nuclei. These factors are counteractive in achieving the narrow PSD generally required for IGL and need to be controlled.

Crystallization from solution is carried out to purify and separate a substance of high value from an impure solution. Early lactose studies (Herrington, 1934) looked into preventing crystallization in various processes, such as in ice cream (which gave a salty texture) or in spray dried milk powder (to avoid caking). When considering a whey solution, lactose crystallization can be seen as the removal of lactose from impurities present in the whey solution such as salts, proteins and fats.

Crystallization is a rate process, time is required for crystal growth, and supersaturation is the fundamental driving force. Supersaturation can be understood when referring to Figure 6 below. Starting in the unsaturated zone, where the solute is fully soluble, then cooling the solution and moving to the labile zone, the Solubility Limit ($C_s$) is passed, and a supersaturated solution is achieved. Thus, a supersaturated solution is a solution with solute concentration higher than equilibrium or saturation solute concentration for a given temperature. When

passing the solubility limit there is also a metastable zone where crystallization occurs, but this is very slow (days). The further the solution is cooled past the metastable zone, the faster crystallization is likely to occur (hours) (Myerson, 2002). Other methods to produce a supersaturated solution can be to evaporate excess water, or to add a substance to lower the solubility limit such as ethanol, which is common in anti-solvent crystallization.

Using chemical potential, supersaturation can be represented in the following dimensionless form:

$$\frac{\mu - \mu^*}{RT} = ln\frac{a}{a^*} = ln\frac{\gamma c}{\gamma^* c^*}$$

Equation 2 Chemical potential dimensionless form (Myerson, 2002)

where $\mu$ (J.gmol$^{-1}$) is the chemical potential, $c$ (g solute/100 g solvent) is the concentration, $a$ (-) is lactose activity, $\gamma$ (-) is an activity coefficient, $R$ (J.gmol$^{-1}$.K$^{-1}$) is the universal gas constant, $T$ (K) is temperature and * represents the property at saturation.

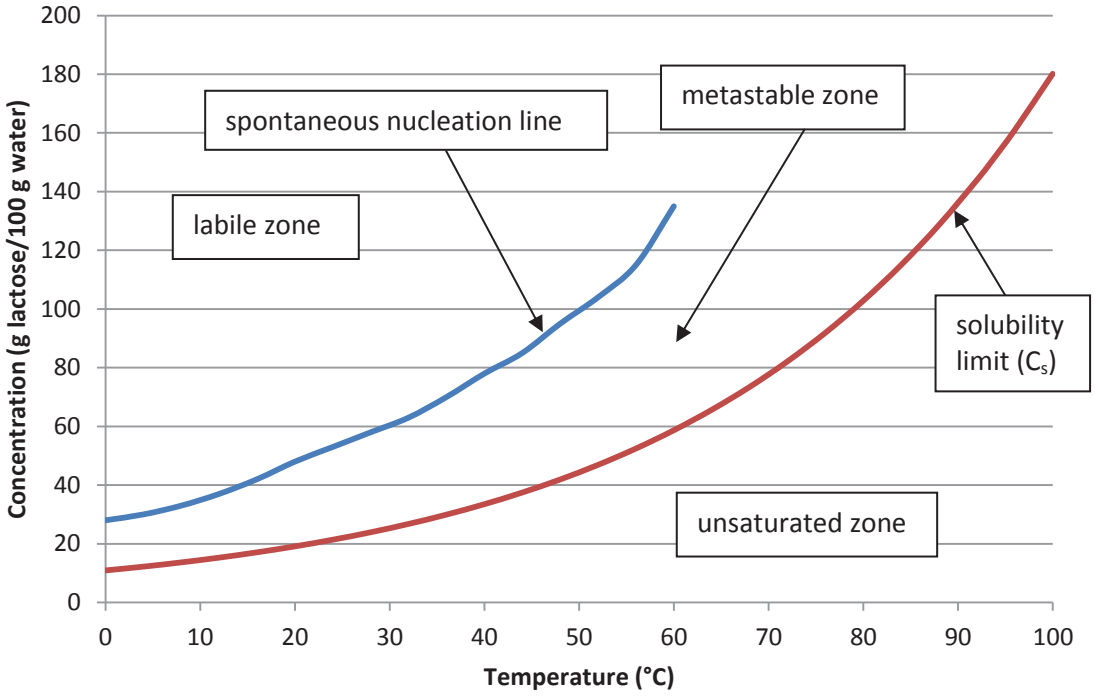


Figure 6 Lactose solubility curve; using equations from McLeod (2007)

As will be discussed in the following sections, crystallization is a two-step process (Myerson, 2002):

- Separation or birth of new crystals (nucleation)
- Growth of new crystals

### *2.3.1 Lactose Nucleation*

Nucleation is the spontaneous formation of crystals under the condition of a supersaturated solution. Myerson (2002) listed the following mechanisms for nucleation:

| **Primary** | **Secondary** |
|---|---|
| Homogeneous | Initial Breeding |
| Heterogeneous | Polycrystalline Breeding |
| | Macroabrasion |
| | Dendritic |
| | Fluid Shear |
| | Contact |

Primary homogeneous nucleation occurs under the condition of a pure solution; water and only the product to be crystallized. Primary heterogeneous nucleation occurs when there are foreign particles in the solution, and is discussed further in Section 2.3.1.1. Secondary nucleation is known to occur when there are crystals of the same species present in the supersaturated solution, and is discussed further in Section 2.3.1.3.

Different rates of nucleation will occur depending on the location of the system with regards to the solubility limit (Figure 6). When passing across the solubility limit from the unsaturated region, the supersaturated zone can be further divided into two regions, “metastable” and “labile” (Herrington, 1934; Ting & McCabe, 1934). Originally the metastable region was defined as the zone where inoculation (of seed crystals) was necessary for the crystallization process to occur, and crystal growth developed from the seed crystals only. The metastable zone was later altered to the region where the probability of nucleation occurring was very small (~0), and thus crystallization was slow and difficult. Alternatively, the labile region is where spontaneous nucleation occurs, or later defined as the region where crystallization probability is high and thus fast and easy. There is a broad transition region between the metastable and labile regions. It has been shown that it is possible to move from the metastable region to the labile region with no crystallization occurring by carefully controlling and eliminating mechanical shock (Ting & McCabe, 1934). It was also found that the weight and size of the seed crystals, and stirring speed has an effect on nucleation.

Erdemir, Lee, and Myerson (2009) developed a two-step model to describe the nucleation of crystals from solution and compared their results to the classical one step model. The classical model states organized clusters group together to form nuclei; however the two-step model

suggests a more complicated route of a significantly sized cluster forming first, followed by a reorganization of that cluster into an ordered structure; depicted in Figure 7.

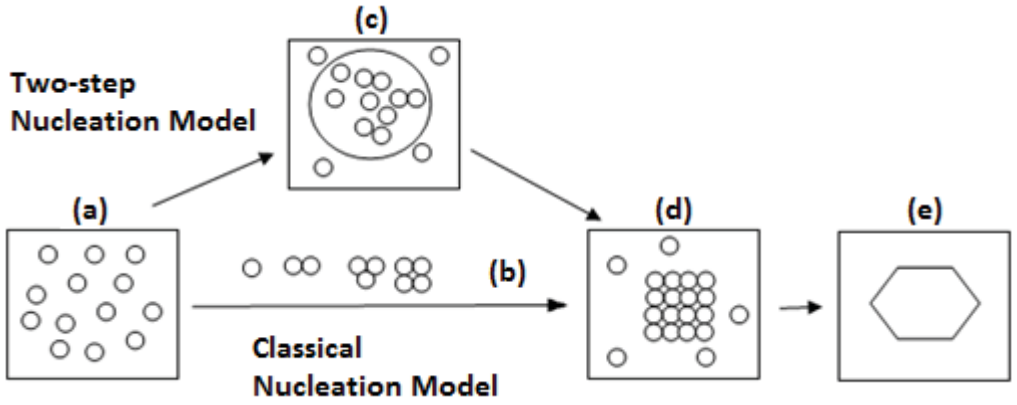


**Figure 7 Crystal pathways for the classical nucleation model and two-step model: (a) supersaturated solution, (b) ordered subcritical cluster, (c) liquid-like cluster, (d) ordered crystalline nuclei, (e) solid crystal; redrawn from Erdemir *et al*., (2009)**

Erdemir *et al*., (2009) has asserted that classical nucleation theory is based on many flawed assumptions:

- Clusters are modelled as spherical drops, having uniform interior densities and sharp interfaces; leads to assumption that nuclei embryos have the same molecular arrangement as that in a large crystal
- Curvature dependence of surface tension is neglected
- Growth of clusters takes place one monomer at a time; also pre-existing cluster interactions and breakages are ignored
- Nucleation rate is time-independent; process is considered in terms of steady state
- Clusters are incompressible and the vapour surrounding them is an ideal gas, thus formation of clusters does not change the vapour state

#### 2.3.1.1 Primary Nucleation

Supersaturation, Equation 3, is the main driving force for primary nucleation and can be represented as the difference in chemical potential between crystal phase and solution phase.

$$\Delta\mu = \mu - \mu^* = kT_K lnS_R$$

**Equation 3 Nucleation driving force equations (Kashchiev & van Rosmalen, 2003; McLeod, 2007; Myerson, 2002)**

where $k$ (J.K$^{-1}$) is the Boltzmann constant, $T_K$ (K) is the absolute temperature of the solution, $S_R$ is the supersaturation ratio ($C/C^*$), and $C$ (#.m$^{-3}$) is concentration of crystals in solution.

Classical nucleation theory describes the variables that affect the rate of primary nucleation.

The homogeneous primary nucleation rate, $J_{Hom}$ (#.m$^{-3}$.s$^{-1}$), Equation 4, is derived from the Arrhenius reaction velocity equation. The # symbol is used henceforward to signify number.

$$J_{Hom} = a_1 exp\left(\frac{16\pi\sigma_i{}^3 V_m^2}{3(kT_K)^3(lnS_R)^2}\right)$$

Equation 4 Homogeneous primary nucleation equation (Kashchiev, 2000)

where $a_1$ (#.m$^{-3}$.s$^{-1}$) is the pre exponential factor, $\sigma_i$ (J.m$^{-2}$) is the interfacial energy and $V_m$ (m$^3$) is the molecular volume.

Heterogeneous primary nucleation rate, $J_{Het}$ (#.m$^{-3}$.s$^{-1}$), Equation 5, occurs via a surface and includes a factor, $q_1$ (-), which compensates for the reduced energy barrier to be overcome, caused by the surface.

$$J_{Het} = a_1 exp\left(\frac{16\pi\sigma_i{}^3 V_m^2(q_1)}{3(kT_K)^3(lnS_R)^2}\right)$$

Equation 5 Heterogeneous primary nucleation equation (Kashchiev, 2000)

Total primary nucleation, $J_T$ (#.m$^{-3}$.s$^{-1}$), Equation 6, is a combination of homogeneous and heterogeneous nucleation; however heterogeneous nucleation will dominate due to the lower energy barrier.

$$J_T = J_{Hom} + J_{Het}$$

Equation 6 Total primary nucleation (Kashchiev, 2000)

### 2.3.1.2 Induction Time

Induction time is the period of time before an observable number of nuclei can be seen following the initiation of supersaturation. Induction time therefore relates the ability of the system to stay in metastable equilibrium and is useful when studying primary nucleation. Following theoretical consideration, induction time is generally split into three time periods: the relaxation time, the nucleation time and the growth time. Relaxation time refers to the time for cluster distributions to react to imposed supersaturation, nucleation time refers to the time to produce stable nuclei (Equation 8), and growth time refers to the time to observe nuclei. The time it takes to detect an evident number of nuclei, $t_N$ (s), can be seen through the relationship of nuclei number per volume, $N_N$ (#.m$^{-3}$), and $J_T$, Equation 7.

$$t_N = \frac{N_N}{J_T} = \frac{N_N}{a_1 exp\left(-\frac{16\pi\sigma_i{}^3 V_m^2}{3(kT_K)^3(lnS_R)^2}\right)}$$

Equation 7 Induction time

The critical nucleus size, $n_c$ (#), number of molecules making up a particle which does not dissolve back into solution, can be predicted by Equation 8 (Kashchiev, 2000).

$$n_c = \frac{32\pi V_m^2 {\sigma_i}^3}{3(kT_K)^3(lnS_R)^3}$$

Equation 8 Critical nucleus size (Kashchiev, 2000)

### 2.3.1.3 Secondary Nucleation

Secondary nucleation occurs in the presence of other materials, and a common instance is from crystal seeding. Secondary nucleation is the dominant nucleation mechanism in the metastable region (Figure 6) and in industrial crystallizers because a lower energy barrier is required to be overcome. Collision, attrition and contact, and shear nucleation are the dominant secondary nucleation mechanisms in industrial processes (Agrawal, 2012). Attrition is the breakage of crystal into smaller pieces, contact refers to crystal impact with a surface (e.g. impeller), and shear refers to the movement of fluid past a crystal. It is theorised via these mechanisms that pre-critical clusters are removed from the crystal surface and grow into new nuclei. In a sucrose crystallization experiment (Srisa-nga, Flood, & White, 2006), it was found that the secondary nucleation threshold (SNT) decreased as the induction time increased, and was independent of temperature when absolute supersaturation was used for the driving force. The SNT is the lower limit of the metastable zone, in which secondary nucleation occurs.

### 2.3.1.4 Effects of Mixing

Nucleation of α-lactose monohydrate is greatly affected by mixing (Raghavan, Ristic, Sheen, & Sherwood, 2001; Shi, Liang, & Hartel, 1990; Vallevega & Nickerson, 1977), even though fundamental nucleation equations do not incorporate a mixing term. It is therefore important to consider the different types of mixing and mixing effects in any crystallization process. Some of the mixing techniques below are covered in more detail in section 2.4.1 Nucleation Techniques.

#### *2.3.1.4.1 Ultrasound and Orifice Flow*

McLeod (2007) undertook a review on the previous research articles that used ultrasound for nucleation and growth in crystallization, for which there were many. Ultrasound is used to enhance nucleation because it causes cavitation. Orifices apply a restriction in the flow, causing cavitation as well. Newly formed cavitation sites act as nucleation sites. The effect of cavitation sites forming and collapsing is reported to: increase mass transfer, improve the diffusion process, and decrease induction time.

A study into rapid lactose recovery (Bund & Pandit, 2007b) from paneer using sonocrystallization found that seeding and pH levels were the most influential parameters for maximizing lactose recovery and purity. A lactose recovery of more than 90% and purity of 97 to 99% can be obtained with paneer whey with 1 hour stirring time and effective ethanol concentration of 85% v/v (Bund & Pandit, 2007a). The roundness and elongation of the crystals obtained were found to be comparable to commercial analytical grade lactose. McLeod (2007) experiments investigating venturi flow found that varying the orifice diameter affected the nucleation rate, but remained constant once a critical supersaturation was reached. Application of ultrasound and orifice flow studies shows the possibility for producing a desired number of nuclei.

#### *2.3.1.4.2 Agitation*

Agitation or mixing is generally used to combine two different materials. However in the case of primary nucleation of crystals, there is only one phase. The effects of mixing can be summarized as follows: increasing the amount of agitation increases the amount of nucleation and decreases the induction time; however the overall particle size is decreased with increasing agitation (McLeod, 2007).

McLeod (2007) carried out experiments to investigate the effects of mixing on nucleation, which included: agitation, shear and flow through a venturi. Overall, it was concluded agitation increases nucleation rate which is in agreement with other studies. Mechanical mixing, with a Rushton turbine, was found to increase nucleation with increasing turbine speed, explained by the Strouhal relationship.

#### *2.3.1.4.3 Shear Flow*

The crystallization literature has shown consistently that for the crystallization of polymers, increasing the shear effect also increases nucleation. However, it is less definitive for colloidal suspensions; shear has been reported to decrease and enhance nucleation rate (McLeod, 2007). Above a certain shear rate it has been found that no changes in nucleation rates occur (Agrawal, 2012).

### *2.3.2 Lactose Growth*

Crystals from the nucleation phase of crystallization are formed at the smallest size possible for the particular imposed conditions (Equation 8). The crystals subsequently grow due to the surrounding supersaturated condition and solute molecules will add to the nuclei; this is

known as crystal growth. Crystal growth can be considered to follow these steps (Farhadi & Babaheidary, 2002):

- Bulk diffusion of growth units through the diffusion boundary layer
- Surface diffusion of growth units through the adsorption layer
- Integration of growth units into the crystals

From analysis of these three steps it can be seen that the slowest step will be the limiting or controlling factor for crystal growth, and different growth patterns would be exhibited depending on the limiting step.

The growth of crystals is often defined in terms of a change in a particle dimension with time, known as linear growth rate, but can also be related to a particular face such as the second largest face of the crystal (Myerson, 2002). The majority of lactose crystal growth was found to occur in one direction of its principle axis (Dincer, Parkinson, Rohl, & Ogden, 1999; van Kreveld & Michaels, 1965) giving rise to the typical tomahawk shape of lactose; as shown in Figure 3. It has been found that the growth rate of a broken crystal is faster until the damage area is restored, but if the top of crystal is broken off, it does not grow back (van Kreveld & Michaels, 1965).

Crystal growth is considered to occur via two mechanisms, spiral and two-dimensional growth. In a recent article (Dincer, Ogden, & Parkinson, 2009a) it has been confirmed that spiral growth occurs on the (010) face of the α-lactose monohydrate crystal. The following four models, spiral growth $G_s$ (μm.min$^{-1}$), mononuclear growth $G_m$ (μm.min$^{-1}$), polynuclear growth $G_p$ (μm.min$^{-1}$) and birth and spread growth $G_B$ (μm.min$^{-1}$), were used in looking at growth on the (010) face of the α-lactose monohydrate crystal by Dincer *et al.,* (2009a):

$$G_s = F_s \frac{\sigma^2}{\sigma_1} \tanh \frac{\sigma_1}{\sigma} \; and \; \sigma_1 = 9.5\gamma_i \alpha_d / \varepsilon_s kT x_s$$

**Equation 9 Spiral growth model**

$$G_m = k_g s^3 (lns)^{1/2} e^{-\frac{\emptyset_b{}^2}{3(kT)^2 \ln(s)}}$$

**Equation 10 Mononuclear growth model**

$$G_p = k_g (s-1)^{\frac{2}{3}} s^{\frac{1}{3}} (lns)^{1/6} e^{-\gamma_i{}^2 / 3(kT)^2 \ln(s)}$$

**Equation 11 Polynuclear growth model**

$$G_B = k_g (s-1)^{5/6} e^{-\gamma_e{}^2 V_m h_s \pi / 3(kT)^2 (s-1)}$$

**Equation 12 Birth and spread growth model**

$$s = \frac{C_T}{C_S - f_1 K(C_T - C_S)}$$

Equation 13 Supersaturation ratio (Visser, 1982)

$$\sigma = (C_T - C_S)/C_S$$

Equation 14 Relative supersaturation (Zumstein & Rousseau, 1987)

where $C_s$ (g lactose/100 g water) is the equilibrium solubility of lactose, $C_T$ (g lactose/100 g water) is the supersaturated bulk concentration, $\sigma$ (-) is the relative supersaturation, $\sigma_1$ (-) and $F_s$ (µm.min$^{-1}$) are BCF model constants, $\gamma_i$ (J) is the edge free energy of a growth unit at the edge of a step, $\gamma_e$ (J.m$^{-2}$) is the edge free energy, $\alpha_d$ (m) is the distance between incorporated growth units, $\varepsilon_s$ (#) is the number of incorporating spirals, $x_s$ (m) is the mean distance travelled by an absorbed molecule before it desorbs, $k_g$ (µm.min$^{-1}$) is the growth rate constant, $h_s$ (m) is the step height, $\emptyset_b$ (J) is the bond energy, *s* (-) is the supersaturation ratio and $f_1$ (-) is the temperature dependent factor for the depression of solubility of α-lactose by β-lactose.

The linear growth rate of lactose is commonly expressed as power law function of supersaturation (Butler, 1998):

$$G = k_{gs} \Delta C^{n_1}$$

Equation 15 Liner growth rate expressed as a power law function of supersaturation

$$\Delta C = C_T - C_s$$

Equation 16 Supersaturation

where *G* (µm.min$^{-1}$) is the linear growth rate, $k_{gs}$ (µm.min$^{-1}$.100 g water/g lactose) is the linear growth rate constant, $n_1$ (-) is the exponent for crystal growth, and *ΔC* (g lactose/100 g water) is the supersaturation.

The effects of supersaturation and temperature are known to alter crystal growth behaviour and many articles result in contradictory information. Calculations by Butler (1998) using $k_{gs}$ incorporated a relationship for changing temperature; however McLeod (2007) found when using absolute alpha supersaturation, temperature was independent and a constant value for $k_{gs}$ could be used.

### 2.3.2.1 Effects of Impurities

Understanding the effect of impurities is important as they can cause changes in the growth rate. Many impurities act as a growth inhibitor for lactose crystallization. This can be seen with slower growth rates for pharmaceutical grade lactose compared to non-ionic lactose, where

the growth inhibitor lactose phosphate has been removed (Dincer*, et al.*, 2009a). Different salts can positively or negatively affect lactose crystallization; Butler (1998) has reviewed the literature on the effects of different salts on lactose crystallization and her findings are summarised as follows:

- Increase or decrease the growth rate depending of the type and concentration of salts
- Decrease lactose solubility

The morphology of the crystal can also be altered by impurities; for example as β-lactose concentration is increased there is an increase in growth in the a and b direction for α-lactose monohydrate crystals (Dincer*, et al.*, 1999). In general, the effects of impurities can be summarised as follows (Roetman, 1972):

- Shield the crystal surface preventing molecules from becoming incorporated into the crystal lattice
- Change the supersaturation and thus change lactose solubility
- Change the viscosity and diffusivity and effective diffusivity of the solution
- Change the rate of mutarotation and α-lactose availability

### *2.3.3 Growth Rate Dispersion*

Growth rate dispersion (GRD) causes a widening of the PSD. GRD is known to occur even when crystals are growing under identical conditions, such as temperature, supersaturation, and time. Understanding GRD is important when developing methods for producing IGL with a narrow PSD.

Growth rate dispersion is manifested in crystallizing lactose solutions as a range of growth rates in seed populations (Jelen & Coulter, 1973; Liang, Hartel, & Berglund, 1987). This gives rise to different sized crystals. Shi, Hartel and Liang (1989) carried out experiments looking at the growth of single crystals under identical conditions. They found that each crystal had a different but constant growth rate; known as the constant crystal growth (CCG) model. The current view of growth rate dispersion is a deviation on McCabe's ΔL law (McCabe, 1929) which proposed that all crystals grow with the same linear growth rate when subjected to identical growing conditions. Another difference is that the crystal growth rate is not affected by crystal size, and in fact no correlation can be found between growth rate of individual lactose crystals and their particle size (Shi*, et al.*, 1989; Zumstein & Rousseau, 1987). It has been proposed by Zumstein and Rousseau (1987), that the cause of growth rate dispersion is a result of dislocation of the networks of individual crystals, and that the effects of growth rate dispersion will vary because dislocation networks will vary between seed crystals and larger

developed crystals. It has also been proposed that the variation in number and location of spirals (growing on crystal faces) could be a cause of growth rate dispersion (Dincer, *et al.*, 2009a).

The dependence of the crystal growth rate, $G$, on relative supersaturation, $\sigma$, is given by the Burton-Cabrera-Frank (BCF) growth theory below (Zumstein & Rousseau, 1987):

$$G = a_2 \frac{\epsilon\sigma^2}{\sigma_1} \tanh \frac{\sigma_1}{\epsilon\sigma}$$

**Equation 17 Burton-Cabrera-Frank growth theory**

where $\epsilon$ (-) is the screw dislocation activity and $a_2$ (µm.min$^{-1}$) is a constant.

Growth rate can also be approximated by a power law expression:

$$G = k_g \sigma^{n_1}$$

**Equation 18 Growth rate power law expression**

where $k_g$ and $n_1$ are found by fitting to growth kinetic data.

The distribution parameters, $\overline{k_G}$ (µm.min$^{-1}$) and $\sigma_{kg}^2$ (µm$^2$.min$^{-2}$), are related to the mean, $\overline{G}$ (µm.min$^{-1}$) and variance of the distribution of crystal growth rates $\sigma_G^2$ (µm$^2$.min$^{-2}$) by:

$$\overline{G} = \overline{k_G} \sigma^{n_1}$$

**Equation 19 Mean time averaged crystal growth rate**

$$\sigma_G^2 = \sigma_{kg}^2 \sigma^{2n_1}$$

**Equation 20 Variance of crystal growth rate**

β-Lactose has been found to change the morphology of α-lactose monohydrate crystal (Dincer, *et al.*, 1999). Dincer, Ogden, and Parkinson (2009a, 2009b) confirmed that α-lactose monohydrate crystals display different growth rates for the particular faces when considering the tomahawk structure (Figure 3). Varying growth rates have been attributed as a cause for growth rate dispersion. For example the $(0\bar{1}\bar{1})$ face grows the fastest when β-lactose concentrations are low. However, since β-lactose has the same galactose moiety as the α-lactose, β-lactose joins to the glucose molecule on the $(0\bar{1}0)$ and the $(0\bar{1}\bar{1})$ face. The result of an increase in β-lactose concentration is that the once fast growing $(0\bar{1}\bar{1})$ face is now slow growing because of the growth inhibition effect of the integrated β-lactose.

Growth rate and growth rate dispersion are similar for the (010), (110) and (100) faces, where the overall growth rate of the lactose crystal is similar to the (100) face. The variance in growth rate dispersion for the (010) face is twice that of the (110) and (100) faces and 10 times that of

the $(0\bar{1}\bar{1})$ for the same temperatures and supersaturation (Dincer, Ogden, & Parkinson, 2009b).

Growth rate, $G$, is related to supersaturation, $s$, by the equation given by Dincer *et al.*, (2009b):

$$G = k_0 \exp(-\frac{E_a}{RT})(s-1)^{n_1}$$

**Equation 21 Growth rate related by supersaturation**

where $k_0$ (μm$^2$.min$^{-2}$) is the frequency factor and $E_a$ (kcal.mol$^{-1}$) is the activation energy.

The variances for growth rate, $\sigma_G^2$ (μm$^2$.min$^{-2}$), can be found from the following equations where variance increases exponentially with temperature and supersaturation (Dincer*, et al.*, 2009b; Shi*, et al.*, 1989):

$$\sigma_G^2 = a_1(s-1)^{b_1}\exp(-\frac{E_a}{RT})$$

**Equation 22 Growth rate variance**

where the constants $a_1$ and $b_1$ (-) are developed from non-linear regression.

However, experimental data has shown at low relative supersaturation below 0.6 the previous equation does not hold, and the following equation was developed (Dincer*, et al.*, 2009b):

$$\sigma_G^2 = a_1 exp(b_1(s-1))\exp(-\frac{E_a}{RT})$$

**Equation 23 Growth rate variance at low supersaturation**

### 2.3.3.1 Common History Seed

The use of common history seed crystals (Butler, 1998) is a particularly useful method for modelling the growth rate dispersion of lactose crystallization in a batch setup. Common history seed crystals are defined to all have had the same growth conditions (temperature, supersaturation and time) and to have been nucleated at the same time. Sizes of common history seed crystals are directly proportional to the growth rate multiplied by growth time, and each crystal has an inherent growth rate which leads to growth rate distribution (Figure 8).

The use of common history seed crystals is underpinned by three assumptions:

1. Each crystal has a constant relative growth
2. No further nucleation occurs after the initial nucleation event
3. No breakage or agglomeration occurs during growth

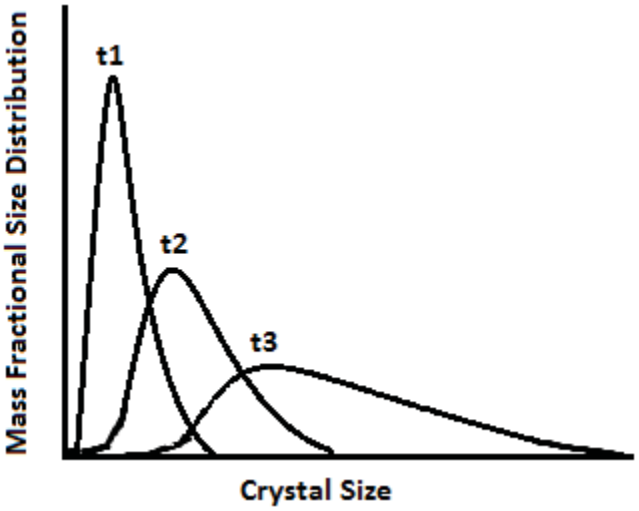


Figure 8 Growth of common history seed plotted on a linear scale; redrawn from Butler (1998)

### *2.3.4 Crystal Growth Measurement Techniques*

There has been a great deal of research into various techniques for measuring crystal growth, and the following list summarizes these with correlating articles.

Comparative techniques:

- Comparing the rate of concentration change (Haase & Nickerson, 1966; Twieg & Nickerson, 1968; Whittier & Gould, 1931)
- Comparing the size of individual crystals (Michaels & van Krevald, 1966; van Kreveld & Michaels, 1965)
- Clusters of crystals (Nickerson & Moore, 1974)

Quantitative measurements:

- Increase in weight (Bhargava & Jelen, 1996; Jelen & Coulter, 1973)
- Increase in weight of seed crystals (Thurlby, 1976)
- Equivalent circular diameter (Shi*, et al.*, 1989)
- Equilibrium crystal size (Shi*, et al.*, 1990)
- Heat of crystallization (Darcy & Buckton, 1998; Darcy & Wiencek, 1998)
- Weight (Achilles, 1997)
- Concentration (Loffelmann & Mersmann, 2002)

Water activity:

It is possible to determine the amount of α-lactose monohydrate from the water activity, thus not being affected by coloured solution if using typical refractive techniques. The following

linear relationships were experimentally developed for lactose with a mean absolute error of 0.037% (Bhandari & Burel, 2007):

Pure lactose solution, $\Delta L_m = 1874.4\Delta a_w$ and whey solution, $\Delta L_m = 1155.2\Delta a_w$

where $\Delta L_m$ (g lactose/100 g water) is amount of α-lactose monohydrate crystals and $\Delta a_w$ (-) is the difference in water activity after and prior to crystallization.

Raman spectroscopy:

Raman spectroscopy has successfully been used to distinguish between samples containing α-lactose monohydrate and amorphous lactose (Murphy, Prescott, & Larson, 2005). X-ray powder diffraction is commonly widely used but requires advanced hardware and thermal analytical techniques and is also used for semi-quantitative determination of crystallinity of lactose samples with amorphous regions.

Refractometry and laser light scattering have been used to measure lactose growth kinetics such as growth rate constant and overall crystal size respectively (Mimouni, Schuck, & Bouhallab, 2005).

### *2.3.5 Industrial Crystallization*

Industrial lactose crystallization processes use concentrated whey permeates as feed stocks (Figure 9). In addition to this, there is a preference for using sweet whey over acid whey. Sweet whey with a pH of 5.9-6.3 is considered better then acid whey with a pH of 4.4-4.6 because of the extra problems created from the high mineral concentration. Protein is removed to give a whey protein concentrate stream, the concentrated lactose permeate is then crystallized in large temperature-controlled batch crystallizers. The crystal slurry is put through a separation stage of washing and drying to obtain final dried crystals. Butler (1998) investigated industrial crystallized lactose characteristics, such as growth rates, solubility, mutarotation kinetics and equilibrium alpha lactose ratio in permeate, concluding simulated whey ultra-filtrate embodied these factors well.

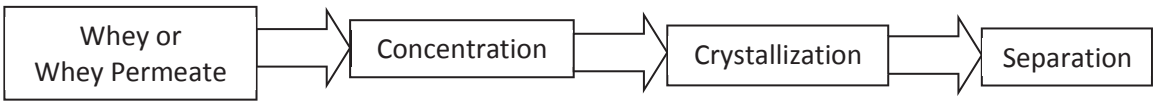


**Figure 9 Generalized industrial lactose crystallization process**

Typically the industry $d_{50}$ crystal size is large, generally ranging from 200 to 500 μm, with a span in the range of 2 to 2.5 (Werner, Tretiakov, Paterson, & McLeod, 2002). The industrial focus is to maximise yield and therefore maximise the $d_{50}$ particle size; span is usually an

afterthought. Typical IGL has a smaller $d_{50}$ and a narrower span; modified or alternative production processes are required.

## 2.4 Narrowing the Particle Size Distribution

Many processes require particles with a small distribution of particle sizes, however the lactose industry typically uses stirred batch crystallization processes and a wide distribution band of particles is produced. New methods targeting nucleation and growth aspects have to be designed to produce the narrow and consistent PSD that is required for IGL. Modifications to existing commonly used industry techniques may also be appropriate.

### *2.4.1 Nucleation Techniques*

#### 2.4.1.1 Single Nucleation Event

Primary and secondary nucleation is a major factor contributing to the widening of the PSD. If the crystallization process can be limited to a single nucleation event, then variation in the PSD will be due to differential growth rates alone. New techniques to achieve this are being developed, such as the application of ultrasound energy or orifice flow to supersaturated lactose. Through the use of ultrasonic assisted crystallization, factors such as size, shape, surface and PSD can be controlled. The application of ultrasound causes cavitation, which causes a sudden increase in supersaturation, and thus nucleation is also increased. Experiments showed that the best results for ultrasonication and controlling the PSD of lactose came when glycerin was also added to the solution (Dhumal, Biradar, Paradkar, & York, 2008). Approximately 50% of particles were found in the desired size range of 63 to 90 µm compared to approximately 30% under normal batch crystallization. A similar study on salbutamol sulphate crystallization for pulmonary delivery found sonocrystallization produced fine elongated crystals, in addition higher ultrasound amplitudes and lower temperatures produced smaller crystals with a narrower PSD (Dhumal, Biradar, Paradkar, & York, 2009).

Flow through an orifice is another technique which could be used to produce a single nucleation event. Orifice flow causes cavitation, which some attribute to temporary increases in supersaturation, similar to ultrasonic energy. McLeod (2007) concluded using flow through venturi increased nucleation and was related to the orifice dissipating energy. This study also showed the possibility for a single nucleation event to produce a desired and known number of nuclei; Figure 10 shows a strong negative linear trend for crystals numbers formed and Cavitation number. Continuous orifice nucleation is discussed further in Chapter 5. Use of this

technique in combination with limitation of further primary and secondary nucleation, could prove to be a successful way to produce a narrow PSD.

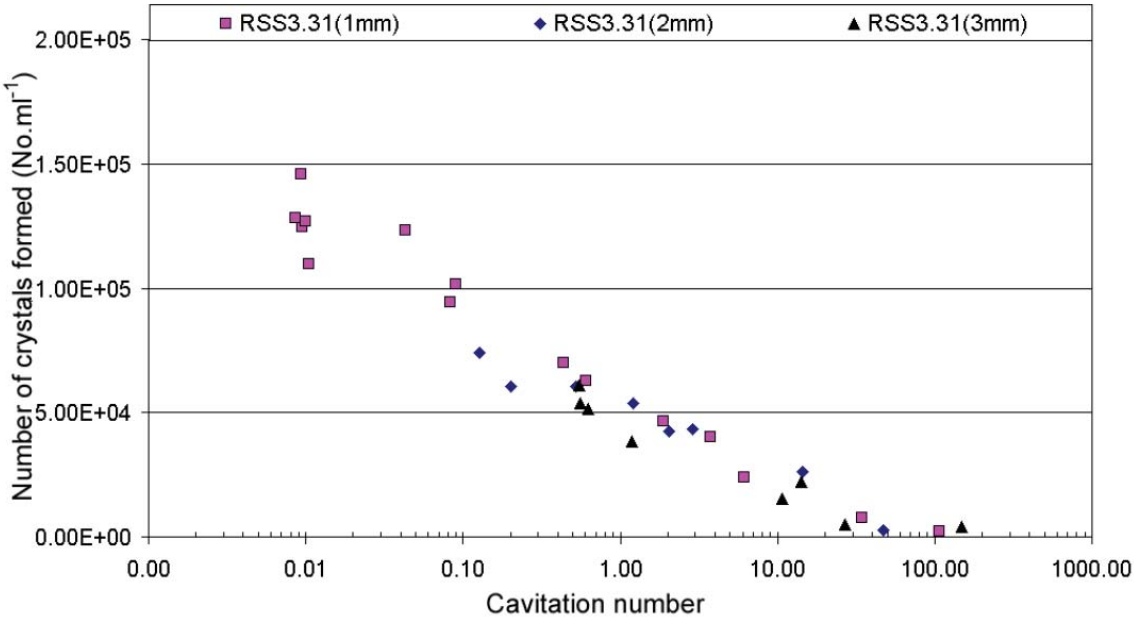


**Figure 10 Number of crystals formed versus cavitation number for varying office diameters and constant relative supersaturation; reproduced with permission from McLeod (2007)**

### 2.4.1.2 Supercritical Fluids

The use of dense gases or supercritical fluids for processing pharmaceutical compounds has been discussed in detail by Foster *et al*., (2003) in a review article. A promising supercritical fluid technique reviewed was the Aerosol Solvent Extraction System (ASES); see Figure 11. An organic solvent is mixed with a dense gas antisolvent, and sprayed into a vessel. The solute is precipitated and extracted from the solvent because supersaturation occurs. Small and uniform particles can be generated from a high supersaturation. Rapid expansion of supercritical solutions (RESS) offers fine particles with a narrow PSD, if a compound is soluble in the supercritical solvent (Jarzebski & Malinowski, 1995). Gas-antisolvent crystallization (GAS) is where a compound is first dissolved in a liquid, which has a greater solubility than in the super critical antisolvent.

Research into the use of solution enhanced dispersion by supercritical fluids (SEDS) on lactose (Palakodaty, York, & Pritchard, 1998), found that the rate of crystallization could be altered by changing the carbon dioxide flow rate. The morphology of the resulting crystals was also affected and the mean particle size was between 5 and 31 microns. Though not relevant to lactose crystallization due to small particle sizes produced, SEDS has been shown to be

successful in producing lactose blends with certain drugs for inhaler devices (Schiavone, Palakodaty, Clark, York, & Tzannis, 2004).

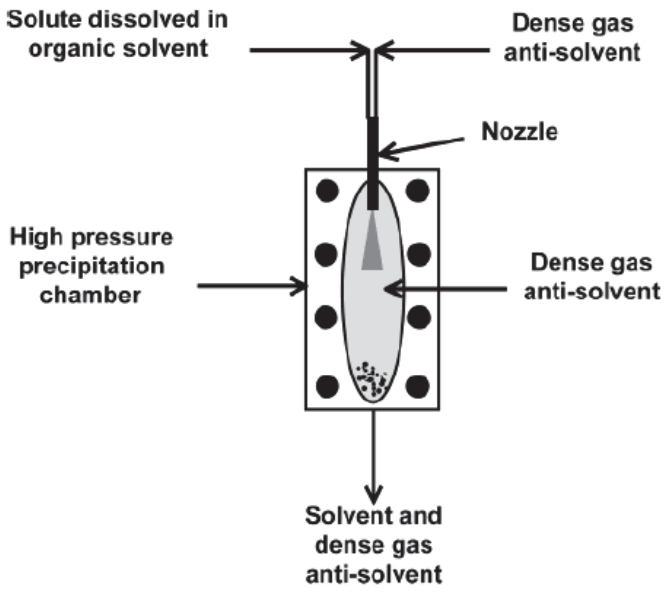


Figure 11 Schematic diagram of the ASES process; reproduced with permission (Foster *et al.*, 2003)

### 2.4.1.3 Seeding

Seeding is widely used to control the PSD. By limiting primary nucleation, seeding can be used to produce the desired secondary nucleation. In an ammonium sulphate crystallization seeding experiment (Kalbasenka, Spierings, Huesman, & Kramer, 2007), it was found that the seeded batch experiments produced a median crystal size with a lower spread than that of an un-seeded crystallization, and hence a lower PSD. Approximately 100 µm sieved seeds were used, because below this size the seeds would dissolve in the initial solution. It was found that there was initially negative growth as fines dissolved, followed by positive growth. In a similar manner, a bisulfate salt was crystallized with a lower PSD (Kim *et al.*, 2005). Although this work focused on the acid base reaction for the salt produced, it was found that the seeds acted as nuclei for growth. Also, by keeping the working level of supersaturation low, the secondary nucleation rate can be limited and thus the PSD narrowed.

In a seeding study involving potassium alum (Doki, Kubota, Sato, & Yokota, 2001; Kubota, Doki, Yokota, & Sato, 2001), it was found that a unimodal crystal product distribution could be obtained once the critical seed concentration was reached. This occurred regardless of the cooling mode used. Secondary nucleation is known to occur at high supersaturation concentrations. Higher seed loading produced lower supersaturation peaks compared to lower seed loading; thus secondary nucleation is decreased at higher seed loading.

### *2.4.2 Growth Techniques*

#### 2.4.2.1 Droplet-Based Crystallization

Monodisperse emulsions are gaining interest as a method for controlling the PSD. Emulsions consist of a dispersed and continuous phase, both of which are liquid. Using techniques to control the size of the dispersed phase droplets, it is possible to control the upper size limit of a crystal growing within a droplet. This is because the aqueous dispersed droplet is a reservoir with a defined amount of solute. Slow and fast growing crystals are controlled to reach the same final particle size after excess time; see Figure 12.

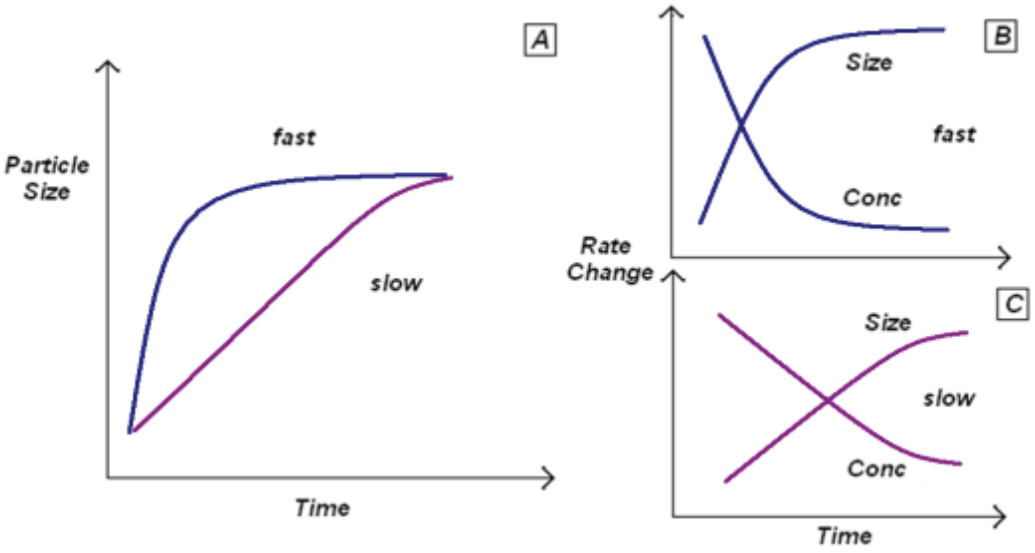


**Figure 12 Single crystal growth within a drop, A: Change in particle size with time for fast and slow growing crystals, B&C: Rate change of size and concentration with time for fast and slow growing crystals**

The fast growing crystal will utilise all solute and stop growing, whereas the slow growing crystal will take a longer time to use all the solute, but both crystals will reach the same final particle size (R. D. Dombrowski, Litster, Wagner, & He, 2007). This method effectively counteracts growth rate dispersion. A potential problem with this technique occurs in microemulsions where the solute is able to transfer between droplets in the dispersed phase leading to uncontrolled conditions (Elwell, Roberts, & Coupland, 2004).

Monodisperse emulsions must have a CV, Equation 24, of less than 10%, and different methods are capable of achieving this. A technique which achieved a droplet CV of less than 10% was straight through microchannel emulsification (Kobayashi, Mukataka, & Nakajima, 2005). This technique pushes the dispersed phase up through a microchannel plate containing small oblong gaps of known dimensions into the continuous phase flowing past. This particular technique was also shown to have a relatively high throughput.

$$CV = \frac{SD}{\bar{x}}$$

**Equation 24 Coefficient of variation (spread of size distribution)**

where *CV* (-) is the coefficient of variation and *SD* (-) and $\bar{x}$ (-) are the number-based standard deviation and mean of measured drop or crystal size.

Reversed micelles can be defined as emulsions of water in oil (Yano, Furedi-Milhofer, Wachtel, & Garti, 2000), where water droplets are dispersed via a surfactant. It is possible to control and study crystal growth when nucleating within reversed micelles.

By controlling the conditions for the emulsions it is also possible to change the properties of the crystals formed. In the crystallization of glycine it was found that β and μ polymorphic forms were found in the emulsions where normally only the α polymorph is found from bulk solution crystallization (Allen *et al.*, 2002). It was also found that while macroemulsions, drop diameter greater than 0.1 μm, can control crystal size, microemulsions cannot as there is material transfer between droplet boundaries (micellar domains) and crystals grow significantly larger than the original microemulsion domain size.

Choice and mode of action for the emulsifier is essential when using emulsions as a means of controlling size and morphology of crystals (Davey, Hilton, & Garside, 1996). Emulsions are greatly affected by the dispersion phase hydrophobicity and mixed surfactant concentration, and by controlling these, droplet size and PSD is altered (Yuyama, Watanabe, Ma, Nagai, & Omi, 2000). The smaller the droplet, in microemulsions for example, the greater the undercooling required for crystallization (Montenegro, Antonietti, Mastai, & Landfester, 2003). An increase in undercooling is attributed to the suppression of heterogeneous nucleation and the associated increase in the size of the metastable region (Montenegro*, et al.*, 2003).

The use of emulsions is one method for creating a drop-based environment for crystallization. It is also possible to create droplets within a carrier fluid spatially confined by external equipment. R. D. Dombrowski *et al.*, (2007) created lactose droplets of a known volume into a carrier fluid which was subsequently held in capillary tubing, with a diameter close to the droplet diameter. This technique was highly effective for narrowing the PSD, the crystal CV was as low as 7% (span much less than 1), when considering drops with only one nucleated crystal. However, a problem common to drop-based crystallization techniques is zero or multiple crystals nucleating within a single drop; as shown in Figure 13. This leads to a wider PSD and increases the crystal CV to 16%, which is still better than the typical bulk crystallization CV of 40% (span less than 1 and approximately 2 respectively).

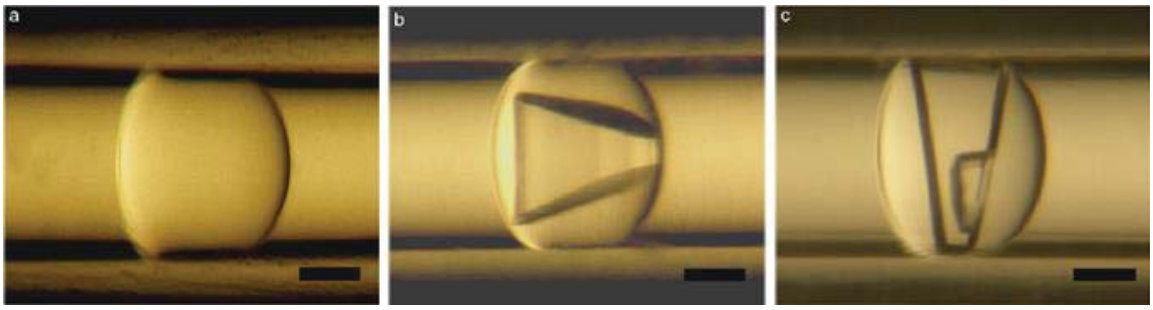


**Figure 13 Lactose crystals growing within a drop; reproduced with permission (R. D. Dombrowski, *et al.*, 2007)**

Another common issue to drop-based crystallization is ensuring the correct volume of the droplets. This can be overcome using capillary techniques. Capillary flow experiments (Barrero & Loscertales, 2007) have shown it is possible to control droplets down to the nano-meter range. Using this technique there is also control of particle mean size and distribution. Many other similar techniques also exist for achieving the desired result. Most common methodologies for microsphere production (Berkland, Kim, & Pack, 2001) are:

- Precipitation
- Spraying
- Phase separation
- Emulsion techniques

Poly($_{D,L}$-lactide-co-glycolide) (PLG) microspheres have been fabricated via spraying through a nozzle with acoustic excitation and an annular, non-solvent carrier stream (Berkland*, et al.*, 2001). The acoustic method produced droplets down to 30 µm with a very narrow size distribution, greater than 95% were within 1 to 1.5 µm, whereas the carrier stream method produced droplets down to 1 µm but had a wider size distribution.

A microfluidic flow-focusing device was created to generate mono-dispersed droplets of controlled shape and size, 10 to 1000 µm, and then solidified *in situ* (Xu *et al.*, 2005). Along with a narrow size range and a controlled shape of particles, it was found that this technique could be used with a range of materials and also has scale up potential, to produce a large number of particles. Microfluidic crystallizations offer a unique way to control kinetic pathways through the phase diagram and to gain a better understanding of nucleation and growth. Droplet-based microfluidics is usually performed by creating a nano-sized droplet in an inert carrier oil stream. In a recent critical review on microfluidic crystallization (Leng & Salmon,

2009), this technique is becoming increasingly important for studying crystallization; features of this technology are:

- High throughput experiments with low volume (~1 nL) can be achieved
- Exceptional control of mass and heat transfer allow precise kinetic routes to be designed
- New experimental conditions can be created because of less turbulence and gravity effects, confinement and large surface volume ratio

Types of data acquisition for microfluidic crystallization include:

- On-chip solubility measurements
- Probing polymorphism
- Nucleation kinetics (nL scale)
- Confined space nucleation and growth

Ju, Zeng, Zhang, and Xu (2006) used a microchannel reactor to crystallize zeolite NaA (a mixture of silicate and aluminate). The microchannel reactor was essentially stainless steel capillary tubing immersed in an oil bath. Although the aim of this experiment was to create a fast continuous crystallization method, it was also found that the resulting crystals had a narrow PSD compared to typical batch produced crystals.

#### 2.4.2.2 Containerless Protein Crystallization

In typical batch crystallization, the nuclei in the supersaturated solution tend to attach to various surfaces, such as walls, other particles, and the surface in contact with air; as a result this effects the crystal morphology and requires a lower driving force than homogeneous systems (Lorber & Giege, 1995). Lorber and Giege (1995) investigated a novel technique for containerless crystallization in which a crystallization solution was placed at the interface between two silicon fluids, essentially making them floating drops. It was found the behaviour of these crystals was similar to crystals grown in sealed glass tubes, and heterogeneous crystallization was minimized.

In a similar experiment to create containerless conditions and to study nucleation kinetics and induction time, a levitated droplet system was used (Knezic, Zaccaro, & Myerson, 2004). This Electrodynamic Levitation Trap allowed the suspension of a charged microdroplet inside an electric field, where dust and environmental conditions are controlled. Induction times and nucleation of droplets were found to be random, and were in accord with other experimental values in the crystallization literature.

Frontana-Uribe and Moreno (2008) have reviewed and discussed the use of internal and external electric fields in protein crystallization. The use of electric fields is seen as a way to counteract convective mass transport, caused by gravity, and it is believed a crystal with better mechanical and optical properties can be obtained.

#### 2.4.2.3 Gels

Typical batch crystallization requires heavy mixing to suspend the crystals, which avoids caking and undesired aggregates. The main consequence of this is the widening of the PSD due to increased secondary nucleation from particle interactions and heterogeneous growth from random distribution of concentrations. The addition of a gel changes the viscosity of the solution and suspends the crystals without agitation. This creates a homogeneous concentration for growth and reduces the effects of secondary nucleation (Zeng, Martin, Marriott, & Pritchard, 2000); these factors combine to narrow the PSD. A particular type of gel that can be used for this purpose is a Carbopol® (The Lubrizol Corporation, Ohio, USA) gel. A Carbopol® gel is a group of polyacrylic acid polymers cross-linked with either allylsucrose or allyl ethers of pentaerythritol. Results using Carbopol® gels (Zeng*, et al.*, 2000) enabled 73% of the lactose crystals to be grown within the desired inhalation grade lactose particle size range of 60 to 90 µm (span much less than 1). However, relating back to IGL production objectives of the current work, potential purity issues was a barrier to using this technique.

#### 2.4.2.4 Real Time Monitoring

It is important to mention that through the precise control of the crystallization process, it may be possible to adequately control the PSD to within the desired conditions. Antisolvent such as ethanol, can be added, which increases nucleation, and solvent (water) is added to dissolve fines and drives the process into the under-saturated zone; this is the principle behind direct nucleation control (DNC) of crystallization, in combination with heating or cooling (Abu Bakar, Nagy, Saleemi, & Rielly, 2009). In DNC a Lasentec® (Lasentec Corporation, Washington, USA) focused beam reflectance measurement (FBRM) is used to count newly formed particles. The main results from this are that larger (>250 µm) particles are maximized where smaller (<22 µm) particles are dissolved and kept to a minimum, thus narrowing the PSD.

Liotta and Sabesan (2004) also demonstrated the use of real time feedback to control crystallization, and produce a narrow PSD. Their experiment combined *in situ* laser backscattering with *in situ* total reflectance Fourier transform infrared (ATR-FTIR) spectroscopy. The feedback mechanism controlled supersaturation by adjusting the temperature level, corresponding to a previously experimentally determined metastable

curve. This system again promotes growth, and limits nucleation rate. More recent results using the ATR-FTIR technique (Yu, Chow, & Tan, 2006) also support the idea of being able to control PSD. Seeding control, through size distribution and loading, was found to be important. Paracetamol with crystal sizes above 400 µm was crystallized with CV's as low as 23%. This type of control is known as closed loop supersaturation control or S-control. However, typical industrial practice is to use temperature cooling profiles or T-control. Interestingly in a crystallization experiment with glycine, S-control did not appear to improve crystal quality significantly over T-control (Chew, Black, Chow, & Tan, 2007). This was attributed to the fast growth characteristics of glycine, but a significant improvement was found between seeded and un-seeded solutions for both T-control and S-control.

### *2.4.3 Modified Industry Techniques*

With modified use of existing crystallization technologies the possibility exists to directly produce inhalation grade lactose with the desired narrowed PSD online with the crystallization process. The existing industry crystallization production focus needs to be changed from purely maximising yield, which generally means larger particles and a wide PSD, to producing the desired narrow and constant PSD of crystals. This is an aspect seemingly missing in detail in the literature, and warrants further investigation. Figure 14 below shows the main industry paths to solid liquid separation which could be used for obtaining a narrow PSD

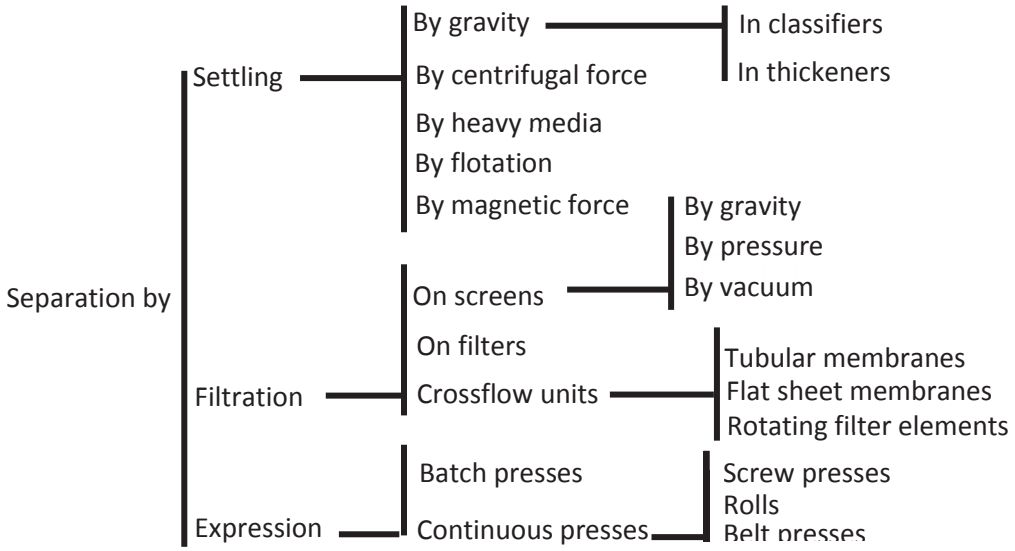


**Figure 14 Main industry paths to solid-liquid separation; redrawn from Green and Perry (2008)**

The rest of this section looks into the settling options, ignoring the filtration and expression techniques due to likely surface crystal growth, blockages and contamination issues. Industrial

techniques of milling and sieving are already used for obtaining narrow PSDs and have been discussed previously in Section 2.2 Dry Particle Inhalers.

### 2.4.3.1 Gravity Sedimentation

Clarifiers or settlers are affected by the following feed characteristics (Green & Perry, 2008):

- General chemical makeup of the solids and liquor phases
- Feed solids concentration
- Particle size distribution
- Particle specific gravity
- Liquid specific gravity
- Liquid-phase dissolved materials concentration
- Temperature
- pH

For sedimentation of different binary sized particles it has been found that the total hold up, $\alpha_h$ (-), is an important characteristic for the particles to settle without particle interaction (Lockett & Al-Habbooby, 1973). Each particle falling through liquid has an upward interstitial velocity, $u_i$ (m.s$^{-1}$) with respect to walls of the tube:

$$u_i = \frac{Q}{A_c(1-\alpha_h)}$$

**Equation 25 Upward interstitial liquid velocity**

where $Q$ (m$^3$.s$^{-1}$) is the upward volumetric flow rate and $A_c$ (m$^2$) is the tube cross sectional area.

The particle fall velocity, $v_L$ (m.s$^{-1}$) and $v_S$ (m.s$^{-1}$), of large and small particles with respect to the walls of the tube:

$$v_L = \frac{S_L}{\alpha_{hL} A_c}$$

**Equation 26 Large particles fall velocity relative to tube wall**

$$v_S = \frac{S_S}{\alpha_{hS} A_c}$$

**Equation 27 Small particles fall velocity relative to tube wall**

where $S_L$ (m$^3$.s$^{-1}$) and $S_S$ (m$^3$.s$^{-1}$) refers to volumetric down flow of large and small particles, and $\alpha_{hL}$ (-) and $\alpha_{hS}$ (-) are the large and small particle total hold up.

Particle slip velocity is calculated by summing the upward interstitial liquid velocity and the particle fall velocity. When $\alpha_h$ is less then 0.4 it can be assumed particle interactions do not occur (Lockett & Al-Habbooby, 1973), and the Richardson and Zaki equations (Richardson & Zaki, 1997) apply for particle fall velocities, for example large particle:

$$u_i + v_L = v_{L\infty}(1 - \alpha_{hL} - \alpha_{hS})^{n_L - 1}$$

Equation 28 Large particle fall velocity

where $v_{L\infty}$ (m.s$^{-1}$) is the terminal fall velocity of a single isolated particle and $n_L$ (-) is an exponent constant.

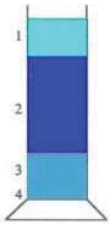


Figure 15 Zones of batch sedimentation of binary mixture

There are distinct zones in batch sedimentation of binary mixtures (Lockett & Al-Habbooby, 1973), as can be seen in Figure 15. Starting from the top there is the clear liquid zone (no particles), first zone (only small particles present), and second zone (small and large particles present).

### 2.4.3.2 Inclined Settlers

A continuous inclined settler is capable of separating particles on the basis of size and density (Figure 16), and Davis & Gecol (1996) have developed a model to predict this. Faster settling particles separate on the inclined surface where they primarily make up the coarse underflow.

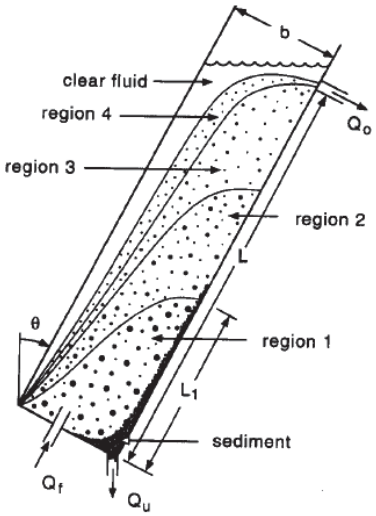


Figure 16 Inclined settler with overflow; reproduced with permission (Davis & Gecol, 1996)

Davis, Zhang, and Agarwala (1989) have formulated a model which predicts the PSDs obtained in the overflow and underflow of a continuous inclined settler, shown schematically in Figure 17. By changing the value of the correction factor for settling velocity, $k_1$ (-), the theory can be extended to concentrated solutions, where hindered settling effects become more important. A consequence of increased hindered settling, particle concentrations greater than 10%, is that a higher amount of slower settling, smaller particles are present in the overflow (Davis & Gecol, 1996). If the goal is to remove smaller particles, increasing feed concentration improves efficiency.

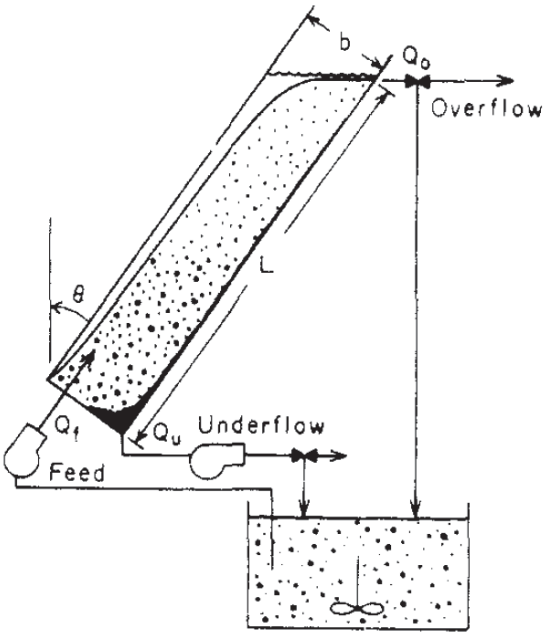


**Figure 17 Continuous inclined settler for steady-state particle classification; reproduced with permission (Davis, *et al.*, 1989)**

It was found by both theory and experiment (Davis, *et al.*, 1989) that a single batch inclined settler was rather inefficient, with the coarse fraction containing particles of all sizes. Improvements on this model and experiments were carried out with an underflow-product recycle stream for single and multiple inclined settlers (Zhang & Davis, 2002). Low recycle rates improve efficiency, with greater amounts of fines in the overflow and a coarser underflow, but higher recycle rates cause instabilities in the settler and thus efficiency is decreased.

### 2.4.3.3 Fluidized Bed

Inclined plates increase efficiency of liquidized fluidized bed segregation rates (Doroodchi, Fletcher, & Galvin, 2004). Doroodchi *et al.,* (2004) improved on a previously developed kinematic model (Galvin & Nguyentranlam, 2002) where the suspension concentrations and length of suspension along an inclined channel were reported against fluidization velocity. The

model was found to give an accurate description for the batch system and could be modified to predict results for a continuous system. A computational fluid dynamics model study (Doroodchi, Galvin, & Fletcher, 2005) has been carried out giving similar results to a kinematic model in predicting the expansion behaviour. This model is not recommended for use due to its complexity but does provide information regarding the flow behaviour of the system. More recently a generalized segregation and dispersion model has been developed (B. K. Patel, Ramirez, & Galvin, 2008), using a shell balance approach, and validated against binary system experimental data.

#### 2.4.3.4 Lamella and Tube Settlers

Lamella settlers are essentially inclined channels stacked together to form channels. Slurry is fed in near the middle to the top of the lamella, and particles are removed via gravity separation. Co-current flow occurs with the slurry flow and "sludge" that settles out on the lamella plates, where an upward flow of the effluent is induced. Typical lamella plate angles are between 45 and 60° (Leung & Probstein, 1983).

In tube settlers the slurry flows up an angled tube and sludge settles out in a counter current manner. A higher settling angle is required to settle the same amount of sludge since gravitational forces are opposed in counter current flow (Leung & Probstein, 1983). Both lamella and tube settlers are efficient at removing fine particles.

#### 2.4.3.5 Reflux Classifier

A reflux classifier, seen in Figure 18, is a combination of a traditional fluidized bed and inclined lamella settler, which enables a higher system throughput (Laskovski, Duncan, Stevenson, Zhou, & Galvin, 2006). Reflux classifiers can include multiple inclined plate sets to remove different fractions from the feed (Nguyentranlam & Galvin, 2001; Zhang & Davis, 2002). Laskovski, *et al*., (2006) worked out an empirical relationship for segregation efficiency, which is related to throughput. The product of the Reynolds number and aspect ratio of the inclined channels accounted for loss in segregation efficiency. The general segregation efficiency, $\eta$ (-), equation obtained was:

$$\eta = \frac{1}{1 + 0.133 \cos\theta \, Re_p^{1/3} (L/w_p)}$$

Equation 29 Reflux classifier segregation efficiency

where $\theta$ (°) is the channel angle of inclination, $Re_p$ (-) is the particle Reynolds number based on terminal velocity, $L$ (m) is the channel length and $w_p$ (m) is the perpendicular distance of the channel.

At high enough Reynolds numbers, settling is no longer affected by particle size and particle density becomes the main factor. Also, a higher channel aspect ratio increases particle re-suspension and moves towards density based separation (Zhou, Walton, Laskovski, Duncan, & Galvin, 2006).

It is possible to determine, with some accuracy, the operational cut point and throughput factor of a particular reflux classifier system through kinematic analysis. Nguyentranlam and Galvin (2001) predicted a cut-point within 9% using the operating parameters and geometry of the inclined channel.

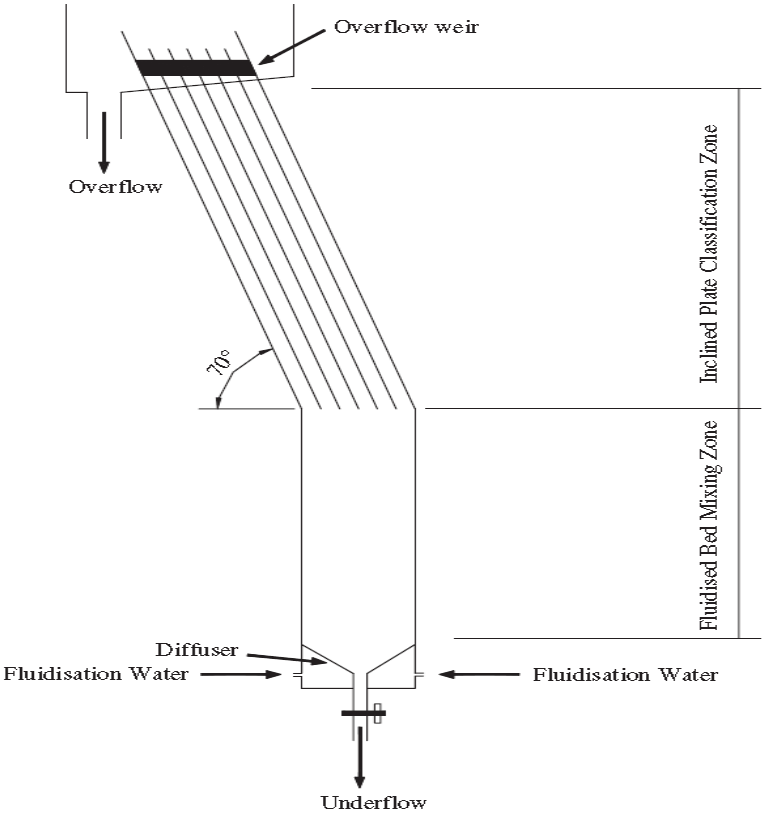


**Figure 18 Semi-batch reflux classifier; reproduced with permission (Laskovski, *et al.*, 2006)**

Doroodchi, Zhou, Fletcher and Galvin (2006) carried out research into a modified reflux classifier, which showed improved classification and higher throughputs. In this work a reflux classifier was essentially split fed fluidizing water, so only a small fraction of feed water was introduced at the base and rest was introduced in the side of classifier higher up. Laminar conditions were able to be achieved at the base because of lower fluidizing velocities and thus

improved separation occurred in the underflow. A sharpness index, *SI* (-), shown in Equation 30, as high as 0.91 was reached for the separation, from an initial SI of approximately 0.67.

$$SI = \frac{d_{25}}{d_{75}}$$

**Equation 30 Sharpness Index**

where $d_{25}$ (µm) and $d_{75}$ (µm) are the sizes of a particle having a 25% and 75% probability respectively of reporting in the underflow.

### 2.4.3.6 Settler or Elutriator

An elutriator can be considered as a very simple, but useful separating device. A vertical tube elutriator basically consists of upward flow of water in a tube, with a solids feed point generally around the middle of the tube (Biddulph, 1986). Particles with a terminal settling velocity lower than the water velocity will be carried into the overflow and particles with a greater terminal settling velocity than the water velocity will appear in the underflow. Due to turbulence from high water flows the separation process does not occur at 100% efficiency, with small particles in the underflow and large particles in the overflow (Biddulph, 1986).

In a vertical tube elutriator the use of baffles is needed to reduce small particles in the product under flow. This is because without baffles, the velocity is highest in the middle of the tube and near zero at the walls. A downward particle flux then occurs at low velocity near the walls where smaller particles can travel downwards (Biddulph, 1983). Pressure drop in elutriators can be decreased with correctly spaced wall baffles (Davies & Graham, 1988; Davies & O'Hagan, 1988).

### 2.4.3.7 Hydrocyclones

The hydrocyclone can be compared to an enhanced sedimentation process under higher forces of gravity (Moir, 1985). Heavier and larger particles are thrown towards the outer walls of the cyclone and move downwards and out through the underflow, while smaller particles remain in the centre and move up through an air core in a spiral pattern into the overflow. Hydrocyclones can be designed to remove particles down to a size of 44 µm (Lakos separator). Figure 19 illustrates the principle parts and flow patterns occurring in a hydrocyclone.

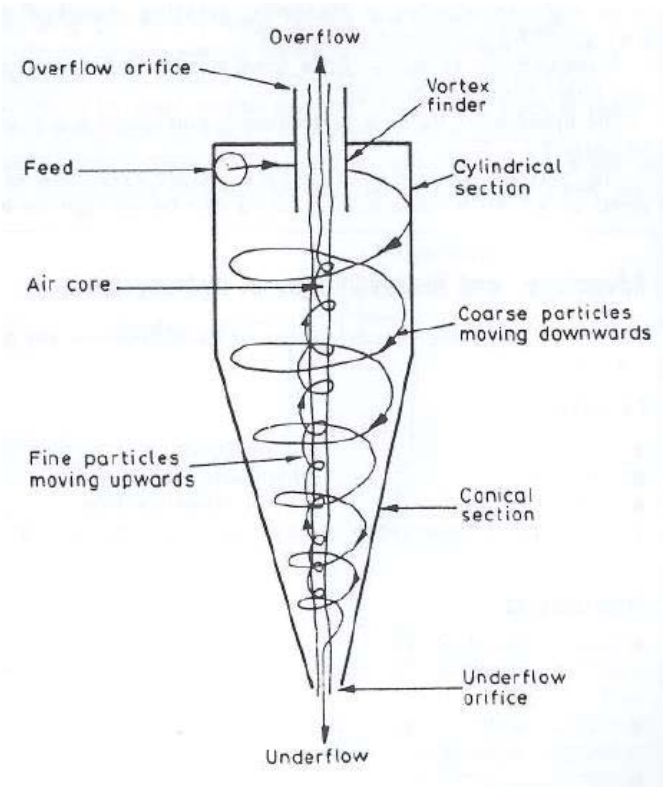


Figure 19 Principle parts of cyclone and flow patterns; reproduced with permission (Moir, 1985)

Table 3 below summarises the advantages and disadvantages of using a hydrocyclone.

| Advantages | Disadvantages |
|---|---|
| Simple | Must be feed at a constant volume and solids concentration for successful operation |
| Compact | Require careful protection from oversized feed |
| No moving parts | High power consumption |
| Inexpensive | High wear |
| Minimum feed hold up | Cut size related to throughput |
| Short residence time | |
| Able to make separations at finer sizes than mechanical classifiers | |

Table 3 Advantages and disadvantages of hydrocyclones

Many hydrocyclones exhibit an unexpected increase in the separation curve in the fine particle range; see Figure 20. This increase is known as the fish-hook effect and has been observed and studied by many researchers (Gerhart, 2001; Kerkhoff, 1997; Kraipech, Chen, Parma, & Dyakowski, 2002; Neesse, Dueck, & Minkov, 2003; Plitt, 1971; Roldanvillasana, Williams, & Dyakowski, 1993). This effect is where certain particles appear to settle faster than the velocity described by Stokes law. If the desired $d_{50}$ particle range is 50 to 90 µm, this effect is not expected to be a problem.

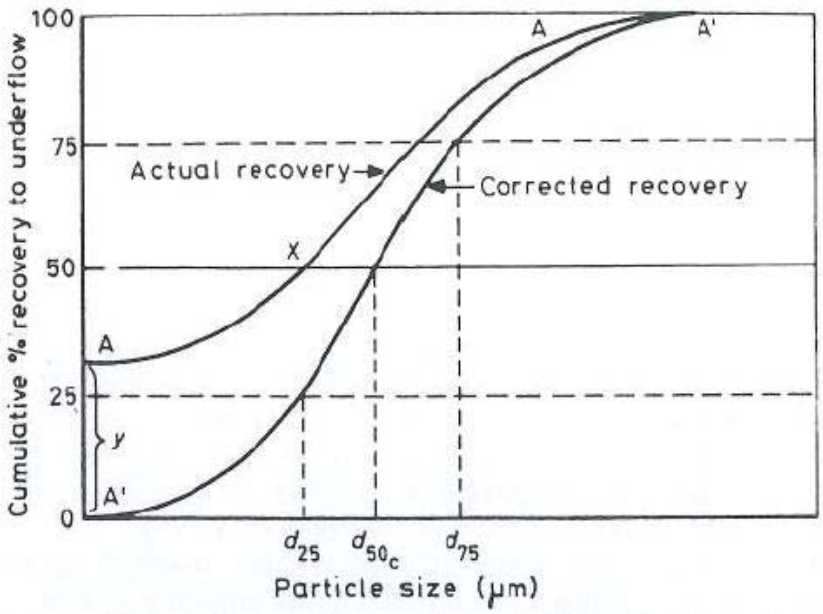


**Figure 20 Recovery and corrected recovery curves; reproduced with permission (Moir, 1985)**

Liu, Chu, Wang, and Yul, (2008) have shown that pre-settling particles before entering the hydrocyclone increases the particle classification efficiency. Seen in Figure 21 below, the traditional hydrocyclone has been modified with a volute chamber which arranges the particles to enable greater separation, giving a coarser underflow and a finer overflow.

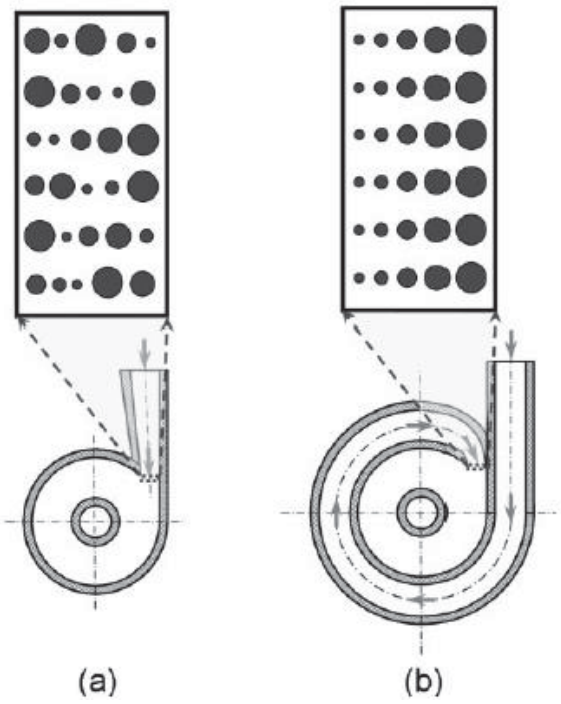


**Figure 21 Traditional (a) and new-type hydrocyclone (b) with volute chamber; reproduced with permission (Liu, *et al.*, 2008)**

In another attempt to increase particle separation of hydrocyclones, two 10 mm hydrocyclones were connected in series (Hwang, Lyu, & Nagase, 2009). It was found that the

$d_{50}$ value can be decreased significantly but the $d_{100}$ cannot. Ultimately the particle classification sharpness cannot be improved, which was attributed to the fish-hook effect. In addition to these results it was found that when Stokes number exceeds a critical value it can accurately describe the efficiency of the hydrocyclone. Separation efficiency is also affected by temperature conditions. In experiments using 10 mm hydrocyclones (Cilliers, Diaz-Anadon, & Wee, 2004), when increasing from 10°C to 60°C, there was increased dewatering due to a higher bypass which also caused a lower cut size, but classification efficiency decreased.

The air core in a hydrocyclone produces a vortex, causing radial and axial turbulence just under the vortex finder (Chu, Yu, Wang, Zhou, Chen, & Dai, 2004). Chu *et al*., (2004) carried out experimental work which showed the replacement of this air core with a solid core could increase the separation efficiency. A higher separation sharpness and lower corrected cut size was found, although when the cone shape was changed from parabola type to hyperbola type, separation performance improved dramatically.

### *2.4.4 Span Summary*

Summarised in Table 1 are the narrow PSD methods discussed and the $d_{50}$, span and impurity relevance to the desired IGL production objectives. Droplet based crystallization, settling and hydrocyclone classification appear most promising as they satisfy the $d_{50}$, span and impurity objectives.

| Method | Usable | Summary |
|---|---|---|
| Typical industrial batch | No | $d_{50}$ generally >>90 µm, span>1 |
| Sieving and milling | Yes | Current IGL post crystallization processing methods |
| Single nucleation event | Yes | Successive nucleation acts to increase span |
| Supercritical fluid | No | $d_{50}$ generally <<50 µm, span<1, potential contamination issues |
| Droplet based | Yes | $d_{50}$ control to 50-90 µm, span<1, limited to drops on a surface due to contamination criterion |
| Gels | No | $d_{50}$ control to 50-90 µm, span<1, contamination issues |
| Real time monitoring and antisolvent | No | Fines removal via supersaturation control, contamination issue |
| Seeding | Maybe | Doesn't reduce span, controls nucleation event |
| Settling | Yes | $d_{50}$ control to 50-90 µm, span<1, no contaminants |
| Hydrocyclone | Yes | $d_{50}$ control to 50-90 µm, span<1, no contaminants |

Table 4 Narrow PSD techniques relevance to IGL production

## 2.5 Conclusions

Inhaler grade lactose is most commonly used as a drug carrier in asthma inhalers and the desired properties for this work are a $d_{50}$ of 50 to 90 μm, span less than 1 and no contaminants. Due to growth rate dispersion, typical industrial crystallization processes produce lactose crystals with a wide particle size distribution and a span of around 2. Crystallized pharmaceutical grade lactose commonly undergoes additional processing in the form of milling and sieving to achieve the consistent properties required for inhaler grade lactose.

The literature review investigated factors relevant to lactose crystallization with a focus on methods to produce a narrow particle size distribution. Successive nucleation events increase the particle size distribution and the use of a single nucleation event with subsequent controlled growth conditions will be core to any new crystallizer design.

Three potential methods for producing a narrow particle size distribution were proposed for further investigation: droplet growth (crystallization), hydrocyclone (separation) and inclined settler (separation). The next chapter assesses these techniques.

# Chapter 3 – Potential IGL Production Methods

The use of droplet growth, settling, or a hydrocyclone were found in Section 2.4 to be prospective methods to achieve the desired IGL production objectives. A more in-depth look into the theoretical span predictions for each method is presented below.

## 3.1 Droplet Growth

One of the techniques found important from the literature for narrowing the PSD, was growing a lactose crystal within a drop. A theoretical model was developed which shows particle diameter increase with time for a single lactose nucleus within a lactose solution drop; refer to Appendix A.9 for the assumptions and Matlab code. This model utilized the maximum size a crystal can grow to in a drop (Equation 31), crystal growth (Equation 15), and changing supersaturation with time. Diffusion was estimated to be faster than particle growth and therefore was ignored. The initial lactose droplet concentration is specified, which determines the droplet volume needed for a desired crystal size. The simulation for a maximum crystal size of 80 µm can be seen in Figure 22 below. The initial growth to 70 µm is fast, but as the lactose concentration in the drop depletes, the growth of the crystal slows down.

$$B_{max} = \left( \frac{V_d \rho_f \left( (C_T/(100 + C_T)) - C_s/(100 + C_s) \right)}{0.95 \alpha_V \rho_{lc}} \right)^{1/3}$$

Equation 31 Maximum crystal size in a drop (R. D. Dombrowski, *et al.*, 2007)

where $B_{max}$ (m) is the largest dimension (height) of the tomahawk crystal, $\alpha_V$ (-) is the shape factor (estimated to be 1/12), total volume of the tomahawk is therefore equal to $B^3 \alpha_V$, $V_d$ ($m^3$) is the droplet volume, $\rho_f$ ($kg.m^{-3}$) is the fluid density, and $\rho_{lc}$ ($kg.m^{-3}$) is the lactose crystal density.

The shape factor is equivalent to a conversion factor, where $\alpha_V$ for a sphere would be π/6.

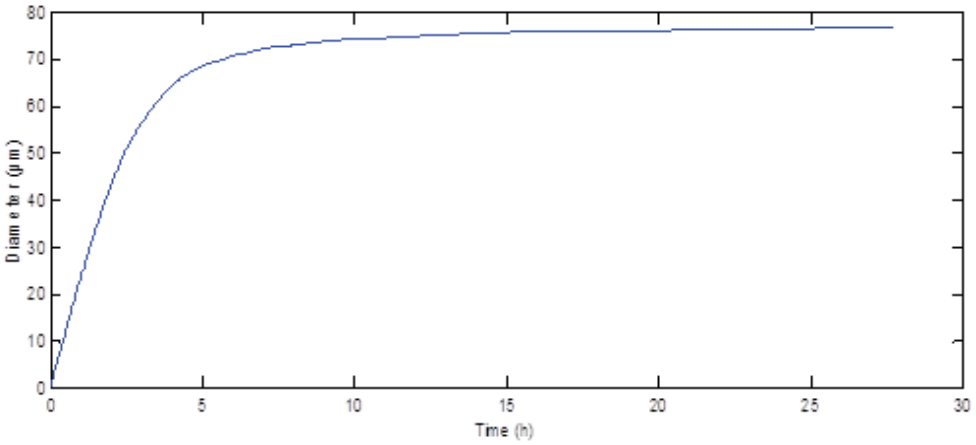


Figure 22 Growth time for a crystal to reach a specified diameter within a lactose drop

By controlling the droplet size and concentration, and assuming one nucleus per drop, growth rate dispersion can be counteracted to produce a very narrow crystal span. From the results of the theoretical model, a plan was put in place to design and build a device which could place lactose drops of a desired volume onto a surface and automatically take images, as depicted in Figure 23.

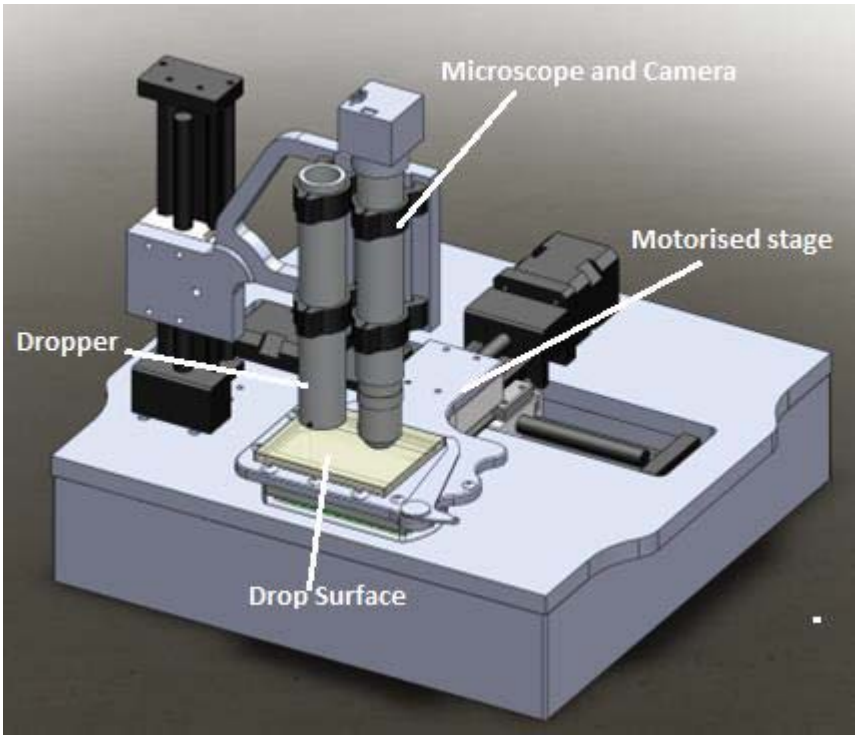


**Figure 23 Automated drop on demand and imaging device**

The device built was modified from an automated pollen image analyser (Pollen Research Team, Massey University), to include a lactose dropper, but was only partially completed. A plain surface, with no additional carrier medium such as oil, was utilized for growing the lactose due to the specifications of high lactose purity required for IGL. The second function of this device was to have the capability of monitoring the change in each crystal size with time via image capture. The main task left for completing this device was the installation of a piezoelectric droplet device, required to create one off lactose droplets of a desired volume on demand. Due to the time consuming nature and potential scalability issues, the development of this method was abandoned.

## 3.2 Inclined Settler

Crystallization using the external separation technique of continuous inclined settlers is an existing technology with the potential to obtain a narrow PSD. Theoretical inclined settler equations from the literature were solved to determine product PSD and potential yield. For an inclined settler, the normalized probability size density function, on a volume basis, $P(v)$ (s.m$^{-1}$), is given by the following equations, where subscripts $o, u$ and $f$ corresponds to overflow, underflow and feed respectively (Davis*, et al.*, 1989):

$$P_o(v) = \frac{\big(Q_o - S(v)\big)P_f(v)}{\int_0^{u_c}\big(Q_o - S(v)\big)P_f(v)dv} \; when\, u < u_c$$

**Equation 32 Normalized probability size density function for the overflow contition 1**

$$P_o(v) = 0 \; when\, u > u_c$$

**Equation 33 Normalized probability size density function for overflow condition 2**

$$P_u(v) = \frac{Q_f P_f(v) - P_o(v)\int_0^{u_c}\big(Q_o - S(v)\big)P_f(v)dv}{Q_f - \int_0^{u_c}\big(Q_o - S(v)\big)P_f(v)dv}$$

**Equation 34 Normalized probability size density function for underflow**

Volumetric inclined settling rate, $S(v)$ (m$^3$.s$^{-1}$), is given by:

$$S(v) = uw(L\sin\theta + w_p\cos\theta)$$

**Equation 35 Volumetric inclined settling rate**

Settling velocity, u (m.s$^{-1}$), is given by:

$$u = \frac{k_1 d^2\big(\rho_s - \rho_f\big)g}{18\mu_v}$$

**Equation 36 Settling velocity related using Stokes law**

where is $Q$ (m$^3$.s$^{-1}$) is volumetric flow rate, $w$ (m) is channel width, $k_1$ (-) is the correction factor for settling velocity, $d$ (m) is particle diameter, $\rho_s$ (kg.m$^{-3}$) is solid density, g (m.s$^{-2}$) is gravity, $\mu_v$ (Pa.s) is viscosity of the fluid, and $u_c$ (m.s$^{-1}$) is the cut off settling velocity for the overflow.

The equations were solved such that feed with a starting span of 1.08, was continuously passed through Settler 1 with a 100 µm cut, and the overflow was then processed by Settler 2 with a 60 µm cut. The overall process is depicted in Figure 24, although not modelled it is assumed crystals coming from settler 2 would undergo a centrifuge step remove excess liquid.

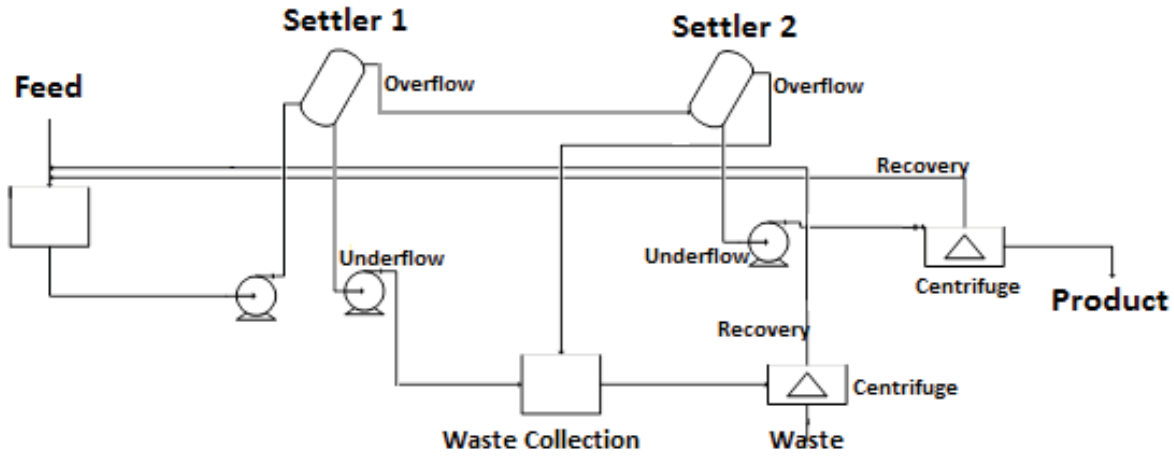


Figure 24 Simplified continuous process flow diagram (PFD) of an inclined settler setup; Appendix A.9 contains the same PFD with stream concentrations for each processing step

Theoretical results using a single 100 µm inclined settler cut reduces the initial PSD span from 1.08 to 0.66 (Figure 25). The subsequent 60 µm cut further reduces the span to 0.57 (Figure 26). The starting $d_{50}$ changed from 93 to 62 µm with the first cut, and then to 65 µm with the second cut. An overall yield of 20% was predicted.

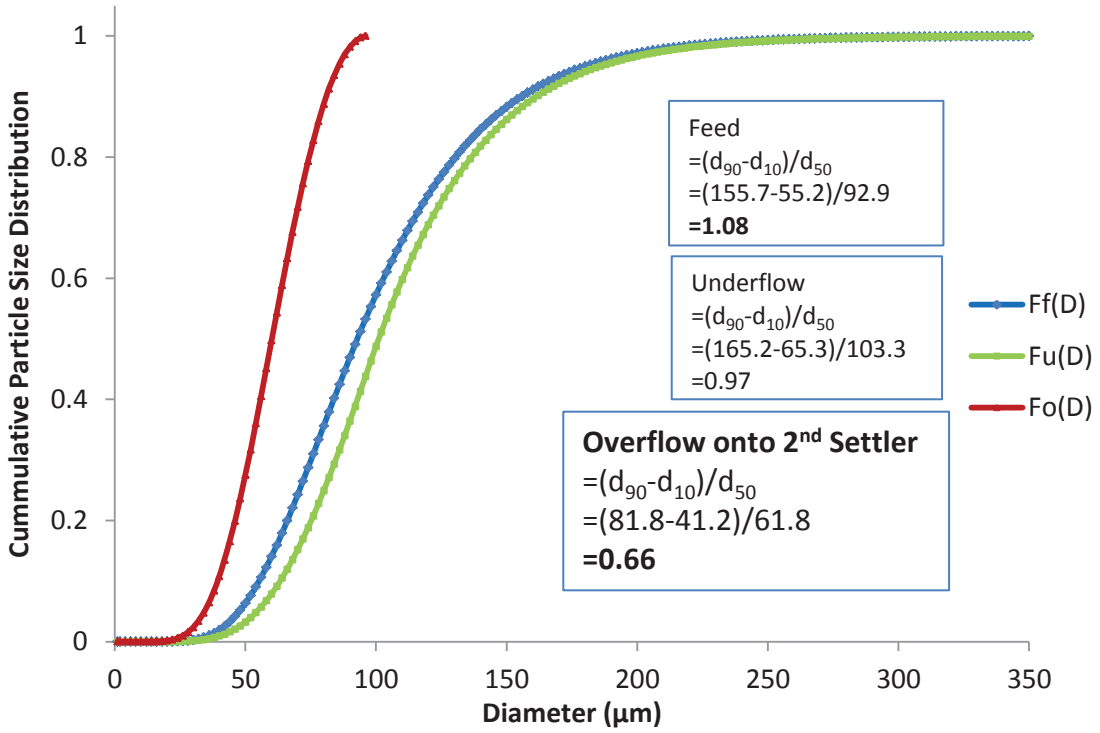


Figure 25 Simulated inclined settler cumulative PSD after 1st 100µm cut

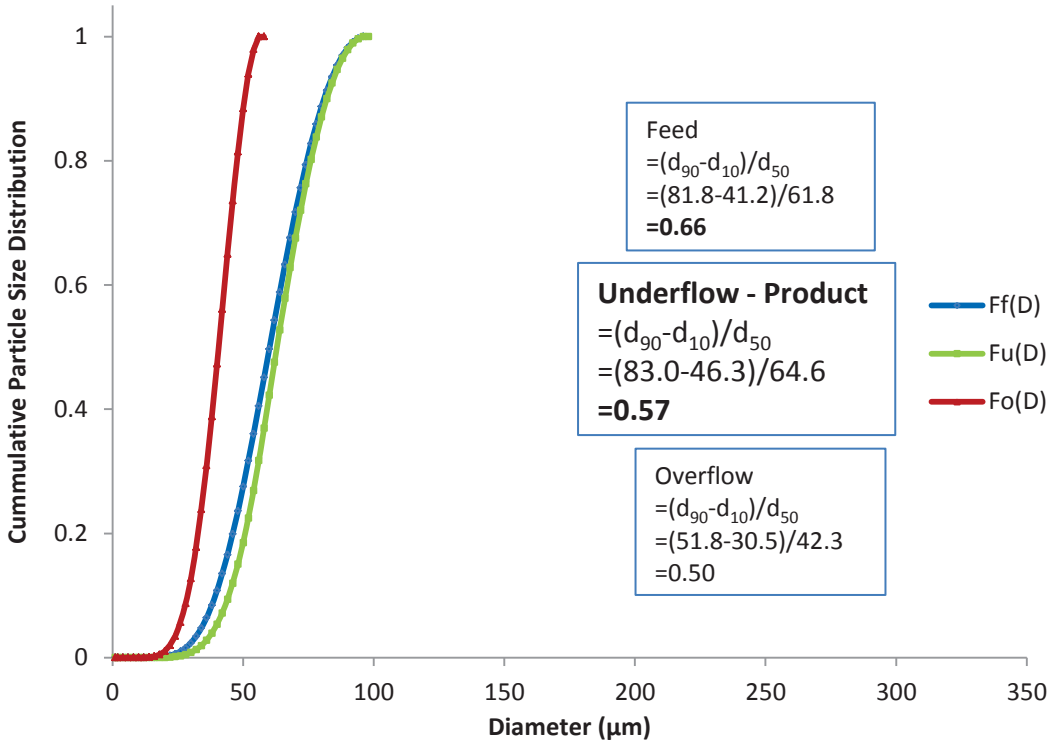


Figure 26 Simulated inclined settler cumulative PSD after 2nd 60µm cut

The simulation predictions for two inclined settler cuts satisfy the desired IGL production objectives for span and $d_{50}$.

## 3.3 Hydrocyclone

In a similar manner to the inclined settler, hydrocyclone equations were solved with a starting feed span of 1.08 undergoing one hydrocyclone cut. Flintoff, Plitt and Turak, (1987) have given following equations for hydrocyclone performance, which were used for determining the effectiveness of a hydrocyclone as a classification method for lactose crystals:

$$d_{50c} = F_1 \frac{39.7 D_c^{0.46} D_i^{0.6} D_o^{1.21} {\mu_v}^{0.5} e^{0.063 c_V^P}}{D_u^{0.71} h^{0.38} Q^{0.45} \left[\frac{\rho_s - 1}{1.6}\right]^{k_2}}$$

Equation 37 The corrected cut/classification size

$$m_c = F_2 1.94 \left(\frac{D_c^2 h}{Q}\right)^{0.15} e^{\left(\frac{-1.58S}{1+S}\right)}$$

Equation 38 The classification index

$$\Delta P = F_3 \frac{1.88Q^{1.8} e^{0.0055C_V^P}}{D_c^{0.37} D_i^{0.94} h^{0.28} (D_u^2 + D_o^2)^{0.87}}$$

**Equation 39 The pressure drop**

$$S = F_4 \frac{18.62\rho_p^{0.24} (D_u/D_o)^{3.31} h^{0.54} (D_u^2 + D_o^2)^{0.36} e^{0.0054C_V^P}}{D_c^{1.11} P_c^{0.24}}$$

**Equation 40 Volumetric flow split (volumetric flow in underflow/volumetric flow in overflow)**

$$C(d) = 1 - exp[-0.693(d/d_{50c})^{m_c}]$$

**Equation 41 Classification function**

$$R_f = \frac{S}{S+1}$$

**Equation 42 Recovery of water to underflow**

$$S(d) = C(d) + R_f(1 - C(d))$$

**Equation 43 Selectivity function**

$$O(d) = F(d)\big(1 - S(d)\big)$$

$$U(d) = F(d)S(d)$$

**Equation 44 Overflow and underflow PSD, O(d) and U(d) respectively**

where $d_{50c}$ (m) is the corrected cut size, $m_c$ (-) is the classification index, $\Delta P$ (Pa) is the pressure drop, $S$ (-) is the volumetric flow split, $C(d)$ (-) is the classification function, $R_f$ (-) is the recovery of water to the underflow, $S(d)$ (-) is the selectivity function, $D_c$ (m) diameter of cyclone, $D_o$ (m) diameter of vortex finder, $D_u$ (m) diameter of spigot, $D_i$ (m) diameter of inlet, $h$ (m) free vortex height, $P_c$ (Pa) is the cyclone inlet pressure, $C_V^P$ (%) is the percent solids in feed by volume, $d$ (m) size of particle, $\rho_p$ (kg.m$^{-3}$) density of feed pulp, $F_1, F_2, F_3, F_4$ (-) are calibration parameters and $k_2$ (-) is an exponent for the effect of solids density, and $F(d)$ (-) is the feed PSD.

The result of a single hydrocyclone cut with a $d_{50c}$=60 µm (Figure 27), achieved a span of 0.66, $d_{50}$ of 56 µm and overall yield of 17%. The use of a hydrocyclone cut also satisfied the desired IGL production objectives for span and $d_{50}$.

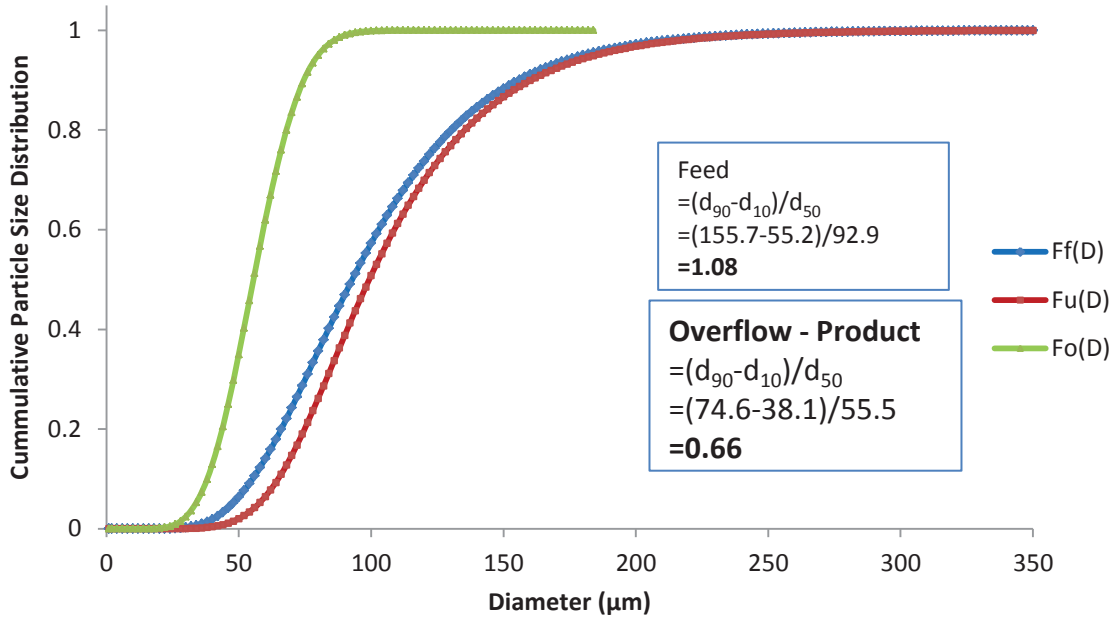


Figure 27 Hydrocyclone cumulative PSD with a $d_{50c}$ of 69µm

## 3.4 Potential IGL Production Methods Summary

The droplet method has great promise to produce a tailored narrow PSD, but was rejected due to scalability issues. Theoretical calculations were carried out for an inclined settler and hydrocyclone using a feed with an 80 µm log mean normal distribution. Two cuts were made with the inclined settlers, where performance was not affected by which way around cuts occurred (Figure 25 and Figure 26). Only one pass was made for the hydrocyclone feed (Figure 27), because attrition and yield problems are expected with more passes. A summary of the results can be seen in Table 5 below. Section 7.4.4.5 also shows that a hydrocyclone cut can still achieve a final span of less than 1 when the input span is higher (spans of 1.4-1.8).

| Inclined Settler | Hydrocyclone |
|---|---|
| Span = 0.57 | Span = 0.66 |
| Overall Yield = 20% | Overall Yield = 17% |
| Little to no attrition | Attrition problems expected |
| Dilution hassles | Theoretically can handle concentrated suspensions |
| Relatively slow, but good separation results | Fast, but average separation results |
| **Best Option** | |

Table 5 Comparison of results for inclined settler and hydrocyclone

It was established in theory that inclined settlers and a hydrocyclone cut would work to obtain the desired IGL $d_{50}$ and span, with the inclined settler chosen as the best option. However both these methods are external separation techniques with low yields. It is desired to obtain a narrow PSD *directly* from the crystallization process.

## 3.5 Continuous Settling Crystallizer

Instead of externally processing a crystallization stream with an inclined settler, a crystallization step incorporating settling, termed the continuous settling crystallizer (CSC) is proposed for theoretical development and is discussed in detail in Chapter 6. The basis for the CSC involves feeding a pre-nucleated stream into the bottom of a vertical column which flows up to the top under laminar conditions. Growth of the nuclei and settling of large crystals occurs inside the column. Once the nuclei have grown to a large enough size, where the terminal particle settling velocity opposes the fluid velocity, they will settle out from the column. An inherently slow growing crystal will travel further up the column before growing to the terminal particle diameter compared to an inherently fast growing crystal. Different growth rate crystals settle out from the column at the same final particle size, counteracting growth rate dispersion.

## 3.6 Conclusions

Three potential methods for producing a narrow particle size distribution were studied in detail: droplet growth (crystallization), hydrocyclone (separation) and inclined settler (separation). Droplet growth counteracts growth rate dispersion by controlling the maximum size a crystal within the drop can reach. This process is ideal for tailoring a narrow particle size distribution; however issues occur with scalability and producing drops without contamination. A hydrocyclone separates fines from large particles using centrifugal force, while an inclined settler uses gravitational force. Both methods, in theory, are capable of processing a post-crystallized lactose stream to a span less than one, with the inclined settler being slightly more efficient. These methods were considered to be additional processing steps; therefore the novel method of combining a single nucleation event and incorporating laminar settling into a continuous crystallizer, termed the continuous settling crystallizer, was proposed for further development.

# Chapter 4 – Lactose Stokes Shape Factor

Parts of this chapter have been published in a paper titled “Stokes Shape Factor for Lactose Crystals” (Shaffer, Paterson, Davies, & Hebbink, 2011).

## 4.1 Introduction

The previous chapter into potential new crystallizer designs for producing inhaler grade lactose (IGL) concluded that a crystallizer which incorporates settling would be a worthwhile development. Gravity settlers and classifiers used in the production of particles of a specific size range require knowledge of the particle settling parameters. Settling parameters can be readily predicted for spherical particles using established relationships for drag coefficients widely available in the literature and standard texts. Lactose crystals, however, are not spherical and while there are several approaches to estimating the settling velocity of a non-spherical particle, these all require information on particle shape. Generally, lactose crystals conform to a well-defined geometry, exhibiting a tomahawk shape (van Kreveld & Michaels, 1965; Walstra, Jenness, & Badings, 1984) as depicted in Figure 28. The two principal dimensions, as can be measured when the crystal is lying on a flat surface in its most stable position, are its height, *B*, and its width, *A*. But, despite their importance industrially, there is little definitive information on shape that can be used with confidence to predict their terminal settling velocity.

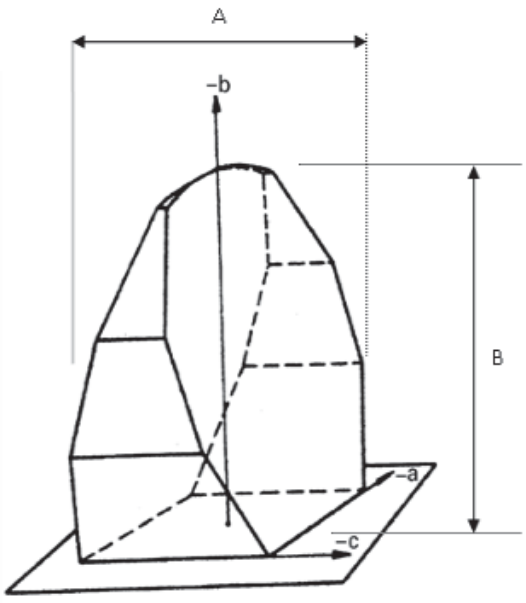


**Figure 28 Diagram of tomahawk shaped alpha-lactose crystal; redrawn from van Kreveld and Michaels (1965)**

Factors for characterizing particle shape are used in widely differing contexts, and are defined in many different ways. For example researchers (Bouwman, Bosma, Vonk, Wesselingh, &

Frijlink, 2004) were interested in quantifying the shape and roughness of granulated pharmaceutical powders and considered eight different shape factors. Their work concluded the combination of a roughness factor and a new projection shape factor gave a good indication of granule shape and roughness. Stokes shape factor has also been related to sphericity of non-spherical agricultural particles for flowability (Xie & Zhang, 2001).

In this work, interest resides in particle descriptors that enable the estimation of terminal settling velocity, $u_t$ (m.s$^{-1}$), at very low particle Reynolds numbers, $Re_p$ *(-)*, and attention has been confined to the Stokes shape factor, $k_{st}$ (-).

For $Re_p$ <~1, Stokes law applies well, and the terminal velocity of a spherical particle is explicitly related to particle density, $\rho_s$ (kg.m$^{-3}$), fluid density, $\rho_f$ (kg.m$^{-3}$), fluid viscosity, $\mu_v$ (Pa.s), particle diameter, $d$ (m), and acceleration due to gravity, $g$ (m.s$^{-2}$), by the expression given in Equation 45; see for example, Rhodes, (2008):

$$u_t = \frac{d^2(\rho_s - \rho_f)g}{18\mu_v}$$

**Equation 45 Crystal terminal settling velocity**

The utility of using $k_{st}$, defined in Equation 46, in calculations with non-spherical particles was demonstrated by Pettyjohn and Christiansen, (1948):

$$k_{St} = \frac{u_t}{u_{tv}}$$

**Equation 46 Stokes shape factor**

where $u_t$ is the actual terminal settling velocity of a particle; $u_{tv}$ (m.s$^{-1}$) is the terminal settling velocity of a spherical particle having the same density and volume as the particle volume, $V_p$ (m$^3$); the equivalent volume diameter of the particle, $d_v$ (m), used in the calculation of $u_{tv}$, is thus $\left[\frac{6}{\pi}V_p\right]^{1/3}$.

Using Equation 45, writing $u_t$ in terms of a Stokes diameter, $d_{St}$ (m), defined as the diameter of a spherical particle of the same density and the same terminal velocity, writing $u_{tv}$ in terms of $d_v$ and then substituting into Equation 46, it follows that:

$$k_{St} = \frac{{d_{st}}^2}{\left[\frac{6}{\pi}V_p\right]^{2/3}}$$

**Equation 47 Stokes shape factor in terms of particle volume**

Thus if $V_p$ can be measured or estimated, and an appropriate value of $k_{st}$ is known, the terminal settling velocity of a non-spherical lactose crystal can be calculated. The work described here

was undertaken to directly measure $k_{St}$ for lactose crystals and to investigate the relationship between sedimentation characteristics and crystal geometry.

## 4.2 Experimental

### *4.2.1 Crystal Preparation*

Measurements were made on crystals sampled from populations grown in quite different environments. Lactose crystals were obtained from a process line before milling and rinsed with distilled water. However, typical stirred vessel crystallization methods cause damage to the lactose crystal morphology. To assess the effect of this crystal damage, large undamaged tomahawk shaped lactose crystals were grown in a supersaturated lactose agar gel.

Forty grams of pharmaceutical grade alpha lactose monohydrate (DMV-Fonterra-Excipients, New Zealand) were dissolved in 100 grams of distilled water in a beaker by heating the solution to 80°C. Agar-agar was added (1 g), mixed and dissolved. The solution was then poured into two 200 mL test tubes, which were then placed in a 25°C water bath to cool. Before the solution had gelled - agar gels at ~38°C - approximately 0.1 g 300 micron lactose seed crystals (pharmaceutical grade alpha lactose monohydrate, DMV-Fonterra-Excipients, New Zealand) were dropped into the tubes. All tubes were then kept in the water bath at 25°C. After 48 hours the test tubes were examined for crystals. To recover grown crystals, the test tubes were heated slightly to 40°C, softening the agar gel. To fully dissolve the agar gel would have required heating to at least 85°C, which was not desirable as this would have also dissolved the lactose crystals. Most of the agar was dissolved by lowering the pH of the solution to pH=0 by adding 36% HCl. Undissolved gel lumps were removed by a coarse filter under vacuum while desired crystal size was retained. The crystals were washed with lactose solution, filtered again and rinsed with distilled water and then dried in an oven at 80°C for 2 hours.

### *4.2.2 Terminal Velocity*

The principal dimensions, *A* and *B*, of individual crystals were measured under a microscope; see Figure 28. The crystal weight for the first 9 gel-grown crystals was also measured using high precision scales (Sartorius M2P), to an accuracy of 1µg.

Settling experiments were carried out by dropping single crystals into a transparent sedimentation vessel so that they fell along its longitudinal axis. They were allowed to fall through 50 mm to reach terminal velocity, then the time taken to travel a known distance was measured using a stopwatch; the process was repeated five times. For the first 9 gel-grown

crystals, the sedimentation vessel was a 500 mL measuring cylinder and the distance traversed was 100 mm; and the crystals were collected for recycling using a stainless steel cup positioned below the traverse zone (Figure 29). For all the other crystals, both the remaining gel-grown crystals and the plant-grown crystals, the sedimentation vessel was a 1 L beaker and the traverse distance was 60 mm; instead of collecting the crystals in a cup, they were allowed to fall to the bottom of the beaker and were removed and recycled using a pipette.

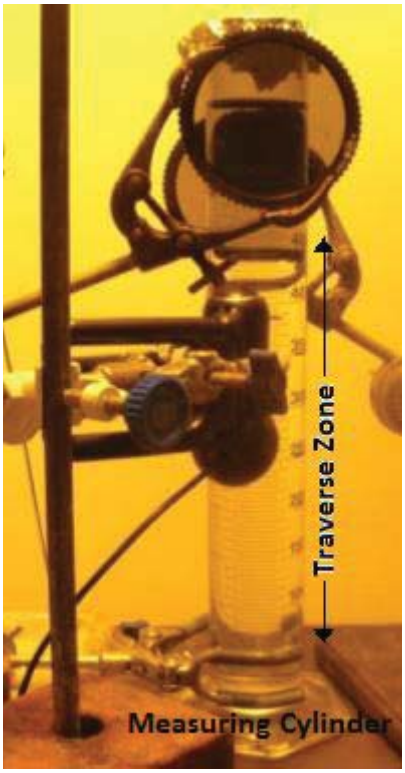


**Figure 29 Initial sedimentation vessel consisting of a 500mL measuring cylinder**

The sedimentation vessel contained fluid consisting of glycerol and supersaturated lactose solution (30 grams of lactose per 100 grams of water). Glycerol was used to control the viscosity of the lactose solution so that $Re_p$ <~1 and Stokes law was applicable. The settling fluid temperature was equilibrated with the surrounding air temperature, which varied between 20-25°C. The settling fluid viscosity for the temperature range was measured using a RHEOPLUS/32 V2.81 rheometer. The glass sphere method was also used for comparison. In the glass sphere method, a spherical glass bead of measured density and diameter is dropped into the fluid, and its terminal velocity measured; viscosity is calculated using Equation 45. New settling fluid solutions were prepared and viscosity altered appropriately for each crystal size. The viscosities ranged from 0.005 to 0.111 Pa.s. The density of fluid in the measuring cylinder ranged from 1128 to 1227 $kg.m^{-3}$.

## 4.3 Results

### *4.3.1 Gel Selection*

Before large undamaged alpha-lactose monohydrate crystals were grown for settling experiments, tests were carried out to determine the best gel to grow lactose crystals. The specifications for the gel required were to be able to grow single large crystals, to be a gel in room temperature, and be easy to extract the lactose with minimal processing after growth. The gels available for testing were: alginate, xanthan gum, gellatin, gellan gum, pectins, κ and λ carrageens, and agar. Williams and Phillips (2000) cover the gel information discussed below.

Alginates are thermally irreversible and were not considered for crystal growth, due to the difficulty of crystal extraction. Xanthan gum is resistant to degradation by acids and bases, high temperatures, freezing and thawing, enzymes and prolonged mixing, and was also not considered due to the difficulty of crystal extraction. Gellatin is thermo-reversible and was tested for crystal growth, but didn't produce lactose crystals. Gellan gum solid transition occurs at about 50°C depending on the concentration and a thermo-reversible gel forms on cooling in the presence of cations, and was considered for crystal growth. Gellan gum formed lactose crystal clusters making it unsuitable; Figure 30 shows these crystals before and after gel extraction.

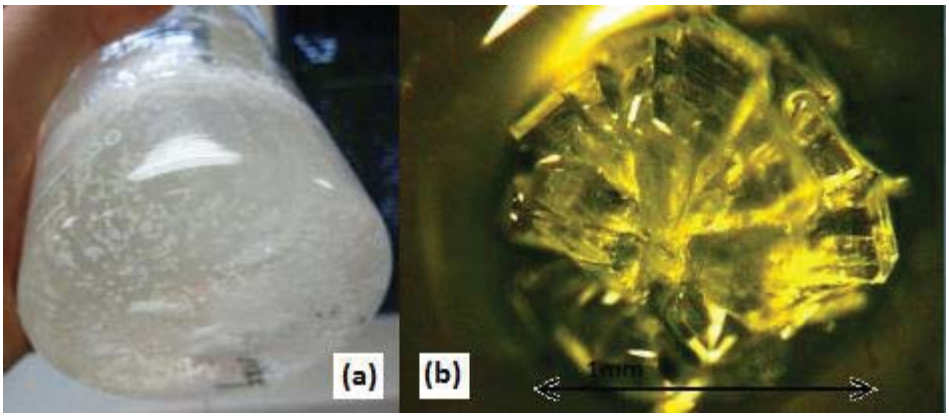


**Figure 30 Gellan gum testing: (a) lactose crystals before gel extraction and (b) after viewed under a microscope**

High methoxyl pectins require 55-85% sugar and a pH of between 2.5 and 3.8 in order to set, and were not considered for growing lactose crystals. Low methoxyl pectins are not as stable to heat as alginates, and were considered for crystal growth. Small (<50 μm) lactose crystals formed when using low methoxyl pectin and also did not form a strong enough gel to suspend the crystals; one side of the crystal would have been growth limited and this gel was dismissed. Figure 31 shows low methoxyl pectin grown crystals before and after gel extraction.

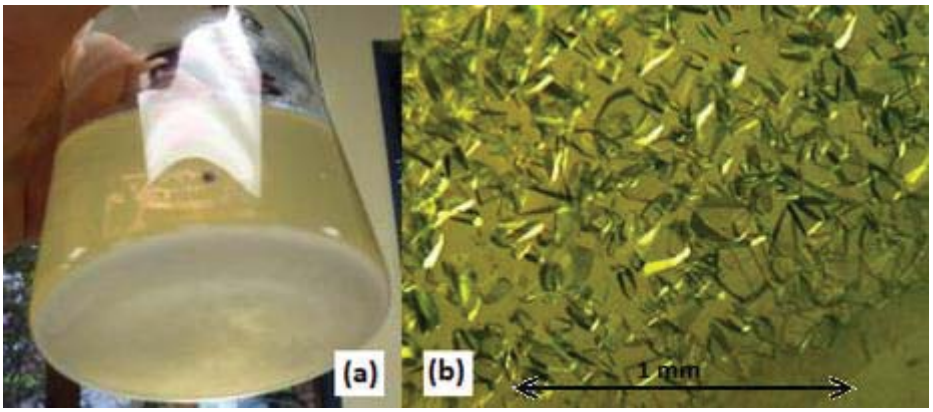


**Figure 31 Low methoxyl pectin testing: (a) lactose crystals before gel extraction and (b) after viewed under a microscope**

κ and λ-carrageenan form thermo-reversible gels on cooling in the presence of appropriate counter ions, and were considered for crystal growth. κ-carrageenan formed tomahawked shaped lactose crystals but also did not form a stable gel to suspend the crystals, so this gel was dismissed. λ-carrageenan suspended the crystals but formed clusters and this gel was dismissed. Figure 32 and Figure 33 shows κ and λ-carrageenan grown crystals before and after gel extraction.

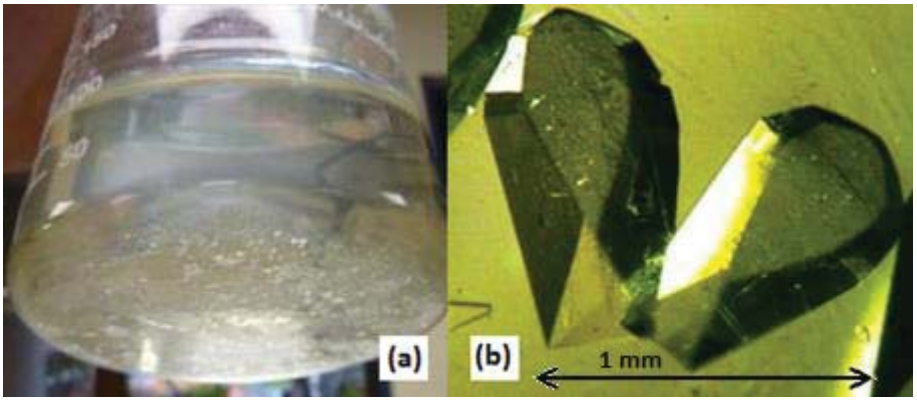


**Figure 32 κ-carrageenan testing: (a) lactose crystals before gel extraction and (b) after viewed under a microscope**

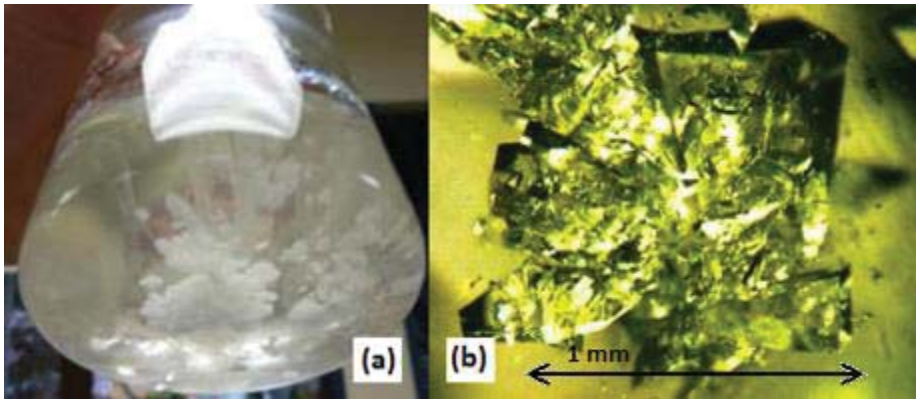


**Figure 33 λ-carrageenan testing: (a) lactose crystals before gel extraction and (b) after viewed under a microscope**

Agar is thermally reversible - melts above 85°C - and is sensitive to acids, and was considered for crystal growth. Agar gel suspended the crystals and formed single tomahawked shaped crystals, and this gel was selected for crystal growth. Figure 34 shows agar grown crystals before and after gel extraction.

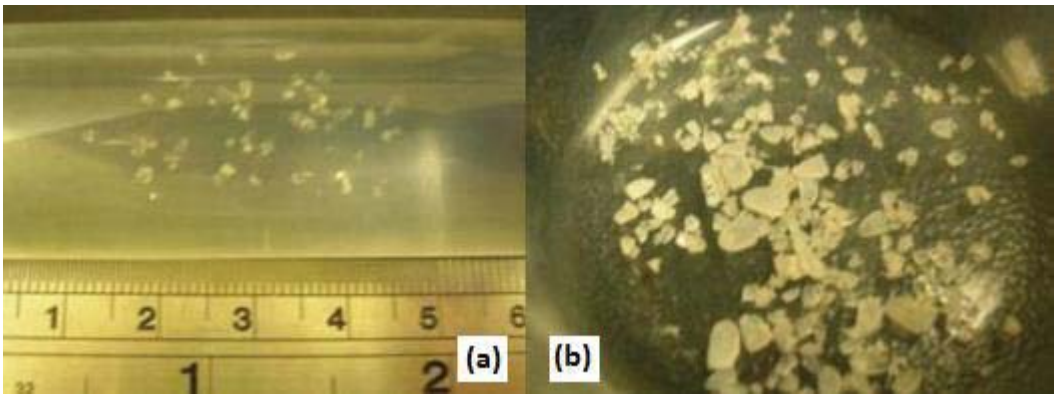


Figure 34 Agar testing: (a) lactose crystals before gel extraction and (b) after

### *4.3.2 Settling*

Lactose gel-grown crystals traversing the sedimentation vessel were visually tracked with the aid of a video camera for the first 9 gel-grown crystals. The video camera enabled the general orientation of the falling lactose crystals to be compared. The lactose crystals settled with the large tomahawk base positioned downwards and the Apex tip positioned upwards. This also occurred for crystals that were initially dropped into the fluid with a different orientation, the crystal changed to the specified orientation while settling.

### *4.3.3 Elongation Ratio*

Elongation ratio, *E* (-), was calculated for each crystal; *E* is defined as the ratio of crystal height to crystal width, *i.e.* with reference to Figure 28, the ratio [*B/A*]. For the gel-grown crystals, for which $0.34\ mm \leq B \leq 1.70\ mm$, the mean value for the 35 crystals measured was 1.44±0.07 at the 95% level of confidence. The mean value for the 21 plant-grown crystals, $0.30\ mm \leq B \leq 1.69\ mm$, was 1.37±0.07 at the 95% level of confidence. Figure 35 shows *E* plotted as a function of crystal height, *B*, for both crystal populations; while there is some scatter, there is no apparent trend with crystal height.

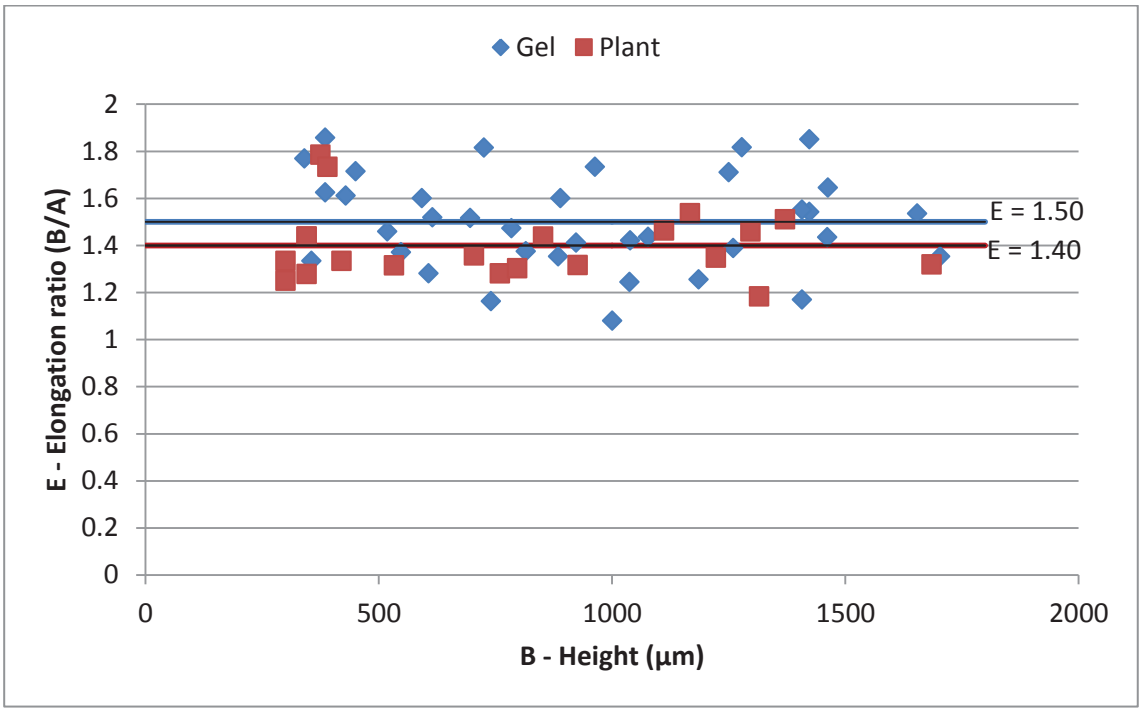


**Figure 35 Elongation ratio values plotted against height for gel and plant grown tomahawk alpha lactose crystals**

### *4.3.4 Stokes Height Factor*

Plots of Stokes diameter, $d_{st}$, versus crystal height, $B$, for both the gel-grown and the plant-grown crystals suggest a strong linear correlation between these parameters as can be seen in Figure 36; $R^2$>0.96 for both populations. The ratio [$d_{st}/B$] has been termed the Stokes height factor, $B_{St}$ (-), and can be obtained for each population from the slope of the trend line fitted to the experimental data; the fitted lines have been forced through the origin to be consistent with the definition of $B_{St}$, though for very small particles, Stokes law is not expected to apply (Mazo, 2002). The Stokes height factor, $B_{St}$, for which $0.30\ mm \leq B \leq 1.70\ mm$, was calculated to be 0.595±0.007 and 0.643±0.008 for gel-grown and plant-grown lactose crystals respectively at the 95% level of confidence, which is significantly different.

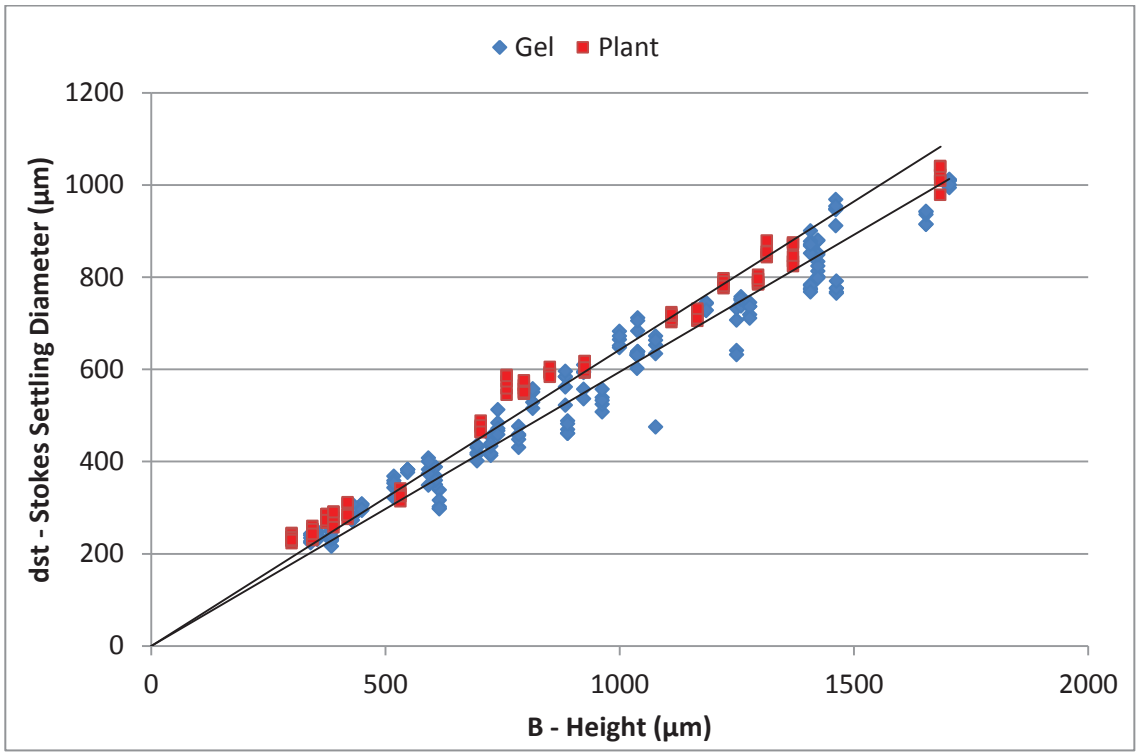


Figure 36 Stokes settling diameter versus measured height for gel and plant grown tomahawk alpha lactose crystals

### *4.3.5 Stokes Diameter*

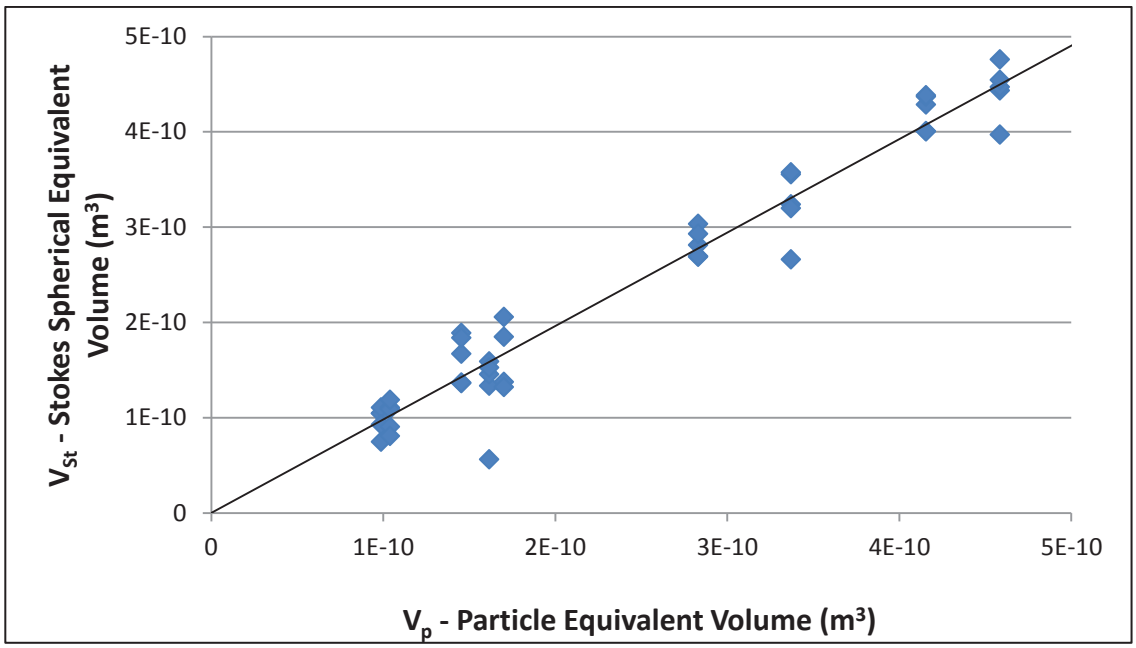


Figure 37 Stokes spherical equivalent volume versus particle equivalent volume from measured mass of large gel-grown tomahawk alpha lactose crystals

Figure 37 is a plot of Stokes equivalent spherical volume, $V_{St}$ ($m^3$), defined in Equation 48, against particle volume, $V_p$, for the 9 gel-grown crystals which were weighed (repeat settling

measurements included). Crystal height was between 0.88 mm and 1.65 mm; $V_p$ was calculated using a particle density of 1540 kg.m$^{-3}$ (Roelfsema, *et al.*, 2002).

$$V_{St} = \frac{\pi {d_{St}}^3}{6}$$

**Equation 48 Stokes equivalent spherical volume**

It is evident that there is a strong linear relationship between $V_{St}$ and $V_p$, with the data in Figure 37 well correlated by Equation 49 (including the 95% level of confidence):

$$V_{St} = (0.98 \pm 0.03)V_p$$

**Equation 49 Lactose empirical Stokes spherical volume relationship for gel grown crystals**

The Stokes diameter is thus virtually the same as the equivalent volume diameter. Using this relationship in Equation 48, the Stokes shape factor, Equation 47, is 0.99.

## 4.4 Discussion

### *4.4.1 Particle Size Conversion*

Lactose crystal height was used as the description of particle size. Converting from other commonly accepted industrial definitions of particle size involves a simple conversion factor depending on the definition used. If using a particle size based on a sieve analysis, which in principle obtains the particle width, the sieve particle size will be multiplied by the elongation ratio. The elongation ratio is the ratio of the height, *B*, to the width, *A*. The elongation ratio was found to be 1.44±0.07 and 1.37±0.06 for gel-grown and plant-grown lactose crystals respectively (95% CI), which falls within the range of 1.4-1.7 previously found for commercial grade lactose (Bund & Pandit, 2007a; Dhumal, *et al.*, 2008; Larhrib, Martin, Marriott, & Prime, 2003). The converted lactose crystal height can then be multiplied by the Stokes height factor to obtain the Stokes settling diameter.

### *4.4.2 Stokes Spherical Equivalent Volume*

The crystal weight was measured for the first 9 gel-grown crystal measurements. Figure 37 shows the relationship between the Stokes spherical equivalent volume and the particle equivalent volume. The particle volume was calculated from the measured mass of the corresponding lactose crystals and crystal density. Volume calculated from mass (and crystal density) can be considered as the true particle volume, as this volume excludes any pores or

voids. *A* strong linear relationship exists between the Stokes spherical equivalent volume and particle equivalent volume, Equation 49. The Stokes diameter is the spherical diameter (of same density) which gives the same settling velocity for the crystal; however these results show that the Stokes settling diameter for lactose crystals is virtually the same as the particle spherical volume equivalent diameter. Typical particle sizing instruments calculate particle diameters using light scattering techniques. These light scattering techniques commonly calculate the particle spherical volume equivalent diameter. If it is desired to correlate diameters obtained from light scattering instrument to Stokes settling diameter, then these results imply no conversion is required. This is due to the 1:1 relationship with Stokes spherical equivalent settling diameter.

### *4.4.3 Stokes Height Factor*

The plant-grown lactose crystals were obtained from a crystallization process line before milling. The reason the plant-grown lactose crystal $B_{St}$ is different from the value for gel-grown crystals is attributed to damage sustained during the crystallization and recovery stages. Under normal crystallization conditions highly concentrated mixed slurries are used, leading to particle-particle and particle-wall interaction. Similar interactions will also be occurring during the drying stages. The damage causes the plant-grown lactose crystals to be more spherical than the gel-grown crystals, and have a $B_{St}$ relationship closer to 1. This is because the $B_{St}$ relationship is based on particle height and Stokes spherical diameter, as a crystal is damaged the height becomes closer to the Stokes spherical diameter. This damage can be studied by comparing the gel-grown and plant-grown crystal microscope images, see Figure 38; the highlighted edges show the irregularity in the plant-grown crystal (c) compared to the smooth gel-grown crystals (a and b). To confirm if the $B_{St}$ values for gel-grown and plant-grown crystals were significantly different a statistical analysis was carried out. A T-test resulted in a P-value that was much less than 0.05 and it is concluded that the $B_{St}$ values for gel-grown and plant-grown lactose crystals are significantly different. The $B_{St}$ value can be used in settling equations which require the settling diameter of crystals. In an online crystallization process where invasive sampling techniques aren't viable, $B_{St}$ information could be used with images of the growing crystals to calculate Stokes diameter.

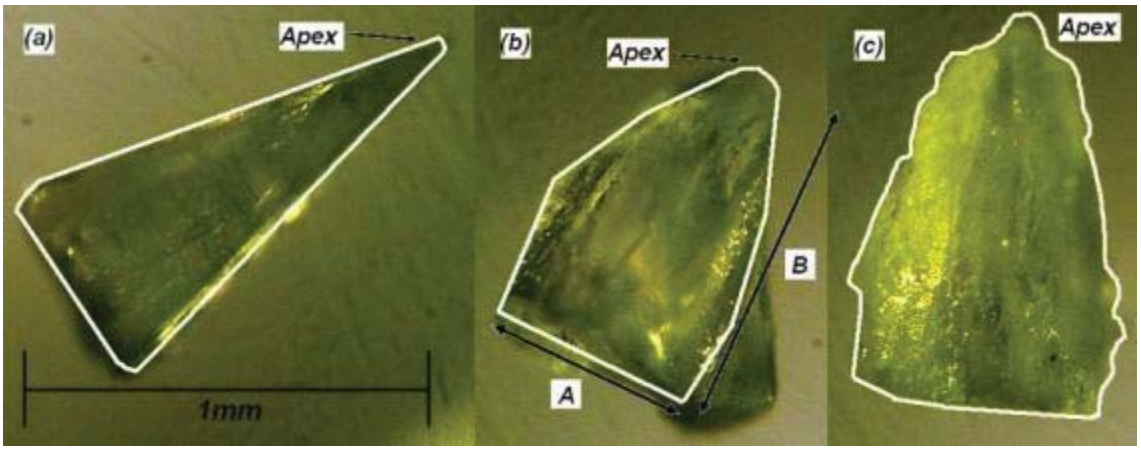


**Figure 38 Tomahawk alpha lactose crystals viewed under the microscope: (a) and (b) are gel-grown, and (c) is plant-grown**

If settling is combined with the crystallization nucleation and growth process it is assumed the tomahawk shape would be undamaged and represented well by the gel grown crystals. Assuming the geometrical proportions of lactose crystals are the same at different crystal sizes, the Stokes height factor can also be used for lactose crystals outside of the particle size range tested. IGL crystals desired $d_{50}$ is in the range of 50 to 90 µm.

### *4.4.4 Errors and Variation*

The simplicity of measuring terminal crystal settling velocity and using the corresponding Stokes law equations is an effective method for formulating a Stokes height factor for the irregularly (tomahawk) shaped lactose crystal. The scatter seen in the results of Figure 35 to Figure 37 can be attributed in part to experimental errors. Although the settling experiments are relatively simple to carry out, many factors need to be controlled and kept constant to ensure reliability. Temperature changes can affect the fluid properties of solubility, density and viscosity. This affects the settling time of the falling crystal. The sedimentation vessel was equilibrated with ambient temperature. The measuring cylinder fluid temperature would have been better controlled if placed in a temperature controlled room. Bouwman *et al.,* (2004) also commented on the temperature dependency and time consuming nature for Stokes shape factor determination. Another deviation in results could have arisen from foreign matter attached to the lactose crystals. This may have occurred when the lactose crystals were grown in the lactose agar gel (to ensure large undamaged tomahawk shaped crystals) and some remaining gel may have been present even after washing and drying. This was visually noticed for some of the crystals grown, and therefore these crystals were not used in the settling experiments. Foreign matter may have also been introduced when measuring the dimensions of the lactose crystals. Careful handling of the small crystals was also needed to avoid crystal surface damage (altering morphology) and lost crystal mass. Glycerol was used to alter the

lactose solution viscosity so the crystal was settling in the Stokes region. If the homogeneity of the glycerol and lactose solution was not 100%, this would have led to periods of increased or decreased settling rates for the crystals, leading to variation.

Data variation could also arise from differences in the crystal faces due to growth rate dispersion. Growth rate dispersion happens when different growth rates occur, even when crystals are subjected to identical growth conditions. This gives rise to variation in morphology of the lactose crystal. The Stokes height factor multiplied by the lactose crystals height gives the Stokes settling diameter. This assumes that the ratio of height to other dimensions of crystal remains the same. For instance the elongation ratio was 1.44±0.07 and 1.37±0.06 for gel-grown and plant-grown lactose crystals respectively. There was some difficulty in accurately measuring the width of the lactose crystal, due to the tomahawked shaped lactose crystal not lying flat on the surface. These results still indicate, that even for crystals growing under identical conditions, the different faces of lactose crystals grow faster or slower leading to slight variation of geometrical proportions. This will ultimately cause variation in the results, regardless of how precisely the experiment was carried out.

## 4.5 Conclusions

Experiments have been conducted with tomahawk shaped alpha-lactose crystals to measure their physical characteristics and settling parameters. A Stokes height factor, $B_{St}$, defined as the ratio of the Stokes settling diameter of a crystal to its height, has been determined and was 0.595±0.007 and 0.643±0.008 for gel-grown and plant-grown crystals respectively. Elongation ratios, height, B, divided by width, A, for the gel-grown crystals were 1.44±0.07 and for plant grown crystals, 1.37±0.06 where $0.3\ mm \leq B \leq 1.7\ mm$. The Stokes shape factor was measured for gel-grown crystals and was 0.99. Settling velocity can thus be estimated directly from knowledge of crystal height, crystal width, or crystal volume.

The gel grown lactose crystals measurements would best represent lactose crystals before the extraction and drying stage of industrial crystallization. The calculated sedimentation factors could be used in a lactose crystallization that incorporates laminar settling, such as the continuous settling crystallizer. The next chapter investigates a controlled single nucleation method, which can be used in producing a pre-nucleated feed stream to be fed into the continuous settling crystallizer.

# Chapter 5 – Continuous Orifice Nucleation

## 5.1 Introduction

The lactose crystal properties investigated in the previous chapter provide reliable settling information for use in the development of the continuous settling crystallizer (CSC). The second aspect of the CSC, states that crystals grow within a settling column and limited nucleation occurs. A single nucleation point prior to the column growth stage, producing a constant feed stream with a desired number of nuclei, is required.

Fundamental nucleation equations suggest supersaturation level is the primary factor for controlling nucleation. However, the application of energy to a supersaturated solution, via mixing or turbulence, is a well-established method for increasing primary nucleation and achieving the crystal counts required in industrial crystallization processes. The three principle factors affecting primary nucleation are supersaturation level, supersaturation time, and level of mixing. For primary spontaneous homogeneous nucleation to occur, the supersaturation level of the solution should be in the labile zone – refer to Figure 6.

The supersaturation time includes time to reach supersaturation and subsequent time at supersaturation before the nucleation event occurs. The majority of literature experimental investigations into lactose nucleation prepare supersaturated solutions via a slow cool method. A lack of fundamental understanding seems to exist on the cooling time length to reach a final supersaturation and its effect on nucleation once mixing is introduced.

The level of mixing, subsequent to supersaturation being reached, affects the nucleation rate. McLeod, Paterson, Bronlund and Jones (2010), Raghaven *et al*., (2001), and Shi *et al*., (1990), have clearly shown increasing mixing increases nucleation by reducing the induction period, and increasing the total number of nuclei produced. The induction period is the time before a measurable amount of crystal appears.

Reviewing potential nucleation mixing events from the literature (Section 2.4.1) revealed orifice flow is a viable technique. Batch orifice nucleation involves slowly cooling a solution to supersaturation and passing the fluid through an orifice restriction causing cavitation and turbulence. Cavitation is typically defined as the formation of a vapour phase in a liquid (Arndt, 1981). Orifices are widely used for creating cavitation in flowing liquids, because they create a drop in static pressure (Yan & Thorpe, 1990). The lowering of the hydrodynamic pressure is responsible for cavitation, which is caused by the reduction in pressure in a flowing liquid or in an acoustical field. Cavities will collapse once pressure increases or flow velocity decreases.

Figure 39 depicts flow through an orifice and the degree to which cavitation occurs can be described by the dimensionless cavitation number, $\sigma_c$ (#):

$$\sigma_c = \frac{P_3 - P_v}{\frac{1}{2}\rho_w {u_o}^2}$$

**Equation 50 Cavitation number (Yan & Thorpe, 1990)**

where $P_3$ (Pa) is the downstream pressure, $P_v$ (Pa) is the water vapour pressure, $\rho_w$ (kg.m$^{-3}$) is the water density and $u_o$ (m.s$^{-1}$) is the average liquid velocity at the orifice.

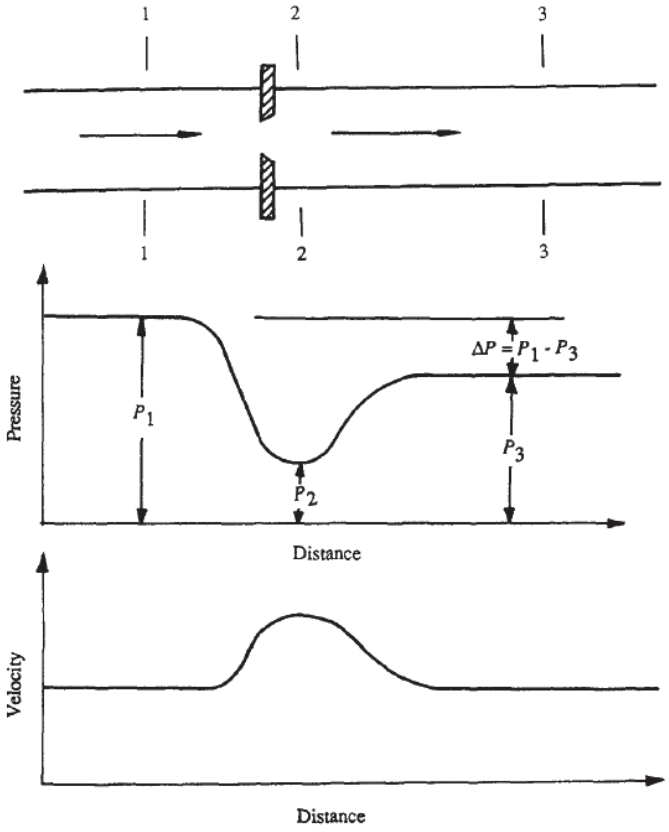


**Figure 39 Pressure and velocity profiles through an orifice; reproduced with permission (Yan & Thorpe, 1990)**

From *in situ* imaging, it can be seen with increasing flow conditions through the orifice, choking can occur, which is when there is a transition from bubbly flow to angular jet flow, and finally leads to supercavitation. Supercavitation has the following effects on downstream flow (Figure 40):

- Region A – a single cavity with a liquid jet in the middle of a vapour pocket
- Region B – white clouds where the big cavity breaks into smaller cavities which collapse (short 3-5cm in length)
- Region C – a clear liquid region where all the cavities have collapsed (Yan & Thorpe, 1990)

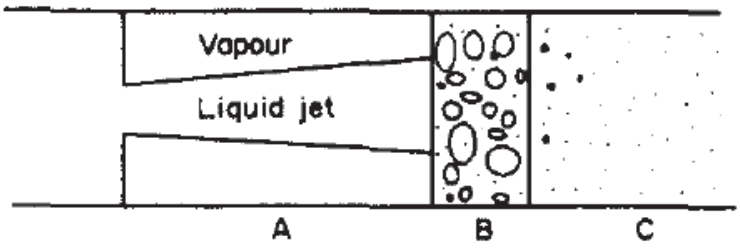


**Figure 40 Flow regions at super cavitation: region A-super cavity; region B-white cloud region; region C-clear liquid; reproduced with permission (Yan & Thorpe, 1990)**

Batch venturi nucleation experiments carried out by McLeod *et al.,* (2010) proved successful in producing a controlled nucleation event. Batch nucleation consisted of slowly cooling the solution and then passing through a venturi and into a dilution tank. Growth occurred in an impeller-stirred vessel. It was reported that Cavitation number and Reynolds number were found to give good predictions of nuclei amount expected and they concluded that Strouhal number (frequency of vortex shedding multiplied by orifice diameter divided by orifice velocity) gave the best mechanism for describing results across all venturi orifice diameters tested. The batch orifice trials of McLeod *et al.*, (2010) also showed a trend for increasing number of crystal per mL with Reynolds number above a critical supersaturation. Crystal numbers were counted under a microscope in a Neubauer chamber. McLeod *et al.*, (2010) showed approximately 50,000 crystals per mL formed at Cavitation numbers of 1-1.5, Strouhal numbers of 5,000-9,000, and Reynolds numbers of 1,500-10,000 (Figure 41). A lactose concentration of 90.48 g/100 g was used, giving an absolute alpha lactose supersaturation of 24.10 g/100 g or relative alpha lactose supersaturation of 3.09 at 40°C.

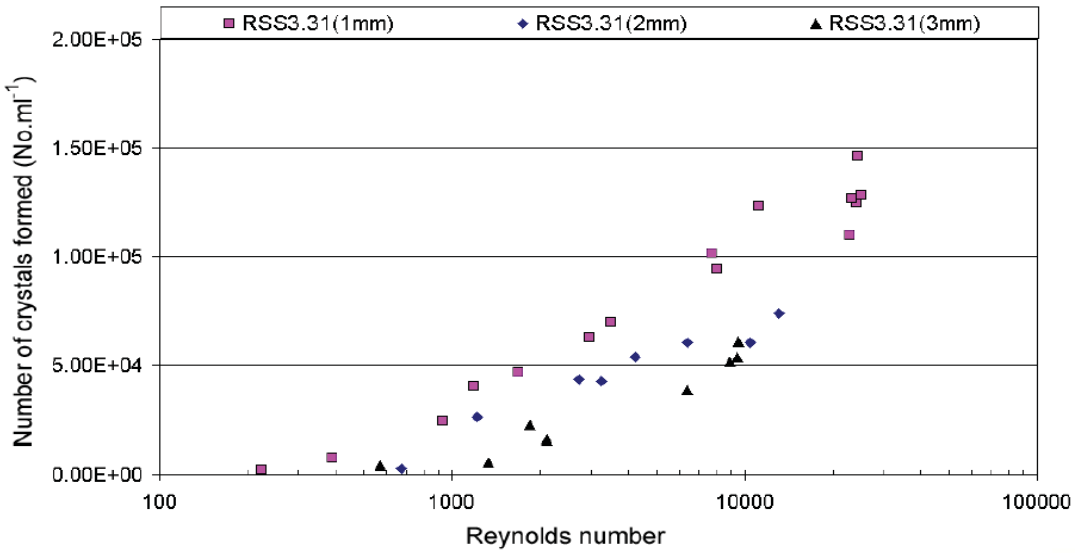


**Figure 41 Numbers of crystals formed versus Reynolds number for venturi flow of different diameters, constant relative supersaturation; reproduced with permission (McLeod, *et al.*, 2010)**

### *5.1.1 Preliminary Orifice Flow Experiments*

Preliminary orifice flow experiments were carried with the initial aim to be able to produce a known number of crystals per mL on a continuous basis that could be used as the feed stream for the CSC. In comparison to the batch-cooled high orifice flow rate experiments by McLeod *et al.*, (2010), the experiments reported here were designed with lower flow rates and to be carried out on a continuous basis. Three factors at 2 levels were investigated on the orifice flow stream: rate of cooling to final supersaturation (0 to 30 min and 60 to 90 min), time at supersaturation before orifice flow (0 min and 30 min), and whether an orifice was present. To achieve this, an 80°C saturated lactose solution (64.5 g lactose/100 g water) was cooled to supersaturation by immersing a beaker in a water bath set at different temperatures to reach a final temperature of 25°C (absolute alpha supersaturation, $S_\alpha$=17.4 g/100 g). A wait time of 0 or 30 min was applied. The solution was then pumped, using a Masterflex L/S peristaltic pump, through a 0.15 mm orifice at 13 mL.min$^{-1}$ (Re=485 and $\sigma_c$=0.46), and combined with a slightly supersaturated lactose stream ($S_\alpha$=1 g/100 g at 25°C) at 20 mL.min$^{-1}$. The combined stream had a flow rate of 33 mL.min$^{-1}$ and $S_\alpha$=4.2 g/100 g at 25°C. Samples were collected and grown in an impeller-stirred (300 rpm) 250 mL beaker for 4 and 24 hours. After the growth period six 10 µL sub-samples were measured in the Neubauer counting chamber to obtain a crystal concentration; averaged results are summarised in Table 6.

| Cool Rate | Wait Time | Orifice Flow | 4 Hour Growth (#.mL$^{-1}$) | 24 Hour Growth (#.mL$^{-1}$) |
|---|---|---|---|---|
| slow | yes | yes | 3.3E+03 | 1.9E+04 |
| slow | no | no | 6.5E+02 | 1.8E+04 |
| slow | no | yes | 3.6E+03 | 3.5E+04 |
| slow | yes | no | 5.2E+03 | 1.5E+04 |
| fast | yes | yes | 1.2E+04 | 1.0E+05 |
| fast | no | no | 2.3E+03 | 2.8E+04 |
| fast | no | yes | 5.5E+03 | 5.1E+04 |
| fast | yes | no | 8.2E+03 | 1.5E+04 |

**Table 6 Preliminary orifice flow average experimental results**

These preliminary experiments highlighted a number of areas of concern:

1. An indication that a significant amount of nucleation was occurring from evaporative based and impeller contact nucleation as crystal numbers increased with growth time
2. The peristaltic pump used pressure rating was too low, <2 bar, and could not handle the high pressure drop through the orifice
3. The Neubauer counting chamber accuracy was considered poor for the number range of crystals being counted; 1 crystal counted represented 500 crystals per mL

4. No clear trends using two-factor analysis of variance without replication test

The main difference between these results and those by McLeod, *et al.*, (2010), was that the supersaturated stream was prepared by rapid cooling with no significant wait time. A revised experimental procedure was developed, Section 5.2, with the objective to investigate the factors believed to be important for a controlled continuous nucleation event. The following factors were investigated:

- Orifice flow rate (Reynolds number)
- Wait (residence) time subsequent to rapid cool down before orifice flow
- Orifice flow time

## 5.2 Experimental

Unless otherwise stated concentration values are reported in grams of total lactose/100 grams water. The general procedure consists of producing a nucleated highly supersaturated, concentrated, stream and combining with a slightly supersaturated, dilute, stream at a set ratio, producing a slightly supersaturated growth stream.

| Orifice Reynolds Number | "Concentrated" Solution 83.13 g/100 g | | | "Dilute" Solution 22.98 g/100 g | | |
|---|---|---|---|---|---|---|
| | Flow Rate ($mL.min^{-1}$) | α-Lactose (kg) | Water (kg) | Flow Rate ($mL.min^{-1}$) | α-Lactose (kg) | Water (kg) |
| 500 | 42.6 | 3.724 | 4.070 | 69.7 | 0.548 | 2.238 |
| 1000 | 85.2 | 5.698 | 6.226 | 139.5 | 0.607 | 2.479 |

**Table 7 Continuous orifice nucleation experimental setup values**

Table 7 represents experimental conditions and solution amounts prepared by adding alpha lactose monohydrate (Wynhale™ Inhalation lactose, DFE Pharma) to reverse osmosis water into an adequately sized vessel, 20 L and 5 L for the concentrated and dilute solution respectively, using an overhead stirrer with open turbine type impeller for mixing. The concentrated solution was heated to and maintained at 80°C (undersaturated). The temperature was controlled via a PI controller linked with the tank's heating element and a temperature probe in the solution. The dilute solution was prepared in a similar manner to the concentrated solution, but the vessel was cooled to 25°C by placing it in a 25°C water bath, measured with a digital thermometer. The dilute solution prepared corresponded to an absolute alpha lactose supersaturation of 0.4 g/100 g water.

The continuous orifice nucleation process starts with the concentrated solution pumped through a pipe heat exchanger and rapidly cooled to 25°C, using a 24°C water bath. The pipe heat exchanger had an internal diameter of 4 mm and total length was adjusted with flow rate,

such that the rate of cooling was consistent in all the experiments. The concentrated stream at 25°C corresponded to an absolute alpha lactose supersaturation of 25 g/100 g, placing it in the labile or spontaneous nucleation region. A wait time post-cooling was achieved with a one hour average residence chamber. The concentrated stream was then pumped through a 0.31 mm orifice using a high-pressure peristaltic pump head and tubing with a 6 bar pressure rating. The flow rate of the concentrated stream through the orifice was altered to achieve two Reynolds numbers, 500 and 1000, at the orifice, approximately 1.5 and 3.1 bar pressure drop respectively. After passing through the orifice, the highly supersaturated stream was diluted to the growth concentration, 42 g/100 g, which corresponded to an absolute alpha lactose supersaturation of 8.2 g/100 g, in the upper end of the metastable region. This limited further primary and secondary nucleation, but allowed crystal growth. Three control samples with no orifice flow and 12 orifice flow samples were collected 2 minutes apart in 100 mL test tubes. The test tubes were sealed and placed horizontally in a custom built mixer, capable of holding 15 100 mL test tubes, and controlled with a variable speed motor to move the test tubes through approximately 5 revolutions per minute. The custom built test tube roller was used to suspend crystals for the growth time, but limit additional nucleation from evaporation and mixing which predominantly occurs via impeller mixing.

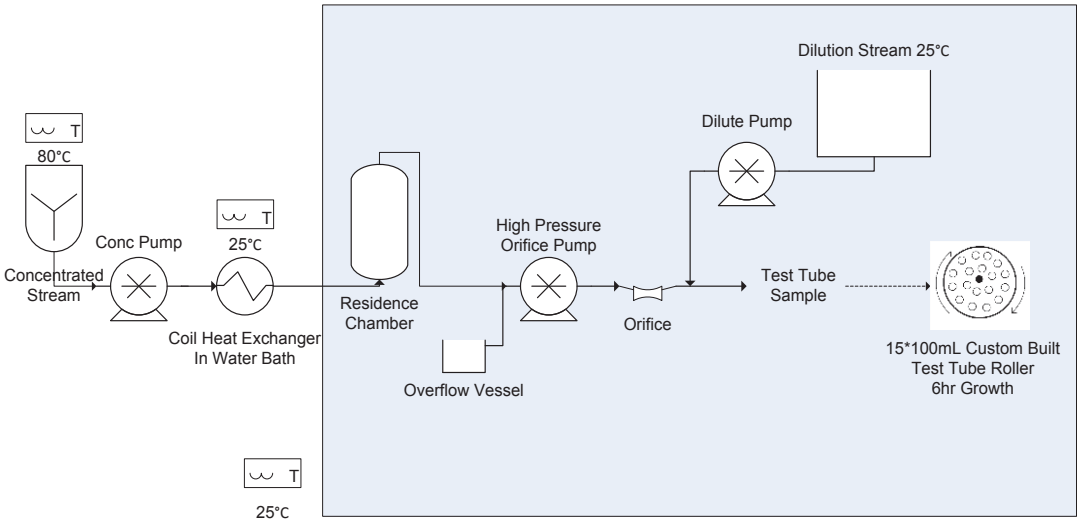


**Figure 42 Continuous orifice nucleation experimental setup**

Figure 42 is a schematic diagram of the continuous orifice nucleation process. After six hours of growth time the samples were analysed in a Malvern MasterSizer 2000, by adding a known volume to slightly supersaturated lactose background solution. The volumetric results were then converted to crystal numbers per mL. At least 3 repeats for each orifice Reynolds and wait time condition were carried out; all values are presented in the Results Section.

## 5.3 Results

### *5.3.1 Crystal Numbers*

From here on Reynolds 500 and Reynolds 1000 refers to orifice Reynolds numbers equal to 500 and 1000 respectively. Each Reynolds condition can be further separated into orifice flow with no wait time (NW) or with a wait time (W). This graph labelling in this section defines orifice flow rate, orifice Reynolds number and wait condition; for example Q46.Re500 NW defines an orifice flow rate of 46 mL.min$^{-1}$, orifice Reynolds number of 500, and no wait time before orifice flow. The different orifice flow conditions tested all exhibited a similar trend of increasing crystal numbers with time, which can be seen in Figure 43. After approximately 15 minutes of orifice flow the system appears to reach steady state and these values were used for calculating averages and statistical comparison. The averaged crystal numbers for each condition were: Reynolds 500 NW =1.06±0.07x10$^{9}$ #.mL$^{-1}$, Reynolds 500 W =1.00±0.06x10$^{9}$ #.mL$^{-1}$, Reynolds 1000 NW =1.23±0.11x10$^{9}$ #.mL$^{-1}$, and Reynolds 1000 W =0.51±0.16x10$^{9}$ #.mL$^{-1}$ at the 95% level of confidence. The control samples, flow did not pass through an orifice, crystal numbers were all significantly less than the orifice flow conditions at the 95% level of confidence. T-tests carried out found no significant difference between combined Reynolds numbers conditions and Reynolds 500 no wait and wait conditions. Reynolds 1000 no wait and wait numbers were found to be significantly different.

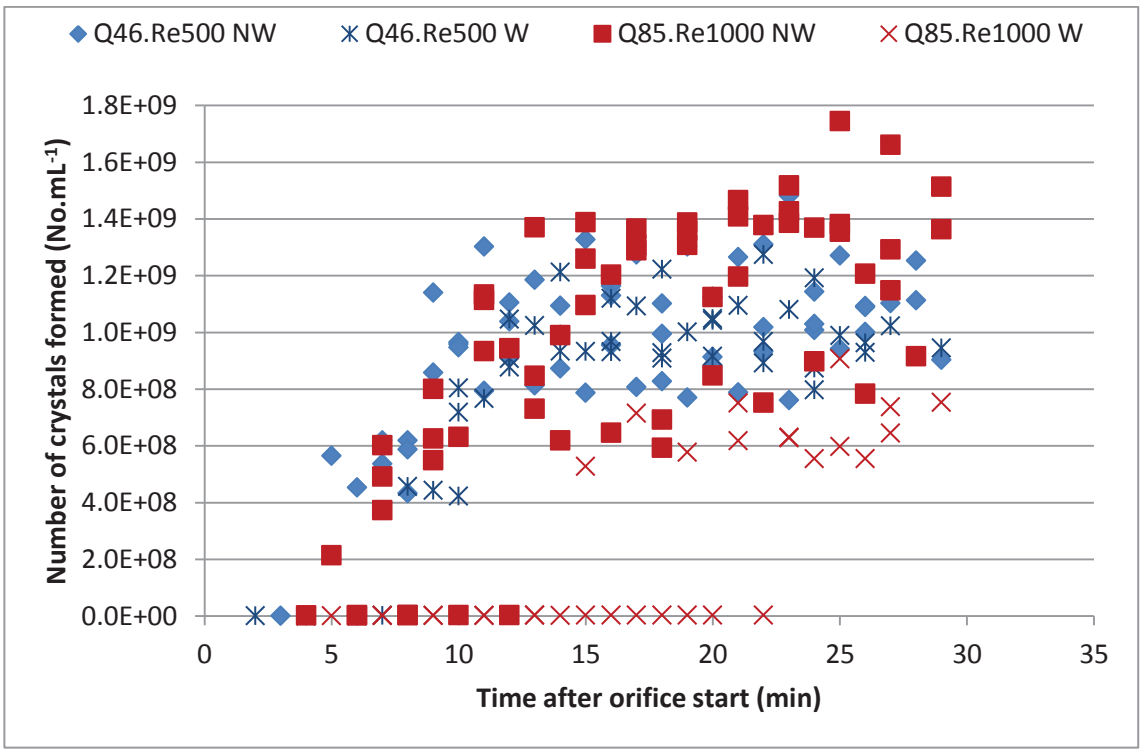


**Figure 43 Steady state values for number of crystals per mL for all conditions, Q46 and Q85 corresponds to the orifice flow rate in mL.min$^{-1}$, NW=no wait and W=wait**

The number of crystals formed versus final growth concentration, converted from refractive index measurements using a developed equation contained in Appendix A.9, is shown in Figure 44 (log scale). There is a significant positive trend for the combined data with the slope different from zero at the 95% level of confidence. This means an increase in the final numbers of crystals in a growth sample can be partly attributed to an increased final growth concentration, which is made up from the combination of the concentrated and dilute streams.

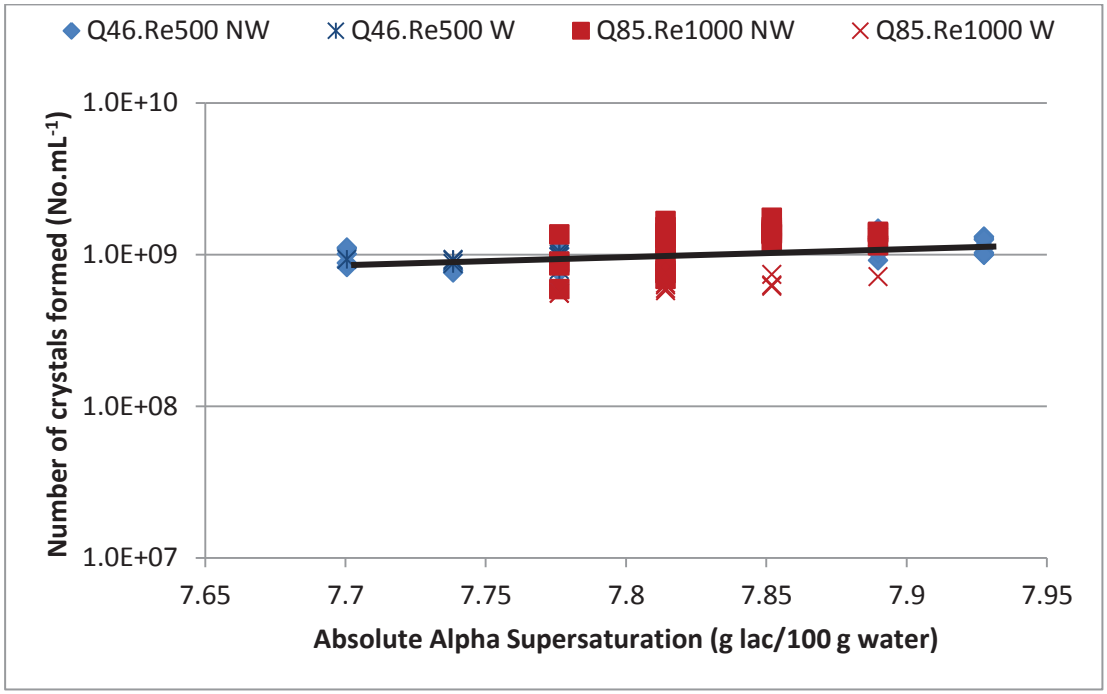


**Figure 44 Steady state values for number of crystals per mL against absolute alpha lactose supersaturation for all conditions, Q46 and Q85 corresponds to the orifice flow rate in mL.min$^{-1}$, NW=no wait and W=wait**

### *5.3.2 Particle Size Distribution*

The steady state particle size distribution (PSD) $d_{10}$, $d_{50}$ and $d_{90}$ values are plotted against orifice flow time for the different conditions tested (Figure 45, Figure 46 and Figure 47), including run replicates. No apparent trend in steady state particle size with orifice flow time can be seen for all conditions tested. For each of the conditions tested the $d_{10}$, $d_{50}$ and $d_{90}$ values were averaged and 95% level of confidence calculated presented in below:

| Condition | $d_{10}$ (µm) | $d_{50}$ (µm) | $d_{90}$ (µm) |
|---|---|---|---|
| Reynolds 500 NW | 1.27±0.1 | 5.66±0.1 | 13.9±0.3 |
| Reynolds 500 W | 1.62±0.1 | 6.51±0.2 | 15.2±0.7 |
| Reynolds 1000 NW | 2.10±0.2 | 8.93±0.3 | 21.0±0.8 |
| Reynolds 1000 W | 3.20±0.1 | 10.1±0.3 | 23.8±1.0 |

**Table 8 Average particle size distribution, $d_{10}$, $d_{50}$, and $d_{90}$ results for each orifice condition, NW=no wait and W=wait**

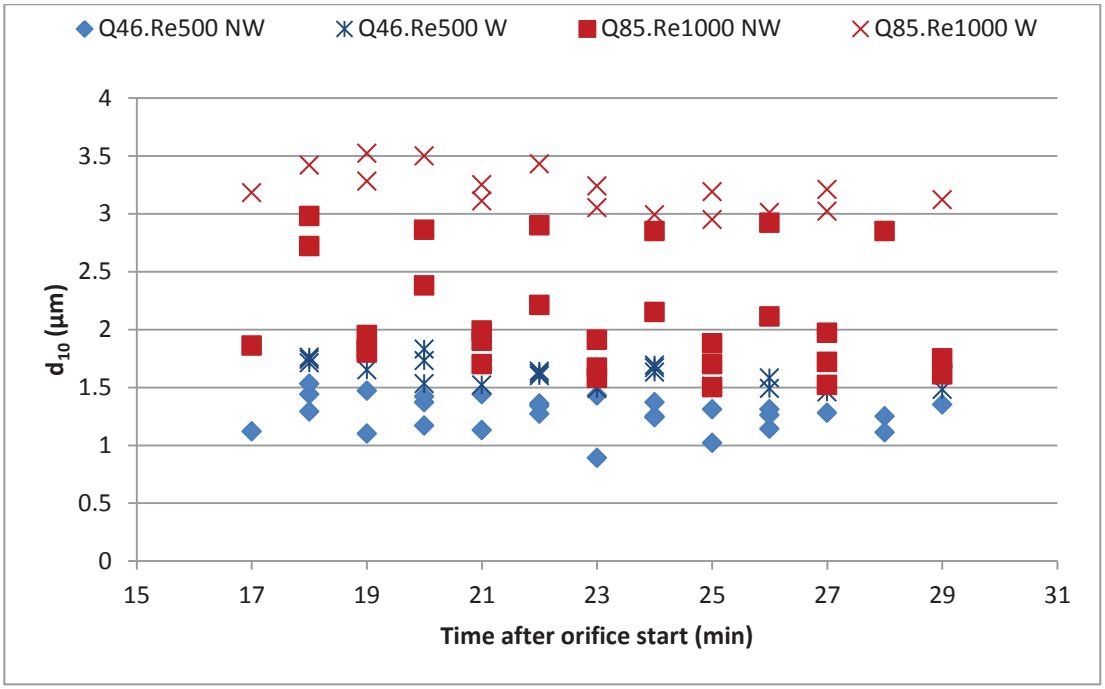


Figure 45 Steady state Malvern MasterSizer $d_{10}$ size values for all orifice conditions, Q46 and Q85 corresponds to the orifice flow rate in $mL.min^{-1}$, NW=no wait and W=wait

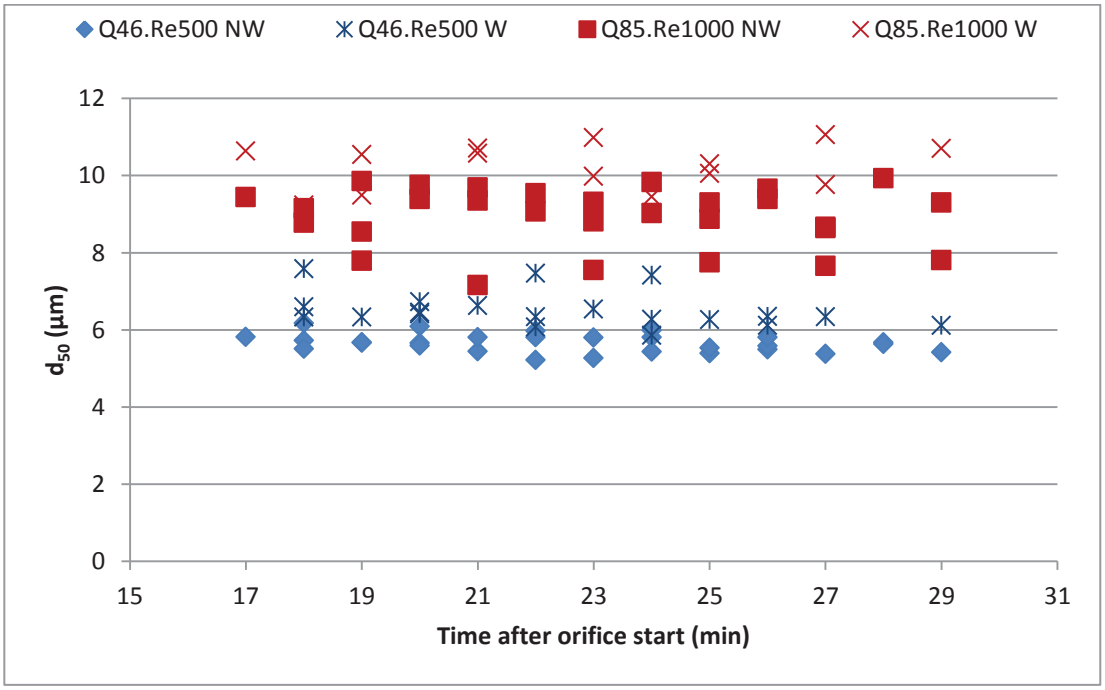


Figure 46 Steady state Malvern MasterSizer $d_{50}$ size values for all orifice conditions, Q46 and Q85 corresponds to the orifice flow rate in $mL.min^{-1}$, NW=no wait and W=wait

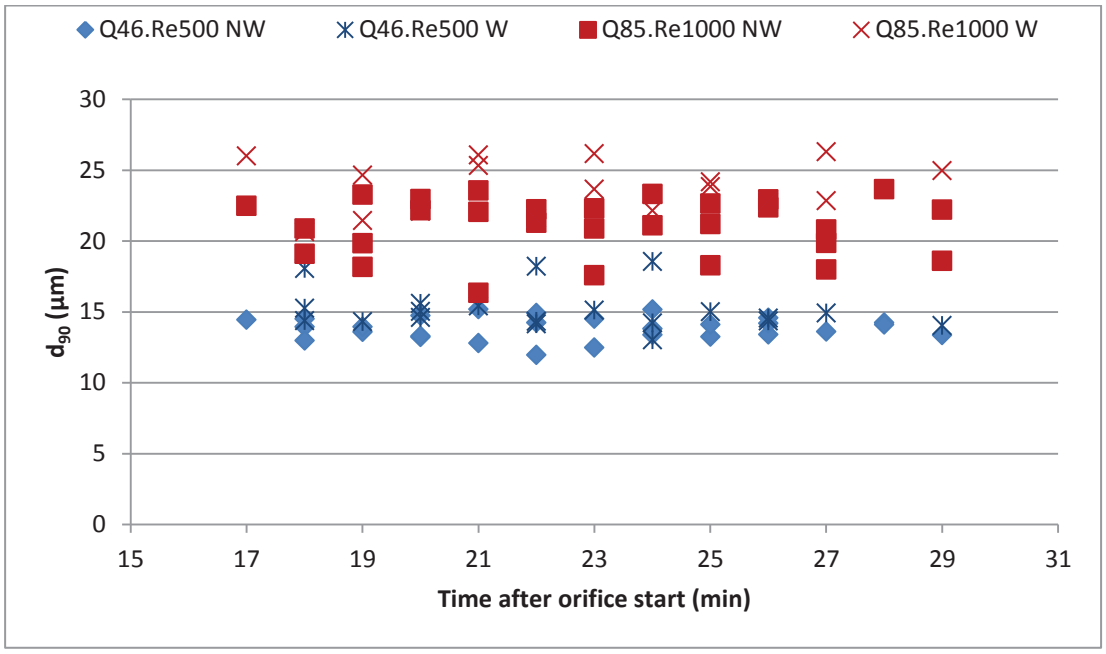


**Figure 47 Steady state Malvern MasterSizer $d_{90}$ size values for all orifice conditions, Q46 and Q85 corresponds to the orifice flow rate in mL.min$^{-1}$, NW=no wait and W=wait**

A t-test was performed and at the 95% level of confidence for the $d_{10}$, $d_{50}$ and $d_{90}$ values. The Reynolds 1000 W and NW conditions were significantly larger than the Reynolds 500 W and NW conditions. Additionally, for each Reynolds 500 and 1000 condition, the wait condition had a significantly larger particle size compared to no wait condition.

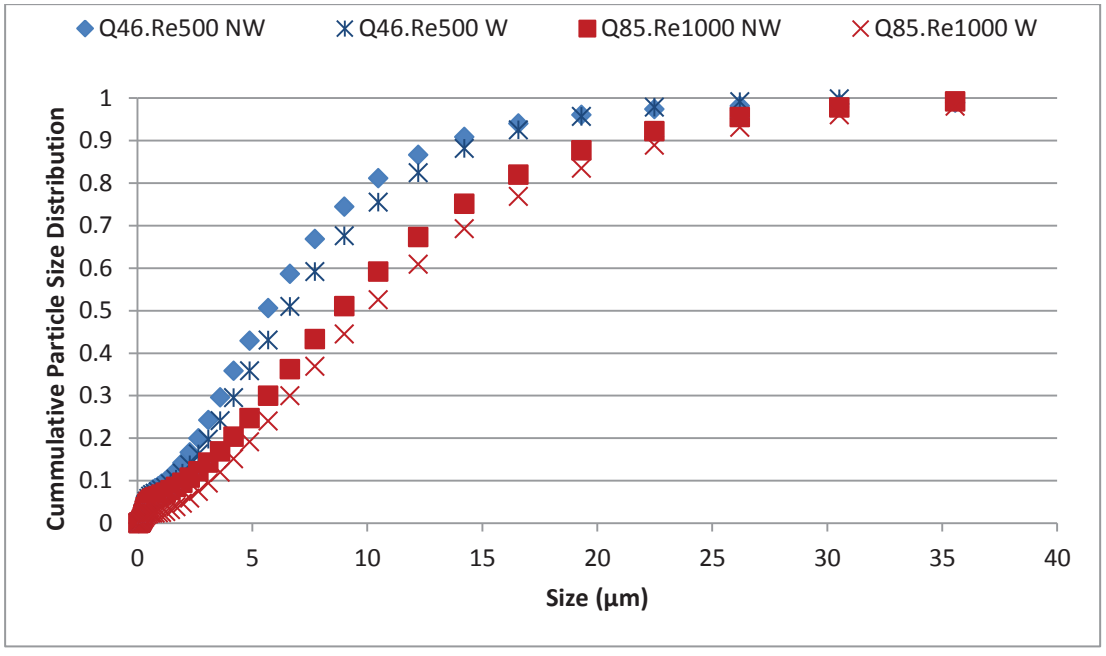


**Figure 48 Averaged cumulative particle size distributions (volume basis) for all orifice conditions, Q46 and Q85 corresponds to the orifice flow rate in mL.min$^{-1}$, NW=no wait and W=wait**

Cumulative particle size distributions were averaged and plotted for all the conditions tested (Figure 48). The trend of increasing particle size between no wait and wait, and Reynolds 500

and Reynolds 1000, can be seen with the curves moving right on the size axis. Spans were averaged for the different conditions tested: Reynolds 500 no wait 2.22±0.04, Reynolds 500 wait 2.07±0.04, Reynolds 1000 no wait 2.11±0.03, Reynolds 1000 wait 2.03±0.04 at the 95% level of confidence. Span decreases with a wait time for each Reynolds number condition, and the combined Reynolds 1000 conditions have a lower span than Reynolds 500 conditions (t-tests show there is a significant difference at 95% level of confidence).

## 5.4 Discussion

### *5.4.1 Steady State Orifice Flow Values*

Once flow through the orifice was started, all experiments showed increasing crystal numbers (Figure 2) and decreasing particle size with time, until steady state values were reached. This happened after approximately 15 minutes and may have been due to the replacement of residual wash water within the orifice pump and pipe system by the nucleation solution. These equilibrium values were used for analysis because they enabled steady state comparison between the conditions tested.

### *5.4.2 Crystal Numbers*

Two levels of orifice Reynolds numbers, 500 and 1000 were used, a cavitation number of 1.85 and 0.46 respectively, but no significance difference in crystal numbers was found between the conditions. From the results of McLeod *et al.*, (2010), it is expected that there would be an increase in crystal numbers at higher Reynolds numbers or lower Cavitation numbers. Figure 41 shows the Reynolds numbers tested by McLeod *et al.*, (2010) ranging from 200 to 20,000 and there is a positive trend for Reynolds numbers above 1000 with increasing crystal numbers; however in the Reynolds number range from 500 to 1000 there is no clear indication for an increase in crystals numbers. This would suggest larger Reynolds numbers are required in the current experiment to show the trend for increasing crystal numbers. A similar result occurs for the cavitation numbers which ranged from 0.01 to 100. The ratio of velocity at orifice and orifice diameter is 30,000 to 60,000; this is at the high end of McLeod *et al.*, (2010) results, which ranged from 1,000 to 100,000.

To confirm the trend shown by McLeod *et al.*, (2010), that increased Reynolds numbers, above 1000, would result in increased crystal numbers, additional higher continuous orifice flow rate experiments were carried out. Lactose solution, at a flowrate of 144 mL.min$^{-1}$, was passed through a 0.31 mm orifice (Re=1700, $\sigma_c$=0.16 and $\Delta$P=7.1 bar). However pressure limitations were reached with the high pressure peristaltic pump setup used. The pump head and tubing

were pressure limited to 6 bar, and orifice flow generally dropped to around 128mL.min$^{-1}$ (Re=1500, $\sigma_c$=0.21 and $\Delta$P=5.8 bar) with time. This meant the final growth concentration was less than the previous Reynolds 500 and 1000 conditions. With reference to Figure 44, the high orifice flow runs, final absolute alpha supersaturation was measured to be within 7.7-7.75 g/100 g. The higher flow rate tests were also limited by the increased amount of lactose required (>10 kg needed for a 30 min run). When the orifice pressure drop was close to the maximum pump operating pressure, blockages occurred much more easily. Two no wait runs where the orifice did not block were carried out, with Reynolds numbers ranging from 1500 to 1700, and the average steady state crystal numbers measured was 1.65±0.39x10$^9$ #.mL$^{-1}$. This is higher than the Reynolds 500 and 1000 conditions.

Within each flow condition, orifice flow was tested with and without a wait time. A t-test carried out showed the Reynolds 500 wait time condition gives lower crystal numbers with a 79% level of confidence, considered not significant at the 95% level of confidence. The Reynolds 1000 condition t-test shows wait time results have significantly lower crystal numbers. However, on analysing the initial growth concentration for the Reynolds 1000 no-wait time results, the concentration was found to be significantly higher than the Reynolds 1000 wait-time results. When combining all experimental results it was found, using linear regression, that crystal numbers increased with growth concentration (Figure 44). Although the same initial solution concentrations were prepared for each run, pump flow rate variation caused the final growth concentrations to vary. A higher final growth concentration indicates a higher ratio from the concentrated orifice nucleated stream, and therefore an increase in crystal numbers occurs. This could explain why there is a significant difference between Reynolds 1000 wait time crystal numbers and Reynolds 1000 no wait time crystal numbers. When comparing crystal number results from the combined Reynolds 500 conditions with the Reynolds 1000 conditions, the Reynolds 1000 conditions were found to be less with a 67% confidence, and not considered significant.

Overall, for all conditions tested, the crystal numbers in this work, ~1x10$^9$ #.mL$^{-1}$, were higher than those measured by McLeod *et al.*, (2010), which were of the order of 1x10$^5$ #.mL$^{-1}$. This is explainable as crystal sizes were analysed via the Malvern MasterSizer and subsequently converted to a number per mL, whereas McLeod *et al.*, (2010) used a microscope counting method. The small crystal sizes measured by the Malvern MasterSizer are significant when considered on a number basis. It is likely that most crystals below 5 µm were uncountable using a standard microscope, and in these experiments greater than 99% of the crystals were

below 5 µm. This is reinforced by the preliminary results which were counted under a microscope and were similar in magnitude as McLeod *et al.*, (2010).

The crystal numbers per mL for the two conditions tested would be too high for the CSC. The crystal volume percent resulting in the column would start to cause hindered settling. In addition, orifice blockages did happen on at least one occasion after time. This was likely due to crystal or foreign particle becoming trapped in the orifice. Therefore due to potential orifice blockages when operating on a longer 16+ hour basis, a different, more robust single nucleation event experimental setup needs to be developed; see Section 5.4.4.

### *5.4.3 Particle Size Distribution*

The Malvern MasterSizer was used to obtain reliable information on PSD at the different orifice flow conditions tested. The Reynolds 500 condition showed that a wait time gave significantly larger crystals for the $d_{10}$, $d_{50}$ and $d_{90}$ particle sizes. This was also true for the Reynolds 1000 condition. When comparing particle sizes from all results between lower and higher Reynolds numbers, it was also found the $d_{10}$, $d_{50}$ and $d_{90}$ were significantly larger for the higher Reynolds number conditions. These results suggest the addition of a wait time or higher Reynolds numbers leads to faster growing crystals when total numbers are considered to not differ significantly, which was found to hold for the low Reynolds number condition, but not the higher. However an argument for significant number difference has been proposed earlier. Alternatively less “smaller” crystals could result in a larger volumetric PSD. This would be plausible if numbers dropped significantly between having a wait time or a Reynolds condition, which was not found to be the case. Research has shown that large particle sizes can increase due to agglomerates (A. M. Williams, Jones, Paterson, & Pearce, 2009). But because crystal numbers stayed the same, this is only plausible if numbers increased and resulting crystals agglomerated, the net effect being the same number of crystals. Growth conditions were selected to be the same between experiments, so this is unlikely to have occurred. The growth concentration measurements were compared against particle size and no apparent trends were seen for the conditions tested.

Averaged cumulative volume distribution plots of the steady state values for each condition show the difference in PSD. No wait time and lower Reynolds number conditions have smaller particles. In the case for the CSC the primary interest resided with crystal numbers, even though the final span did decrease slightly with the addition of a wait time and at the higher Reynolds number. Longer growth times were not tested and it is unknown if the span would change with longer growth times. Assuming common history seed proposed by Butler (1998)

holds true, this would suggest growth rate dispersion would be relative with growth time and the span would remain unchanged.

### *5.4.4 Alternative CSC Single Nucleation Method*

A new method was developed to produce a nucleated feed stream, which could be fed into the CSC. For reliability, mechanical mixing (stirring) was chosen for the nucleation step. Simply replacing the orifice with a mixed vessel sounds viable in theory, but a number of problems are encountered when operating on a continuous basis with low flow rates. Firstly, it becomes difficult to assume a "single" nucleation point, as fluid will experience an average amount of mixing with time, with the potential for crystal build up. Additionally a sealed nucleation vessel capable of handling the CSC column head pressures would be required. To ensure all fluid experienced the same nucleation conditions, a batch nucleation mixing step with subsequent dilution to just above supersaturation was developed.

The batch nucleation step involved preparing a hot saturated lactose solution and cooling it overnight to the controlled ambient air temperature of 25°C with no mixing, resulting in a highly supersaturated solution. Intense impeller mixing was then applied inducing primary nucleation (and some secondary nucleation due to crystals already formed). The nucleated solution was then diluted to a concentration just above supersaturation. The resulting slightly supersaturated solution contained nuclei, but no further nucleation would occur and very minimal growth due to the low supersaturation. When starting the CSC column, the dilute nucleated stream was re-concentrated to the desired growth concentration on a continuous basis and fed into the CSC column. This occurred by combining the dilute nucleated stream with a hot saturated lactose stream and rapidly cooling down to the room temperature (25°C). The order of these steps for the concentration process was found to be important, such that additional nucleation and growth did not occur in the pipes prior to column entry. The detailed procedure for preparing the nucleated CSC feed stream is given in Section 7.3.1. The initial dilute nucleated stream Malvern MasterSizer measurements are shown in Table 9 for the different types of lactose used; as expected crystal volume concentration is low leading to potential measurement errors, typical Malvern MasterSizer sampling procedure requires higher obscuration levels. Table 10 and Table 11 in Section 6.3.1 show the results of 100 mL bottle roll controls prepared utilising this batch impeller mixing technique. The bottle roll method was similar to the custom built test tube mixer, used to gently mix the solution and suspend crystals without the need for impeller mixing. The final PSD produced after a controlled growth period was very consistent for the different runs, indicating the reliability of the method.

| Type | Concentration (Volume %) | $d_{10}$ (µm) | $d_{50}$ (µm) | $d_{90}$ (µm) | Span |
|---|---|---|---|---|---|
| IGL-1 | 0.0014±0.0018 | 2.4±0.2 | 6.3±1.0 | 27.0±16.2 | 3.56±1.94 |
| 200M-1 | 0.0009±0.0003 | 2.9±0.2 | 7.2±0.3 | 25.5±6.6 | 3.13±0.87 |
| 200M-2 | 0.0003±0.0002 | 2.9±0.3 | 6.3±1.3 | 14.7±9.0 | 1.77±1.04 |

**Table 9 Initial dilute nucleated stream Malvern MasterSizer measurements**

Two methods of ultrasonic mixing were tested in early attempts to increase the nucleation number in the feed stream. A 60 W ultrasonic bath and a 60 W ultrasonic transducer were attached to the outside of the cooling pipe containing concentrated lactose solution. Ultrasound was applied to the concentrated stream, both during and after cooling, and prior to dilution to the final feed concentration for growth. No significant increases in the final crystal concentration were detected. It is speculated that the level of ultrasound intensity or lactose supersaturation was not high enough; typically acetone is also used with ultrasonic mixing to lower the nucleation energy barrier to be overcome (Bund & Pandit, 2007c; Kougoulos, Marziano, & Miller, 2010; S. R. Patel & Murthy, 2009, 2011).

## 5.5 Conclusions

Continuous orifice nucleation experiments were carried out to assess the effect on crystal numbers and the particle size distribution. The factors altered were orifice Reynolds numbers, 500 and 1000, and whether a wait time prior to orifice flow occurred. An apparent effect on crystal numbers was not observed for the wait time and Reynolds number conditions tested. However, a wait time and increased orifice Reynolds number lead to an increased particle size for the continuous orifice nucleation of lactose, suggesting that these conditions produced faster growing crystals. Resulting spans obtained were significantly lower for higher Reynolds orifice flow and with the addition of a wait time. The current low flow rate and small orifice diameter setup is deemed unreliable to operate on a continuous (16+hour) basis due to the high pressures and possibility of blockages occurring. Without better equipment, a robust alternative single nucleation event utilising impeller mixing was developed for use with the continuous settling crystallizer setup. In the next chapter, a theoretical model for the continuous settling crystallizer is developed, which will be used to assess the theoretical particle size distribution and span.

# Chapter 6 –Continuous Settling Crystallizer Theoretical Model

## 6.1 Introduction

In the two previous chapters, lactose crystal settling properties and single nucleation techniques were studied providing background information for a continuous settling crystallizer (CSC) theoretical model to be developed. The aim of the CSC was to continuously produce inhaler grade lactose (IGL), conforming to the desired particle size distribution (PSD) targets set out in Chapter 1.

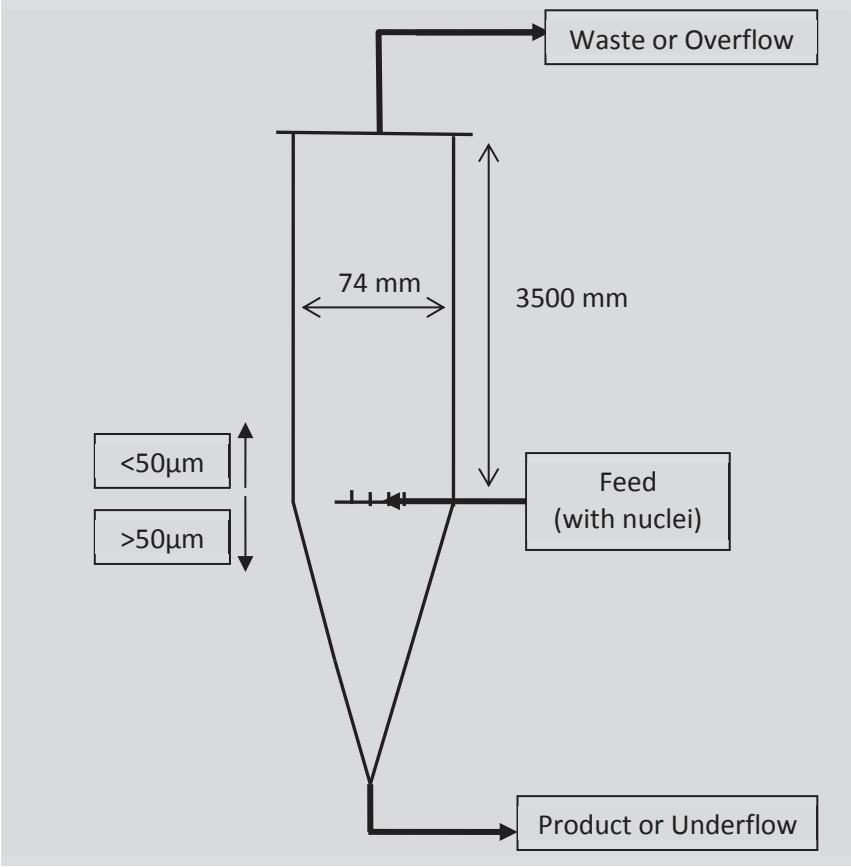


Figure 49 Basic schematic of a continuous settling crystallizer (CSC)

A literature investigation found particle settling post crystallization was a viable technique for meeting the stated IGL production objectives. However, carrying out settling post crystallization was viewed as an additional processing step and a single-step novel crystallization process to produce IGL was desired. Incorporating settling based size classification into a functioning crystallizer led to the CSC concept. The main component in the CSC is one vertical cylindrical column. A pre-nucleated supersaturated lactose stream is fed in near the bottom of the column and flows up the column until exiting into the overflow stream. The generalised concept for the CSC is depicted in Figure 49. The pre-nucleation occurs via mechanical mixing of a highly supersaturated solution, which is subsequently diluted to a

growth concentration. The nuclei entering with the feed stream grow inside the column and settle out into the product stream. The conditions inside the column are such that the growing crystals settle under gravity according to Stokes Law. Stokes law describes the settling of spherical particles well when the particle Reynolds number is less than 1 (Equation 45).

Common seed history, as discussed in Section 2.3.3, confirms that fast and slow growing crystals arise from a single nucleation event. Growth rate dispersion from the fast and slow growing crystals leads to unwanted particle spans under normal growth conditions. The CSC column allows a significant proportion of slow growing crystals to reach the terminal settling crystal diameter due to the column height, and subsequently settle from the column into the product stream. In contrast the fast growing crystals do not travel as high up the column before growing to their terminal settling crystal diameter. A trade off in height exists between minimising slow growing crystals reaching the overflow stream and maximising yield. By altering the net upwards column fluid velocity, the crystal terminal settling diameter changes and particle size selection can occur. The potential for scalability exists through increasing the column radius or adding additional columns. Net flow rates, growth concentration and height would be kept constant to produce the same PSD product as a smaller radius column.

## 6.2 CSC Theoretical Model Development

### *6.2.1 Model Aim*

Under normal operating conditions, lactose nuclei and fluid will enter the CSC column at a constant rate. The aim of the CSC theoretical model is to follow individual lactose crystals position, movement, and growth after entering the CSC column. Growth rate dispersion will be taken into account by assigning different but constant growth rates to the individual crystals entering the column. Parallel to modelling crystal development, the lactose fluid position, movement and concentration will also be monitored, enabling a correlation with the lactose crystals to calculate settling and growth rates. In a similar manner to the lactose crystals, lactose fluid will be split up in to individual fluid sections of a known volume. Lactose crystals that have grown large enough, opposed the fluid flow, and settled out from the column into the product stream will enable the $d_{50}$ and span to be calculated.

### *6.2.2 Model Assumptions*

The following assumptions were made in developing the theoretical CSC model:

- No vertical diffusion of water or soluble lactose between fluid sections.
- Crystals move vertically only. Pressure differential calculations on particles show minimal radial movement occurs (Appendix A.2).
- Crystals are assigned a longest length dimension, which is converted to a spherical diameter for settling calculations. Previous settling studies showed single crystals terminal settling orientation occurs with large base first.
- Constant feed properties. The feed entering the crystallizer has the same nuclei number, fluid lactose concentration and flow rate with time.
- No nucleation occurs within the crystallizer. The supersaturation growth rate is chosen to maximise growth but limit nucleation.
- Constant fluid temperature and no heat losses, therefore no convection effects at the fluid boundaries.
- Initially for simplicity a constant fluid velocity across the pipe radius was assumed, in order to test the idea that a narrow particle size would be obtained.
- Operated at low particle loading and laminar fluid flow, therefore eddies, mixing, and particle-particle interaction are ignored.
- Individual fluid sections are assumed to have a constant cross-sectional cylinder area with height. Cross-sectional area can change between fluid sections depending on crystallizer geometry chosen.
- The model currently does not allow for overflow crystals to be recycled to the feed. However the crystallizer will be operated such that approximately 0% of crystals reach the overflow stream. In theory this stream can be concentrated and recycled back into the feed to increase the yield.
- The product stream is not modelled. Once crystals settle below the height at which they enter, they are assumed to be product crystals. There is also no net downwards movement of fluid, and therefore the product stream is crystal only.

### 6.2.3 Model Formulation

The model formulation can be split into five key equations, 1-rate of individual crystal diameter increase, 2-rate of individual crystal movement, 3-rate of fluid section lactose depletion, 4-rate of fluid section water depletion and 5-rate of fluid section movement.

**1) Rate of individual crystal diameter increase = Constant growth rate by supersaturation**

Particle growth rate, $G_n$ (µm.min$^{-1}$), is a function of the unique growth rate constant, $k_{gs,n}$, multiplied by the fluid section supersaturation, as shown in Equation 51:

$$\frac{d(G_n)}{dt} = \left[k_{gs,n}\left(C_{\alpha,m} - C_{\alpha s,m}\right)^{\alpha_1}\right] / \alpha_v$$

**Equation 51 Particle growth rate incorporating specific crystal growth rate and fluid section m concentration**

where $C_{\alpha,m}$ (g lactose/100 g water) is the α-lactose concentration of the fluid section, $C_{\alpha s,m}$ (g lactose/100 g water) is the α-lactose solubility concentration of the fluid section, $\alpha_1$ (-) is an exponential growth factor=1.31, and $\alpha_v$ (-) lactose tomahawk shape factor=0.60.

Individual particle growth rate was initially predicted using Equation 52, but the growth rate distribution was later matched to experimental batch grown controls.

$$k_{gs,n} = 0.0165(\text{abs}(\exp^{(\text{randn}(1,1)*a_1+b_1)}))$$

**Equation 52 Initial growth rate constant prediction**

where randn was a random number, and $a_1$(-) and $b_1$(-) were system specific constants.

Alpha lactose concentration of the fluid section used in calculating growth rate:

$$C_{\alpha,m} = ls_m/(100w_m)$$

**Equation 53 Alpha lactose concentration of fluid section**

where $ls_m$ (kg) is the fluid section soluble lactose mass and $w_m$ (kg) is the fluid section water mass.

Alpha lactose solubility concentration of the fluid section used in calculating growth rate:

$$C_{\alpha s,m} = [C_s - R_D K_S(C_T - C_s)]/(1 + K_S)$$

**Equation 54 Alpha lactose solubility concentration of fluid section**

where $C_s$ (g lactose/100 g water) is the soluble lactose concentration, $R_D$ (-) is the correction factor for α-lactose depression, $K_S$ (-) is the solubility effect constant, and $C_T$ (g lactose/100 g water) is the total lactose concentration.

Soluble lactose concentration used in calculating α-lactose solubility:

$$C_s = 10.9109\exp^{(0.02804Tc)}$$

**Equation 55 Total lactose solubility concentration (McLeod, *et al.*, 2007)**

where $Tc$ (°C) is the solution temperature.

Correction factor for alpha lactose depression used in calculating α-lactose solubility:

$$R_D = 0.0187\exp^{(0.0236\mathrm{Tc})}$$

**Equation 56 Correction factor for alpha lactose depression**

Solubility temperature effect constant used in calculating α-lactose solubility:

$$K_S = 0.0024\mathrm{Tc} + 1.6353$$

**Equation 57 Temperature effect of equilibrium constant**

Total lactose concentration used in calculating α-lactose solubility:

$$C_T = C_\alpha(1 + K_S)$$

**Equation 58 Total lactose concentration**

where $C_\alpha$ (g lactose/100 g water) is the alpha lactose concentration.

**<u>2) Rate of individual crystal movement</u> = Fluid section velocity – crystal terminal settling velocity**

Change in Individual crystal position, $z_n$ (m), can be found from the difference in fluid section velocity, $u_{fl,m}$ (m.s$^{-1}$), and crystal terminal settling velocity, $u_{t,n}$ (m.s$^{-1}$):

$$\frac{d(z_n)}{dt} = u_{fl,m} - u_{t,n}$$

**Equation 59 Particle movement, difference in fluid velocity and crystal terminal settling velocity**

The fluid section velocity used in particle movement was based on the change in fluid section position with time. When negligible lactose and water are consumed during the time step and the column geometry remains the same with height, fluid velocity is constant and can be described by Equation 60.

$$u_{fl} = Q_f/A_m$$

**Equation 60 Average column fluid velocity**

Crystal terminal settling velocity used in calculating change in crystal position:

$$u_{t,n} = \frac{(\alpha_v d_n)^2(\rho_{lc} - \rho_f)g}{18\mu_v}$$

**Equation 61 Crystal terminal settling velocity relative to spherical particle diameter**

where $d_n$ (m) is the particle longest length, $\rho_{lc}$ (kg.m$^{-3}$) is the lactose density, $\rho_f$ (kg.m$^{-3}$) is the fluid density, and $\mu_v$ (Pa.s) is the fluid viscosity.

Fluid density used in calculating crystal terminal settling velocity :

$$\rho_f = \rho_w / \left[1 - \frac{C_n(C_T)}{1 + C_T}\right]$$

**Equation 62 Fluid density**

where $C_n$ (-) is a temperature related constant for calculating density.

Fluid viscosity used in calculating crystal terminal settling velocity:

$$\mu_v = \frac{(1 + 0.5\emptyset)}{(1 - \emptyset)^2}\mu_0$$

**Equation 63 Fluid viscosity**

where $\emptyset$ (-) is the effective volume fraction and $\mu_0$ (Pa.s) is the solvent viscosity.

Effective volume fraction used in calculating fluid viscosity:

$$\emptyset = F_r \rho_f V_e$$

**Equation 64 Effective volume fraction**

where $F_r$ is the mass fraction and $V_e$ (m$^3$.kg$^{-1}$) is the effective specific volume.

Solvent viscosity used in calculating fluid viscosity:

$$\mu_0 = 0.03333 exp^{470.5/(118.2+Tc)}$$

**Equation 65 Solvent viscosity**

Effective specific volume used in calculating fluid viscosity:

$$V_e = 0.00135 - 8.9x10^{-6}Tc + 5.5x10^{-8}Tc^2$$

**Equation 66 Effective specific volume**

**3) Rate of fluid section lactose depletion = Lactose mass used by individual crystals during growth**

Change in initial fluid section soluble lactose mass, $ls_m$ (kg), is calculated via the change in the sum of individual particle growth lactose component used during that time period, $\Delta ls_n$ (kg):

$$\frac{d(ls_m)}{dt} = \frac{d(\Sigma \Delta ls_n)}{dt}$$

Equation 67 Mass of soluble lactose in fluid section m

Individual crystal lactose mass used during growth, $\Delta ls_n$ (kg), is found by the change in particle volume, $V_{P,n}$ ($m^3$) multiplied by lactose density:

$$\Delta ls_n = 0.95 \Delta V_{P,n} \rho_{lc}$$

Equation 68 Soluble lactose mass used during crystal growth

The factor of 0.95 in the above equation is due to α-lactose monohydrate crystal incorporating approximately 5% water during growth.

Particle volume used in calculating crystal lactose mass used during growth:

$$V_{P,n} = (\alpha_v d_n)^3 \pi / 6$$

Equation 69 Particle volume (includes particle longest length conversion to spherical diameter)

**4) Rate of fluid section water depletion = Water mass used by individual crystals during growth**

Change in initial fluid section water mass, $w_m$ (kg), is calculated via the change in the sum of individual particle growth water component used during that time period, $\Delta lwc_n$ (kg):

$$\frac{d(w_m)}{dt} = \frac{d(\Sigma \Delta lwc_n)}{dt}$$

Equation 70 Mass of water in fluid section m

Individual crystal water mass used during growth:

$$\Delta lwc_n = 0.05 \Delta V_{P,n} \rho_{lc}$$

Equation 71 Water mass used during crystal growth

Again, the factor of 0.05 is due to α-lactose monohydrate crystal incorporating approximately 5% water during growth

**5) Rate of fluid section movement = New fluid position – old fluid position**

After each time step, the initial fluid section moves to a new position above the newly inputted constant fluid section, and the position of subsequent fluid sections are found from the addition of each identical fluid section volume in the crystallizer. When column geometry is constant, vertical fluid section movement is based on the fluid section velocity:

$$\frac{d(z_m)}{dt} = u_{fl,m}$$

Equation 72 Fluid section height movement

The vertical length component of an individual fluid section, $z_{l,m}$(m), can be calculated as follows, assuming constant column geometry:

$$z_{l,m} = V_{f,m}/A_m$$

Equation 73 Vertical length of an individual fluid section m

where $V_{f,m}$ ($m^3$), is the volume of the fluid section and $A_m$ ($m^2$) is the column cross-sectional area.

The volume of each fluid section currently excludes the crystal component, $lc_m$ (kg), but this was kept below 1% of fluid section mass and can be assumed negligible:

$$V_{f,m} = \frac{w_m + ls_m}{\rho_f}\left[+\frac{\Sigma lc_m}{\rho_{lc}}\right]$$

Equation 74 Volume of fluid section

The equations below are for determining the crystallizer cross sectional area with crystallizer height; constant for a cylinder, but changes with height if a cone is attached to the cylinder:

$$\text{If } 0 \le z \le (\beta Z)\ A_m = \pi {R_T}^2 \text{ (cylinder)}$$

Equation 75 Column area for a cylinder

where β is the solid cylinder height fraction, and $R_T$ (m) is the column radius.

$$\text{If } (\beta Z) \ge z \le (Z)\ A_m = \pi {R_T}^2 + 2\left[\frac{z-0.2Z}{\tan(90-\theta)}\right] \text{ (cone present at cylinder height } \beta Z)$$

Equation 76 Column area for a cylinder with a cone attached to the top

### *6.2.4 Model Solution*

The theoretical model simulated the movement and depletion of supersaturated lactose fluid sections as well as movement and growth of individual lactose crystals within a crystallizer of a defined height, *Z* (m). Fluid sections and crystals were related through their common property

of crystallizer height, $z_m$ and $z_n$. The equations developed for the fluid sections and particles were solved via a three dimensional matrix. Three-dimensional matrices were used to incorporate a time step, $\Delta t$ (s), for particle growth and movement, and fluid section lactose and water depletion and movement. The model was solved for a specified number of constant time steps. Appendix A.9 contains the Matlab CSC theoretical model simulation files. For the fluid and particle matrix, the columns of the matrix contained the functions and the rows contained the individual fluid sections or particles; after each time step, calculations were made and a new matrix was generated (in the third dimension).

#### 6.2.4.1 Fluid Matrix

Fluid section water, soluble lactose and crystal mass entering the column was calculated using the chosen time step multiplied by the flow rate of each component (Equation 77, Equation 78 and Equation 79). The chosen time step alters the individual fluid section volume, and consequently the total number of fluid sections within the column. Flow rate was constant with time; therefore the initial fluid section entering the bottom of the column was also constant with time.

$$w_{m,0} = W_F \Delta t = (W_{Or} + W_{Fr})\Delta t$$

**Equation 77 Water mass for fluid sections entering the CSC column**

$$ls_{m,0} = Ls_F \Delta t = (Ls_{Or} + Ls_{Fr})\Delta t$$

**Equation 78 Soluble lactose mass for fluid sections entering the CSC column**

$$lc_{m,0} = Lc_F \Delta t = (Lc_{Or} + Lc_{Fr})\Delta t$$

**Equation 79 Solid lactose mass for fluid sections entering the CSC column**

where $W_i$ (kg.s$^{-1}$) is the water mass flow rate, $Ls_i$ (kg.s$^{-1}$) soluble lactose flow rate, $Lc_i$ (kg.s$^{-1}$) is the solid crystal component for total feed, overflow-recycled component and non-recycled feed component (subscripts *F*, *Or* and *Fr* respectively), and $\Delta t$ (s) is the simulation time step.

Each individual fluid section has a soluble lactose (Equation 67) and water (Equation 77) component which changes with time depending on the crystal growth that occurs in a time step. Individual particles are matched to a section of fluid by searching the Particle Matrix, through the correlation of particle and fluid section height. This calculates the amount of lactose (Equation 68) and water (Equation 71) consumed by the particles and thus the amount to be removed from the fluid section. Fluid concentration (Equation 53), density (Equation 62) and viscosity (Equation 63) were recalculated after each time step. These changed the individual fluid sections volume (Equation 74) and vertical length within the crystallizer.

The CSC column individual fluid sections distribution and movement can be visualised in Figure 50. Starting from the bottom of the column at $z_m$=0 and $Z$=0. With each time step the fluid section moves to a new height position until $z_m$=$m$ at $Z$=$Z$. The properties of each individual fluid section are recalculated with every time step.

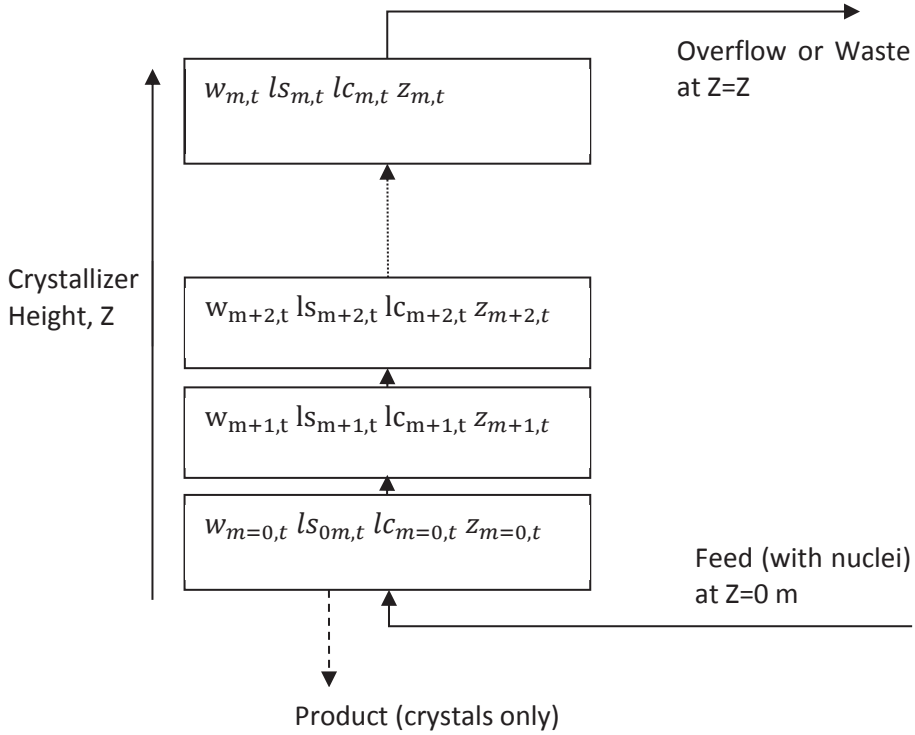


**Figure 50 Schematic of theoretical CSC model fluid sections**

### 6.2.4.2 Particle Matrix

Individual particles are monitored and a specified number of individual particles enter the column with each newly inputted fluid section at height $Z$=0 m. From particle height, the Fluid Matrix was searched, and the new fluid section which the particle resides in was found for each time step. The selected fluid section provided information for fluid concentration (Equation 53 and Equation 54), velocity (Equation 60), density (Equation 62), and viscosity (Equation 63). This information was used in particle growth (Equation 51) and vertical movement calculations (Equation 59 and Equation 61). Particles will stop growing and moving in the column once height is less than $Z$=0 m (product) or greater than $Z$=$Z$ (overflow). Modelling individual particles, with a search function matching a fluid section with particles, results in long simulation times. To reduce computer processing time but to obtain a certain particle or nuclei loading, model calculations for defined individual particle water and lactose

consumption are multiplied by a multiplication factor. The multiplied amount of particles will therefore have the same properties, and not change the span calculations.

Individual particles entering the column at height $Z$=*0 m* movement can be visualised in Figure 51. Crystal movement occurs in the positive $Z$ direction while crystal terminal settling velocity, $u_{t,n}$ (m.s$^{-1}$), is less than average fluid velocity $u_{fl}$ (m.s$^{-1}$), and growth occurs while particle column height position $z_n$ (m) is greater than $Z$=0 m and less than $Z$=$Z$. The properties of individual crystals are recalculated with each time step.

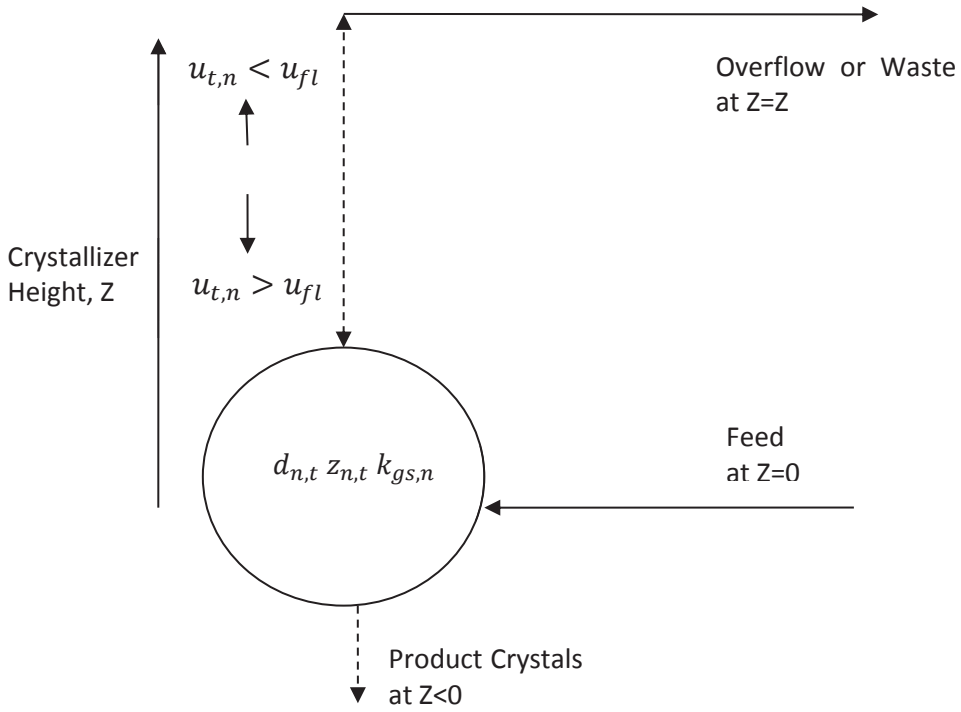


**Figure 51 Schematic of theoretical CSC model individual particle movement**

## 6.3 Theoretical Model Results

### *6.3.1 Batch Model Results*

An appropriate growth rate distribution prediction model was needed for the theoretical CSC simulations to be carried out. The constant crystal growth (CCG) rate data used was from 6 hr batch grown control experiments (sampled from nucleated feed described in Section 5.4.4) for two types of lactose with statistically different inherent growth rates. For each type of lactose the experimental growth conditions were the same as well as the theoretical model simulation conditions. The growth rate distribution arises from converting Malvern MasterSizer volume distribution into a number weighted table of $k_g$ bins (assuming CCG), and within each $k_g$ bin a random $k_g$ is generated; the particle model randomly selects a $k_g$ value from this table. The results for the IGL-1 and 200M-1 batch data are shown in Table 10 and Table 11; an averaged result with the standard deviation is shown. The model was run three times, as each run was unique giving slightly different results due to the random allocation of growth rates to each crystal.

| Condition | $d_{10}$ (µm) | $d_{50}$ (µm) | $d_{90}$ (µm) | Span |
|---|---|---|---|---|
| **Batch Growth Theoretical Model Predictions** | | | | |
| 4hr Growth | 15.2±0.2 | 34.7±0.4 | 71.9±0.3 | 1.64±0.02 |
| 6hr Growth | 22.5±0.5 | 53.9±1.7 | 116.4±11.2 | 1.74±0.15 |
| 16hr Growth | 58.2±0.7 | 142.5±3.8 | 300.2±16.9 | 1.70±0.08 |
| **Batch Growth Experimental Results** | | | | |
| 4hr Growth | 15.4±1.04 | 36.0±2.1 | 71.5±5.4 | 1.56±0.09 |
| 6hr Growth | 21.2±1.5 | 53.7±3.7 | 114.9±11.2 | 1.74±0.14 |
| 16hr Growth | 47.1±8.5 | 158.8±32.4 | 333.2±64.4 | 1.81±0.28 |

Table 10 Comparison of IGL-1 theoretical batch simulations with experimental batch values

| Condition | $d_{10}$ (µm) | $d_{50}$ (µm) | $d_{90}$ (µm) | Span |
|---|---|---|---|---|
| **Batch Growth Theoretical Model Predictions** | | | | |
| 4hr Growth | 7.3±0.3 | 24.5±1.2 | 48.1±5.8 | 1.66±0.15 |
| 6hr Growth | 12.8±1.0 | 37.2±1.7 | 78.7±11.4 | 1.77±0.25 |
| 16hr Growth | 42.5±1.4 | 95.1±4.6 | 189.7±18.1 | 1.54±0.10 |
| **Batch Growth Experimental Results** | | | | |
| 4hr Growth | 10.3±0.3 | 20.7±0.5 | 36.6±1.6 | 1.27±0.06 |
| 6hr Growth | 14.3±0.5 | 32.0±1.8 | 62.1±5.7 | 1.49±0.09 |
| 16hr Growth | 43.7±2.3 | 113.0±7.0 | 208.7±10.0 | 1.46±0.04 |

Table 11 Comparison of 200M-1 theoretical batch simulations with experimental batch values

The generated growth rate distributions allowed for the preliminary investigations into theoretical CSC model predictions to be carried out. The batch model code (Appendix A.9) was a simplified version of CSC theoretical model matrices code. Only one fluid section was specified with no movement, and the volume was specified to give a certain nuclei or crystal loading achieved in practice. Concentration change of the fluid section utilised Equation 53, Equation 67 and Equation 70. Individual nuclei were inputted at time zero (total number to give desired nuclei loading), with no movement function. The change in crystal size utilised Equation 51 to Equation 58, and correlating with the (single) fluid section. Fluid and particle properties were solved for each time step.

### *6.3.2 CSC Model Results*

The CSC theoretical model used the starting assumption of a single fluid velocity throughout the column. When CCG kinetics are assumed, fast and slow growing crystals can be seen following the path in the constant radius column crystallizer shown in Figure 52. A slow growing crystal travels higher up the column than a fast growing crystal before growing to the terminal settling diameter, opposing the fluid flow, and settling out into the product stream. Using a single fluid velocity resulted in a narrow product PSD, approximately 61 µm crystals, when constant column geometry was assumed. Additional column geometries consisting of a cone section and constant radius section were also tested (Figure 53). The effect of the cone section changed the fluid velocities that the fast and slow growing crystals encountered with height, leading to a larger product span and these designs were dismissed.

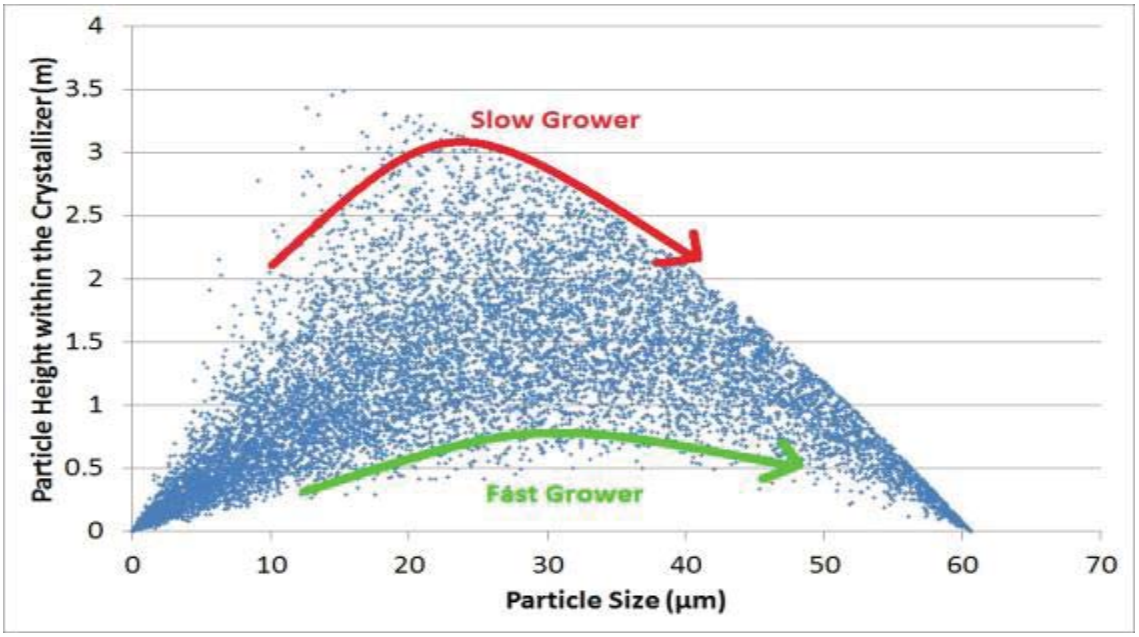


**Figure 52 Theoretical model particle height within the crystallizer column versus particle size at 16 hours of simulation time when single column fluid velocity is assumed**

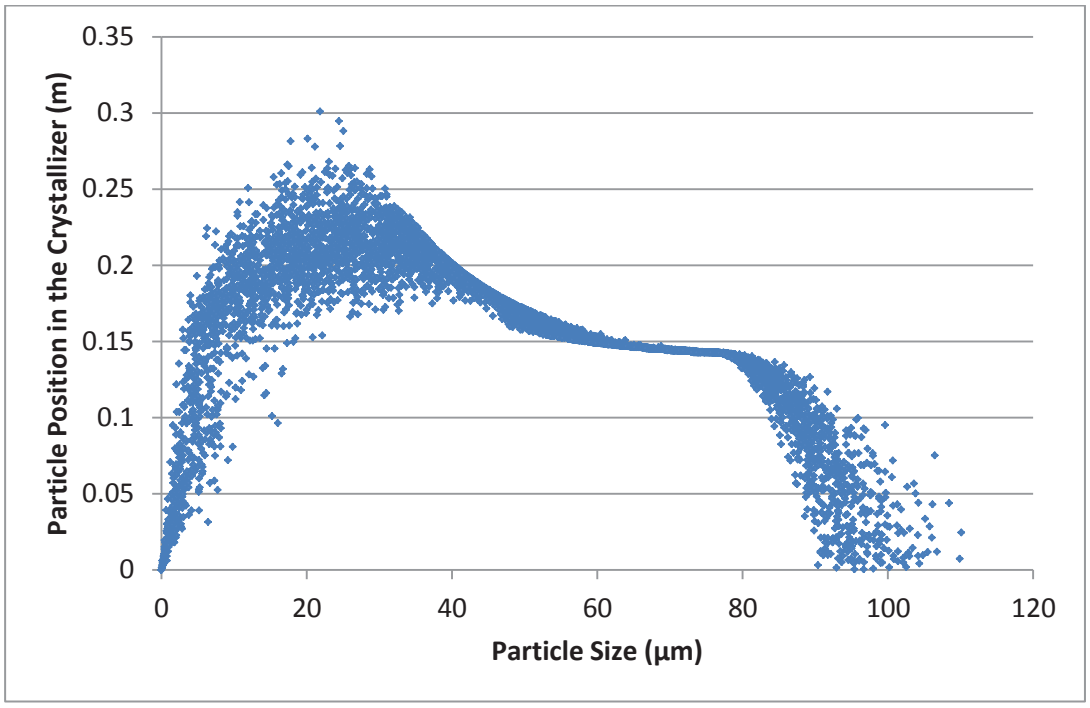


**Figure 53 Model results for particle position within the crystallizer and particle size, crystallizer has a 10° cone angle starting at 40% of the total crystallizer height (0.35 m)**

Column flow with a single velocity predicts a product span of ~0, which was a promising start for the CSC concept. The assumption of single fluid velocity, $u_f$, however does not hold for low Reynolds systems. When operating at fluid Reynolds numbers less than 2000, a laminar flow profile occurs. Laminar fluid flow across the pipes radius, $r$ (m), can be approximated by the parabolic velocity profile, $u_r$ (m.s$^{-1}$), Equation 80 and seen in Figure 54.

$$u_r = 2u_f(1 - r^2/{R_T}^2)$$

**Equation 80 Parabolic laminar flow radius velocity profile across a cylinder**

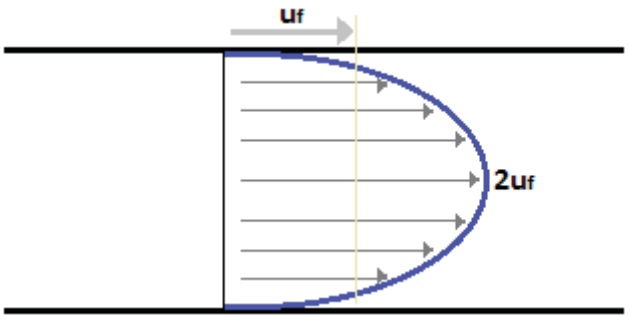


**Figure 54 Parabolic velocity profile across a pipe cross section, redrawn from (Çengel & Cimbala, 2006)**

CSC particle movement, shown in Equation 59, is determined relative to the fluid velocity. When a laminar fluid profile is assumed, radial position of the nuclei entering the column becomes important. A nucleus positioned in the centre of the column will experience a faster fluid velocity compared to near the column wall (Figure 55). The CSC theoretical model was

therefore modified to randomly assign a column radius position to nuclei entering the column. The new product crystal with column radius predictions can be seen in Figure 56, and as expected show a strong correlation. For simplicity the plug flow movement of the fluid sections were maintained, but depending on the particle radius position, the observed fluid velocity was altered for the settling particle according to Equation 80.

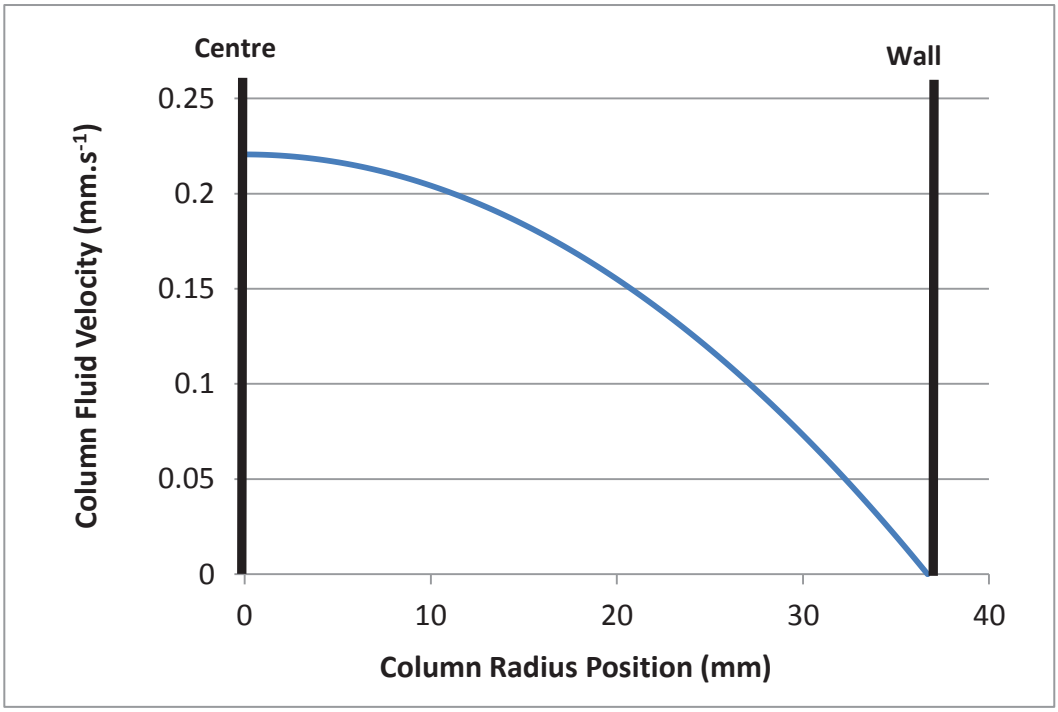


Figure 55 Parabolic velocity profile showing fluid velocity against column radius

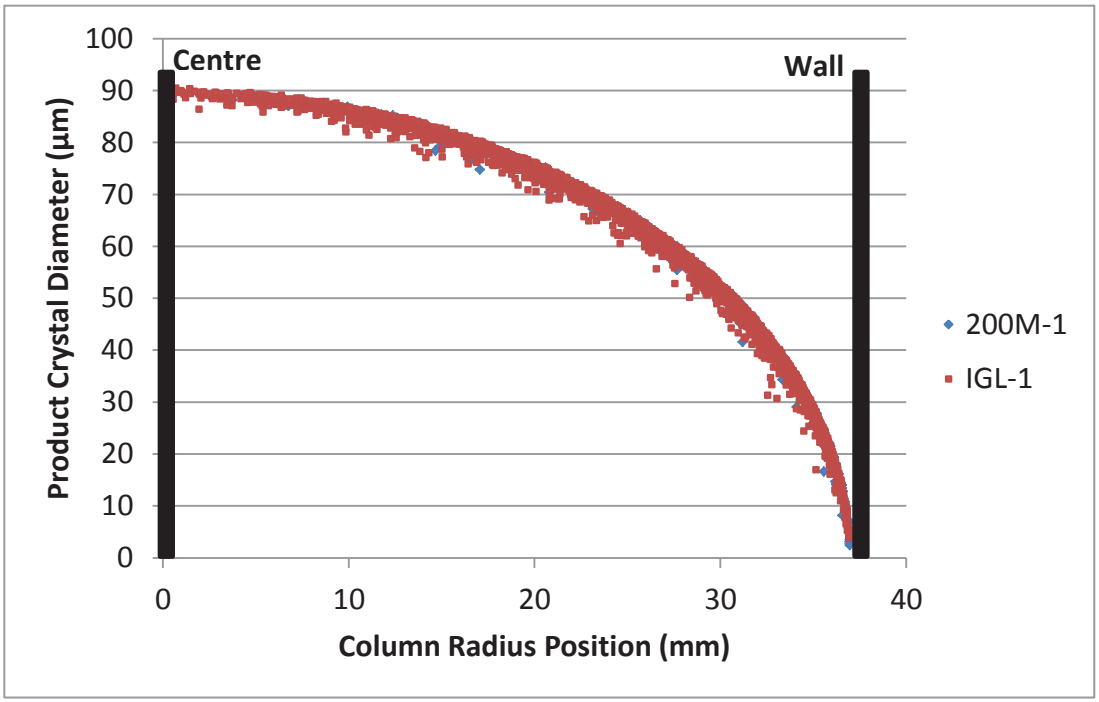


Figure 56 Theoretical model results showing product crystal size produced against column radius position

The CSC model with single fluid velocity required no particle column radius position allocation, but with laminar fluid flow particles were assigned a column radius position. The radius assignment was simplified to a random cross sectional area prediction, $r = \sqrt{rand(A_m)/\pi}$. This was later deemed inaccurate due to the parabolic effect on flow rates with radius position not being taken into account. Nuclei radius input predictions were changed to be volumetric flow based with radial position. Volumetric flow based predictions resulted in an increased amount of particles entering near the centre of column, where the velocity is higher (Figure 55 and Figure 56). The PSD is increased but not the maximum size of particles obtained from any radial position. Experiments and theoretical predictions found that the column fluid concentration did not change significantly with time. To reduce the theoretical model simulation time, constant fluid properties (concentration, density, viscosity) were subsequently assumed. This removed the cumbersome model search function which matched individual particles and fluid sections. All theoretical CSC results shown below were solved with constant fluid properties. Starting conditions for the CSC predictions were: volumetric feed flow rate, $Q_f$=28 mL.min$^{-1}$, $C_T$=42 g/100 g ($S_\alpha$=8.2 g/100 g), Z=3.5 m, Δt=5 s, and 10 unique particles, $P_N$ (#), entering per Δt. From here on the underflow stream will be referred to as the product stream, and likewise the overflow stream will be referred to as waste stream. Table 12 shows averaged product and waste stream results with the associated standard deviation. The model was run three times, as each run was unique giving slightly different results due to the random allocation of growth rates and radius position to each crystal.

| **Condition** | **$d_{10}$ (µm)** | **$d_{50}$ (µm)** | **$d_{90}$ (µm)** | **Span** |
|---|---|---|---|---|
| **Area Based Nuclei Input Theoretical Model Predictions using 200M-1** | | | | |
| Product Stream | 39.1±0.4 | 66.3±0.8 | 83.9±0.5 | 0.68±0.01 |
| Waste Stream | 6.6±0.1 | 21.5±0.8 | 36.8±1.0 | 1.40±0.02 |
| **Volumetric Flow Based Nuclei Input Theoretical Model Predictions using 200M-1** | | | | |
| Product Stream | 51.2±0.4 | 73.2±0.9 | 85.9±0.9 | 0.47±0.01 |
| Waste Stream | 6.7±0.0 | 22.5±0.1 | 36.7±0.3 | 1.33±0.02 |

**Table 12 CSC theoretical model standard conditions using area and volumetric flow based nuclei input and 16 hr run time**

From Table 12, after 16 hours of crystallizer run time for the correct volumetric flow based nuclei input, the theoretical prediction for the product span is 0.47±0.01 with a $d_{50}$ of 73.2±0.9 µm. These theoretical results satisfy the IGL production objectives of a $d_{50}$ between 50 to 90 µm and span less than 1. Additionally, the CSC process utilises pharmaceutical grade lactose and water only, meaning there are no introduced chemicals or contaminants.

### *6.3.3 CSC Theoretical Model Changing Input Conditions*

High and low base theoretical model conditions for growth concentration, crystallizer height, flow rate and crystal growth rate constant were investigated to assess their effect on particle size, crystal concentration and span. A simulation time of 16 hours was used.

#### 6.3.3.1 Particle Size

Increasing growth concentration, Figure 57 and Figure 58, and flow rate, Figure 61 and Figure 62, were found to have the largest effect on increasing product and waste particle size. Increasing growth concentration, increases fluid viscosity and density, and according to Equation 61, particle terminal settling velocity decreases, but growth rate, Equation 51, increases. The net result is a larger equivalent product crystal diameter at a particular column radius position as shown in Figure 65. Increasing growth concentration also affects the nucleation rate, however this was not modelled as the growth concentration was assumed to reside within the metastable region where nucleation is limited. Increasing the flow rate increases the equivalent column radius fluid velocity, and thus corresponding product particle diameter is also increased, as seen in Figure 55 and Figure 56. Alterations to crystallizer height, Figure 59 and Figure 60, and growth rate constant, Figure 63 and Figure 64, caused insignificant changes to the particle size.

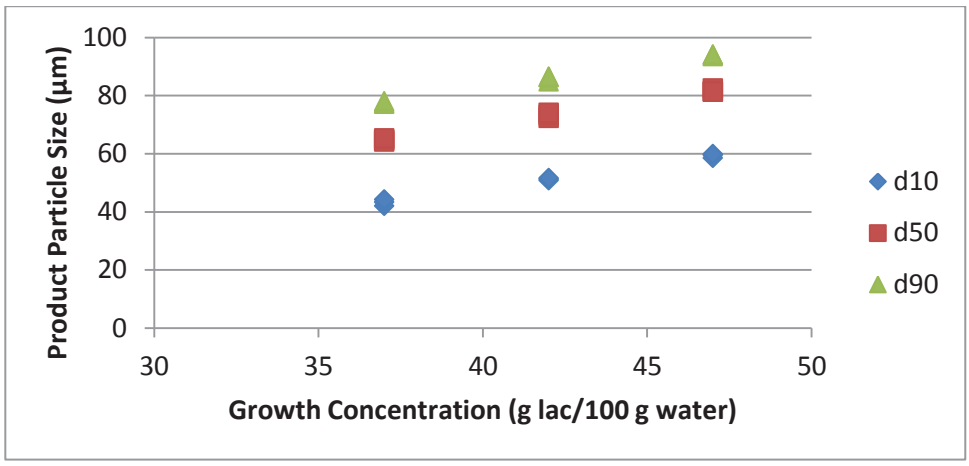


Figure 57 CSC theoretical model product particle size versus growth concentration

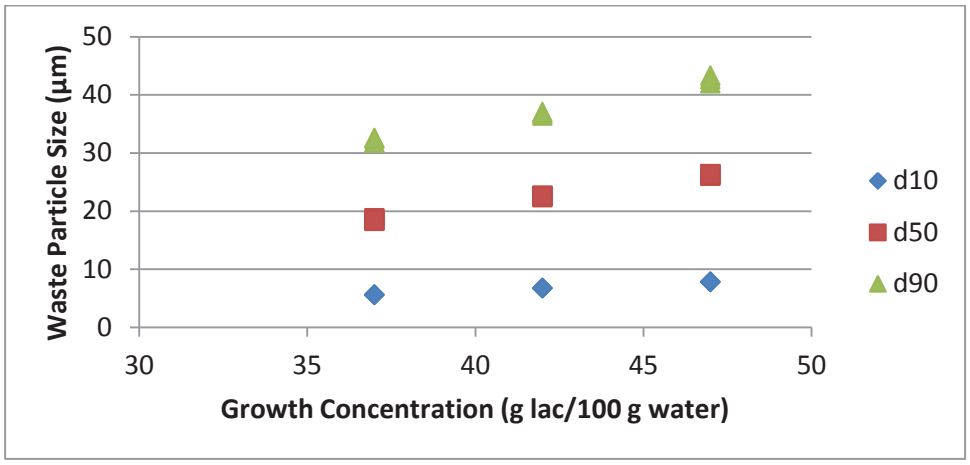


Figure 58 CSC theoretical model waste particle size versus growth concentration

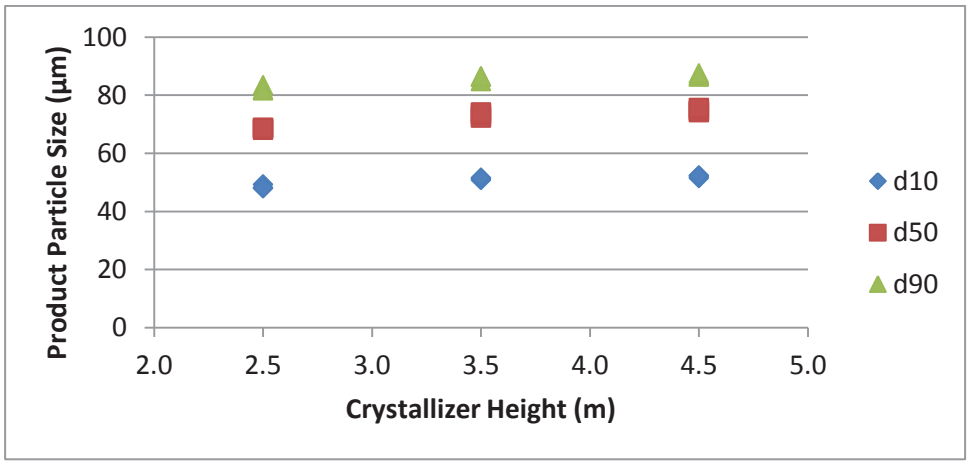


Figure 59 CSC theoretical model product particle size versus crystallizer height

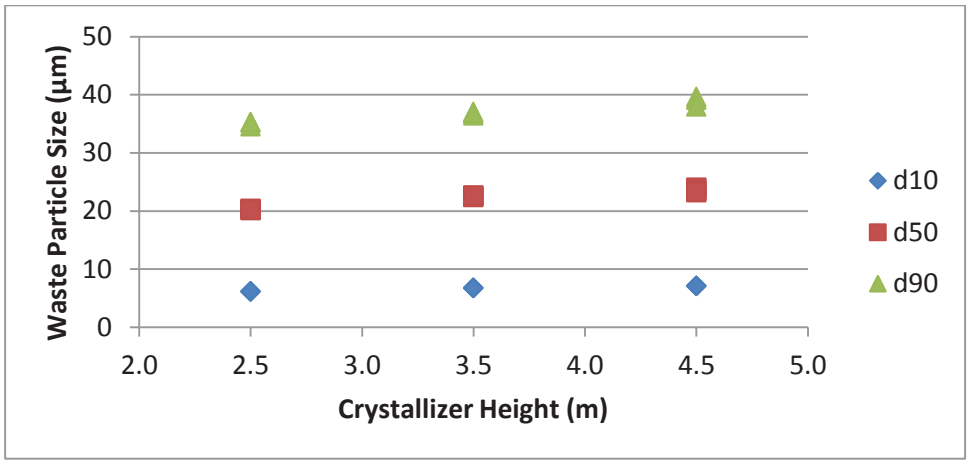


Figure 60 CSC theoretical model waste particle size versus crystallizer height

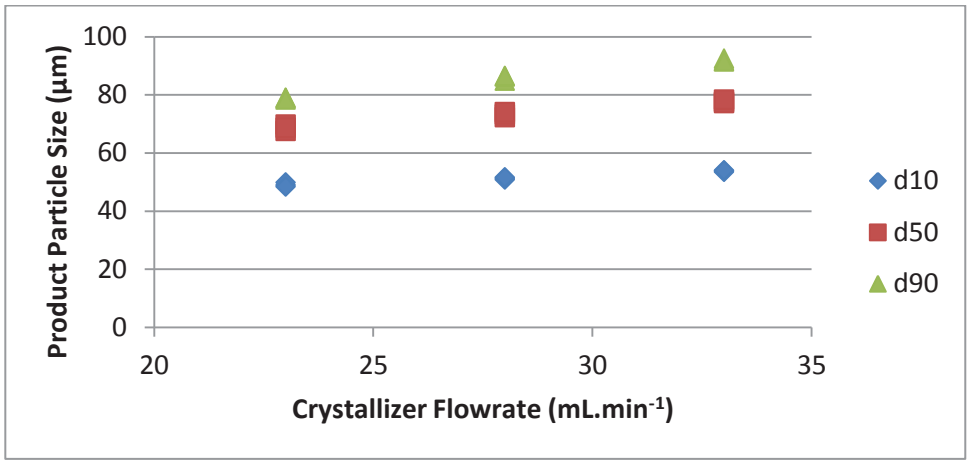


Figure 61 CSC theoretical model product particle size versus crystallizer flow rate

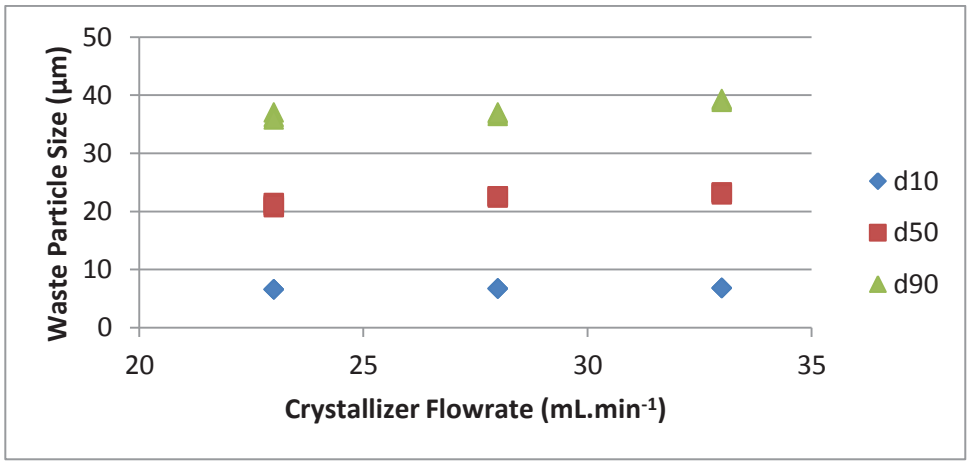


Figure 62 CSC theoretical model waste particle size versus crystallizer flow rate

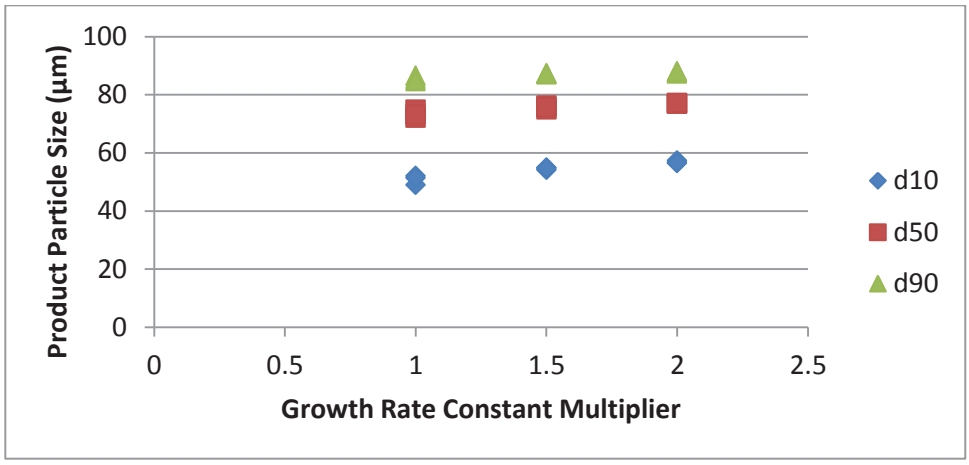


Figure 63 CSC theoretical model product particle size versus growth rate constant multiplier

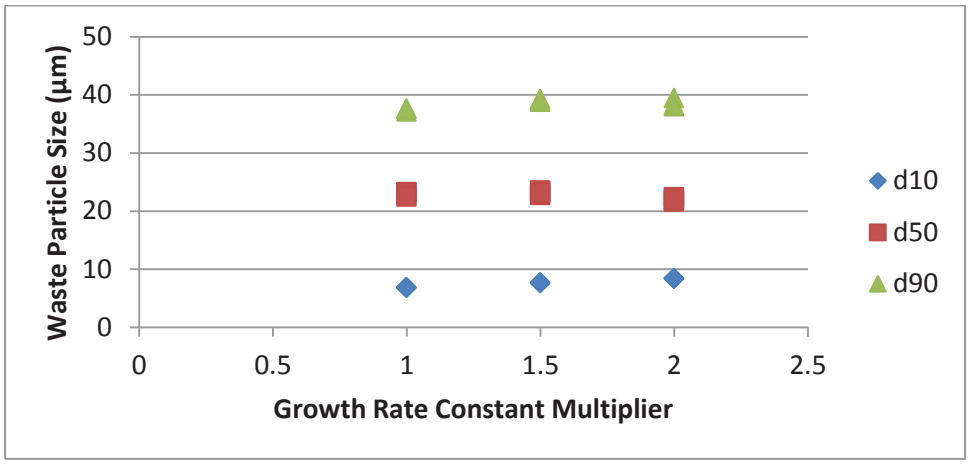


Figure 64 CSC theoretical model waste particle size versus growth rate constant multiplier

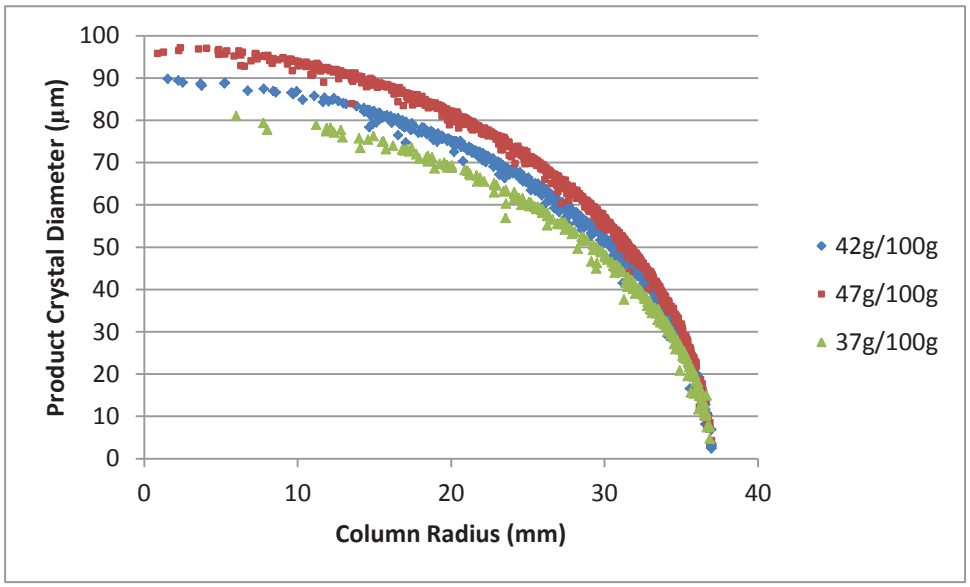


Figure 65 CSC product model solutions showing crystal size selection with growth concentration

### 6.3.3.2 Crystal Concentration

Increasing growth concentration, Figure 66 and Figure 67, and growth rate constant, Figure 72 and Figure 73, have large effects on increasing the product to waste (PW) crystal volume ratio, total product crystal volume divided by total waste crystal volume, through increasing the product stream crystal concentration. Increasing crystallizer height, Figure 68 and Figure 69, causes negligible increases in product crystal concentration. The main effect of increasing the growth concentration and rate constant is to reduce the number of slow growing crystals reaching the top of the crystallizer to exit into the waste stream, and instead these settle into the product stream. Increasing the flow rate, Figure 70 and Figure 71, decreases the PW crystal volume ratio and product concentration. Increasing flow rate increases the terminal settling diameter needed to be reached and thus more crystals end up in the waste stream.

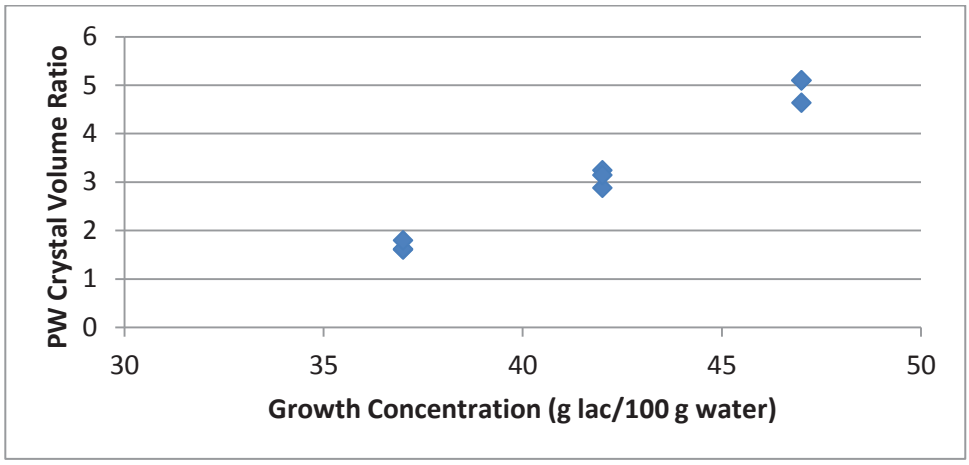


Figure 66 CSC theoretical model PW crystal volume ratio versus growth concentration

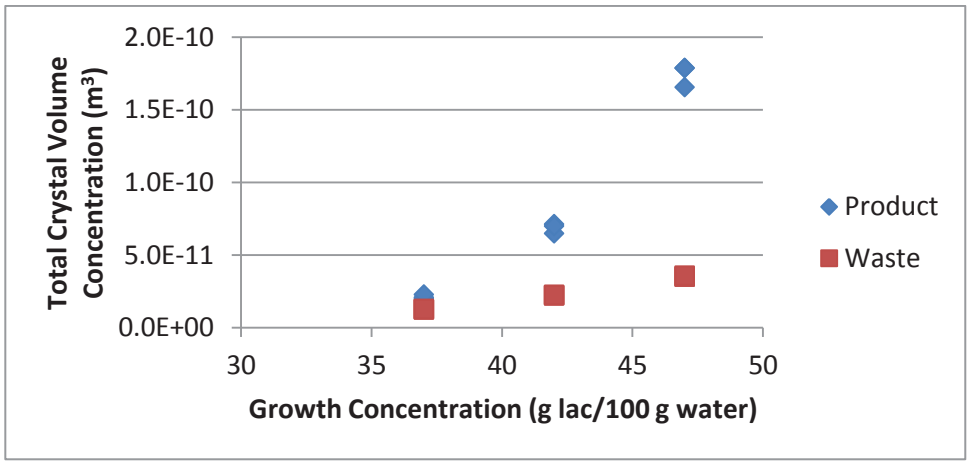


Figure 67 CSC theoretical model crystal volume concentration versus growth concetration

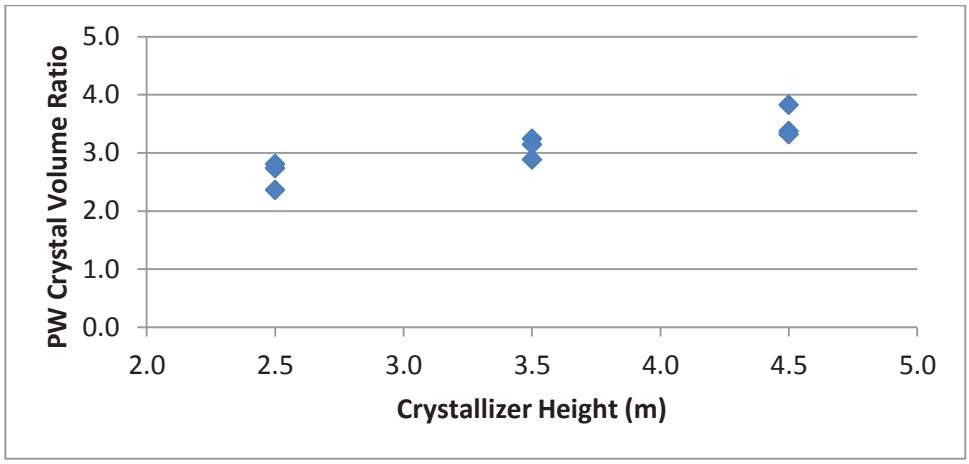


Figure 68 CSC theoretical model PW crystal volume ratio versus crystallizer height

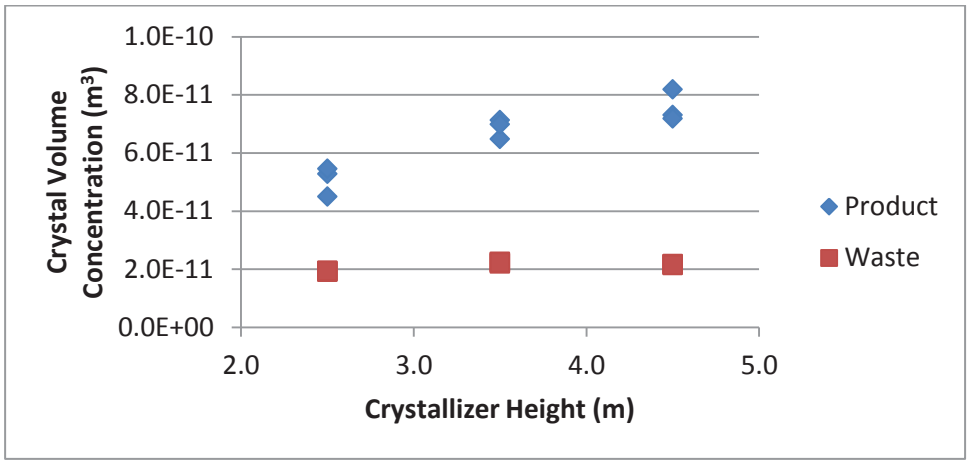


Figure 69 CSC theoretical model crystal volume concentraion versus crystallizer height

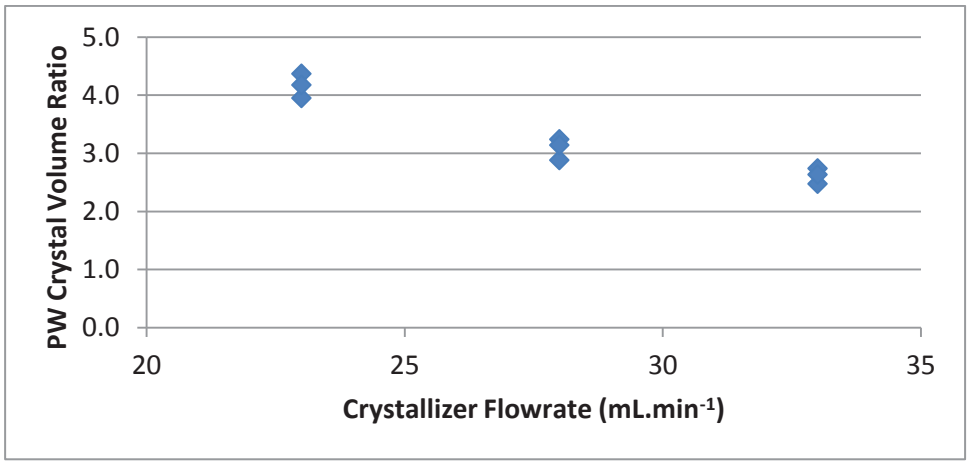


Figure 70 CSC theoretical model PW crystal volume ratio versus crystallizer flow rate

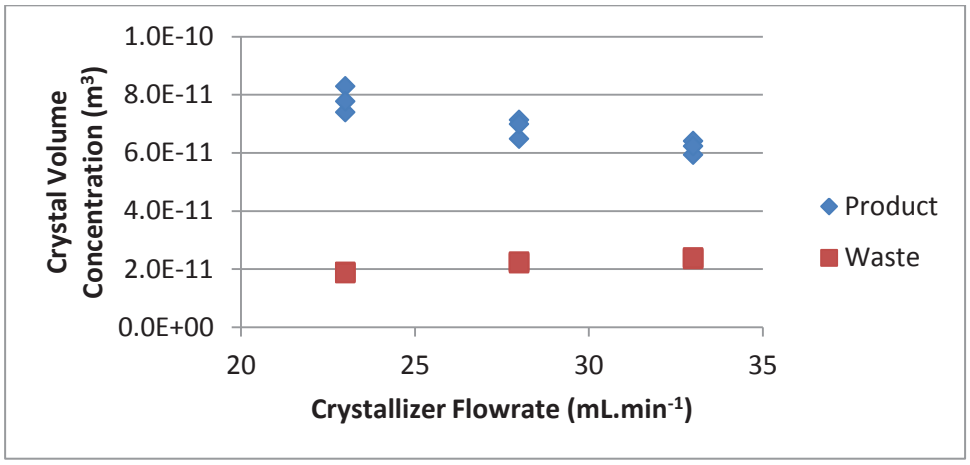


Figure 71 CSC theoretical model crystal volume concentration versus crystallizer flow rate

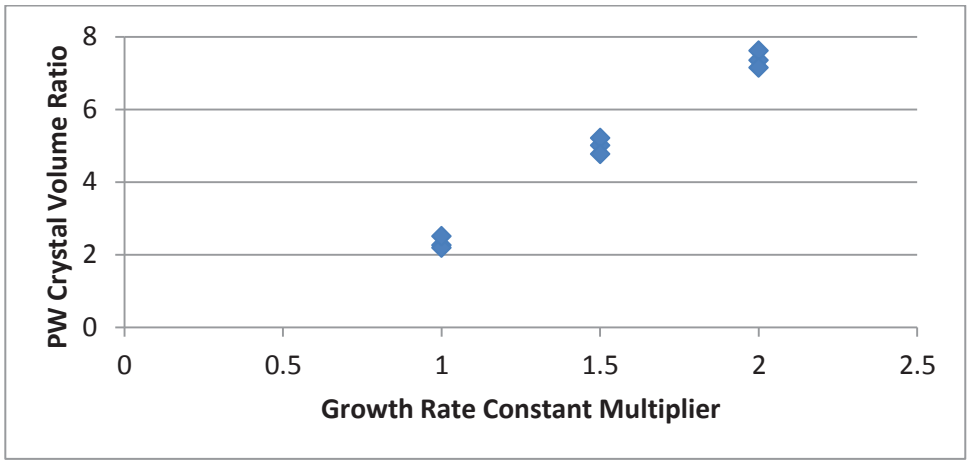


Figure 72 CSC theoretical model PW crystal volume ratio versus growth rate constant multiplier

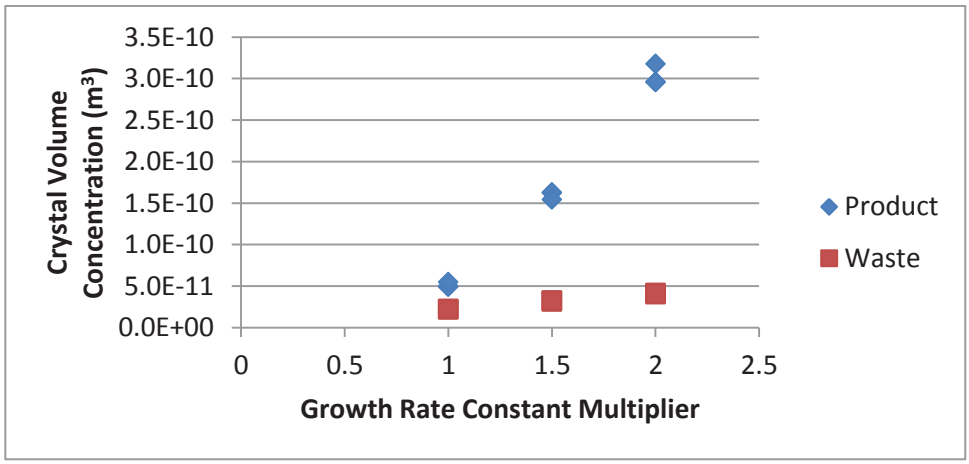


Figure 73 CSC theoretical model crystal volume concentration versus growth rate constant multiplier

### 6.3.3.3 Span

The change in CSC conditions, Figure 74, Figure 75, Figure 76 and Figure 77, tested had very marginal changes to span for both product and waste streams, where the span stayed at or below 0.5 for the product stream. This is because the product and waste PSD is relative to the velocity profile, which can be seen when the incorrect area nuclei input method was used (Table 12).

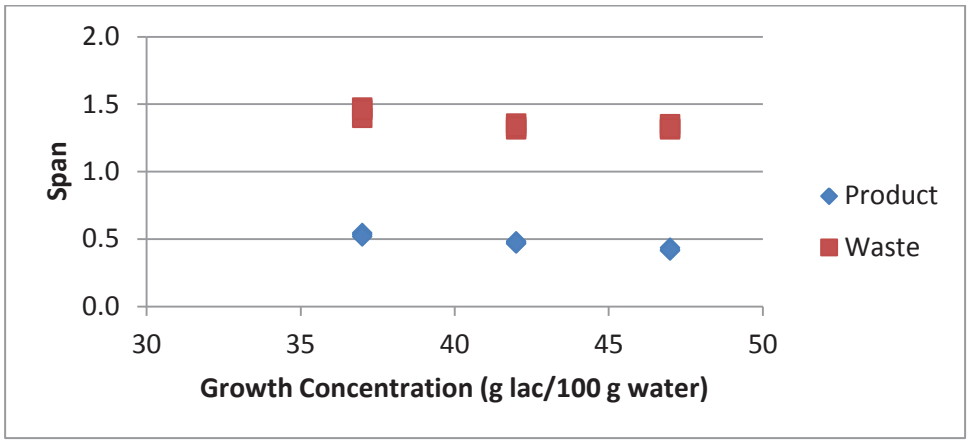


Figure 74 CSC theoretical model span versus growth concentration

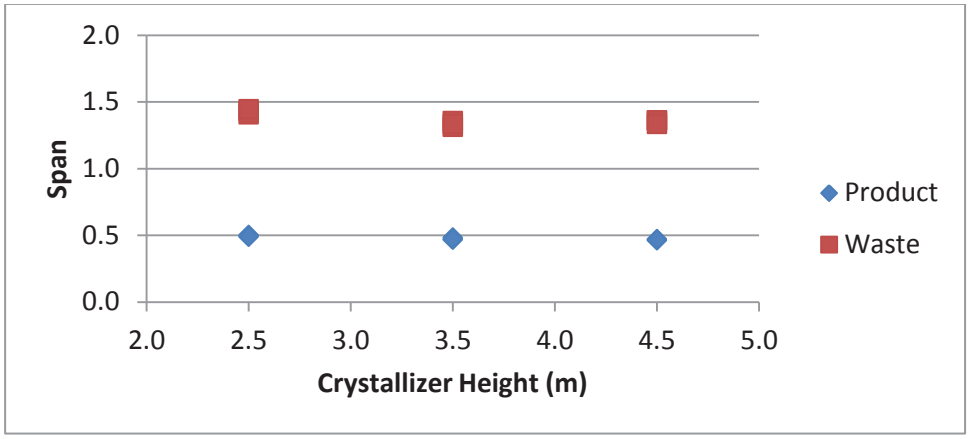


Figure 75 CSC theoretical model span versus crystallizer height

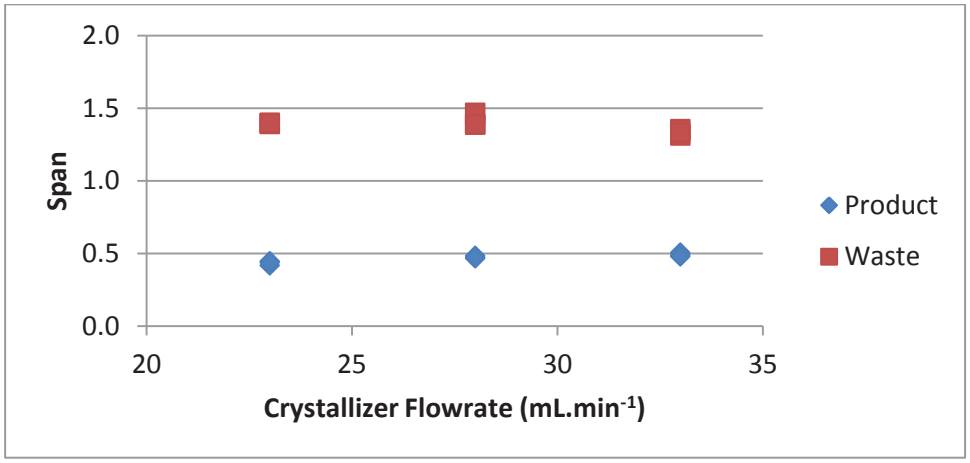


Figure 76 CSC theoretical model span versus crystallizer flow rate

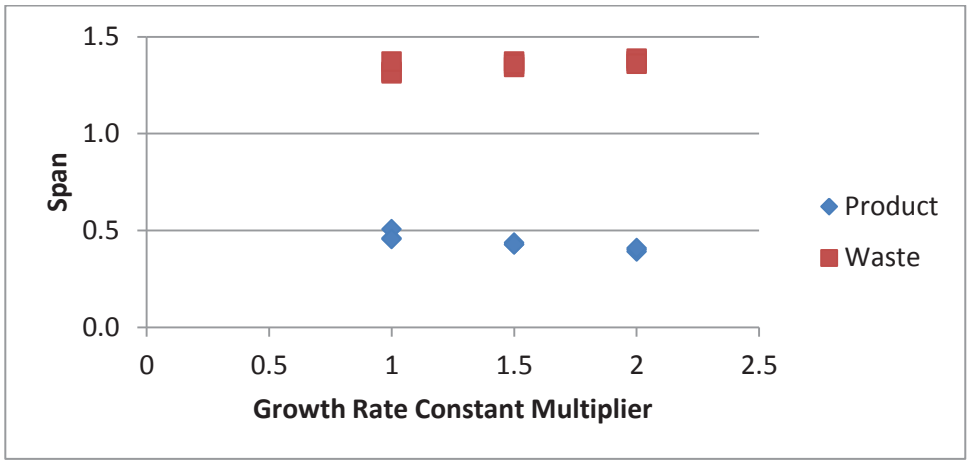


Figure 77 CSC theoretical model span versus growth rate constant multiplier

## 6.4 Conclusions

The flow condition for the initial continuous settling crystallizer theoretical model changed from a single velocity profile to a parabolic velocity profile. Using a parabolic velocity profile increased the product span from near 0 to 0.47±0.01. This meets the desired inhaler grade lactose crystallizer design criterion of a span less than 1. Changing the base model conditions had minor effects on span. The base model conditions also resulted in a $d_{50}$ of 73.2±0.9 µm which resides in the desired inhaler grade lactose product $d_{50}$ size range of 50 to 90 µm. Changing crystallizer concentration and flow rate had the greatest effect on product particle size. Product crystal concentration was shown to increase with growth concentration and crystal growth rates. Finally the concentration of contaminants for the continuous settling crystallizer process will be low due to only pharmaceutical grade lactose and water being used. From the theoretical model investigation into the continuous settling crystallizer it was recommended to continue with the build and development of an experimental lab scale setup, discussed in the following chapter.

# Chapter 7 – Continuous Settling Crystallizer Experimental

## 7.1 Introduction

The continuous settling crystallizer (CSC) theoretical model predictions concluded that experimental development and testing was worthwhile. The CSC is designed to allow, in principle, a pre-nucleated feed stream flowing upwards to settle out 50 to 90 μm crystals after growth has occurred. The product crystal size obtained is directly related to the fluid velocity in the column. The column allows both fast and slow growing crystals to grow and settle out into the product stream at the same final particle size, thus achieving a narrow particle size distribution (PSD) in accordance with the primary objectives. The CSC setup can be seen in Figure 78, Section 7.2 discusses the testing stages prior to reaching this, and Section 7.3 contains the experimental procedure. Insulated 50 L tanks were used for holding dilute nucleated and concentrated hot solution. Peristaltic pumps (Watson-Marlow 120S) combine the nucleated and concentrated stream, passing through a cooling coil submerged in a water bath, and fed into a 3.5 m high (74 mm internal diameter) insulated column. The product stream is pumped from the column, with on-line dilution, to a sink where samples are collected. Likewise the overflow stream is gravity fed via a pipe to the sink.

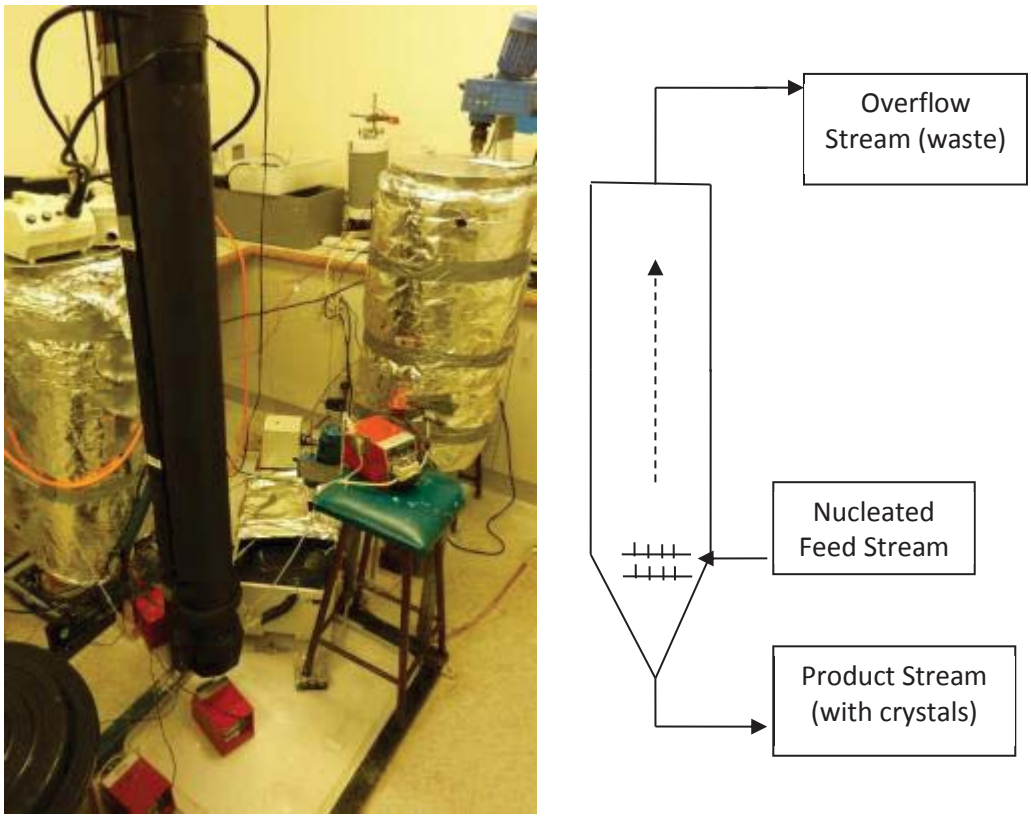


**Figure 78 CSC lab scale setup located in a 25°C temperature controlled room; starting from the left: nucleated feed tank, settling column (black insulation), water bath and cooling coil, concentrated hot tank, and on the right is a schematic representation of the settling column**

## 7.2 Testing Stages

Before reliable experimental CSC runs could be carried out, testing and development of equipment ensued. The purpose was to check that what was occurring in practice upheld the associated theoretical model assumptions. Testing stages can be generalised into the following areas of temperature, feed, product and laminar flow control.

### *7.2.1 Temperature Control*

The height of the CSC setup reaches almost 4 m with additional fittings and an adequately sized room was required to house the equipment:

1) Initially it was installed in the only room with high enough ceilings; however after investigation, it was found the room temperature varied by at least 14°C in a 24 hour period, unacceptable for controlling the column and other tank temperatures.
2) The equipment was shifted to a smaller 25°C temperature controlled room; a hole was installed into the ceiling with an insulated box built in the area above to maintain the temperature from inside the room.
3) Temperature measured in the 25°C room varied by around 3°C, with hot-cold peaks 15 minutes apart; this was not ideal and additional fans and temperature controlled heaters were added to the room to improve this control.

Figure 79 shows all the temperature probe measurements during a typical experimental CSC run. Air temperature (105-108) varies within 2°C measured at 2 minute intervals, uncontrolled stream temperatures (102 and 109-113) and the PID controlled 75°C hot tank (103-104) varies within 0.3°C.

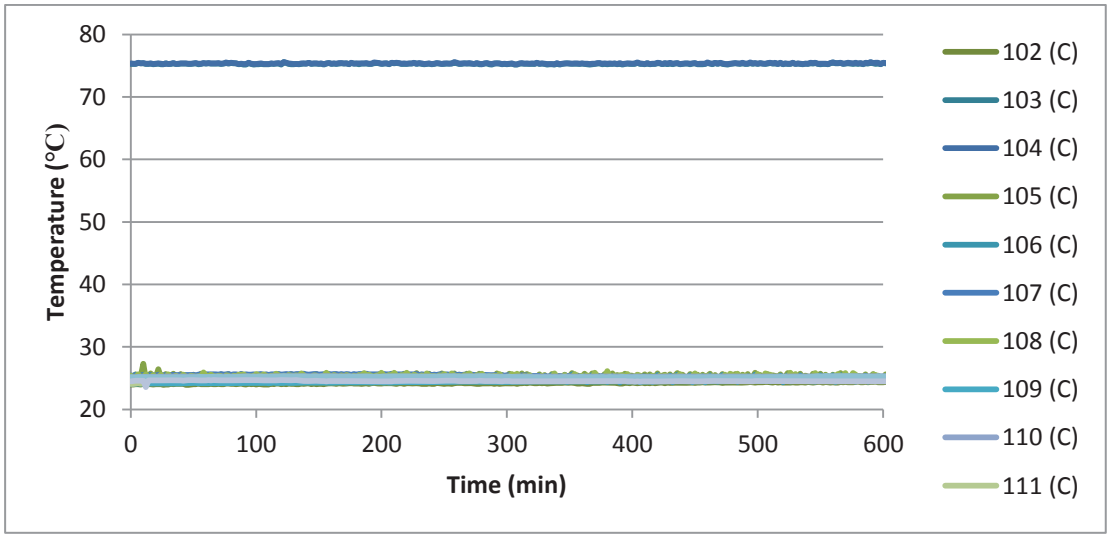


**Figure 79 Typical experimental temperature probe measurements with time in the 25°C temperature controlled room (Run 8)**

Column insulation was later added to ensure any convection-based temperature fluctuations were limited, see Appendix A.3 for calculations. This reduced column side temperature fluctuations to approximately 0.1°C, as seen in Figure 80 (note the expanded temperature axis).

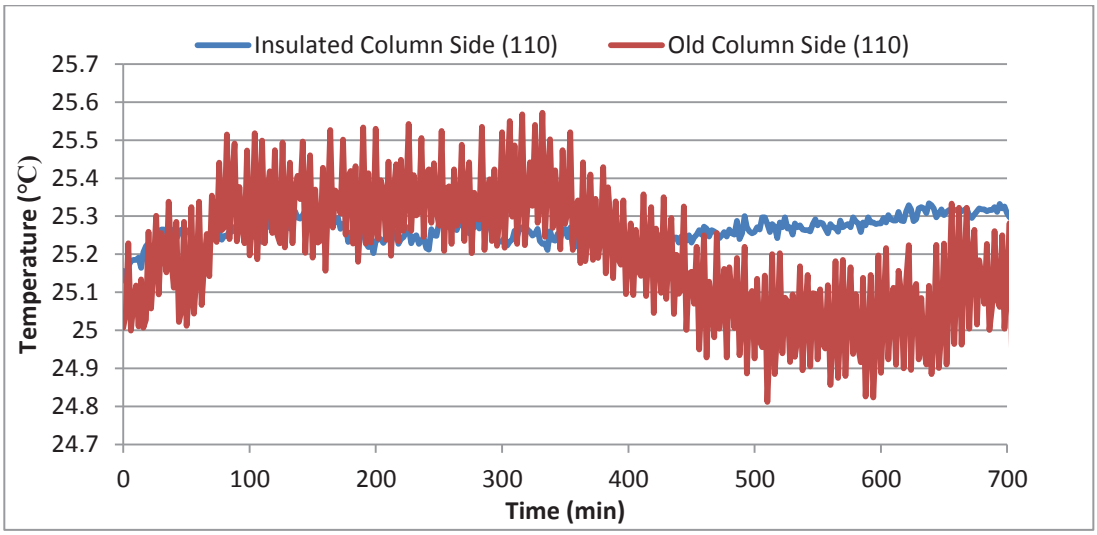


Figure 80 Comparison of temperature measurements for the CSC column, with and without insulation

### *7.2.2 Feed*

#### 7.2.2.1 Single nucleation event

A single nucleation event is required for the CSC to produce a feed stream with the desired nuclei amount. The initial method proposed for achieving this was orifice nucleation, but due to reliability issues, such as blockages, it was changed to a mechanical mixing; see Chapter 5 for details.

#### 7.2.2.2 Inlet Design

The desired flow conditions inside the CSC column are laminar; thus low Reynolds numbers are required. The feed inlet needed to meet two criteria: injecting feed at low Reynolds numbers and minimal cross-sectional column obstruction. By minimising Reynolds numbers at the feed inlet, a faster transition to laminar flow is expected. Minimal cross-sectional area interference allows for more crystal to settle from the column and into the product stream.

The first inlet feed design comprised of feed solution entering a manifold and split to 16 inlet nozzles sticking into the side of the column wall positioned upwards; see Figure 81. The pressure drop across the manifold and individual pipes was calculated to attain even flow split to all 16 pipes. Based on $Q_f$=48 mL.min$^{-1}$, $\rho_f$=1127 kg.m$^{-3}$ and $\mu_v$=2.8 mPa.s, the average velocity coming from each nozzle is 15.9 mm.s$^{-1}$, and Re=12.8, compared to the net column velocity of

0.11 mm.s$^{-1}$, and Re=3.2. This initial design met the criteria for a low Reynolds number and cross-sectional column area intrusion. Experiments were carried out to test whether an even flow rate occurred from each nozzle and showed nozzle flow to be within ±10% of the design flow; see Figure 82.

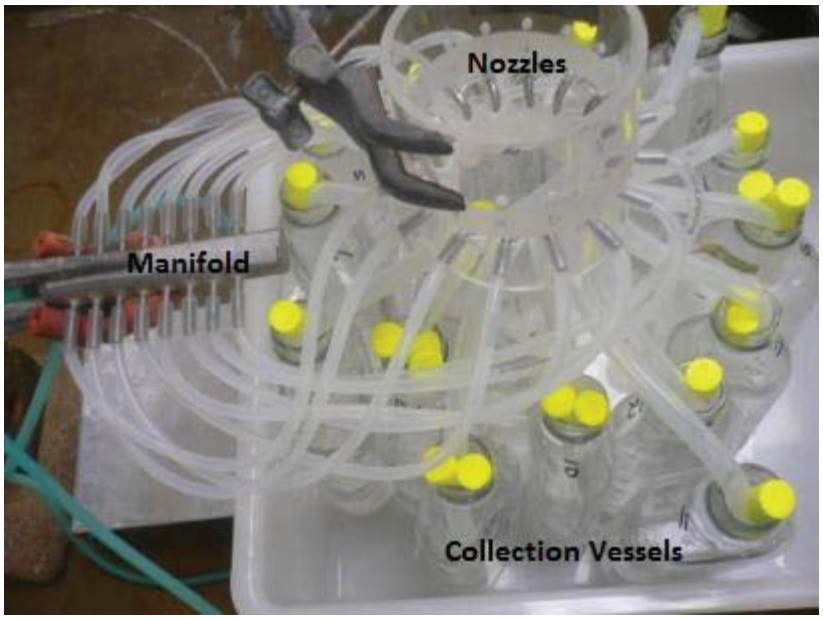


**Figure 81 Manifold with 16 outlets flow rate test, nozzles here are positioned downwards so flow can be collected and compared**

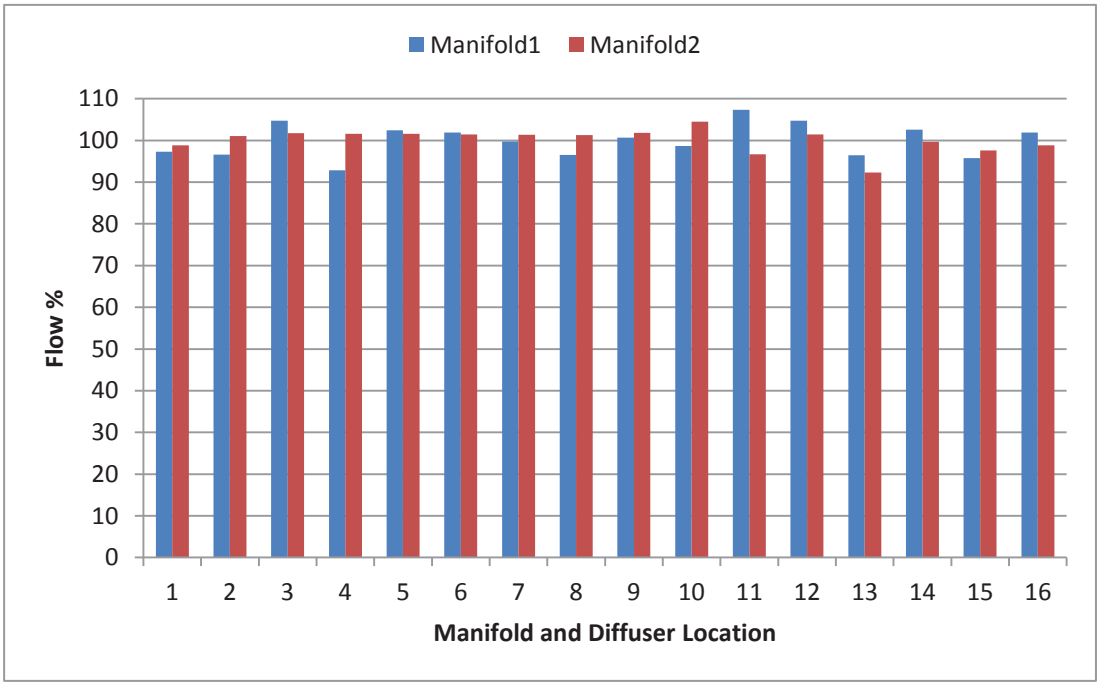


**Figure 82 Graph of flow percent from the 16 nozzles (100% is the design flow rate)**

Additional feed inlet designs were subsequently investigated because of the possibility for the 16-pipe design smaller tubes blocking from an experimental run with lactose as well as the difficulty of cleaning them. The new key design criterion was a single inlet with changeable

heads, to control the flow distribution. The single inlet designs also incorporated lower Reynolds numbers for each head in an attempt to assist the transition to laminar flow in the column. Two heads were designed, one having vertical flow outlets and the other horizontal flow outlets; see Figure 83. The vertical flow outlet design had 93x1.5 mm holes with an average velocity of 4.9 $mm.s^{-1}$ and Reynolds number of 2.9 at each hole. The horizontal flow design consisted of 3 layers of 24x1.1, 20x1.2, and 14x1.8 mm holes with horizontal velocities of 11.7, 11.8, and 7.5 $mm.s^{-1}$ and Reynolds numbers of 5.2, 5.7 and 5.4 (using $Q_f$=48 $mL.min^{-1}$, $\rho_f$=1127 $kg.m^{-3}$ and $\mu_v$=2.8 mPa.s). The different sized holes in the horizontal design were to account for the pressure drop due to gravity exceeding friction, $\Delta P$=22 Pa per 2 mm height increase and 1.1 mm holes=64 Pa, 1.2 mm holes=59 Pa and 1.8 mm holes=25 Pa. From the laminar flow analysis in Section 7.2.4, the horizontal nozzle was chosen for the experimental work that follows.

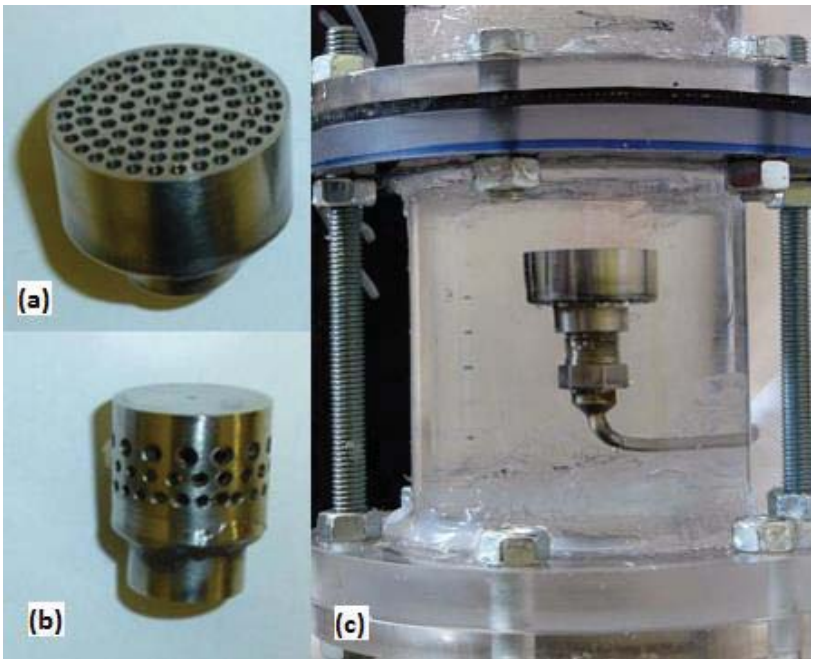


**Figure 83 Single inlet designs, (a) vertical and (b) horizontal nozzles; (c) the vertical nozzle is shown installed in the column**

### *7.2.3 Product*

The product stream withdrawn from the bottom of the column removes settled column crystals. The product stream initially utilized the same design as the 16-pipe feed inlet, and had 16 nozzles directly below the feed nozzles but positioned in the opposite (downwards) direction. Dilute lactose solution was initially used for the product stream, but resulted in column fluid mixing. It was noticed that liquid was rising from the product outlet, even though they were pointing downwards. This was because the product stream density was lower than the feed stream density present in the column. This meant the product stream rose under

normal operations (Appendix A.4). Dye tests were initially used with water in the column to observe the feed and product flow profiles. However, the dye tests did not show any significant product stream mixing and rising, because water was used for both the feed and product stream; hence both streams had very similar densities. Using a fraction of the feed stream for the product stream helped ensure density and temperature consistency and prevent mixing. When the column is completely full, due to the pressure head, it was measured that an additional 1.3 $mL.min^{-1}$ exits from column into the product stream that is pumped from the column; this loss can be accounted for by increasing the feed stream flow rate.

When changing to the single feed horizontal and vertical inlet designs, different product outlet designs were also investigated; such as having a single product pipe inlet. The continued difficulty with the product stream interfering with column flow resulted in the design seen in Figure 84. All product inlets and online dilution were removed from column and settled crystal removal was assisted by using a fraction of the feed stream (feed stream flow rate was increased). The effect of using feed for the product stream will cause additional growth and contain un-grown nuclei. After the product stream was pumped from the column, dilution to a lower supersaturation occurred to limit any further growth before PSD measurements were made.

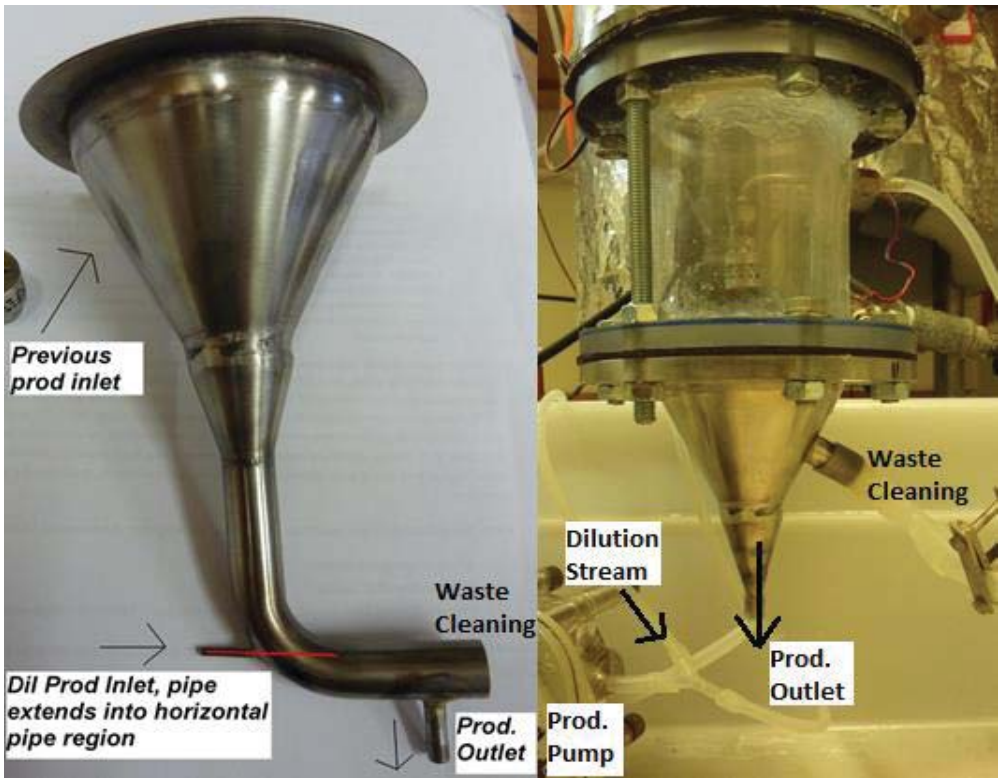


**Figure 84 Product outlet transition; final design shown on the right**

### *7.2.4 Laminar Flow*

The column material chosen was clear Perspex, allowing easy viewing of the column flow and crystal settling; this later changed with the addition of insulation, although viewing windows were installed. To test whether a laminar profile was achieved in the un-insulated column, dye (food colouring) as previously mentioned, was inserted into the 16-pipe feed stream pumping water into the column, no lactose, and recorded via a video camera. At the column average flow rate of 33 mL.min$^{-1}$, the 3.5 m column fills in 7 hr 48 min. Assuming a parabolic laminar flow curve with max velocity equal to twice the average velocity, the shortest fluid residence time in the column would be 3 hr 54 min.

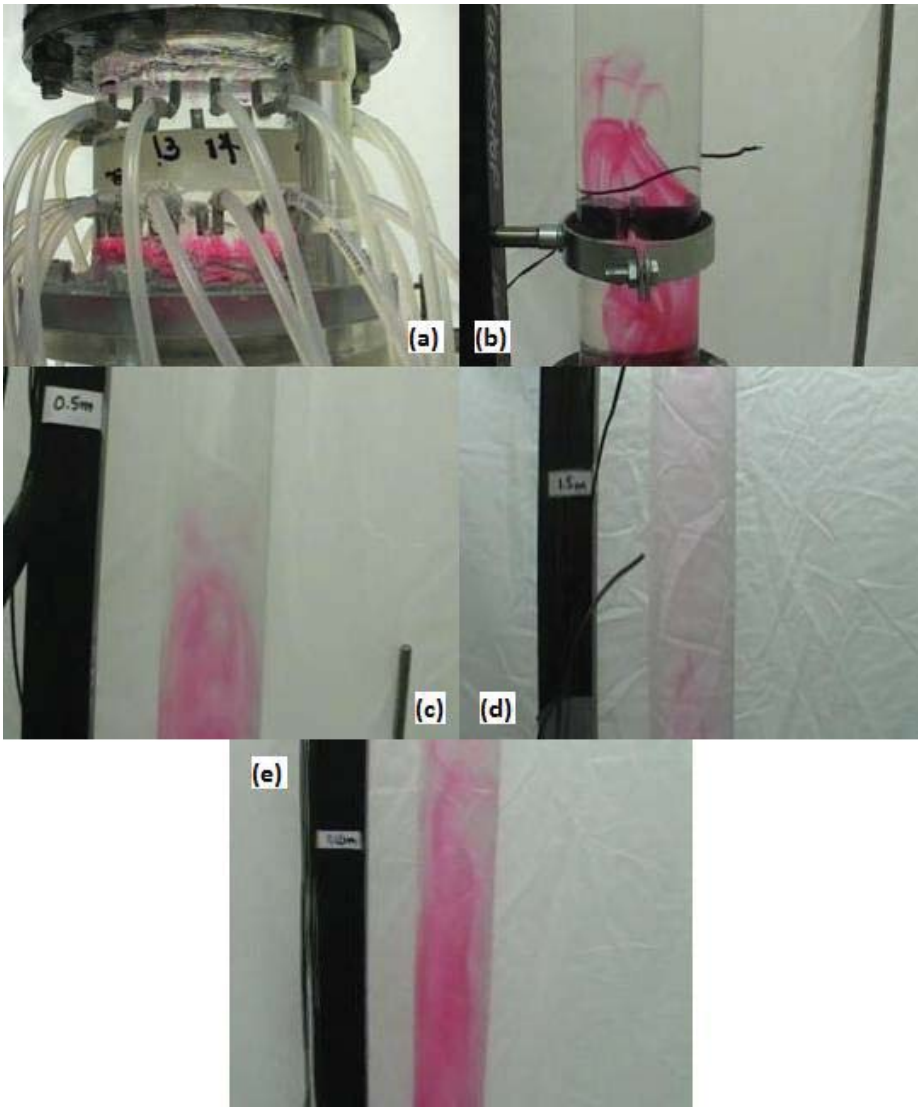


**Figure 85 Following the height of dye fed continuously into the column: (a) feed start (product has been running does not appear to rise),(b) after 10 min, (c) after 22 min, (d) after 70 min laminar top and (e) after 70 min at 1 m**

Figure 85 shows an un-insulated water dye test for the 16-pipe inlet with the product stream operating at the same time as the feed; pictures show the feed inlet at the start time, 0.2 m

above the feed point @ 10 min, 0.4 m @ 22 min, and 1.35 m @ 71 min. A parabolic profile had developed by 0.5 m and the dye reaches the top of the column in 2 to 3 hr. Although hard to see in the pictures, it is noticed that the dye seems to diffuse or mix ahead of the main dye front; the dye becomes fainter in colour. At 70 min assuming laminar flow the dye front should be at around 1.05, not 1.35 m, and this was attributed to the initial inlet velocity, density differences in the water and dye mixture and minor temperature differences. The measured density for the red food colouring dye used was ~1.04 g.mL$^{-1}$.

Computer fluid dynamic (CFD) modelling was carried out by an undergraduate student, Poochet Horkanya, into the three different proposed feed designs; 16-pipe, vertical inlet, and horizontal inlet (Figure 86). Distances to laminar flow of 80, 102 and 110 mm were predicted for the 16-pipe, vertical and horizontal inlets respectively; much shorter than what was found in practice with dye tests. Figure 87 are the corresponding dye tests carried out for comparison with the CFD predictions.

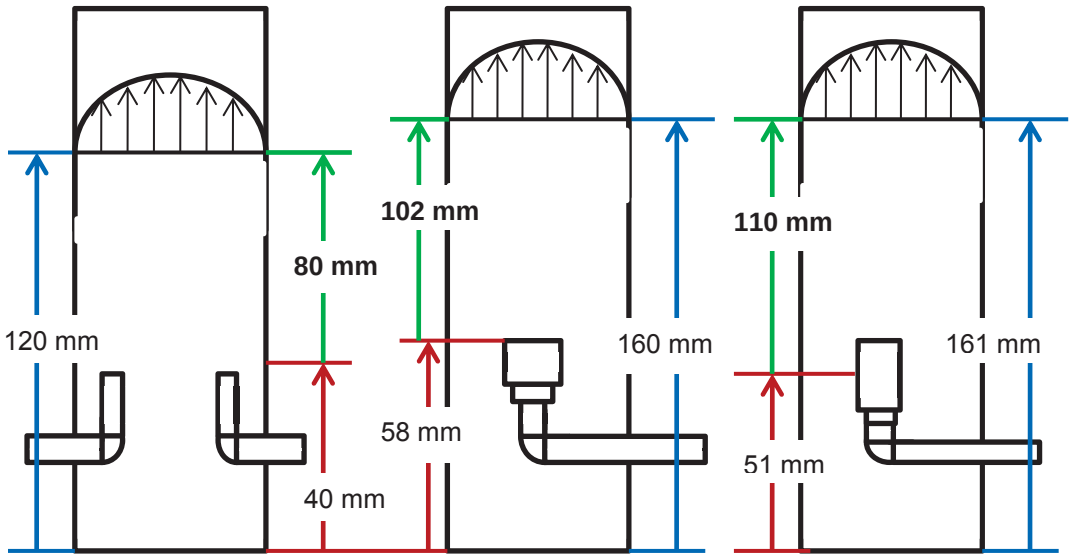


**Figure 86 CFD model distance to laminar flow predictions for the 16-pipe, vertical and horizontal inlets**

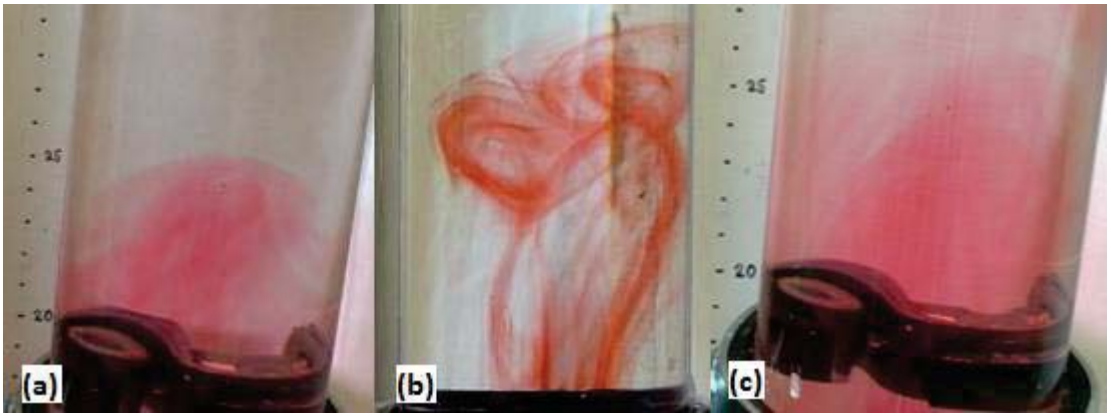


**Figure 87 Water dye images of (a) 16-pipe, (b) vertical and (c) horizontal inlets**

From the CFD simulation, the 16-pipe inlet design had the least distance transition to laminar flow, although the single pipe designs had negligible difference when taking into consideration the total column height. The horizontal inlet had the lowest vertical peaks in velocity occurring. In practice the 16-pipe and horizontal inlet gave the best results, with an inlet $u_f$ equal to 10 $mm.s^{-1}$ and less than 0.8 $mm.s^{-1}$ after 0.25 m of column height. When taking into account the ease of use and cleaning, the horizontal inlet was selected for use in the CSC column.

Initially when the column had no insulation, convection currents were observed in one of the full scale lactose CSC experiments; on one column side fluid containing crystal appeared to be moving up and on the other side was moving down. After column insulation was installed these currents were not observed, although with the smaller viewing windows a full observation of the column could not occur. After the column was insulated, no change in experimental product PSD measurements occurred.

#### 7.2.4.1 Baffled CSC

When plug fluid flow was assumed in the column, a single fluid velocity acts on the growing crystals and a uniform product particle size is produced – refer to Figure 52. However, the parabolic laminar fluid flow profile in the CSC changes the settling times across the column radius and thus increases the particle size range and span coming from the column. A column with sections of baffles was proposed to even out the settling velocities experienced by the particles across the radius of the column (Section 2.4.3.6 Settler or Elutriator), where Biddulph (1983), observed a downward flux of small particles at the wall. The inherent downside to baffling in a crystallization process is the added surface area for crystal to attach to and grow.

Two baffled column designs were tested, as shown in Figure 88; one with minimal baffles and one with maximum baffles. Firstly a column with two 200 mm long flat vertical baffles spaced 200 mm apart up the entire column was built. Unfortunately this design did not affect the laminar flow and the PSD was unchanged. Pressure drop calculations showed approximately no change for the minimal baffle design (Appendix A.5), which would explain these results. A second column design packed with 200 mm long, 12 mm diameter plastic straws was built. Testing of this column revealed a product stream with a very low crystal volume. The fully packed straw column with approximately 40 straws across the column cross-sectional area has a considerably increased internal surface area for more crystal to attach to.


Figure 88 Baffled column designs tested, (a) minimal and (b) maximum before and (c) during testing

### *7.2.5 Measurements*

The Malvern MasterSizer was used to measure the PSD for the product, waste, dilute stream and controls, and Figure 89 is representative of a typical PSD graphical output of a bottle roll control that had been growing for 16 hours. Room air and stream temperatures were recorded into a computer via a data logger. Refractive index measurements were carried out for the feed, product, waste and controls. Turbidity was measured for the nucleated solution. Feed flow rate was initially calibrated using a measuring cylinder and stop watch, and the product and waste streams flow rates were recorded with time.

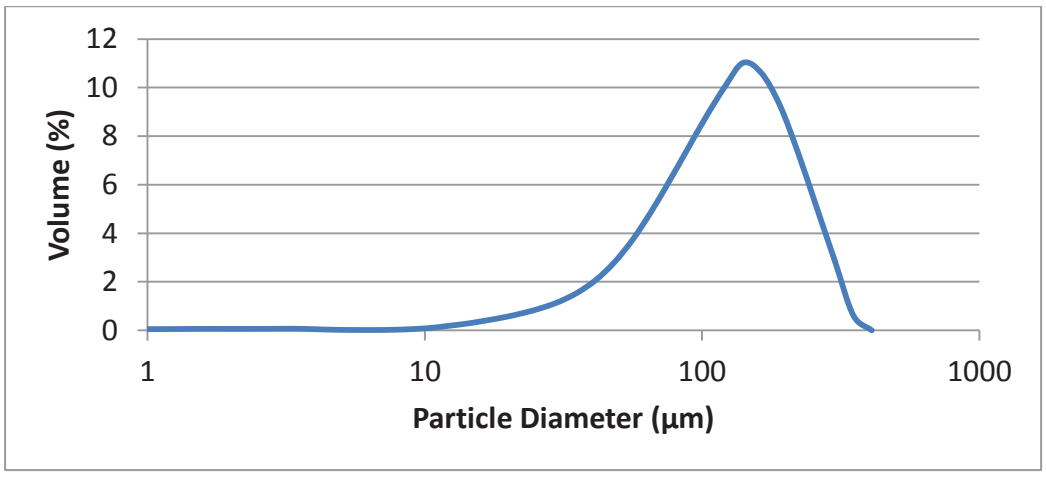


Figure 89 Typical Malvern MasterSizer PSD result, volume % versus particle diameter bin size, for a 16 hour bottle roll control

### 7.2.6 Control Sample

The initial control growth method used a beaker mixed with a turbine style impeller operated at approximately 300 rpm. The stirred beaker was loosely covered with tin foil, although there were gaps around the stirring rod. The control sample was found not to be a fair representation of the nucleation that had occurred in the feed stream entering into the column. This was attributed to additional nucleation occurring via the impeller mixing, such as contact and shear nucleation. Impeller impact has been identified as the main source of secondary nucleation (Agrawal, 2012; Bennett, Fiedelma.H, & Randolph, 1973; Synowiec, Jones, & Shamlou, 1993). The column growth concentration is above the secondary nucleation threshold and right on the expected limits for reduced secondary nucleation. A sealed vessel (100 mL Duran bottle) with slow rolling was set up to grow crystals and compared with the initial impeller-mixed beaker method. The slowly rolled vessel eliminated evaporation, which can cause nucleation through localized increases in supersaturation, and reduced particle-wall and particle-particle interactions. The resulting crystal concentrations in the rolled bottle were significantly lower than the stirred beaker method, subjected to the same initial conditions and growth time; after 24 hours of growth time for the stirred beaker the Malvern MasterSizer measured a 12.8% obscuration level compared to only 1.7% for the rolled bottle, 0.097% and 0.016% volume concentration, respectively. The conclusion was that the stirred beaker had undergone additional nucleation during the growth period, attributed to impeller contact and evaporation.

### 7.2.7 Cleaning

CSC cleaning occurred at the end of each 16 to 20 hour lactose experimental run. Cleaning utilises hot water, which was alternatively pumped through a connection in the product cone and the waste cone. At the top of the column, the waste outlet stream was fitted with a T-Junction, one direction of which is permanently open to the atmosphere. This allows rapid filling from the product cone without pressure build up, and safety during normal operation. A removable pressure plug in the waste outlet cone was also installed, so the waste stream pipe can be utilised for cleaning without building up pressure and causing backflow out of the T-junction.

## 7.3 Experimental

### *7.3.1 Feed Preparation*

Unless otherwise stated values reported are in grams of total lactose/100 grams water. A concentrated lactose solution, 83.13 g/100 g of water, was prepared by adding 7.562 kg of alpha lactose monohydrate (Wynhale™ Inhalation lactose, DFE Pharma) and 8.263 kg reverse osmosis water to a 50 L covered stainless steel tank, stirred and heated to 80°C. Once the solution was transparent, an additional 5 min of heating occurred to ensure remaining nuclei were dissolved. The solution was then emptied into a plastic 20 L pail, covered and left to cool for 25 hours with no mixing, reaching equilibrium with the room temperature of 25°C. The concentrated lactose solution prepared corresponded to absolute alpha lactose supersaturation ($S_\alpha$) of 23 g/100 g.

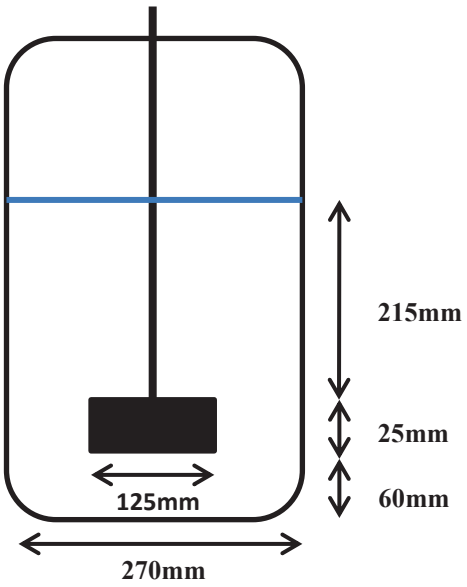


Figure 90 CSC Impeller nucleation event, tank and stirrer dimensions

Before the concentrated lactose solution impeller nucleation event occurred, an undersaturated lactose solution, 5 g/100 g water, was prepared by adding 1.373 kg of alpha lactose monohydrate (Wynhale™ Inhalation lactose, DFE Pharma) to 26.001 kg reverse osmosis water at 25°C. Stirring was then applied to the concentrated lactose solution for 5 min with the overhead mixer set at 600 rpm, inducing nucleation. The nucleation stirring setup is illustrated in Figure 90; single flat bladed impeller was used. Turbidity, refractive index and temperature measurements were made at all stages. The nucleated solution was poured back into a larger 50 L stirred tank and diluted with the undersaturated lactose solution, to just above supersaturation, so additional nucleation was limited. The nucleated dilute solution corresponded to a concentration of 24.45 g/100 g (Stream 1), with a $S_\alpha$ of 1 g/100 g at 25°C.

This solution was then pumped into a second holding tank and coarsely filtered to remove any crystals larger than 100 μm. A second concentrated lactose solution, 64.04 g/100 g (Stream 2), was prepared by adding 19.814 kg of alpha lactose monohydrate (Wynhale™ Inhalation lactose, DFE Pharma) to 28.403 kg reverse osmosis water into a 50 L heated mixed covered stainless steel tank. The solution was heated to and held at 75°C, where the temperature was controlled via a PI controller linked with the heating element. The column feed stream was prepared by combining 24.4 mL.min$^{-1}$ of Stream 1 with 23.6 mL.min$^{-1}$ of Stream 2 and rapidly cooled through a pipe heat exchanger, internal diameter of 4 mm, submerged in a water bath to 25°C at a total flow rate of 48 mL.min$^{-1}$. Flow rates were calibrated via a measuring cylinder and stop watch. The final nucleated feed stream had a concentration of 42 g/100 g, corresponding to a $S_\alpha$ of 8.2 g/100 g of water. The CSC feed preparation process is summarised in Figure 91.

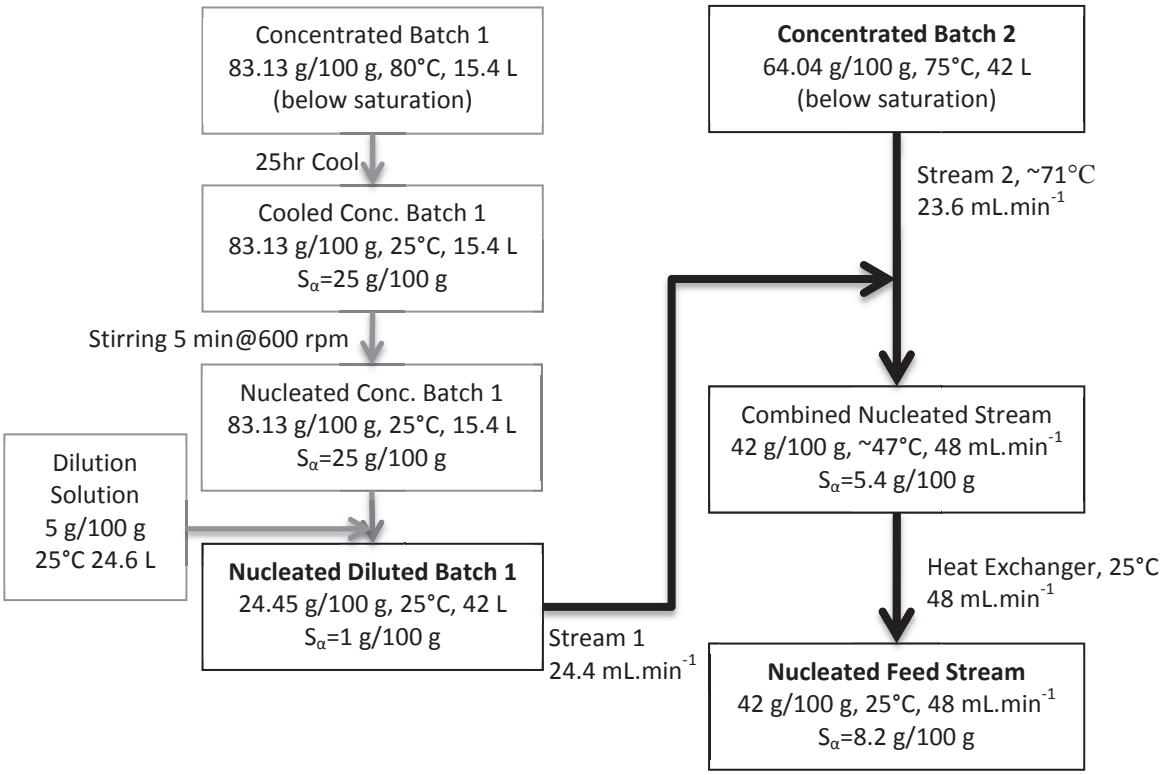


**Figure 91 CSC feed preparation flow chart; $S_\alpha$=absolute alpha lactose supersaturation ($C_\alpha$-$C_{\alpha s}$)**

### *7.3.2 Column Operation*

After the nucleated feed stream flow rate had been calibrated and running for 5 minutes, three control samples were collected in 100 mL Duran bottles, sealed and placed on a custom built bottle roller, controlled by a peristaltic pump motor to achieve approximately 5 bottle revolutions per minute. The bottle roller crystal suspension method was used in an attempt to avoid secondary nucleation which is known to predominantly occur via contact impeller mixing

(Agrawal, 2012). The initial dilute nucleated stream sample was collected and later analysed in the Malvern MasterSizer.

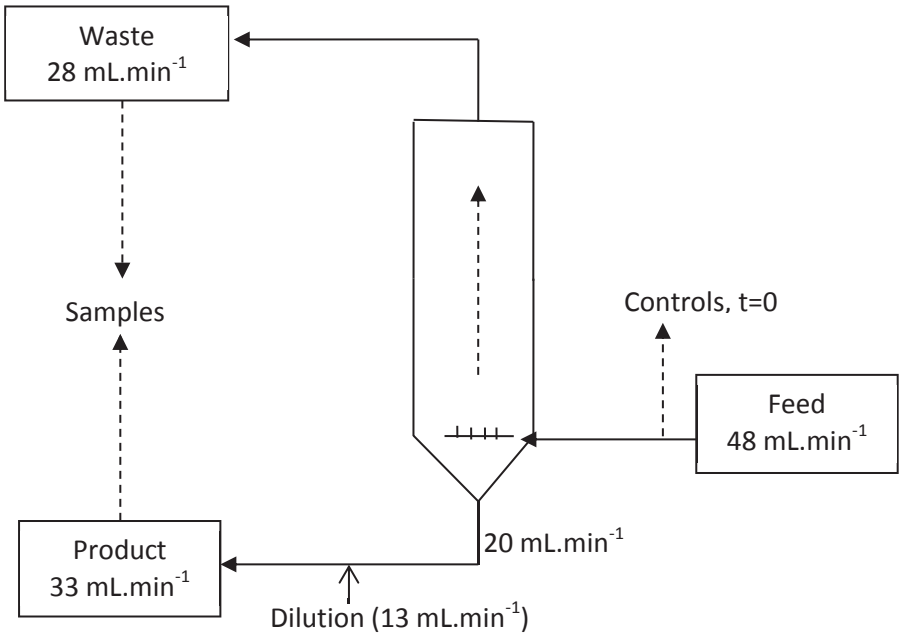


Figure 92 CSC column operation

The nucleated feed solution was then fed into the CSC column at 48 mL.min$^{-1}$. The product stream pump was set at a removal flow rate of 20 mL.min$^{-1}$; thereby an average flow rate of 28 mL.min$^{-1}$ occurred vertically in the column. The product stream was diluted with a water stream, at 13 mL.min$^{-1}$ to a concentration of 24.45 g/100 g, absolute alpha lactose supersaturation of 1 g/100 g (Figure 92). After 2, 4, 6 and 16 to 20 hours of operation samples were collected from the product and waste streams of the column and analysed in the Malvern MasterSizer for PSD measurements. Additional PSD measurements were also obtained for the three controls after 4, 6 and 16 hours of growth time. Slightly supersaturated lactose solution of 24.45 g/100 g was prepared for use as background measurements in the Malvern MasterSizer.

### *7.3.3 Settling Agglomerates*

To see if agglomerates or clusters were present in the column, the following procedure was developed to concentrate large crystals from an initially low crystal content stream, and so they could be viewed and imaged under a microscope. A 2.5 L volume of the 33 mL.min$^{-1}$ product stream was collected. The collection vessel was agitated, and then the solution was poured into a 2 L measuring cylinder up to a fluid height of 0.45 m. The solution was left for 21 min, to allow crystals above 50 μm to settle out over this fluid height, based on Stokes law, Equation 36. The supernatant was then removed with a peristaltic pump so approximately 200

mL remained. The leftover crystal rich solution was remixed and transferred to a smaller container. A 40 µL sample was pipetted into a Neubauer chamber and imaged under a microscope. The settling vessel was later changed to a 10 mm diameter Perspex tube of the same height and settling time; a smaller number of crystals settled, however only a very small number was required for imaging.

## 7.4 CSC Results

### *7.4.1 Feed, Product and Waste Streams*

The Malvern MasterSizer CSC results for the three types of lactose used (IGL-1, 200M-1 and 200M-2) are summarised with 95% CI in Table 13, Table 14 and Table 15; product and waste averages were calculated using samples collected after 16 hours of operation. Refer to Appendix A.8 for details of the experimental run # and the different types of pharmaceutical grade lactose used. Particular results discussed below have a key to indicate experimental run # and sample collection time, for example "17.16:30" refers to run 17, column total run time of 16 hour and 30 minutes. The product $d_{50}$ is within the desired objective of 50 to 90 µm, whereas the product span is significantly greater than the desired objective span of 1, for all types of lactose used. The 200M-1 lactose experimental $d_{10}$ and $d_{50}$ of 22.5±0.6 µm and 53.8±1.6 µm is significantly less than the theoretical predictions of 51.2±0.4 µm and 73.2±0.9 µm, whereas the $d_{90}$ of 98.2±3.0 µm is significantly larger than the predicted 85.9±0.9 µm. The 200M-1 experimental span of 1.41±0.02 is approximately three times the theoretical prediction of 0.47±0.01. The model predictions are not in accord with the experimental results and there are unaccounted experimental deviations, which require further investigation; Section 7.5.4 summarises this discussion.

| | Volume (%) | $d_{10}$ (µm) | $d_{50}$ (µm) | $d_{90}$ (µm) | Span |
|---|---|---|---|---|---|
| Product | 0.0765±0.0151 | 29.3±1.6 | 69.1±2.4 | 132.0±4.3 | 1.49±0.04 |
| Waste | 0.0037±0.0034 | 25.9±10.2 | 48.4±12.0 | 84.1±15.1 | 1.23±0.22 |
| Control 4hr | 0.0215±0.0162 | 15.4±1.3 | 36±2.7 | 71.5±6.8 | 1.56±0.11 |
| Control 6hr | 0.0519±0.0380 | 21.2±1.9 | 53.7±4.7 | 114.9±14.2 | 1.74±0.17 |
| Control 16hr | 0.1815±0.1171 | 47.1±10.8 | 158.8±41.0 | 333.2±81.6 | 1.81±0.35 |

Table 13 IGL-1 CSC Experimental results (Run 2,4,5,9,10), product and waste from 16hr of operation

| | Volume (%) | $d_{10}$ (µm) | $d_{50}$ (µm) | $d_{90}$ (µm) | Span |
|---|---|---|---|---|---|
| Product | 0.0270±0.0024 | 22.5±0.6 | 53.8±1.6 | 98.2±3.0 | 1.41±0.02 |
| Waste | 0.0024±0.0007 | 10.7±1.0 | 23.0±1.5 | 46.6±3.4 | 1.56±0.12 |
| Control 4hr | 0.0145±0.0042 | 10.3±0.3 | 20.7±0.5 | 36.6±1.7 | 1.27±0.07 |
| Control 6hr | 0.0334±0.0109 | 14.3±0.6 | 31.9±2.0 | 62.1±6.2 | 1.49±0.10 |
| Control 16hr | 0.1907±0.0363 | 43.7±2.4 | 113.0±7.6 | 208.7±10.8 | 1.46±0.04 |

Table 14 200M-1 CSC Experimental results (Run 11,12,14-22), product and waste from 16hr of operation

| | Volume (%) | $d_{10}$ (µm) | $d_{50}$ (µm) | $d_{90}$ (µm) | Span |
|---|---|---|---|---|---|
| Product | 0.01578±0.0051 | 30.6±1.1 | 78.2±2.9 | 151±6.9 | 1.54±0.02 |
| Waste | 0.0008±0.0015 | 13.3±6.8 | 28.4±9.5 | 57.1±13.3 | 1.56±0.36 |
| Control 4hr | 0.0186±0.0219 | 13.3±1.3 | 33.5±6.5 | 69.2±18.6 | 1.66±0.21 |
| Control 6hr | 0.0454±0.0431 | 19.3±2.5 | 54.6±13.2 | 112.1±21.8 | 1.70±0.09 |
| Control 16hr | 0.2310±0.0734 | 69.3±2.8 | 174.8±6.2 | 314.9±21.0 | 1.41±0.07 |

Table 15 200M-2 CSC Experimental results (Run 23-25), product and waste from 16hr of operation

The CSC product $d_{50}$ produced when using different types of lactose used is also significantly different; with IGL-1 and 200M-2 lactose producing a similar but larger product $d_{50}$ compared to 200M-1 lactose. This is also seen in the 4, 6, and 16 hour bottle roll controls. Because the same nucleation and experimental run conditions were used each time, this variation is attributed to inherently different growth rates for the different types of lactose used. As reviewed in the literature (Dincer, *et al*., 2009a and Butler 1998), growth rate suppression can arise from various impurities present, such as salts, being incorporated into the crystal during the crystallization process.

| Batch | Before Mixing | | After Mixing | | After Dilution | |
|---|---|---|---|---|---|---|
| | RI | Turbidity | RI | Turbidity | RI | Turbidity |
| IGL-1 | 1.4116±0.0013 | 1.4±0.3 | 1.4121±0.0008 | 84.7±29.2 | 1.3631±0.0004 | 11.6±18.2 |
| 200M-1 | 1.4129±0.0004 | 6.6±12.5 | 1.4129±0.0002 | 63.7±8.5 | 1.3637±0.0001 | 4.6±1.6 |
| 200M-2 | 1.4128±0.0006 | 1.1±0.9 | 1.4132±0.0005 | 48.3±33.4 | 1.3638±0.0001 | 2.4±1.3 |

Table 16 Nucleation solution, RI and turbidity

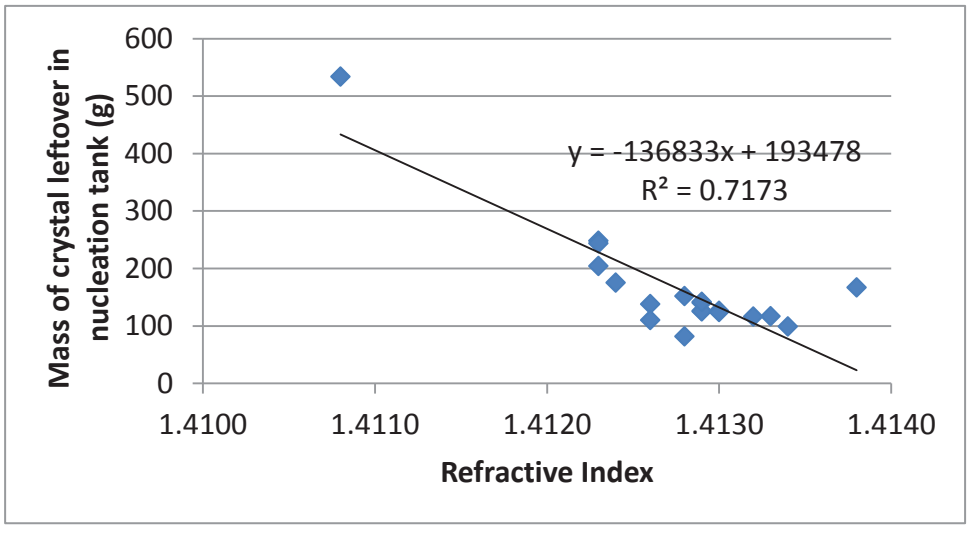


Figure 93 Left over nucleation solution crystal mass versus mixed solution RI

The dilute nucleated feed stream underwent the same preparation and 25 hour ambient cool to 25°C, at which time nucleation mixing and dilution occurred. The turbidity and Refractive Index (RI) measurements, before mixing, after mixing and after dilution can be seen in Table 16. Turbidity measurements indicate the amount of crystal and nuclei present in the solution.

Solution concentration can be directly correlated with RI measurements. After mixing there is a general trend for an increased RI, indicating a slightly inhomogeneous solution concentration from the cool down phase. IGL-1 shows the lowest concentration and highest turbidity after mixing compared to 200M-1 and 200M-2. More crystal in the nucleation tank corresponds to a lower solution concentration, which can be seen in Figure 93. Although not entirely apparent why, more crystallization has occurred during the cool down phase for IGL-1. The different lactose solutions all had the same temperature profiles when cooled at ambient conditions.

Table 17 details the final feed stream RI values for the different batches of lactose, as well as the control measurements. Although the same preparation method was used, IGL-1 has a significantly lower feed growth concentration compared to 200M-1 and 200M-2 (t-test at 95% level of confidence), because of the lower nucleation solution concentration (Table 16).

| Batch | Feed RI | 4 hr Control RI | 6 hr Control RI | 16 hr Control RI |
|---|---|---|---|---|
| IGL-1 | 1.3814±0.0004 | 1.3814±0.0002 | 1.3814±0.0003 | 1.3808±0.0006 |
| 200M-1 | 1.3818±0.0001 | 1.3817±0.0001 | 1.3817±0.0001 | 1.3815±0.0001 |
| 200M-2 | 1.3818±0.0002 | 1.3818±0.0004 | 1.3817±0.0004 | 1.3815±0.0013 |

**Table 17 Comparison of RI between batches of lactose controls**

Septum points were installed into the column, and samples collected at the end of normal CSC runs. 200M-1 lactose results can be seen in Table 18; Height 1, 2 and 3 corresponded to a height of 0.4, 1.4 and 2.8 m respectively. Although the particle size did not match, both experimental and theoretical values show the general trend for decreasing $d_{10}$, $d_{50}$ and $d_{90}$ with height, and an increased span from product stream values. Two septum CSC run results were collected for the 200M-2 lactose, presented in Table 19. Again a decreasing $d_{10}$, $d_{50}$ and $d_{90}$ with height, and an increased span from product stream values were observed. Smaller particle size with height occurs because the larger (faster growing) crystals have opposed the fluid flow and settled, while the decreasing $d_{10}$ and $d_{50}$ acts to increase the span.

| Height (m) | Volume Ratio | $d_{10}$ (µm) | $d_{50}$ (µm) | $d_{90}$ (µm) | Span |
|---|---|---|---|---|---|
| **CSC Experimental Results** | | | | | |
| Height 1 | 0.74±0.28 | 14.8±1.8 | 47.2±2.6 | 92.6±3.9 | 1.65±0.09 |
| Height 2 | 1.00±0.13 | 13.5±0.7 | 36.0±1.3 | 78.0±5.3 | 1.79±0.11 |
| Height 3 | 0.95±0.80 | 14.2±1.3 | 33.9±1.9 | 69.2±6.4 | 1.63±0.18 |
| **CSC Theoretical Predictions** | | | | | |
| 0.40±0.01 | 1.00±0.26 | 29.8±7.4 | 56.1±5.6 | 66.9±4.3 | 0.67±0.17 |
| 1.40±0.01 | 1.00±0.84 | 19.3±10.1 | 51.6±11.3 | 62.2±12.0 | 0.85±0.18 |
| 2.80±0.01 | 0.86±0.15 | 16.0±2.5 | 41.9±5.9 | 51.4±10.9 | 0.83±0.10 |

**Table 18 200M-1 CSC Experimental Septum results (Run 11,12,14-22), from 16hr of operation, compared with 200M-1 standard theoretical CSC model values**

| Height | Volume (%) | $d_{10}$ (µm) | $d_{50}$ (µm) | $d_{90}$ (µm) | Span |
|---|---|---|---|---|---|
| CSC Experimental Results | | | | | |
| Height 1 | 0.0033-0.0052 | 15.5-17.1 | 57.0-58.9 | 124.5-124.8 | 1.83-1.91 |
| Height 2 | 0.0077-0.0086 | 15.0-15.8 | 40.9-42.5 | 91.6-94.3 | 1.78-1.94 |
| Height 3 | 0.0045-0.0054 | 16.5-16.9 | 39.3-39.7 | 79.7-81.4 | 1.61-1.62 |

Table 19 200M-2 CSC Experimental septum results (Run 23 & 25 range shown), from 16hr of operation

### *7.4.2 Malvern MasterSizer Result Variation*

Solution temperature inside the Malvern MasterSizer small volume sampling unit and PSD were measured over a 10 minute time period. Starting at 25°C, temperature increased at approximately 0.1°C per minute. Depending on solution concentration, if the solution temperature becomes too high, the saturation point may be reached and crystal will start to dissolve. With the normal measurement procedure lasting less than 2 minutes, a significant temperature increase is not expected to be a problem. PSD in the sampling unit was also measured with time; shown in Figure 94. An initial rapid decrease in the PSD occurs after 2min, which subsequently evens out with a maximum change in the $d_{90}$ of 10%. This decrease in size has been attributed to the breakdown of agglomerates; refer to Section 7.4.3 for more detail.

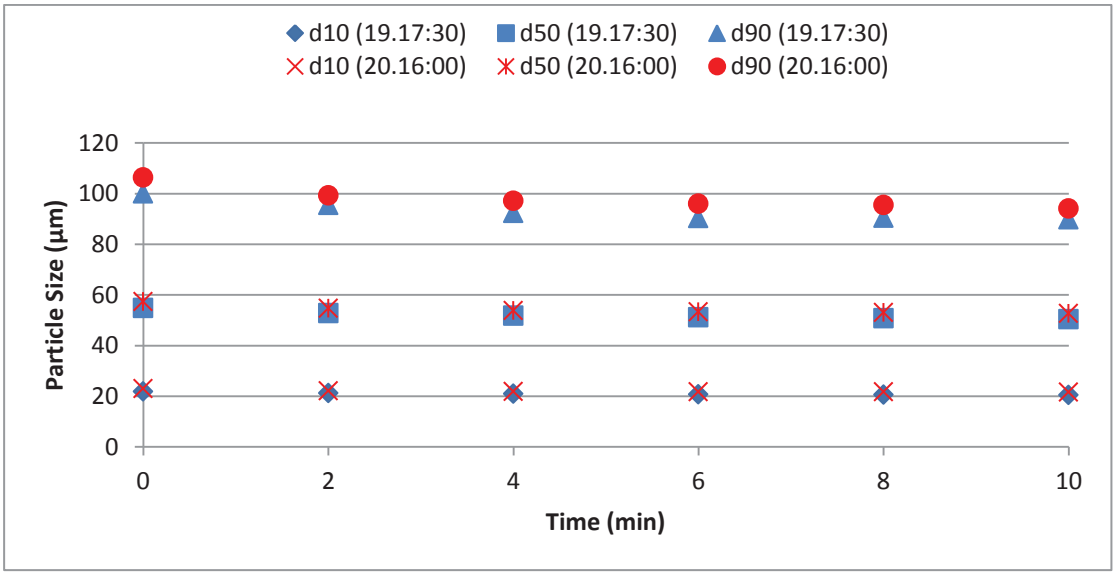


Figure 94 Malvern MasterSizer sample PSD change with time

Product sample obscuration and volume concentration change over a 10 minute time period measured inside the Malvern MasterSizer sampling unit for 2 runs are shown in Figure 95. Run 19 shows during the first 2 minutes there was a slight drop in obscuration and volume concentration, which then increased and levelled out after 6 minutes (max change of 8%). A similar trend initially appears for run 20 but at 8 minutes an unexpected drop occurs. Increasing obscuration is explained by an increased amount of smaller particles.

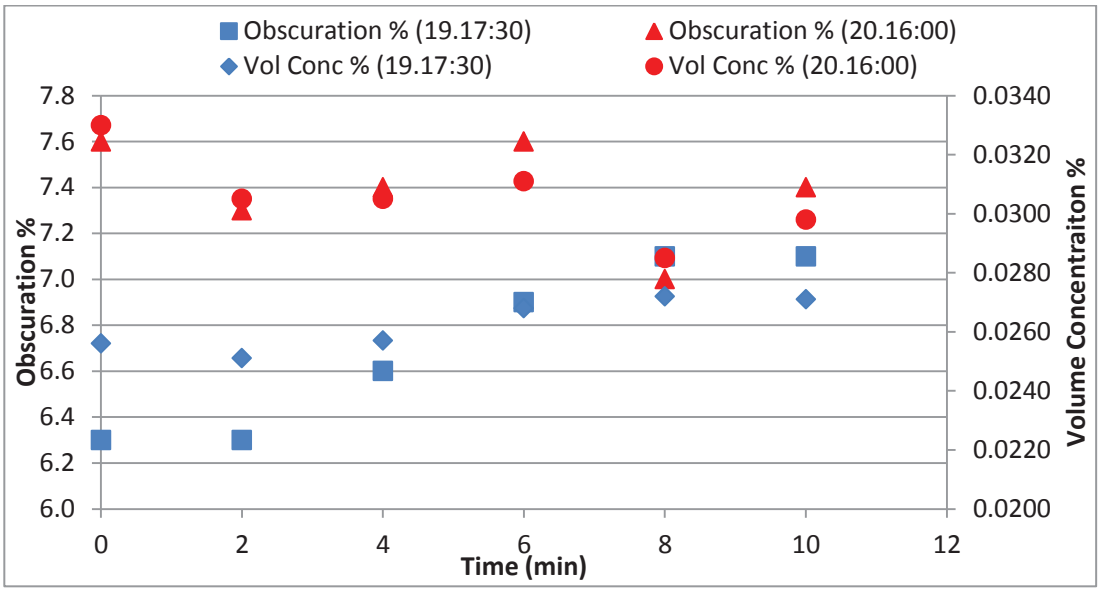


Figure 95 Malvern MasterSizer sample obscuration and volume concentration change with time

A 1 L CSC product sample was collected after 17 hours of operation and sub-samples were measured in the Malvern MasterSizer; PSD results shown in Figure 96, and obscuration and volume concentration measurements are shown in Figure 97. Typical measurement procedure involves cleaning between samples, however only sample unit emptying and refilling with sub-sample occurred for these measurements to assess the effect on initial PSD and crystal build up. Apart from a very minor decrease in all particle sizes with the second sub-sample, no apparent trends in PSD can be seen, which remains constant. This confirms the reliability of the Malvern MasterSizer for obtaining a PSD representative of the original sample.

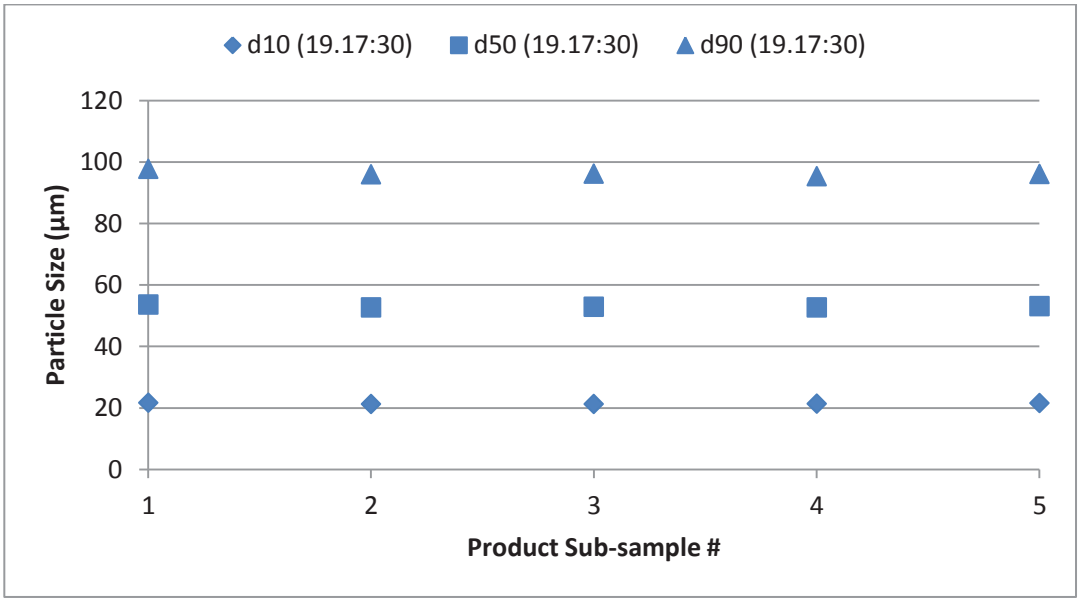


Figure 96 Malvern MasterSizer sub-sample PSD variation

Analysing the Malvern MasterSizer obscuration and volume concentration results, with no cleaning occurring between the sub-samples, Figure 97, it appears some crystal remained from each sub-sample, resulting in an overall 13% increase in the volume concentration. Sample unit cleaning is required to give reliable concentration results between samples, which was why sample unit cleaning was included in the normal measurement procedure.

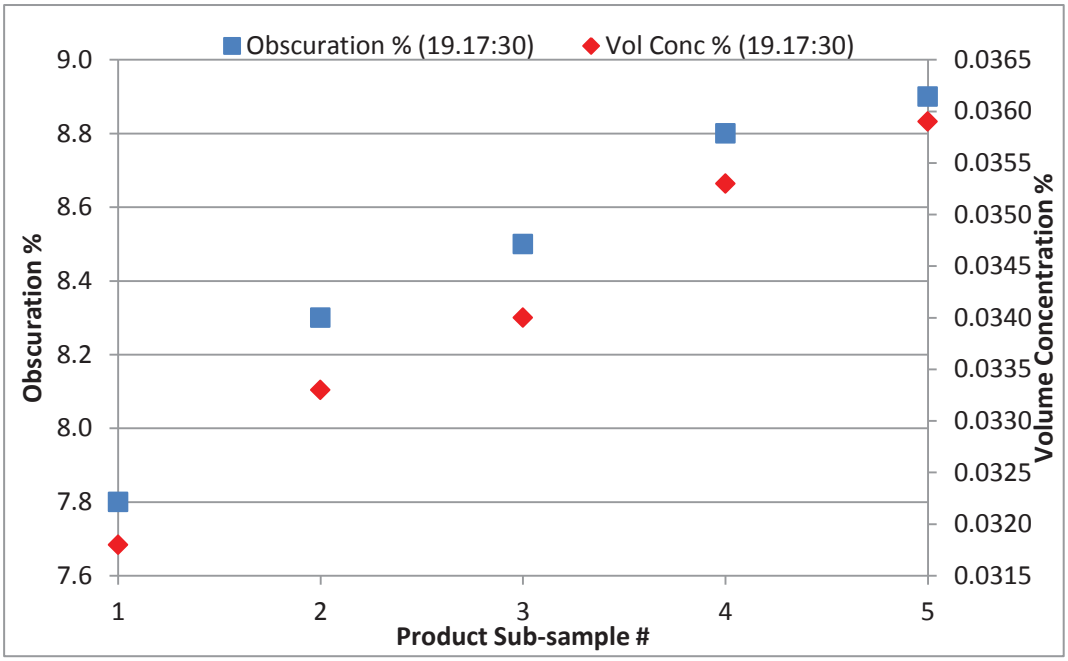


Figure 97 Malvern MasterSizer sub-sample obscuration and volume concentration variation

### *7.4.3 Agglomerates*

The measured CSC product stream PSD revealed a particle size larger than the maximum $d_{90}$ size predicted by the theoretical model, as well as a smaller $d_{10}$ particle size, leading to a span greater than 1. An initial thought was that agglomerates and clusters could have led to larger crystals and also settle out smaller crystals which would otherwise have been lost to the waste stream. The settling method of large crystals, Section 7.3.3, was carried out to confirm if large agglomerates and clusters were present or whether there were just large crystals present.

The microscope images of large crystals settled from the product stream and column septum samples confirmed the presence of agglomerates; see Figure 98. “Agglomerates” are considered to be a random assortment of crystals joined together, whereas “clusters” are joined together at the apex of the tomahawk. Typically large agglomerates were found from the settling tests, with a very minor percent of clusters. The settling experiment was undertaken to find out if agglomerates were present, but was not able to provide quantitative information on the product stream. From qualitative observations of the settled crystals images, it is suggested that 30 to 60% agglomerates are present in the various samples.

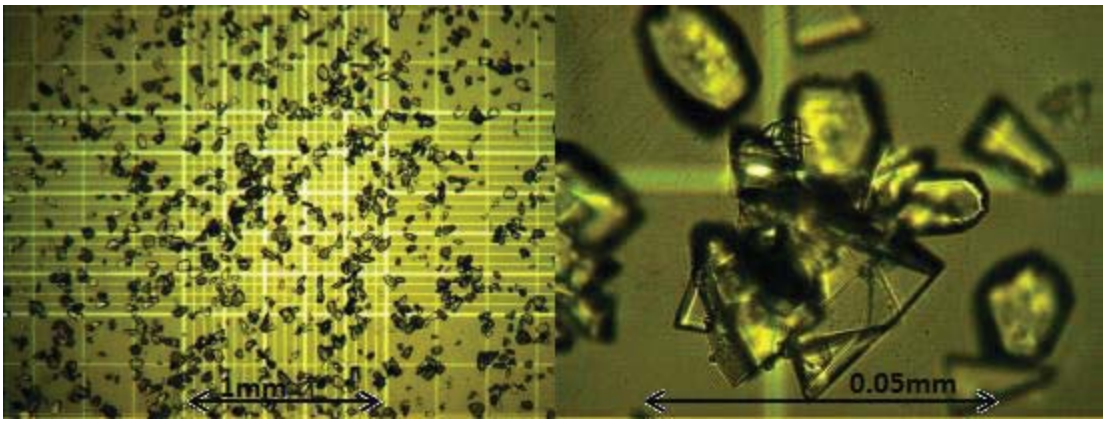


Figure 98 Typical agglomerates found in the CSC product stream and column

After confirming the presence of agglomerates, various impeller based methods were investigated for their ability to break agglomerates. The idea was that the larger agglomerates could be broken down into individual crystals, reducing the $d_{90}$, while maintaining or increasing the $d_{10}$ and $d_{50}$, and thus reducing the span. If the product span was still greater than 1 for the successfully broken agglomerates, the breakdown methods had the capability of being implemented in a column recycle loop; see Section 7.5.5 Agglomeration Solutions for more detail. Due to the potential use in a column recycle loop, impeller turbulence, which could cause the introduction of bubbles into the CSC column, was limited for the breakdown methods chosen. Three impellers controlled by an overhead stirrer were tested, as shown in Figure 99 and were: Blade 1 (2000 rpm), Blade 2 (2000 rpm) and Flat Blade (500 rpm). Blade 1 was similar to the mixing blade inside the Malvern MasterSizer small volume dispersion unit, Blade 2 caused the lowest fluid turbulence and the Flat Blade had the maximum energy transfer. All three impellers were tested in a baffled 400 mL covered vessel containing sub-samples of product lactose solution, collected from a larger volume, and operated for 10 minutes at the specified rpm speed.

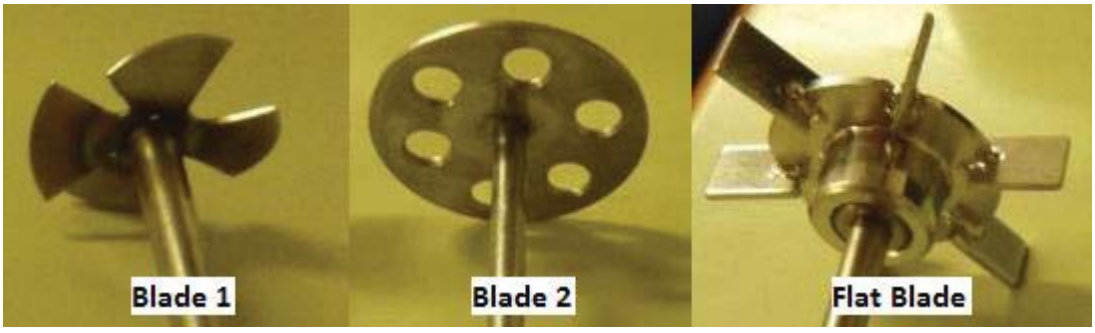


Figure 99 Impellers tested on product stream, Blade 1, Blade 2 and Flat Blade

An additional breakdown method consisting of a small 50 mL enclosed vessel containing a 25 mm magnetic flea (operated at 1500 rpm) with 200 $mL.min^{-1}$ fluid recycle through the vessel was also tested.

Figure 100 shows the change in the $d_{10}$ with mixing time, which started at 30 to 31 µm. After 10 minutes of mixing time, Blade 2 had the greatest effect on decreasing the $d_{10}$ particle size, by approximately 3 to 4 microns. Blade 1 and the Flat Blade had similar reductions to the Malvern MasterSizer of approximately 2 to 3 microns, whereas the flea mixing had a very minor reduction of less than 2 microns.

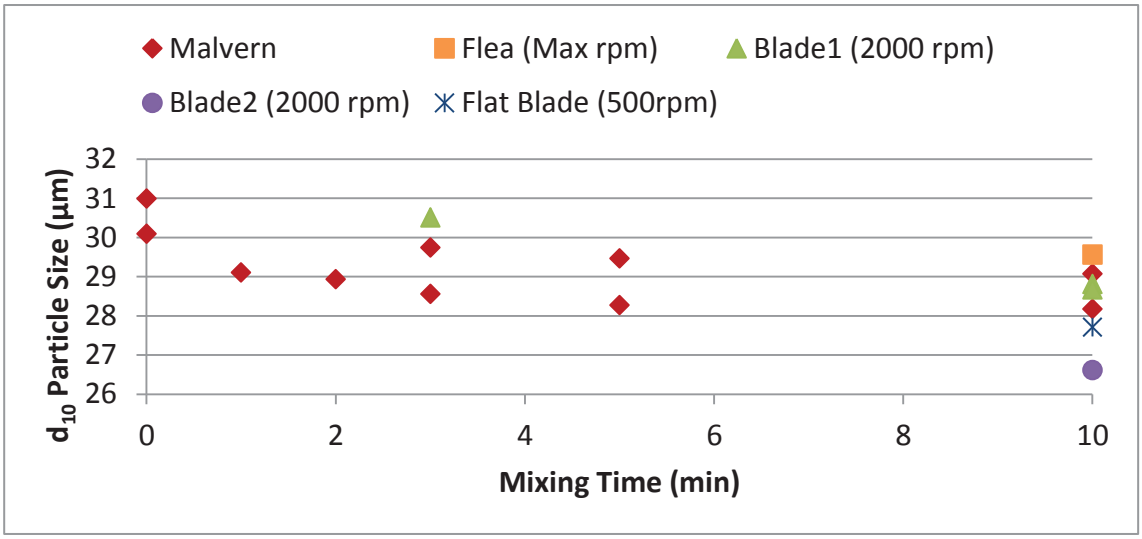


Figure 100 Time of mixing versus $d_{10}$ particle size, Run 25.16:30-18:30

Figure 101 shows the change in the $d_{50}$ with mixing time, which started at 76 to 78 µm. After 10 minutes of mixing time, Blade 2 had the greatest effect on decreasing the $d_{50}$ particle size, with similar reductions to the Malvern MasterSizer of approximately 7 to 8 microns. Blade 1 and the Flat Blade reduced the particle size by approximately 4 to 5 microns, whereas the flea mixing had a very minor reduction of less than 2 microns.

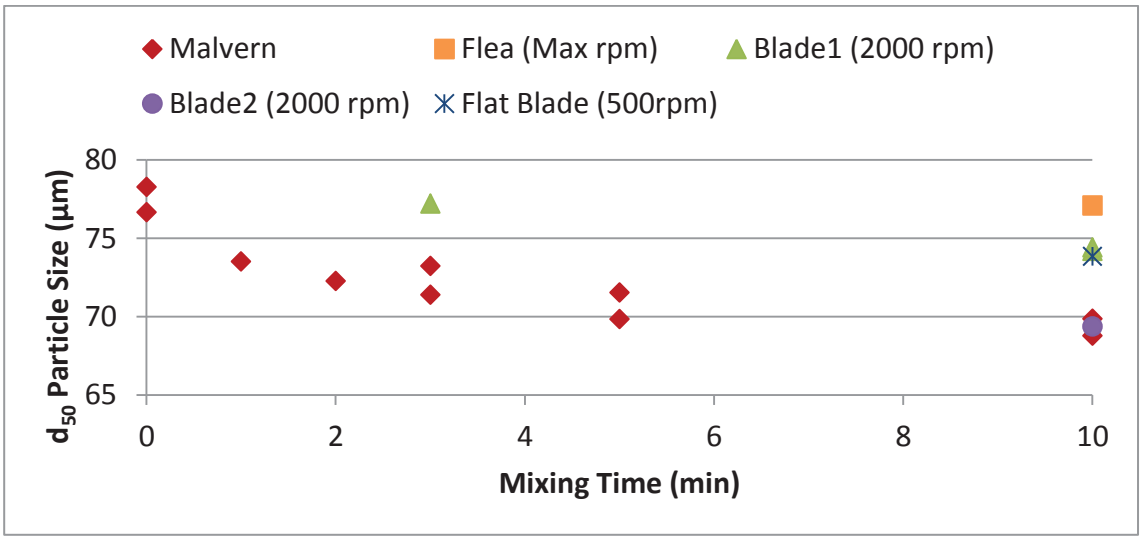


Figure 101 Time of mixing versus $d_{50}$ particle size, Run 25.16:30-18:30

Figure 102 shows the change in the $d_{90}$ with mixing time, which started at 147 to 150 µm. After 10 minutes of mixing time, the Malvern MasterSizer had the greatest effect on decreasing the $d_{90}$ particle size, by approximately 20 microns. Blade 1 and 2 reduced the particle size by approximately 5 microns, whereas the flea mixing and the Flat Blade had little effect.

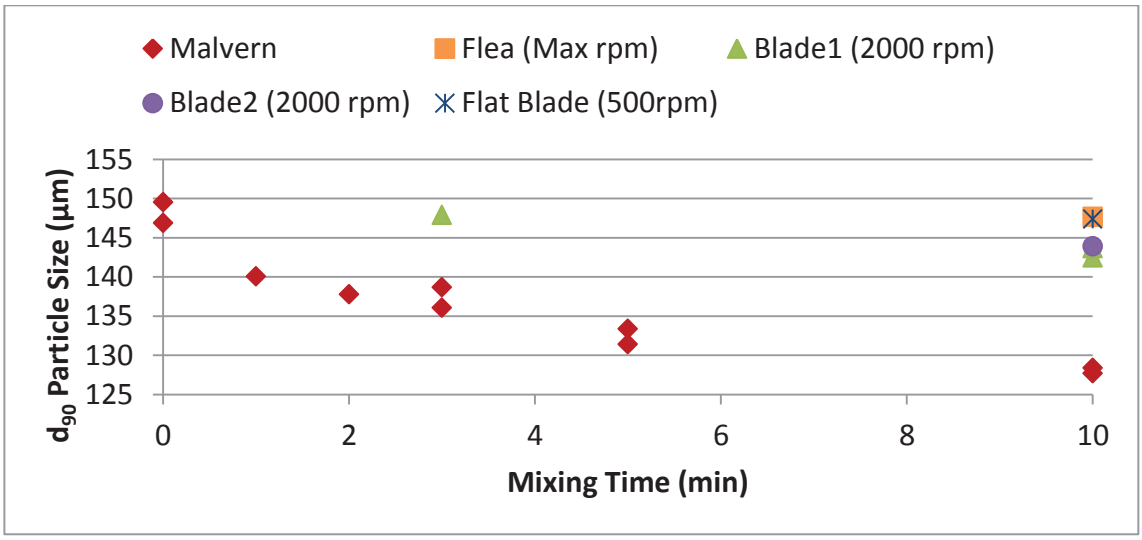


Figure 102 Time of mixing versus $d_{90}$ particle size, Run 25.16:30-18:30

Figure 103 shows the change in span with mixing time, which started at 1.52. After 10 minutes of mixing time, the Malvern MasterSizer had the greatest effect on decreasing the span, by approximately 0.1. Blade 1, Blade 2, and the flea mixing had little effect, whereas the Flat Blade increased the span. No breakdown technique reduces the product span to less than 1 (desired), as although the $d_{90}$ decreased, the $d_{10}$ and $d_{50}$ also reduced. The Malvern MasterSizer proved to give best breakdown results, and this type of mixing setup would be recommended for implementation into an agglomerate breakdown recycle loop.

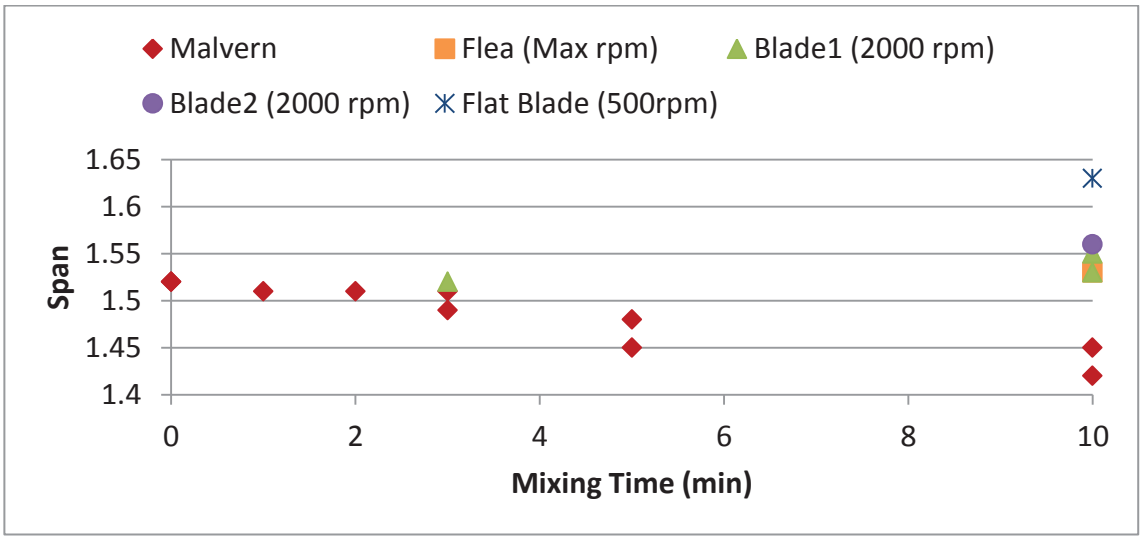


Figure 103 Time of mixing versus span, Run 25.16:30-18:30

### *7.4.4 Product Stream Processing*

A range of post CSC product stream processing tests were carried out. The aims were to assess how the product span and PSD changed and whether improvements could occur on the standalone product stream to achieve the desired span of less than 1.

#### 7.4.4.1 Dilution

The CSC product stream setup was designed with online dilution, which occurred after being pumped from the column, to lower the supersaturation so very limited growth occurred during the PSD measurements. On the basis of Oswald ripening, where small crystals are preferentially dissolved over large crystals, altering the dilution level to just below the saturation limit to dissolve out a certain percentage of crystal (ideally fines), was proposed. However, the crystal concentration of the undiluted product stream was too low to accurately control the dilution process and target the dissolution of a desired crystal percentage (Appendix A.6). Table 20 below shows the effect of an increase in the product stream dilution but remaining above the supersaturation solubility limit (Figure 6). It was found that increasing the product dilution, by increasing the amount of water being added to the product stream coming from the column, decreased the $d_{10}$, $d_{50}$ and $d_{90}$. Even when staying above the saturation limit, targeting the dissolution of fines (an increase in the $d_{10}$) and a decrease in span did not occur. If the product stream crystal volume concentration was higher, then targeting the dissolution of fines might be achievable.

| Concentration | Volume (%) | $d_{10}$ (µm) | $d_{50}$ (µm) | $d_{90}$ (µm) | Span |
|---|---|---|---|---|---|
| **Normal Product Stream** | | | | | |
| 0.79 g/100 g, 25°C | 0.0270 | 22.8 | 56.7 | 103.3 | 1.42 |
| **Product Stream with Additional Dilution** | | | | | |
| 0.26 g/100 g, 25°C | 0.0247 | 20.9 | 53.2 | 98.2 | 1.45 |
| After 2hr Sitting 0.22 g/100 g, 25°C | 0.0253 | 20.4 | 52.7 | 95.4 | 1.45 |

Table 20 Additional product stream dilution for 19.19:00

The solution temperature becomes important as the CSC product stream concentration is lowered closer to the solubility limit. The solubility limit is also affected by temperature and if it increases significantly this will result in the dissolution of crystal. Solutions with an absolute alpha lactose supersaturation of 0.26 g/100 g at 25°C were measured to be further diluted from residual water and lactose background solution leftover in the Malvern MasterSizer sampling unit to 0.18 g/100 g at 25°C. A solution temperature above 25.8°C would now drop

the solution concentration to below the solubility limit, which is possible depending on the uncontrolled ambient temperature in the room housing the Malvern MasterSizer.

### 7.4.4.2 Ultrasound

Ultrasound has been shown to reduce particle size and agglomerates (Kougoulos, *et al.*, 2010). Varying lengths of exposure to ultrasound were tested for effectiveness in reducing large agglomerates and thus reducing the $d_{90}$. The test setup was an ultrasonic 1 kW probe, operated at 20% power, inserted in a 250 mL beaker containing 175 mL of well mixed product solution. It can be seen in Figure 104, after 2 seconds of ultrasound application, the reduction in $d_{10}$ and $d_{50}$ starts to level out, but the $d_{90}$ is still decreasing. A similar trend can be seen for the span shown in Figure 105.

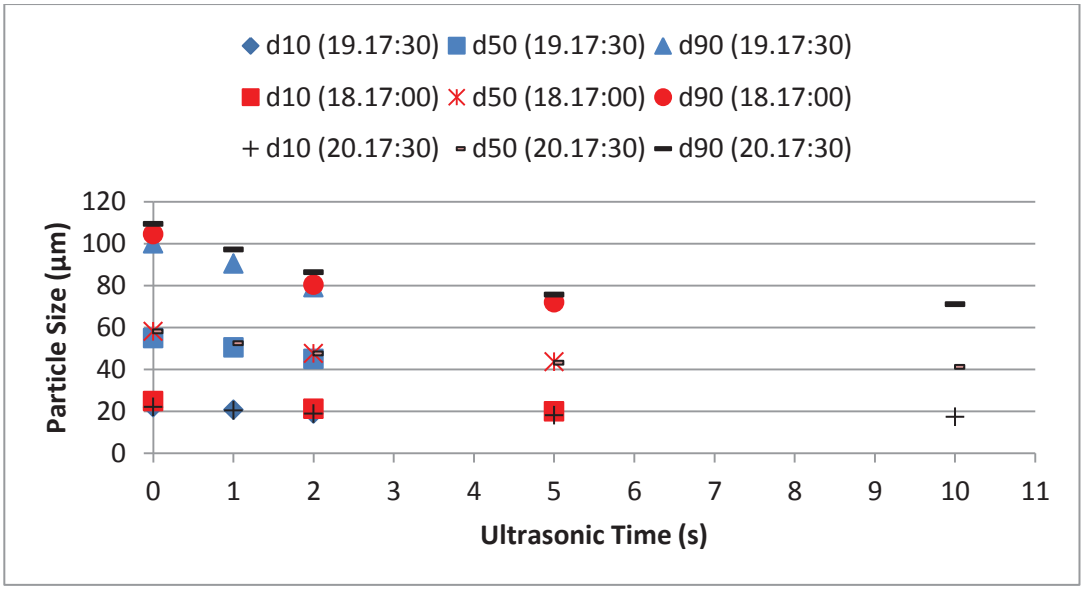


Figure 104 CSC Product stream PSD change with varying times of ultrasound

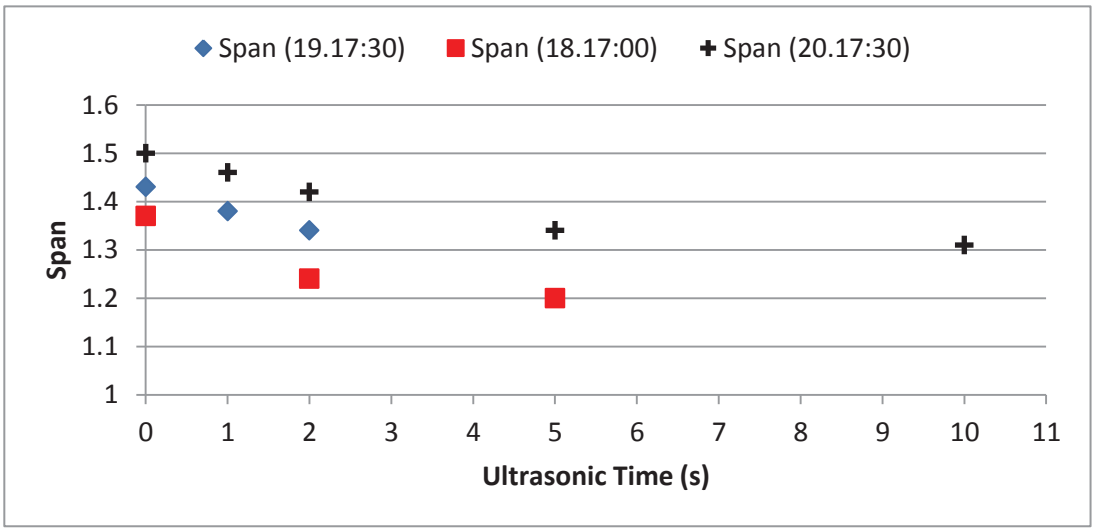


Figure 105 CSC Product stream span change with varying times of ultrasound

Agglomerates at all size ranges are detached, resulting overall in smaller crystals. After 10 s of ultrasound application, span had dropped by 13%, $d_{10}$ by 22%, $d_{50}$ by 29% and $d_{90}$ by 35%. The variation in the measured crystal volume concentration for the different ultrasound sub-samples shown in Figure 104 and Figure 105 was within 7%, therefore crystal dissolution from the ultrasound process was not considered to be occurring.

### 7.4.4.3 Centrifuge

A centrifuge was tested as a method for concentrating the product stream and the resulting PSD was compared with the original CSC product stream. A centrifuge was used to concentrate approximately 2.4 L of product stream to 70 mL.

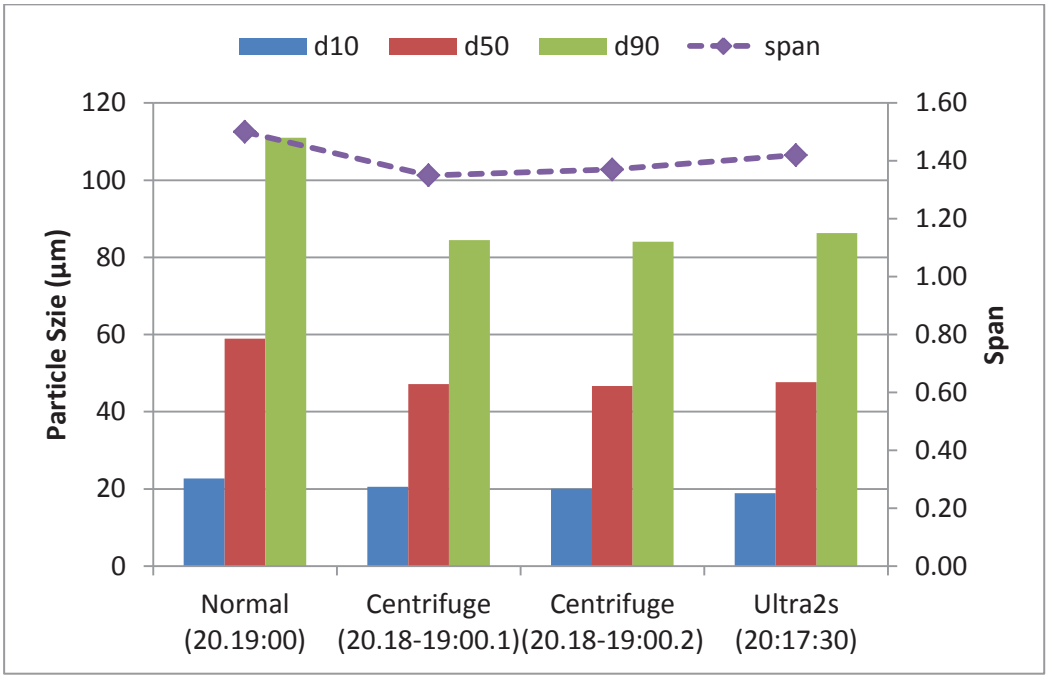


Figure 106 Product stream PSD undergone centrifuge concentration

The two centrifuge results in Figure 106 show that the normal untreated product particle size is reduced, when operated at 10,000 rpm, to a similar magnitude to a product stream exposed to 2 s of ultrasound. The span decreases by less than 0.2 which was not enough to reach the desired span of less than 1.

### 7.4.4.4 Filtering

An appreciable amount of crystal was collected via filtering a large volume of product crystals, and subsequently dried in an oven. Figure 107 shows the PSD results for two runs of filtered product crystal after being added to slightly supersaturated lactose background solution. The filtered crystal PSD measurement method was adapted to utilise a double background solution

rinse in the Malvern MasterSizer sampling unit. It was found the residual cleaning water was dropping the background solution supersaturation to near the solubility limit, causing crystal dissolution. The lactose background solution with an absolute alpha supersaturation of 0.52 g/100 g at 25°C was diluted from residual cleaning water, once in the sampling unit, to 0.11 g/100 g at 25°C. A double rinse of background solution, filling the sampling unit, emptying and refilling before adding crystal, minimised the dilution from residual water. The filtered crystals underwent a reduction in the $d_{10}$, $d_{50}$ and $d_{90}$, indicating that the filtering, drying and addition of crystals to background solution for measurement has separated agglomerates. The effect on span for filtered crystals was marginal and varied between runs.

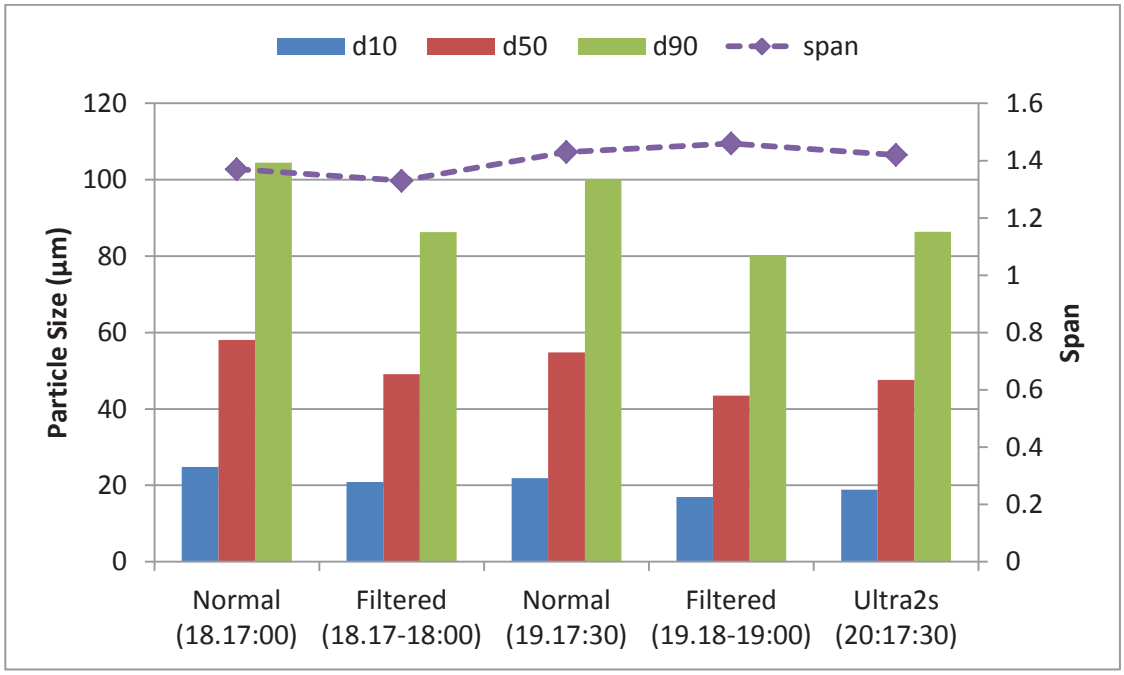


Figure 107 Product PSD for filtered and dried crystals

### 7.4.4.5 Hydrocyclone

A hydrocyclone can act in two ways: by concentrating the product stream, and separating unwanted fines. Although an experimental hydrocyclone was not available for testing, theoretical calculations (Appendix A.9) have shown it would be possible to achieve a product span of 1 with a single hydrocyclone cut on the exiting CSC product stream; see Figure 108. The calculations do not take into account the effect of initial crystal concentration on the separation performance. Additional predictions, Table 21, show it is possible to carry out a single hydrocyclone cut on the batch grown controls; the consequence is more crystal is lost as the starting PSD has a higher span.

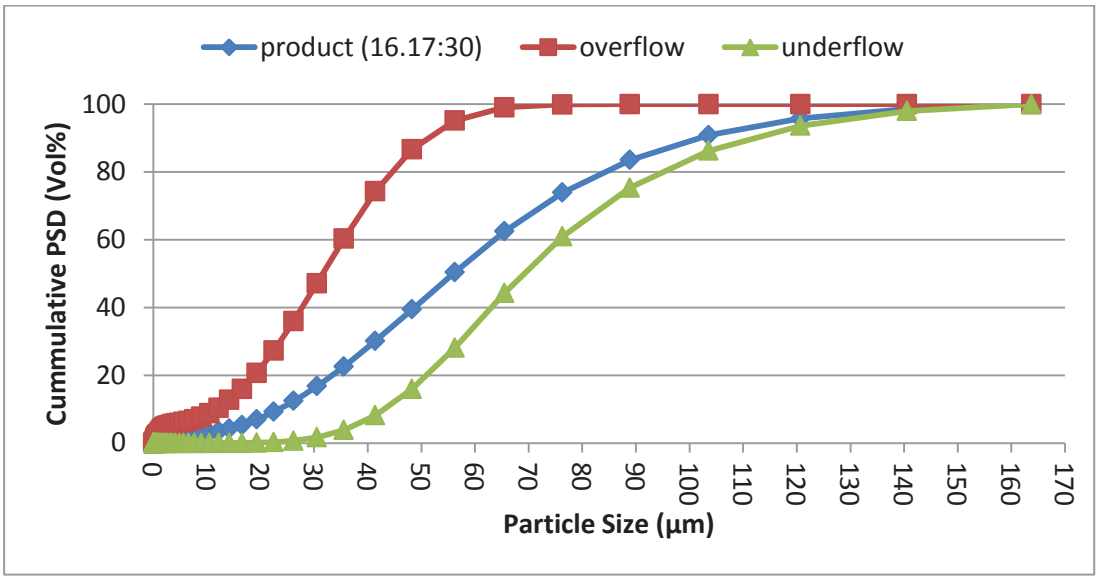


Figure 108 Single pass hydrocyclone product cut selected for an underflow span of 1

| Condition | $d_{50c}$ (µm) | $d_{10}$ (µm) | $d_{50}$ (µm) | $d_{90}$ (µm) | Span | Crystal Vol % |
|---|---|---|---|---|---|---|
| 200M-1 Product (16.17:30) | 46.0 | 23.4 | 56.0 | 101.9 | 1.40 | 100.0 |
| underflow | | 43.0 | 69.2 | 112.2 | 1.00 | 66.8 |
| overflow | | 11.8 | 31.6 | 51.4 | 1.25 | 33.2 |
| | | | | | | |
| 200M-1 Ultrasonic 2s (20.17:30) | 38.2 | 18.8 | 47.6 | 86.8 | 1.43 | 100.0 |
| underflow | | 36.4 | 58.8 | 95.2 | 1.00 | 67.5 |
| overflow | | 7.6 | 25.6 | 42.3 | 1.35 | 32.5 |
| | | | | | | |
| 200M-1 Ultrasonic 5s (20.17:30) | 29.7 | 18.0 | 43.1 | 75.7 | 1.34 | 100.0 |
| underflow | | 30.7 | 50.4 | 81.1 | 1.00 | 75.4 |
| overflow | | 5.7 | 21.0 | 34.0 | 1.35 | 24.6 |
| | | | | | | |
| IGL-1 6hr batch control (9.00) | 68.4 | 21.4 | 53.3 | 109.2 | 1.65 | 100.0 |
| underflow | | 50.8 | 83.8 | 134.6 | 1.00 | 41.4 |
| overflow | | 17.1 | 37.7 | 65.0 | 1.27 | 58.6 |
| | | | | | | |
| IGL-1 6hr batch control(10.00) | 80.0 | 20.6 | 54.9 | 117.6 | 1.77 | 100.0 |
| underflow | | 57.0 | 94.8 | 151.9 | 1.00 | 35.6 |
| overflow | | 16.8 | 40.0 | 73.1 | 1.41 | 64.4 |

Table 21 Summary of hydrocyclone $d_{50}$ cut sizes to achieve a span of 1

## 7.5 Discussion

### *7.5.1 Laminar Flow*

The un-insulated column dye tests showed dye reached the top of the column in around 2 hours. If an ideal laminar profile was present, the time should be closer to the theoretical estimate of 3 hr 54 min. Dye tracer tests from the literature for low flow rate systems show the propagation of the dye due to the density difference with water is likely to be partly responsible for this. The laminar jet nozzle inlets are also causing mixing affects. Literature has shown for laminar fluid jets, with Reynolds numbers around 10, some propagation occurs before dissipation and laminar flow, and Reynolds numbers near 1 have a very small entry length before dissipation occurs (N. Dombrowski, Foumeny, Ookawara, & Riza, 1993; Friedman, Gillis, & Liron, 1968). This propagation can be seen from the 16-pipe feed nozzles in the dye tracer tests which have Reynolds numbers around 13; see Figure 109. The single inlet feed design with a horizontal flow nozzle lowered the Reynolds number, shortening the transition to laminar column fluid flow, and therefore this design was selected for use in the CSC experiments; refer to Section 7.2.2.2 for more detail.

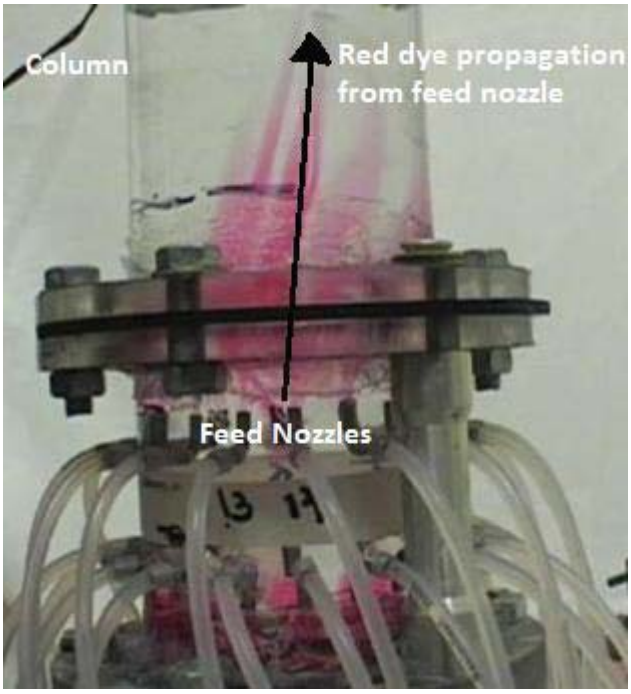


**Figure 109 Start-up photo from 16-pipe dye tracer test, showing initial dye propagation from nozzles**

Column temperature related convection effects were initially identified to be occurring; the room temperature fluctuated by ±1.5°C, and the air felt turbulent at some points in the room. Near the ceiling, and through the roof hole, temperatures were lower on average by around

1°C than the centre of the room. Additional insulation and heating in the roof gap overhead box was added to counteract this.

A problem was exposed when the concentrated stream blocked in one of the initial full scale runs, and the dilute nucleated stream continued to be pumped into the column full of the final feed solution. It was noticed that a fast rolling and random motion of crystals and fluid was occurring in the column, even after all flows were switched off; the mixing effects were greater than the dye water tests. Mixing here has been attributed to the density and temperature differences between the column fluid and the dilute only stream. This follows convection theory, that a hotter solution will have a lower density and rise, and the dilute stream has a lower density and will also rise. Maintaining the consistency of the feed stream with time is therefore crucial to avoid unwanted column mixing effects.

Column baffling, as discussed in the Section 7.2.4.1, was investigated for the effect on the product stream crystals. The aim was to even out the flow experienced by crystals. Two designs of baffling were tested. The first design had minimal baffles, and no change to the product and waste stream PSD occurred. The second design had a maximum amount of baffles, and did affect the product and waste streams. Crystals attached to the baffles, and due to the increased internal column surface area from the baffles, a very low product stream crystal concentration resulted. The nucleation rate from the impeller mixing stage was increased (nucleation mixing time increased from 5 to 10 minutes), so a high enough product crystal concentration could be produced and measured accurately in the Malvern MasterSizer. The product stream PSD result for the increased nucleation fully baffled 200M-2 lactose test was $d_{10}$=18 µm, $d_{50}$=56 µm, $d_{90}$=118 µm and span=1.8. The product span had increased and $d_{50}$ decreased from the normal CSC column 200M-2 product stream results (Table 15). Crystals sampled from the unsettled product stream were viewed under a microscope and qualitatively showed a large number of agglomerates, Figure 110, which was at the high end observed for non-baffled runs. This is likely from the increased crystal concentration causing hindered settling and from crystal building up on the added internal surface with subsequent detachment. Any potential flow improving effects from the baffling are outweighed by the increased surface area and hindered settling; therefore the use of a fully baffled column is not recommended.

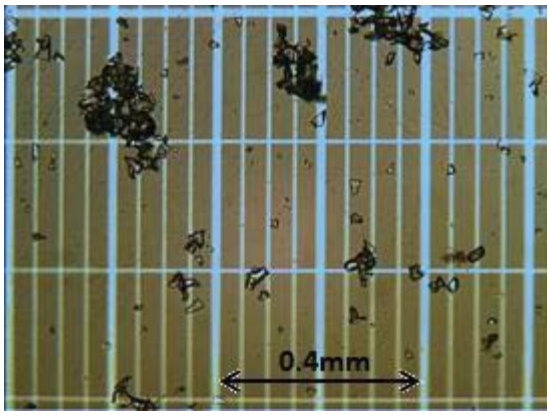


Figure 110 Fully baffled column product stream crystals microscope images (no additional settling)

### *7.5.2 Growth Rate*

Growth rates for the 6 hour batch bottle roll controls are different for the batches of lactose used (Table 13, Table 14 and Table 15), with IGL-1 and 200M-2 having similar but faster growth compared to 200M-1. The explanation for lactose batch PSD variation is not entirely apparent as all batches are particle size fractions of pharmaceutical grade lactose, which are subsequently dissolved in water to the same experimental concentration (Table 17). It is speculated that the different batches may have varying levels of impurities. Total phosphorous in the three types of lactose used was measured by Hills Laboratories (Hamilton, NZ), as an indicator for lactose phosphate, a known lactose growth inhibitor. However, no significant difference was measured between the samples and the average total phosphorus amount measured was 30 parts per million (ppm).

| Sample ID | Phosphorus (ppm) | Type |
|---|---|---|
| 1 | 30 | 200M-1 |
| 5 | 30 | 200M-1 |
| 7 | 30 | 200M-1 |
| 3 | 40 | 200M-2 |
| 6 | 30 | 200M-2 |
| 8 | 30 | 200M-2 |
| 2 | 30 | IGL-1 |
| 4 | 30 | IGL-1 |
| 9 | 40 | IGL-1 |

Table 22 Phosphorus results for the three types of lactose used

The 6 hour batch control growth rate distribution data was used in the theoretical model predictions and if the growth rate distribution of feed crystals is changed, the final product model PSD predictions differ. Figure 111 shows the theoretical CSC product crystal diameter plotted versus growth rate constant for 200M-1 (smaller $k_{gs}$ on average) and IGL-1 (larger $k_{gs}$ on average). As $k_{gs}$ is decreased, more crystals reach the height limitation line, based on the height of the column=3.5 m; crystal is lost to the waste stream if they move past this line. The

net result is a size limitation is imposed on the crystals within the height limitation zone. Significantly decreasing feed nuclei $k_{gs}$ values mean a greater proportion of product crystals are obtained from the height limited area of the graph. This will give a smaller range of crystal sizes that can enter the product stream, and decrease the $d_{10}$, $d_{50}$ and $d_{90}$.

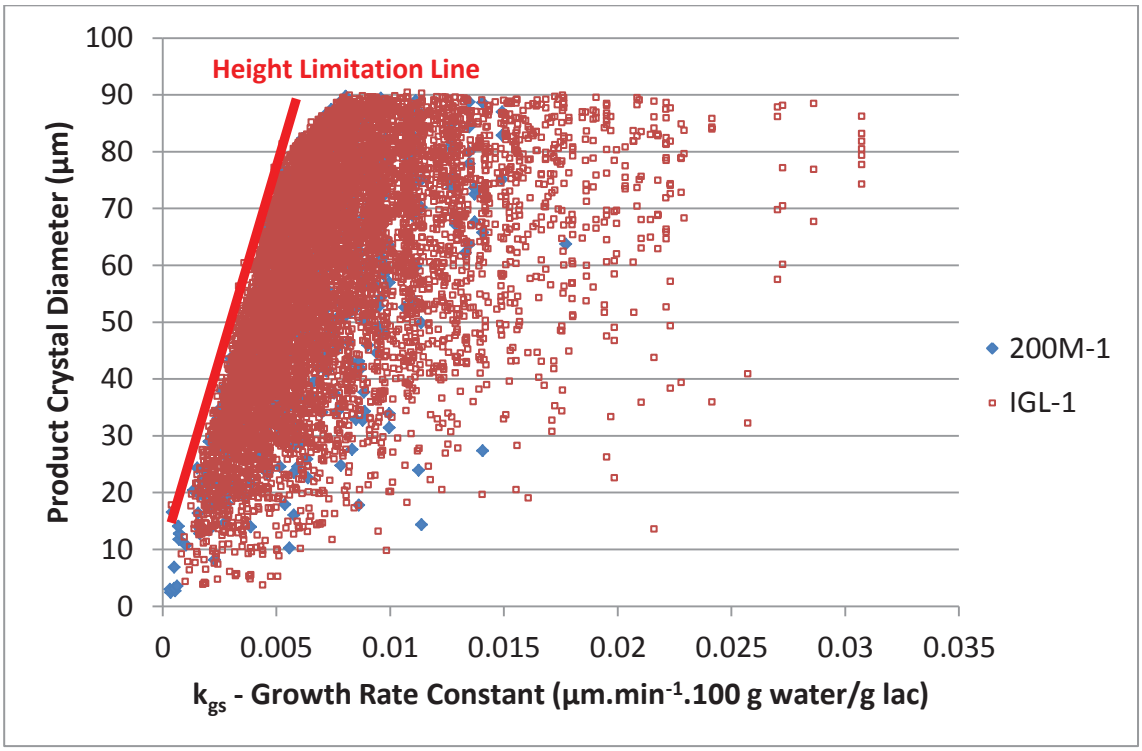


**Figure 111 Theoretical CSC product crystal size and corresponding crystal growth rate for 200M-1 and IGL-1 lactose**

### *7.5.3 Controlled Nucleation Event*

The precursor to the successfulness of the CSC, and other potential inhaler grade lactose (IGL) production methods, is a controlled nucleation event. The controlled nucleation event for the CSC was required to produce nuclei for the feed stream. A sufficient feed nuclei concentration was desired to produce measurable amounts of crystal and obtain product PSD results, measured in the Malvern MasterSizer, and investigate the effectiveness of the CSC method. As discussed in Section 5.4.4, once the batch impeller nucleation event had occurred, the supersaturation was lowered to just above the supersaturation limit so no further nucleation or growth would occur (very limited). The slightly supersaturated nucleated solution was then continuously concentrated to the growth concentration and fed into the CSC column. Ideally these two steps could be replaced with continuously nucleating a smaller volume of the highly supersaturated stream and diluting to the growth concentration. Adequately controlling the supersaturation growth concentration limits additional nucleation, which reduces the span. The batch impeller nucleation method developed was successful for reliably producing a

nucleated feed stream; shown by the consistent PSD measurements in the CSC results and bottle roll controls (Table 13, Table 14 and Table 15). If the feed nuclei concentration was too low, increasing the nucleation mixing time and speed prior to quenching would increase the number of nuclei formed.

### *7.5.4 Theoretical Model Experimental Deviations Summary*

The experimental CSC product span for the different types of lactose used is approximately 3 times the theoretical span predictions obtained using the CSC model described in Chapter 6. An analysis was carried out into what could be causing the product span deviations as well as potential solutions; this is summarised in Table 23.

| Issue/Model deviation | Effect relative to theoretical CSC model product predictions |
|---|---|
| Nuclei bypass with the feed into product stream | Lowers the $d_{10}$. However, feed stream crystal concentration is low relative to the product stream, much less than 10%, which is considered relatively insignificant. |
| Pump flow rate changed with time and tubing broke | Higher quality tubing was installed which can be successfully used for multiple runs. The flow appears to remain constant once the column is full. The product stream increases in flow by ~10% during filling. The feed stream appears to remain relatively constant. Changing feed concentration would cause density variation, and minor density variation, according to Stokes law, would cause significant flow velocity change relative to the overall assumed laminar column flow. |
| Laminar flow development around the feed nozzle | Feed region laminar development was split into two scenarios:<br>1) Plug flow regime was assumed for a small distance; calculated to cause a very minor increase in the $d_{50}$, and span stays approximately the same.<br>2) Fully mixed region of fluid; such as in the product cone itself, would cause minor increases in span. Radial particle redistribution could occur here. However previous dye tracer studies do not indicate any significant mixing is occurring. |
| Radial column particle movement caused by the laminar profile | Calculations into pressure differential acting across a spherical particle under laminar conditions show radial movement inside the column when rising or settling to be insignificant.<br>Convection currents appeared to be occurring and insulation was installed after linking these effects. From 3 observation points radial movement no longer appeared to be occurring, but the product PSD remained the same. |
| PSD of input nuclei | PSD of nucleated feed stream remains relatively constant with time, but the concentration decreases with time, a lower concentration reduces particle-particle interactions in column. The theoretical CSC model solved with and without feed nuclei diameter input did not alter the product PSD and span significantly. |
| Starting with an empty column | Span likely to increase due to empty column affecting flow patterns. However at steady state it is assumed the residual effects shouldn't be significant. |

| | |
|---|---|
| Surface crystal formation | Only minor surface crystal formation is evident, therefore not considered a major problem source. A vibrator was installed onto the product cone, which did not affect span but assisted in reduction of crystal surface build up. |
| Additional nucleation | Nucleation above the feed point could end up with larger particles; growth conditions used, absolute supersaturation of 8.2 g alpha lactose/100 g water, are in the upper metastable region, but below the spontaneous nucleation region. Additionally fluid is only experiencing very low Reynolds numbers; nucleation associated with mixing will be negligible. |
| Ambient temperature fluctuations | The column was insulated, so the net effect on the column was decreased. Any significant column fluctuations will likely be coming from the feed stream temperature and flow variation. |
| Low nuclei number input into the column | Nuclei input are generally sufficient to get reliable 16 hour results. Too high and it is assumed hindered settling, column crystal volume concentration greater than 10%, and agglomeration will cause the span to increase. |
| Growth equation | The literature supported constant crystal growth equation with incorporated growth rate dispersion fits 6 hour batch data well (Table 10 and Table 11). An empirical relationship for a size-dependent growth rate was tested (Aamir, Nagy, & Rielly, 2010), $G=k_{gs}S_{\alpha}^{g1}(1+g_2d)^{g3}$, where G (µm.min) is rate of crystal growth, $S_{\alpha}$ (g lactose/100 g water) is absolute alpha lactose supersaturation, d (m) is particle diameter and $k_{gs}$ (µm.min.100 g water/g lac),$g_1$ (-),$g_2$ ($m^{-1}$),and $g_3$ (-) are growth parameters. This expression was put into the batch model and values changed to match 6 hour control values. When solved for the CSC model, it over estimated the $d_{10}$ and $d_{50}$, but more accurately predicted the $d_{90}$. A combination of growth rate dispersion and size-dependent growth mechanisms could be occurring. |
| **Hindered Settling and Agglomeration** | Particles settling may have the following interactions with rising particles:<br>- move column radius position<br>- shadow, form agglomerates or clusters<br>A video of the column operation shows vertical settling and rising of crystals as expected, however with the occasional rapidly falling large particle; likely to be a agglomerate or cluster. Sampling at different heights along with the product stream was carried out, and microscope images showed a strong presence of agglomerates, and to a lesser extent clusters. |

**Table 23 Summary of investigation into CSC theoretical model deviations**

The investigation into theoretical CSC model deviations found that agglomeration was occurring in the column, which appeared to be a likely explanation for the increased span. Agglomeration occurs when individual crystals interact and subsequently grow together. Under normal batch crystallization processes agglomeration is reduced through the mixing of

the solution at much higher Reynolds numbers. Agglomerates are believed to cause an increase in the span through the following scenarios:

- $d_{90}$ increase, to above theoretically possible crystal sizes, by combing crystals grown to maximum size resulting in a "single" larger particle measured by the Malvern MasterSizer
- $d_{10}$ reduction, agglomerates are not limited to large crystals, smaller crystals which would otherwise be lost can combine and settle out in the low flow region of the column. Settling agglomerates can collect smaller crystals which will not necessarily join to the agglomerate

On a number basis, calculations revealed a very small number (~0.5%) of large crystals can double a volumetric span (Appendix A.7). Agglomerates are considered undesirable and the possibilities of removing them were investigated:

- stopping them from developing in the column would be the ultimate solution, having internal mixing sections or periodic exposure to ultrasound could assist in reducing aggregate formation
- post column product stream processing options such as breakage or removal are also available

### *7.5.5 Agglomeration Solutions*

Under normal settling conditions, agglomerates were found at all measuring positions within the CSC column. Stopping agglomeration from occurring while maintaining laminar conditions is difficult, but separating agglomerates once formed is feasible.

The following column locations, as depicted in Figure 112, could incorporate a method to break agglomerates into individual crystals:

1. Below the feed, this could include the product stream itself, previous tests with product stream ultrasound show the span was reduced from 1.4 to 1.3, but it also reduced all particle sizes.
2. Above the feed, agglomerates would break into small and large crystals, smaller crystals would be reincorporated into the upwards fluid flow, remaining single crystals that are large enough to oppose upwards fluid flow, will settle into the product stream, as per normal.

3. Middle of the column, this provides similar processing to location 2, but not all crystals reach this height, furthermore the settling distance below this point would allow for agglomerates to reform.
4. Top of the Column, similar processing to location 3, except the majority of crystals do not reach this height.

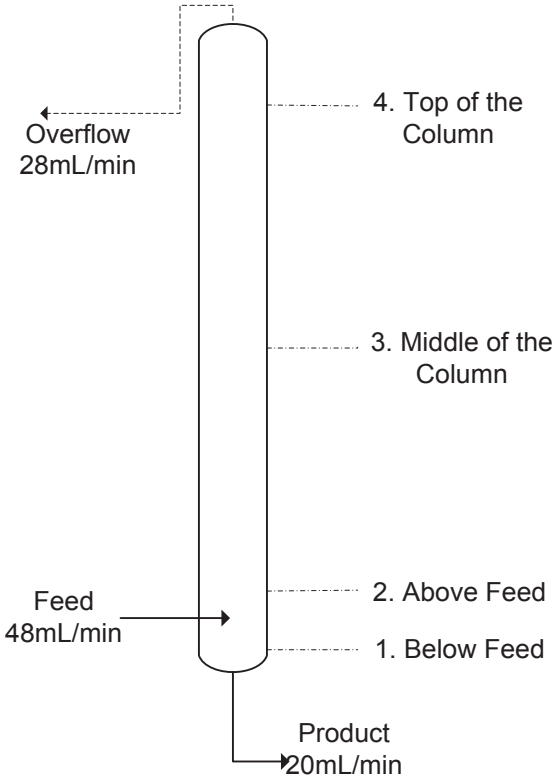


Figure 112 Potential agglomeration reduction locations

Location two is considered the best position to target the separation of agglomerates, and potential span improvement.

Ultrasound application to the product stream was shown to separate some of the agglomerates into individual crystals, therefore the application of ultrasound at Position 2 would be a potential agglomerate reduction solution, providing the column conditions above this point are not significantly changed.

Ultrasound Effect on Column Temperature:

Experimental tests carried out with a 1 kW ultrasonic probe operated at 20%, and inserted approximately 1 mm into 200 mL of water contained in a 250 mL beaker (placed on polystyrene) resulted in a heat transfer rate of 60 W. Stokes law shows minor temperature variations can cause density changes promoting unwanted mixing in a laminar setup; any temperature change above 0.2°C will be considered significant. A simplistic approach shown

below was taken to roughly estimate the heat transfer that could potentially occur if the ultrasonic probe was operated inside the column. Using column conditions of $Q_f$=30 mL.min$^{-1}$, $\rho_f$=1127 kg.m$^{-3}$ and neglecting heat transfer from the heated fluid, the temperature increase, $\Delta T$ (°C), in fluid flowing past a continuously operating ultrasonic probe can be estimated:

$$q = m_{Q_f} C_p \Delta T$$

$$\Delta T = \frac{q}{m_{Q_f} C_p} = \frac{0.06kW}{0.00056\ kg.s^{-1} * 3.32\ kJ.kg^{-1}°C} = 32°C$$

where $q$ (kW) is energy, $m_{Q_f}$ (kg.s$^{-1}$) is the feed mass flow rate and $C_p$ (kJ.kg$^{-1}$°C) is the fluid specific heat capacity.

Temperature change by continuous ultrasound is significant, much greater than 0.2°$C$, and not acceptable for direct column use.

The probe could potentially be setup to act periodically on a zone of fluid. If the probe was operated for 1 s every 320 s, this would cause a 0.1°C increase. In 320 s approximately 160 mL of fluid would have passed. In a 75 mm diameter column this corresponds to a height of 36 mm (the probe tip diameter was 24 mm). Although all column fluid could potentially be treated, settling crystals above 55 µm in size would be missed. A 55 µm crystal settling velocity of 0.23 mm.s$^{-1}$ less the average upwards fluid velocity of 0.11 mm.s$^{-1}$ equals 0.12 mm.s$^{-1}$. This corresponds to an average distance moved of 36.4 mm in 320 s. A 100 µm crystal would move 203.9 mm in this time. The ultrasonic power level tested also caused mixing and cavitation, and it would be difficult to prevent these affecting the laminar flow profile in the column.

An alternative method for online agglomerate destruction was proposed; see Figure 113.

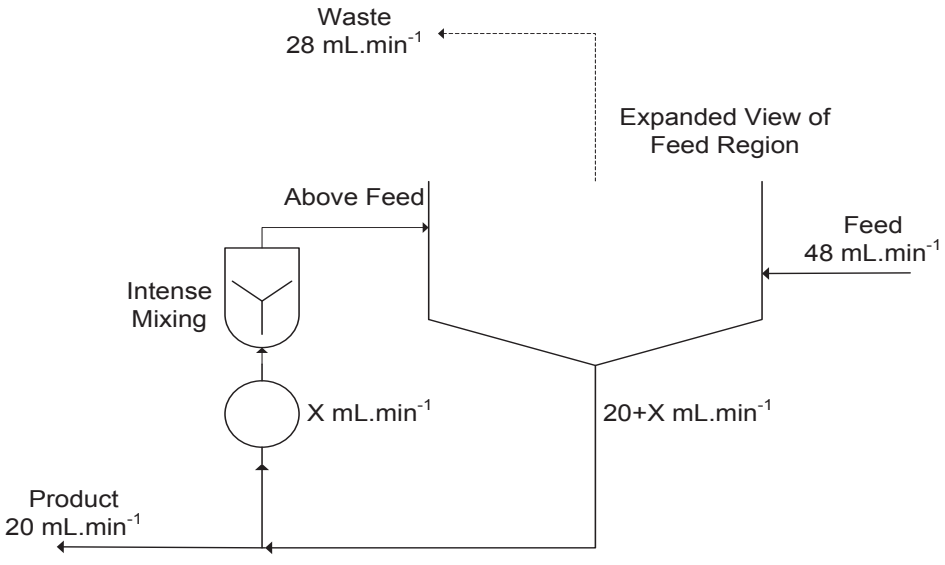


**Figure 113 Potential agglomeration destruction recycle loop design**

This method processes flow coming from the product stream and recycles it back into the column just above the feed. The recirculation loop velocity will be high preventing crystals from settling out. This effectively means the entire section of fluid below the insertion point will become a fully mixed vessel, where crystals exit after a known residence time. Crystals exit at 20 mL.min$^{-1}$ through the product stream, or are re-inserted into the column at 28 mL.min$^{-1}$, whereby small crystals will rise and grow, and the larger crystals will settle back into the recirculation loop. Before implementation of the recycle loop is carried out, the CSC theoretical model needs to be revised to assess the effect of agglomeration and any subsequent reduction.

## 7.6 Conclusions

A reliable continuous settling crystallizer setup was developed. Different batches of lactose were used in the continuous settling crystallizer experiments and found to have statistically different inherent growth rates, calculated through the bottle roll controls. For the continuous settling crystallizer run conditions of a net 28 mL.min$^{-1}$ vertical column flow and absolute alpha supersaturation of 8.2 g/100 g, IGL-1 had a product span of 1.49±0.04 and $d_{50}$ of 69.1±2.4 µm, 200M-1 had a product span of 1.41±0.02 and $d_{50}$ of 53.8±1.6 µm, and 200M-2 had a product span of 1.54±0.02 and $d_{50}$ of 78.2±2.9 µm.

The continuous settling crystallizer product stream crystal concentration was very low, at less than 0.1%; however the aim was not maximisation of yield, but proof of concept. Maximising yield is expected to cause hindered settling and an increase of the span. Agglomeration was proposed as the main point of difference with the theoretical continuous settling crystallizer model; potentially causing the increased product span. An agglomeration term needs to be added to the continuous settling crystallizer model to access whether implementing a agglomeration destruction recycle loop is worthwhile for improving the span.

The original crystallizer process aims were:

- A $d_{50}$ between 50 to 90 µm
- Span less than 1
- Be reproducible
- Have very low levels of contaminants (required for a pharmaceutical product)

All aims had been met except for the second, a narrow PSD, where the span is 1.4 to 1.5; this compares to a typical industrial crystallizer span of 2 to 2.5. Additional product stream processing, such as a hydrocyclone cut, is currently required to produce a span less than 1.

# Chapter 8 – Revised Continuous Settling Crystallizer Theoretical Model

## 8.1 Introduction

The continuous settling crystallizer (CSC) experimental product results were found to have a significantly larger $d_{90}$ and smaller $d_{10}$ and $d_{50}$ than the CSC theoretical model predictions. Consequently the experimental product span was approximately 3 times the theoretical predictions and greater than the objective span of 1. An investigation was carried out into the ***experimental effects*** which could be causing the span deviation from the ideal model conditions, and a summary can be found in Section 7.5. The key model discrepancy revealed from the investigation showed that crystal agglomeration was occurring inside the column. Initial explanations were based around the ability for agglomeration to produce larger crystals, increasing the $d_{90}$, and settling out smaller crystals, decreasing the $d_{10}$. In this section, a range of agglomeration conditions were theoretically modelled first to test this hypothesis before any modifications to the experimental CSC to include an agglomeration destruction recycle loop were carried out.

## 8.2 CSC Agglomeration Term

The agglomeration criteria developed represents the condition where crystals of all sizes can agglomerate. The particle column radius position interaction criterion, Equation 81, states that the particles column radius position must reside within 20% (assumption) of the first crystal's diameter. Under normal model simulations, individual particles column radius position does not change with time. The initial height interaction criterion (AGG1) was solved at each time step, Equation 82, assessing if particles were touching based on particle height position and diameter; as depicted in Figure 114.

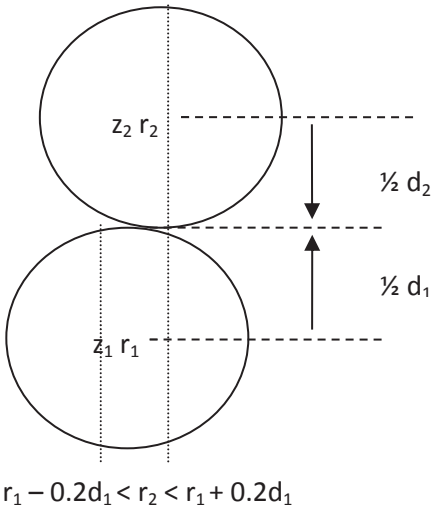


Figure 114 Agglomeration 1 (AGG1) column height and radius criteria

$$r_1 - 0.2d_1 < r_2 < r_1 + 0.2d_1$$

Equation 81 Agglomeration radius criterion (for both AGG1 and AGG2)

$$z_1 + 0.5d_1 \geq z_2 - 0.5d_2$$

Equation 82 Agglomeration 1 (AGG1) height criterion

Using AGG1 height interaction criterion potentially meant crystals could come in and out of contact during the time step movement and not be counted. The AGG1 height interaction criterion was then altered to assess if contact occurred during the time step particle movement, Agglomeration 2 (AGG2) height interaction criterion, Equation 83. Once the two particles interact, for simplicity their masses are combined and the same shape factor is assumed. The agglomeration predictions can be seen in Table 24; where $P_N$ (#) is the individual particle input per time step and PW (-) is the product to waste crystal volume ratio.

$$Using\ z_{1,t1}\ and\ z_{2,t1}: z_{1,t2} \geq z_{2,t2}$$

Equation 83 Agglomeration 2 (AGG2) modified height criterion

| Condition | $d_{10}$ (µm) | $d_{50}$ (µm) | $d_{90}$ (µm) | Span | AGG (%) | PW |
|---|---|---|---|---|---|---|
| **$Q_f$=28 mL.min$^{-1}$, $C_T$=42 g/100 g, 200M-1, t=16 hr, Δt=5 s, $P_N$=10** | | | | | | |
| Product, AGG0 | 51.2±0.4 | 73.2±0.9 | 85.9±0.9 | 0.47±0.01 | 0 | 3.1 ±0.2 |
| Waste, AGG0 | 6.7±0.0 | 22.5±0.1 | 36.7±0.3 | 1.33±0.02 | 0 | |
| Product, AGG1 | 48.2±1.1 | 70.1±1.6 | 85.4±1.1 | 0.53±0.04 | 55.7±0.1 | 2.0 ±0.1 |
| Waste, AGG1 | 6.8±0.1 | 22.7±0.3 | 36.9±0.5 | 1.32±0.02 | 2.2±0.1 | |
| Product, AGG2 | 50.8±1.6 | 73.3±1.4 | 85.5±0.9 | 0.47±0.03 | 38.8±2.7 | 2.3 ±0.2 |
| Waste, AGG2 | 6.8±0.0 | 23.0±0.4 | 37.4±0.3 | 1.33±0.03 | 2.4±0.1 | |

Table 24 Theoretical CSC agglomeration results, AGG0: no agglomeration, AGG1: agglomeration solved using Equation 82, AGG2 agglomeration solved using Equation 83

The agglomeration model particle size distribution (PSD) predictions did not differ significantly from normal model predictions. AGG1 criteria produced a larger number percent of product agglomerates than AGG2 criteria. The experimental product agglomerate percentage is not quantitatively known; however qualitative agglomerate estimates of the settled large product crystals imaged (Section 7.4) range from 30 to 60%, comparing well with predictions. After adding agglomeration conditions to the theoretical CSC model, larger particles can be produced, but agglomerates are removed from the column faster resulting in no significant increase in the $d_{90}$. It is possible the agglomerate settling rates are different due to a change in shape factor, but this has been ignored.

Different scenarios in which particles could interact to form agglomerates and whether it would be possible in the CSC column based on their settling rates can be seen in Figure 115. A downwards arrow represents falling and an upwards arrow represents rising (crystals are still growing). The largest crystals (high flow region) do not interact with each other to produce the

larger crystal sizes measured in practice. Slow growing small crystals in the low flow rate zones can agglomerate and settle out which would otherwise be lost to the waste stream. Overall the CSC theoretical model with agglomeration does not show a significant PSD effect than normal theoretical model conditions, but the agglomeration term is retained in the model because agglomeration does occur in reality. Further CSC theoretical model analysis is required to explain the decrease in $d_{10}$ and $d_{50}$, and increase in $d_{90}$, giving rise to the increased CSC product span.

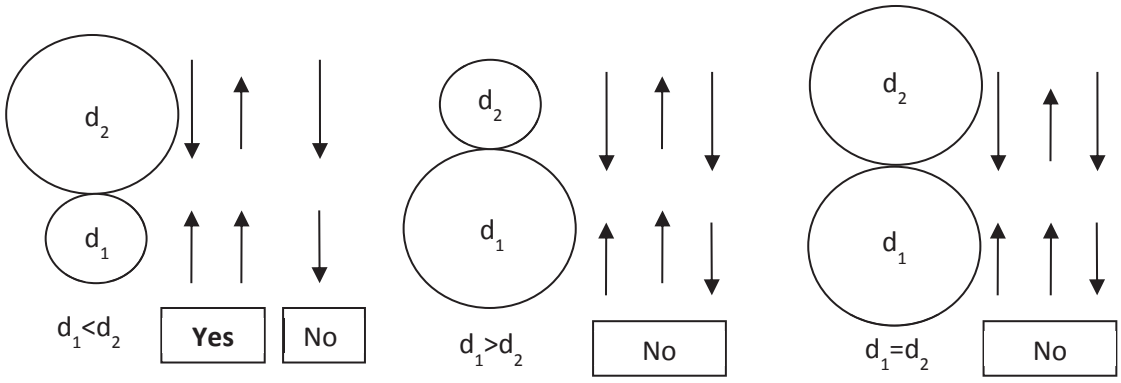


**Figure 115 Theoretical look into particle interactions (constant fluid velocity), only large settling or rising particles can interact with smaller rising particles**

## 8.3 CSC Theoretical Model Factor Analysis

Before making further modifications to the standard theoretical CSC model, it is important to discuss the results of the CSC theoretical model factor analysis. Table 25 summarises

| Stream | $d_{10}$ (µm) | $d_{50}$ (µm) | $d_{90}$ (µm) | Span | AGG% | PW |
|---|---|---|---|---|---|---|
| **CSC Experimental values 200M-1, t=16-18 hr** | | | | | | |
| Product | 22.5±0.6 | 53.8±1.6 | 98.2±3.0 | 1.41±0.02 | - | 11.3±4.3 |
| Waste | 10.7±1.0 | 23.0±1.5 | 46.6±3.4 | 1.56±0.12 | - | |
| **AGG2, t=16 hr, Δt=5 s,$P_N$=10, $d_i$, "Normal model conditions"** | | | | | | |
| Product | 50.8±1.6 | 73.3±1.4 | 85.5±0.9 | 0.47±0.03 | 38.8±2.7 | 2.3±0.2 |
| Waste | 6.8±0.0 | 23.0±0.4 | 37.4±0.3 | 1.33±0.03 | 2.4±0.1 | |
| **AGG2, t=24 hr, Δt=5 s, $P_N$=10, $d_i$** | | | | | | |
| Product | 50.6±0.4 | 70.2±0.5 | 85.1±0.3 | 0.49±0.00 | 48.3±0.6 | 3.5±0.1 |
| Waste | 7.1±0.0 | 22.7±0.1 | 37.4±0.2 | 1.34±0.01 | 2.8±0.0 | |
| **AGG2, t=16 hr, Δt=10 s, $P_N$=10, $d_i$** | | | | | | |
| Product | 51.9±1.1 | 73.7±1.2 | 86.1±1.1 | 0.46±0.01 | 22.1±2.6 | 2.6±0.2 |
| Waste | 6.9±0.1 | 22.9±0.6 | 38.1±0.9 | 1.37±0.03 | 1.3±0.1 | |
| **AGG2, t=16 hr, Δt=5 s, $P_N$=20, $d_i$** | | | | | | |
| Product | 49.9±1.0 | 73.1±1.0 | 85.7±1.0 | 0.49±0.03 | 42.0±1.7 | 2.2±0.1 |
| Waste | 6.8±0.1 | 22.6±0.5 | 37.3±0.7 | 1.35±0.02 | 3.8±3.7 | |
| **AGG2, t=16 hr, Δt=5 s, $P_N$=10, $d_i$=0** | | | | | | |
| Product | 51.8±1.0 | 73.4±0.9 | 86.5±1.3 | 0.47±0.03 | 32.2±2.5 | 3.3±0.2 |
| Waste | 10.3±0.1 | 25.1±0.3 | 38.2±0.3 | 1.11±0.01 | 1.0±0.1 | |

**Table 25 Volumetric flow based nuclei input theoretical model predictions, 200M-1**

solutions for longer time, decreased time steps and increased individual particle input. These were carried to assess any sensitivity issues which may be compromising predictions.

CSC theoretical model factor variations did not show significant changes to the product PSD. However, it is important to note that having no nuclei input diameter, $d_i$=0 m, better matches the experimental waste stream predictions and increases the PW crystal volume ratio. The input nuclei diameter was based on Malvern MasterSizer crystal volume measurements for the experimental nuclei feed stream at 0 hours of growth converted to a number distribution. This gives an inaccurate nuclei number distribution for feed particle size because a significant amount of un-measurable nuclei have yet to grow. This can be seen in Figure 116 when the crystal numbers for the feed at 0 hours of growth and the 4 and 6 hour controls are compared.

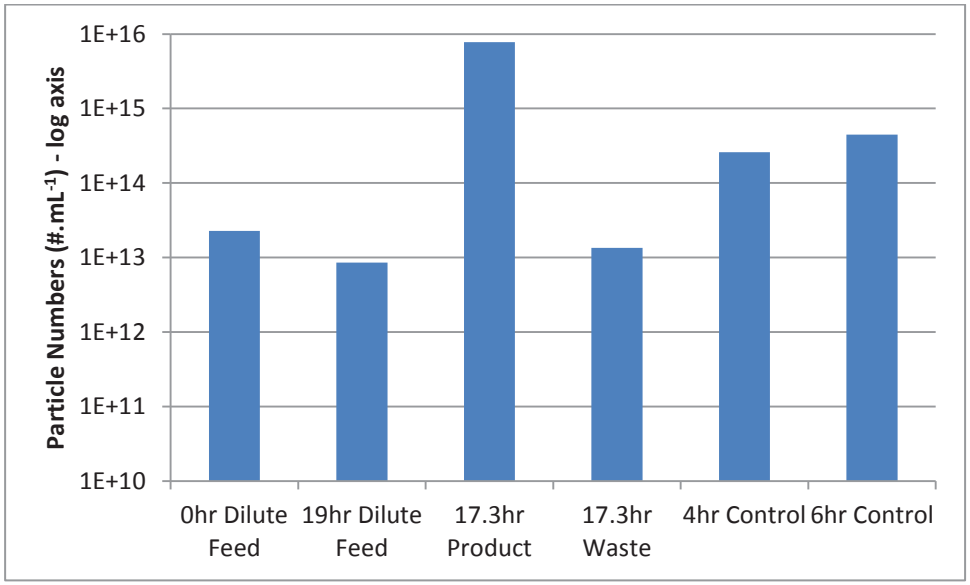


Figure 116 Comparison of crystal numbers for various CSC streams, Run 19

The reason why the theoretical model waste crystal PSD increases by removing the input nuclei diameter is as follows: Although the PW crystal volume ratio increases, the product by waste crystal *number* ratio decreases from $8.1\pm0.6\text{x}10^{-3}$ to $7.0\pm0.1^{-3}$. Without the starting diameter more small crystals enter the waste stream, as they have not grown large enough to oppose the column flow. The average waste crystal size decreased from 5.70±0.2 µm to 3.57±01 µm. Smaller crystals have a lower PSD effect on a volume basis; the $d_{10}$ and $d_{50}$ effectively increases.

## 8.4 CSC Theoretical Model Flow Analysis

A theoretical investigation was carried out into what ***internal flow conditions*** occurring in the column could be causing both small and large particles. A significant number percent of small crystals is required to lower the $d_{10}$, whereas only a small number percent of large crystals is

required to increase the $d_{90}$. Alterations were made to the core CSC theoretical model to test different flow condition hypotheses, and a significant difference was considered when the new theoretical product PSD predictions differed by at least 10%. Sections 8.4.1 to 8.4.6 summarise these results. To completely validate theoretical flow assessments, particle image velocity (PIV) should be carried out on the CSC experimental setup, however as explained in the previous chapter, the measurement apparatus was not available.

### *8.4.1 Random Column Particle Addition*

Particle height criterion for new nuclei entering in the column, normally set at Z=0 m, was modified to allow a small percent of nuclei particles to be inserted at random column heights. This theory can be split into two areas:

- hypothesis that nucleation is occurring because growth conditions are in the upper metastable region; no significant difference was found in predictions
- hypothesis that crystals attach to surfaces, grow, and are subsequently incorporated back into the settling region of the column; *potentially* occurring as crystal was seen to form on column surfaces, but this is a model fitting exercise to obtain the larger crystal sizes needed in the correct quantity. Detached surface crystals also do not explain the increased number of small crystals

### *8.4.2 Fully Mixed Sections*

Theoretical batch results coincide reasonably well with experimental CSC results, therefore it is hypothesized a batch mixing zone combined with a subsequent laminar settling zone may be occurring. The theoretical model was altered to have random particle movement within specific column height zones. The result of this causes an increase across all the particle size ranges. However, a fully mixed column is not observed in practice and this hypothesis is unlikely. The feed region is a potential mixing zone from the feed inlet, but this has been previously shown to only cause minor increases in the overall product PSD.

### *8.4.3 Slow Column Recycle Loop*

A fully mixed zone is unlikely, but it's hypothesized that a slowly mixed zone in the form of a recycle loop is plausible. An unbalanced slow and fast side in the column could be occurring as there is some evidence in practice for this with dye tests just above the feed region. The theoretical model was set up with a slow column side ($0.5u_f$) and a fast column side ($2u_f$). This setup is very complicated with many independent factors to take into account such as correct particle radial input within a side, assessing which particles recycle, and maintaining total flow

rates. Simplified predictions did not show a significant change in product PSD; however improved model fitting may alter these results.

### *8.4.4 Empty Column Fill*

In practice, the experimental column starts from empty, and no terms in the theoretical model account for this. It's hypothesized that laminar flow starts to occur once the column is full and mixing occurs during the fill stage. The theoretical model was altered to have random particle movement during the first 6 hours of column "filling" (~3/4 full), with subsequent laminar conditions. The predictions did not show a significant difference in the product PSD. In reality, the product stream should return to steady state equilibrium with time.

### *8.4.5 Waste Outlet Cone Crystal Recycle*

The waste cone area (with uneven surfaces) at the top of the column has the potential to be a mixed region, settling particles back into the column. The theoretical model was altered to recycle 80% of waste particles back into the column. No significant difference in product PSD occurred.

### *8.4.6 Faster and Slower Column Flow rates*

Normal fluid flow movement occurs according to Equation 80; particle net velocity equals fluid velocity ($u_f$) less terminal settling velocity ($u_t$). An initial assumption was that a faster or slower flow causes larger or smaller crystals. Model predictions carried out with faster flow rates achieved significantly larger particle sizes; increases in the product $d_{50}$ and $d_{90}$ occurred. It is noted that the CSC is height and growth limited and at faster flow rates more crystals are lost from the column into the waste stream. Model predictions carried out with slower flow rates achieved significantly smaller particle sizes; decreases in the product $d_{10}$, $d_{50}$ and $d_{90}$ occurred. A combination of fast and slow flow rates could lead to the experimentally measured span deviations.

## 8.5 Fast and Slow Zones

### *8.5.1 Two Column Model*

A CSC column with a lower flow rate produces smaller crystals and likewise a faster flow rate produces larger crystals, but a link between the two is required. It is hypothesized that channelling explains how a simultaneous decrease in the $d_{10}$ and increase in the $d_{90}$ can occur. A high velocity or channelling section in the column could be due to feed stream temperature or concentration change. Section 7.2.2 illustrated how minor changes in the fluid density

caused a dramatic increase in velocity relative to the average column fluid velocity. The net effect of channelling results in slower velocities elsewhere because the average fluid velocity must be maintained. The high velocity region will produce a larger sized crystal population and the slower velocity region will produce a smaller sized crystal population. To demonstrate the channelling idea, a simplistic two column model was developed. The fast and slow zones were separated into individual columns and product streams combined to predict a span; see Figure 117.

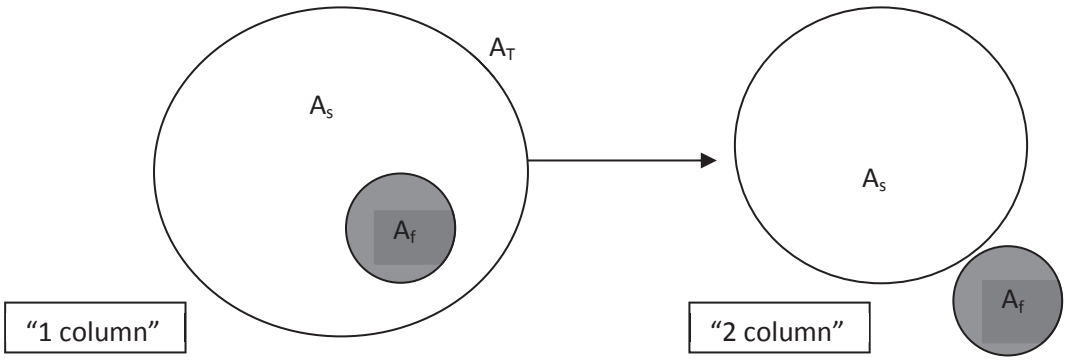


**Figure 117 Simplistic two column theoretical model schematic, shaded area represents fast velocity column**

The individual slow and fast column areas, $A_s$ ($m^2$) and $A_f$ ($m^2$), must equal the initial laminar flow column total area, $A_T$ ($m^2$), Equation 84. Each column flow profile is still represented by the standard laminar fluid profile, Equation 88 and Equation 89. The average fluid velocities of each column, $u_{fs}$ ($m.s^{-1}$) and $u_{ff}$ ($m.s^{-1}$), are altered in ratio to maintain total flow rate, $Q_T$ ($m^3.s^{-1}$), Equation 85. The slow column $u_f$ is divided by the slow column flow factor, $m_s$, Equation 86, and the fast column $u_f$ is multiplied by the fast column flow factor, $m_f$, Equation 87.

$$A_s + A_f = A_T$$

**Equation 84 Column total area**

$$u_{fs}A_s + u_{ff}A_f = Q_T$$

**Equation 85 Column total flowrate**

$$u_{fs} = u_f / m_s$$

**Equation 86 Slow column average fluid velocity**

$$u_{ff} = m_f u_f$$

**Equation 87 Fast column average fluid velocity**

$$u_{r,slow} = 2u_{fs}(1 - r^2/{R_T}^2)$$

**Equation 88 Slow column laminar fluid profile**

$$u_{r,fast} = 2u_{ff}(1 - r^2/{R_T}^2)$$

Equation 89 Fast column laminar fluid profile

A range of two column simulations were carried out using the 200M-1 growth rate data and Figure 118, Figure 119, Figure 120 and Figure 121 show the trends for changing $m_f$ with a constant $m_s$; a dashed lined is plotted to show the corresponding averaged CSC experimental PSD value.

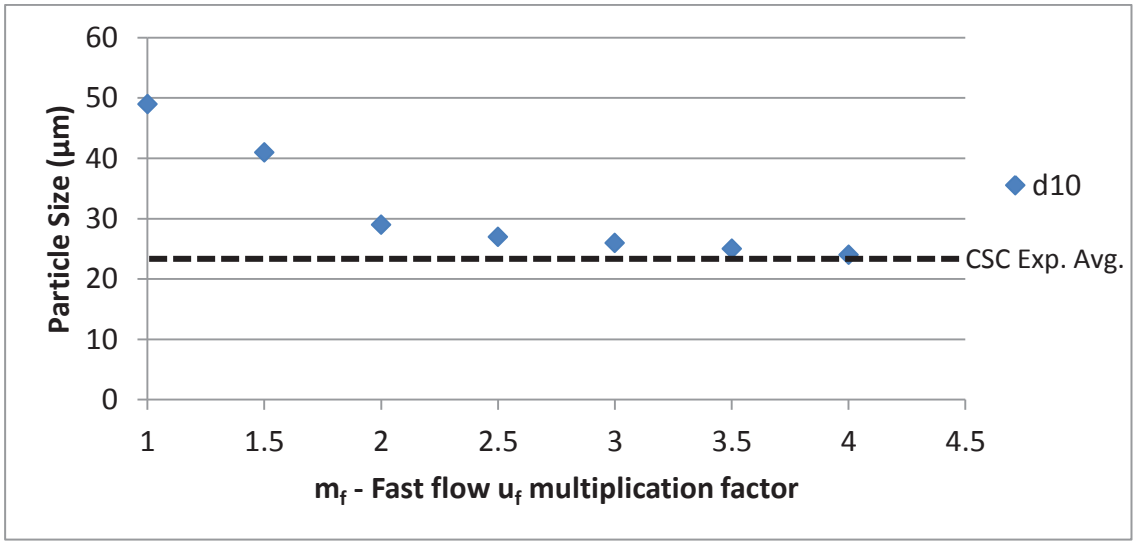


Figure 118 Two column theoretical model product $d_{10}$ particle size versus $m_f$; $m_s$ is constant at 7 (AGG1 used)

Increasing $m_f$ from 1 to 4 with constant $m_s$ causes the product $d_{10}$ to decrease, with a total reduction in particle size of ~25 µm; see Figure 118. The two column product $d_{10}$ prediction matching the CSC experimental product results occurs around $m_f$=4.

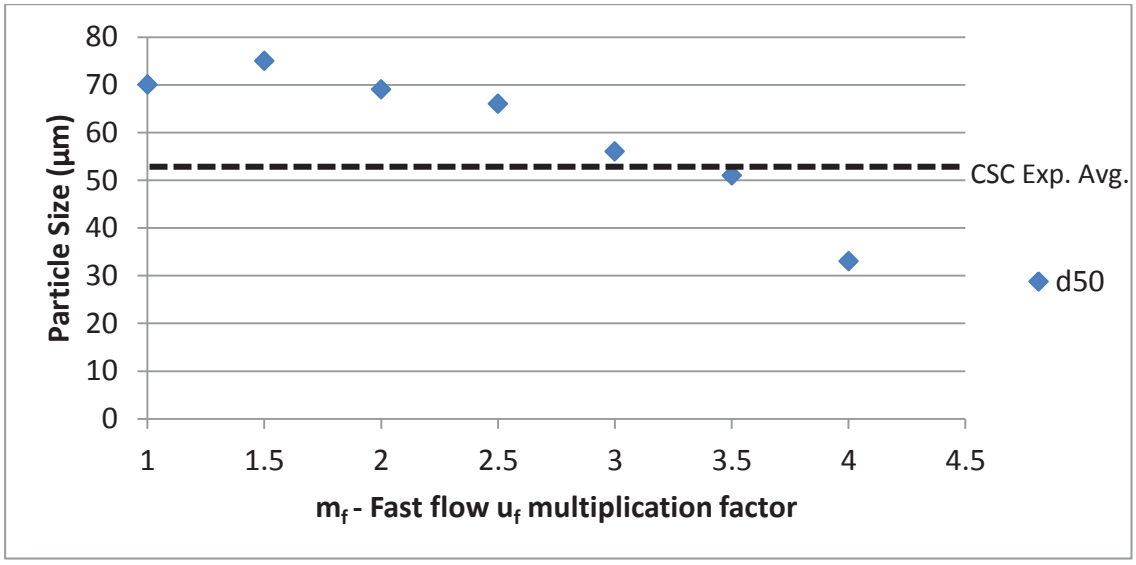


Figure 119 Two column theoretical model product $d_{50}$ particle size versus $m_f$; $m_s$ is constant at 7 (AGG1 used)

Increasing $m_f$ from 1 to 4 with constant $m_s$ causes the product $d_{50}$ to initially increase up to $m_f$=1.5 which subsequently decreases, with a total reduction in particle size of ~40 µm; see Figure 119. The two column product $d_{50}$ prediction matching the CSC experimental product results occurs around $m_f$=3.5.

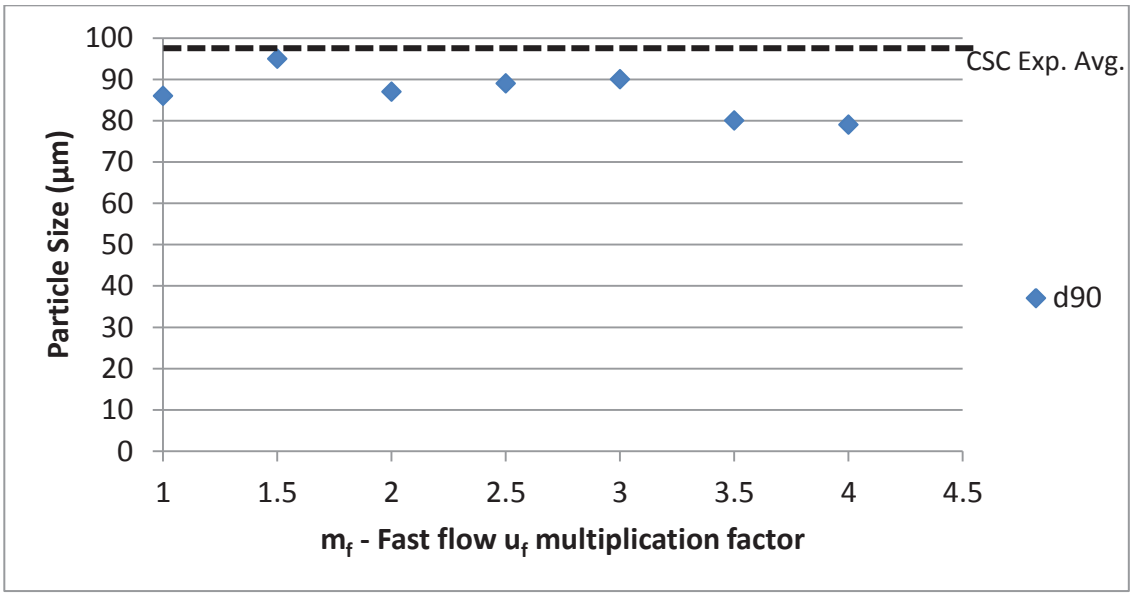


**Figure 120 Two column theoretical model product $d_{90}$ particle size versus $m_f$; $m_s$ is constant at 7 (AGG1 used)**

Increasing $m_f$ from 1 to 4 with constant $m_s$ causes an initial product $d_{90}$ increase up to $m_f$=1.5 which subsequently decreases, with a total reduction in particle size of ~15 µm; see Figure 120. The two column product $d_{90}$ prediction matching the CSC experimental product results occurs around $m_f$=1.5.

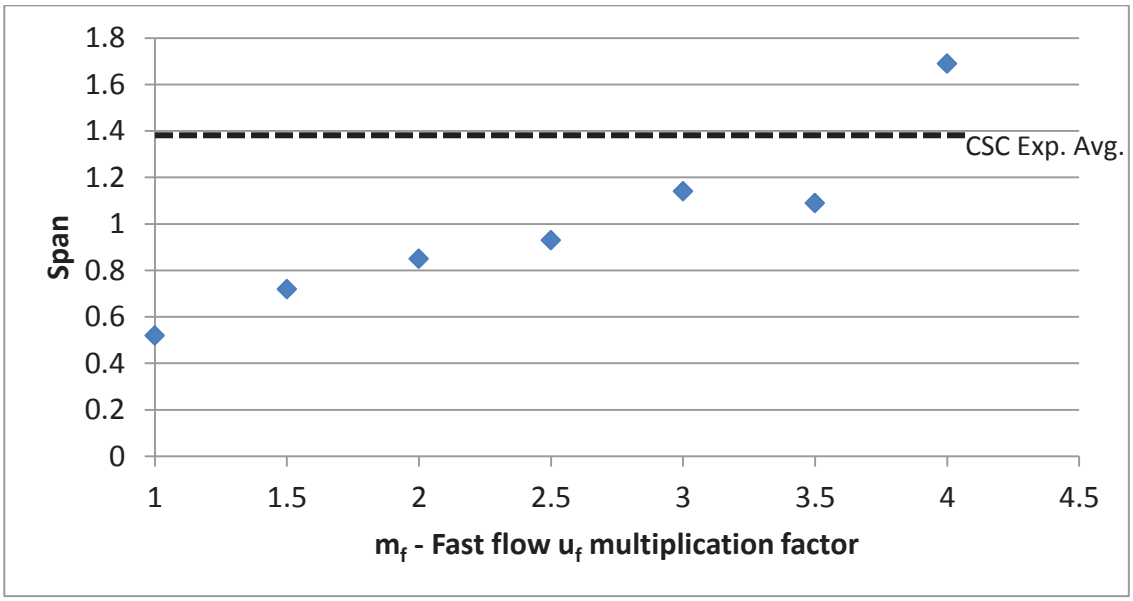


**Figure 121 Two column theoretical model span versus $m_f$; $m_s$ is constant at 7 (AGG1 used)**

Increasing $m_f$ from 1 to 4 with constant $m_s$ causes the product span to increase; see Figure 121. The two column product span prediction matching the CSC experimental product results occurs around $m_f$=3.5.

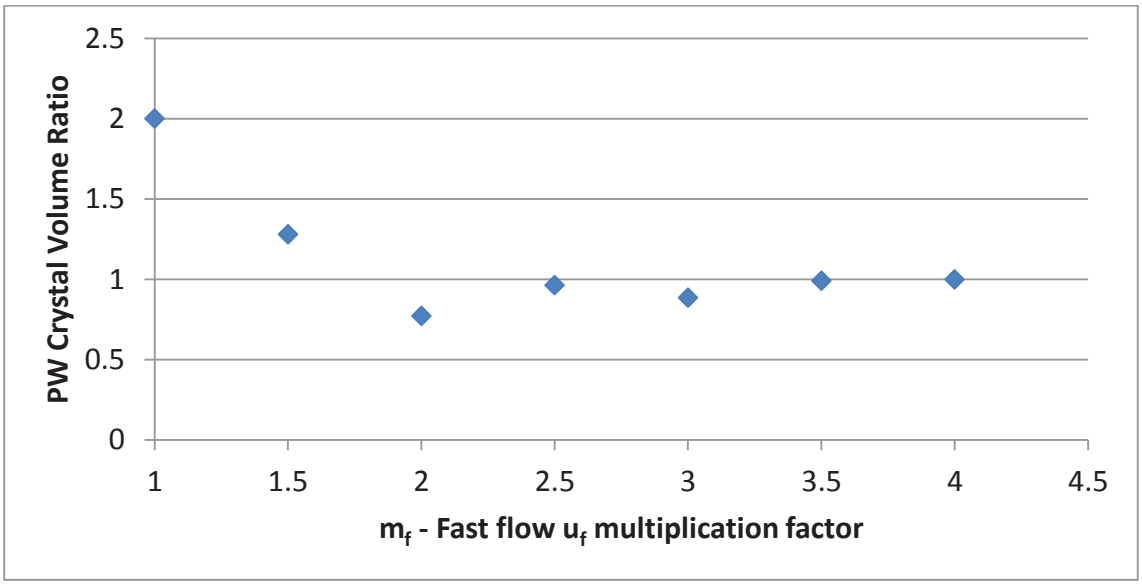


**Figure 122 Two column theoretical model PW crystal volume ratio versus $m_f$; $m_s$ is constant at 7 (AGG1 used)**

Increasing $m_f$ from 1 to 4 with constant $m_s$ decreases the PW crystal volume ratio; see Figure 122. No two-column theoretical condition matched the experimental PW crystal volume ratio. Increasing $m_f$ will decrease the fast column contribution because of washout, the viable area to settle crystals decreases, and therefore the chance of large crystals being formed decreases, and the $d_{10}$, $d_{50}$ and $d_{90}$ all decrease. Span increases but reaches a maximum once the slow column product crystals start to dominate. Above a fluid velocity equal to approximately 0.3mm.$s^{-1}$ no product crystals will be produced, unless there is an increase in crystal growth rate or column height.

A maximum value for $m_s$ exists below which the $d_{10}$ PSD is dominated by the fast column crystals and exceeds the experimental CSC product $d_{10}$ value. Increasing $m_s$ from this value will decrease the PSD but will also decrease the slow column contribution due to the lower flow rate, meaning a very narrow range exists for producing small crystals in a high enough volume percent to contribute to the product span.

When $m_s$=7 and $m_f$=3.5 the model particle size predictions are similar to the experimental results except for the $d_{90}$. The experimental PW crystal volume ratio was unable to be met at any of the model conditions tested; however these conditions provide a starting point for further column flow modifications.

### 8.5.2 Combined Column Model

The simple two column model revealed how the $d_{10}$ can be reduced with the slow column and the $d_{90}$ increased with the fast column. In reality a fusion of the two would occur, leading to the combined column model. Without advanced flow analysis measurements, such as particle image velocimetry (PIV), which was not available, the exact flow conditions of the experimental CSC column for a given height and radius position cannot be explicitly modelled; only approximated with justified reasoning. To simplify modelling calculations, symmetry in the combined column was assumed. The fast zone was assigned to the centre of the column with a slow outer zone; as shown in Figure 123. The fast zone could in fact occur anywhere in the column, and there was some evidence from the dye tests that a fast zone exists off centre. The location of the fast zone should not significantly affect the theoretical results because total area and flow rate conditions are maintained.

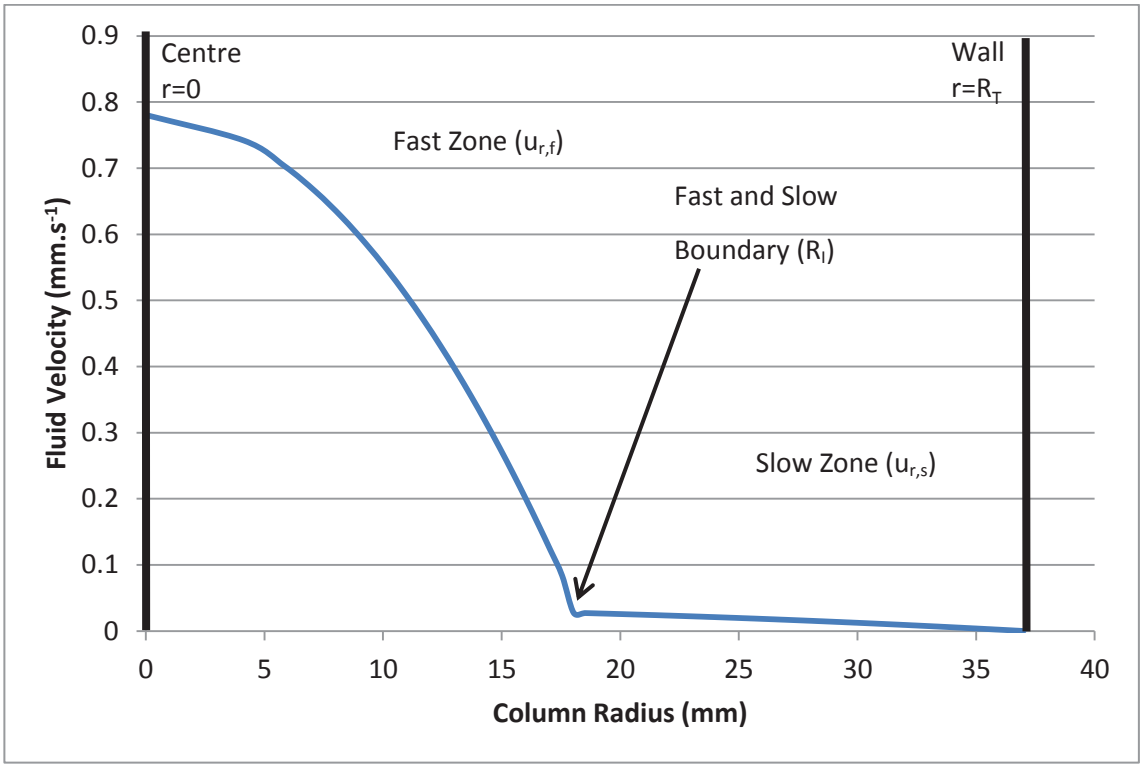


**Figure 123 Combined theoretical column model showing fluid velocity against column radius, $R_I$=18, $m_s$=6**

The fast zone velocity, $u_{r,f}$ (m.s$^{-1}$), Equation 90, has a modified outer radius, $R_F$ (m), Equation 92, to allow for interaction at the fast and slow zone boundary, $R_I$ (m).

$$from\ 0 - R_I;\ u_{r,f} = 2u_f m_f (1 - r^2/{R_F}^2)$$

**Equation 90 Combined column model fast zone velocity**

The slow zone velocity, $u_{r,s}$ ($m.s^{-1}$), Equation 91, is equivalent to the two column slow column velocity solved from $R_I$-$R_T$.

$$from\ R_I - R_T; u_{r,s} = 2u_f/m_s(1 - r^2/{R_T}^2)$$

**Equation 91 Combined column model slow zone velocity**

Through a rearrangement of Equation 90 and Equation 91 solved at $R_I$, $R_F$ can be expressed.

$$R_F = \sqrt{\frac{m_s m_f R_I^2}{m_s m_f - 1 - R_I^2/{R_T}^2}}\ (solved\ at\ R_I)$$

**Equation 92 Combined column model fast zone modified outer radius**

Fast zone flow rate, $Q_F$ ($m^3.s^{-1}$), Equation 93, and slow zone flow rate, $Q_S$ ($m^3.s^{-1}$), Equation 94, can be calculated through the integration of Equation 90 and Equation 91.

$$Q_F = u_f m_f A_I(2 - \frac{A_I}{R_F^2\pi})$$

**Equation 93 Combined column model fast zone flow rate**

$$Q_S = \frac{u_f A_T(2{R_T}^2\pi - A_T) - u_f A_I(2{R_T}^2\pi - A_I)}{m_s{R_T}^2\pi}$$

**Equation 94 Combined column model slow zone flow rate**

where $A_I$ ($m^2$) is the column area at the fast and slow interaction boundary.

Finally the slow zone division factor, $m_s$ (Equation 95), and the fast zone multiplication factor, $m_f$ (Equation 96), can be expressed through the rearrangement of their flow rate equations (Equation 93 and Equation 94).

$$m_s = \frac{u_f A_T(2{R_T}^2\pi - A_T) - u_f A_I(2{R_T}^2\pi - A_I)}{(Q_T - Q_F){R_T}^2\pi}$$

**Equation 95 Combined column model slow zone flow factor**

$$m_f = \frac{m_s R_I^2\pi Q_F - u_f A_I^2(1 + R_I^2/{R_T}^2)}{u_f m_s A_I(2R_I^2\pi - A_I)}$$

**Equation 96 Combined column model fast zone flow factor**

In the combined column theoretical model, specifying $m_s$ or setting $m_s$ to change with height, enables the calculation of $Q_S$, which can then be used to calculate $m_f$. $Q_F$ can then be calculated using $m_s$ and $m_f$. The fast and slow zone boundary can be altered which increases or decreases the flow rate in the corresponding zones; see Figure 124. The trend for increasing $R_I$ towards $R_I=R_T$, while maintaining $m_s$, will result in a decreased $m_f$. Maintaining $m_f$ will result in an increased $m_s$. The boundary can also be maintained and flow rates increased or decreased within each zone. If $m_s$ is increased, $m_f$ must also increase.

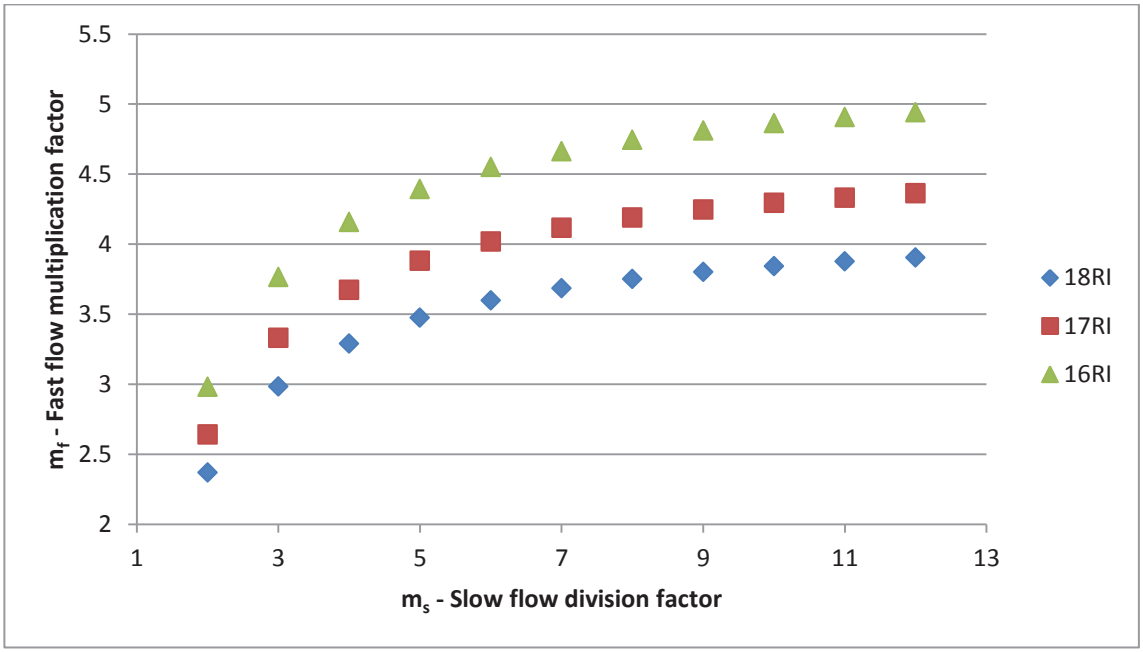


**Figure 124 Fast flow multiplication factor versus slow flow division factor for different radius interface boundaries**

Increasing $m_f$ and $m_s$ when $R_I$ is constant has two main effects on the product crystals; see Figure 125. Firstly, the viable area for crystals to settle in the fast zone is reduced due to larger fluid velocities occurring up to $R_I$. The contribution from the fast zone large crystals is reduced, and the $d_{10}$ and $d_{50}$ will decrease in a similar manner to the two column model. A continued increase in maximum crystal size does not occur because column height and growth rate limitation is already in effect. Secondly with $m_s$ increasing, the slow zone flow velocities decrease, producing smaller crystals and reducing the PSD. For the particular column model conditions, above $m_s=4$, all slow zone crystals settle out into the product stream.

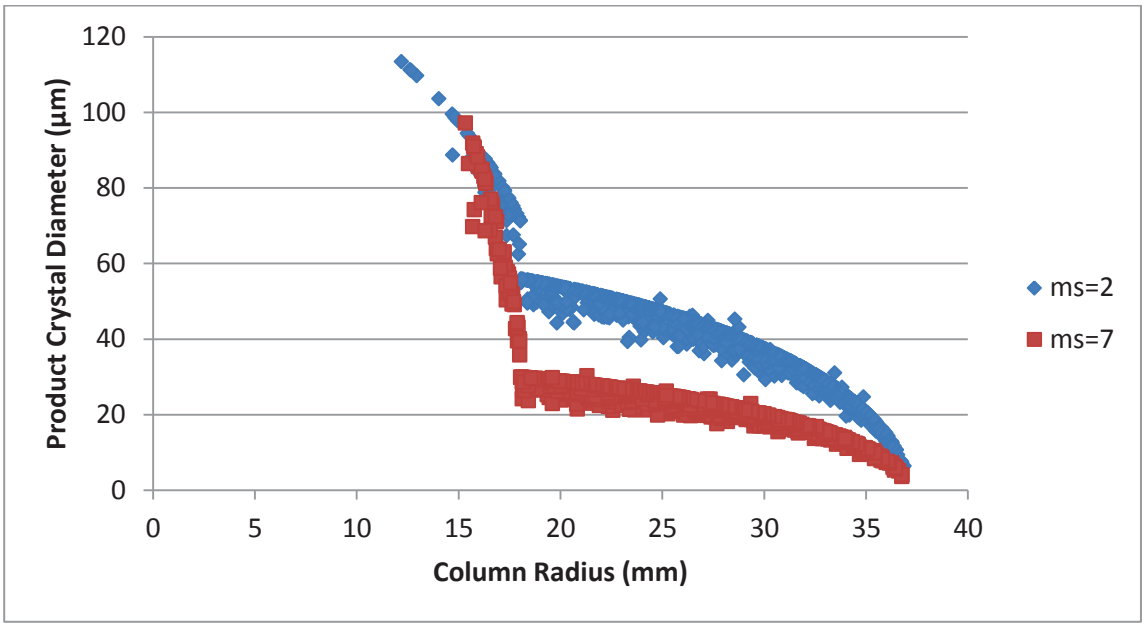


Figure 125 Combined column theoretical model showing crystal diameter against column radius for $R_l$=18 mm

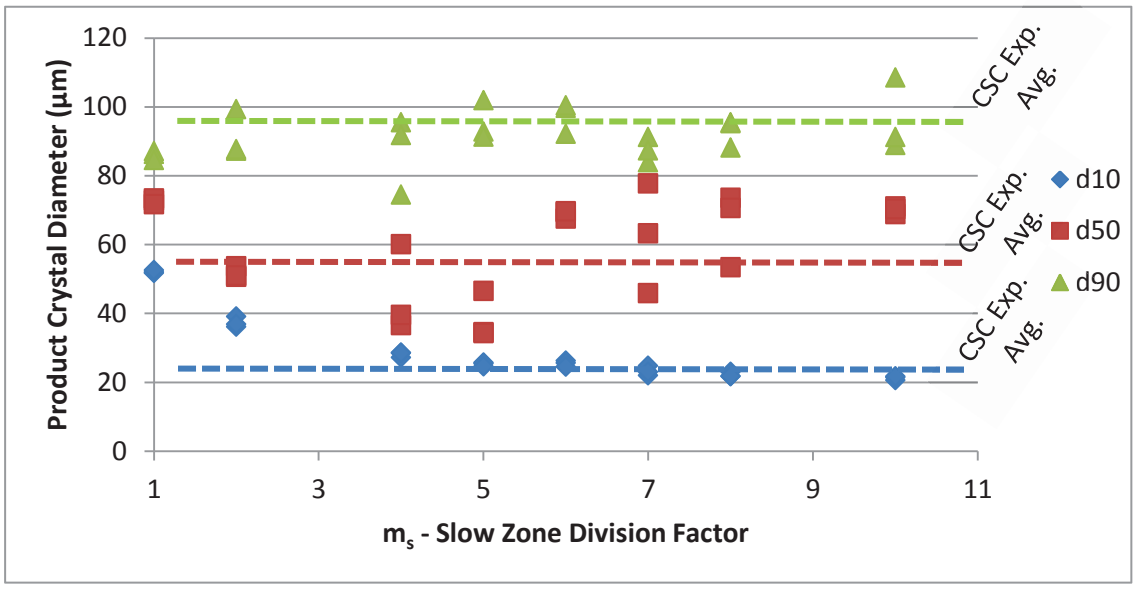


Figure 126 Product crystal diameter versus slow zone division factor for $R_l$=18 mm

Increasing $m_f$ and $m_s$ when $R_l$ is constant beyond $m_s$=3, results in an increased product $d_{50}$; see Figure 126. This can be understood when readdressing how a volumetric span is calculated; larger particles have the greatest influence. Although the slow zone particles are decreasing in size, their contribution to the volumetric span also decreases and a levelling off in the $d_{10}$ occurs. The $d_{50}$ and $d_{90}$ stay approximately the same, because although the fast zone velocity is increasing, no increase in particle size occurs. Fast zone product crystal contribution decreases with the PSD remaining approximately the same. The product particle size variation seen is due to the random functions built into the theoretical model, previously discussed in Chapter 6, and the chance of fast growers placed in a fast zone radius position. The averaged CSC

experimental value for the $d_{10}$, $d_{50}$ and $d_{90}$ are also plotted as a dashed lined with colour corresponding to the particle size. The experimental product $d_{10}$, $d_{50}$ and $d_{90}$ appear to be closely matched to the combined column predictions around $m_s$=5.5.

Increasing $m_f$ and $m_s$ when $R_I$ is constant for the waste crystals, Figure 127, causes a small decrease in the $d_{10}$ and $d_{50}$, and a small increase in the $d_{90}$. Crystals present in the waste stream primarily come from the fast zone. As flow rate increases, the crystals have less time for growth before reaching the waste stream, resulting in a smaller crystal size. The $d_{90}$ variation again is due to the chance of fast growing crystals being randomly placed in the fast flow column radius positions. Overall the combined column waste stream crystal sizes are smaller than experimental CSC waste results. Normal parabolic flow rate model conditions, $m_s$=1, predict experimental results well for the waste stream $d_{10}$ and $d_{50}$, although the $d_{90}$ is lower.

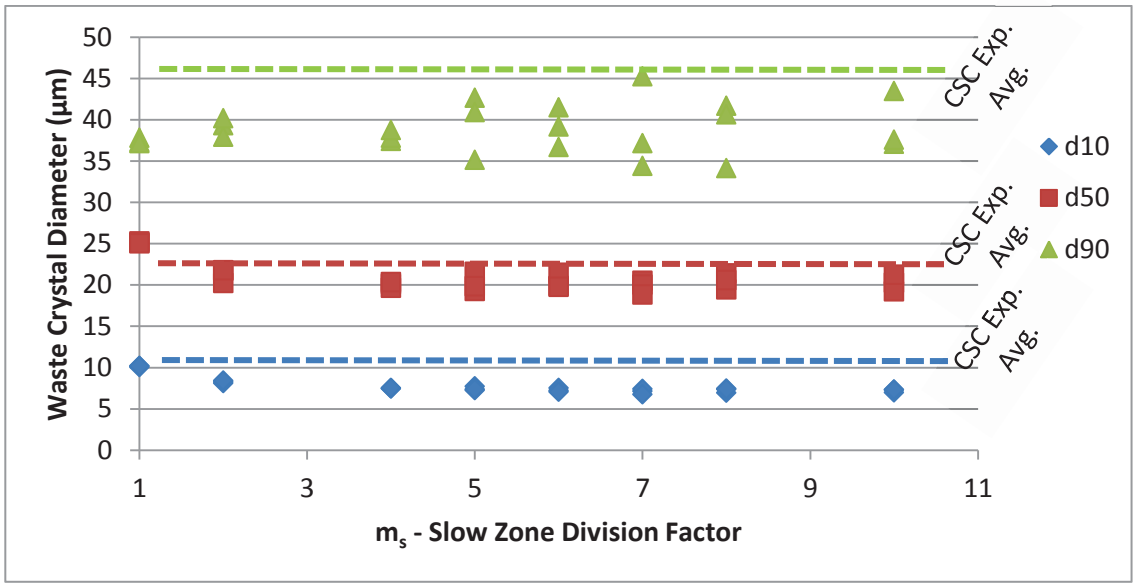


Figure 127 Waste crystal diameter versus slow zone division factor for $R_I$=18 mm

Increasing $m_f$ and $m_s$ when $R_I$ is constant decreases the PW crystal volume ratio (Figure 128 and Figure 129). An increased $m_f$ results in smaller crystals entering the waste stream from the fast zone, while an increased $m_s$ results in smaller slow zone product crystals. Decreasing $m_f$ and $m_s$ increases the viable area for the fast zone crystals to settle, and the contribution of large crystals increases until the fast zone velocity is sufficiently small, equal or lower than the slow zone velocity, meaning the larger crystals will no longer be produced. No combined column condition matches experimental PW crystal volume ratio. The combined column model PW crystal volume ratio is less than the normal column parabolic flow model, which is also less than experimental results.

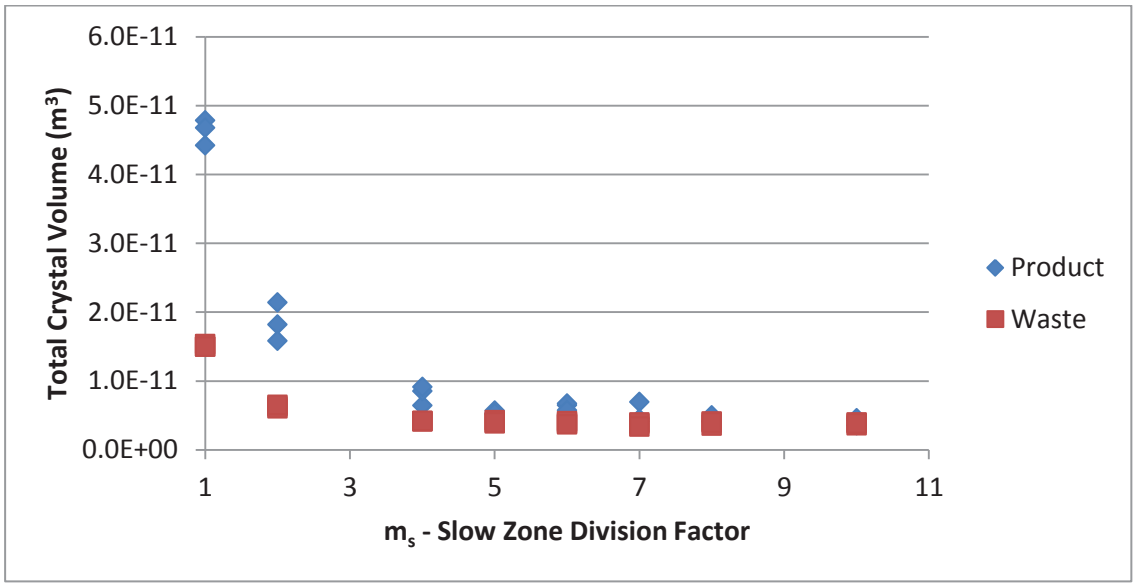


Figure 128 Total crystal volume versus slow zone division factor for $R_l$=18 mm

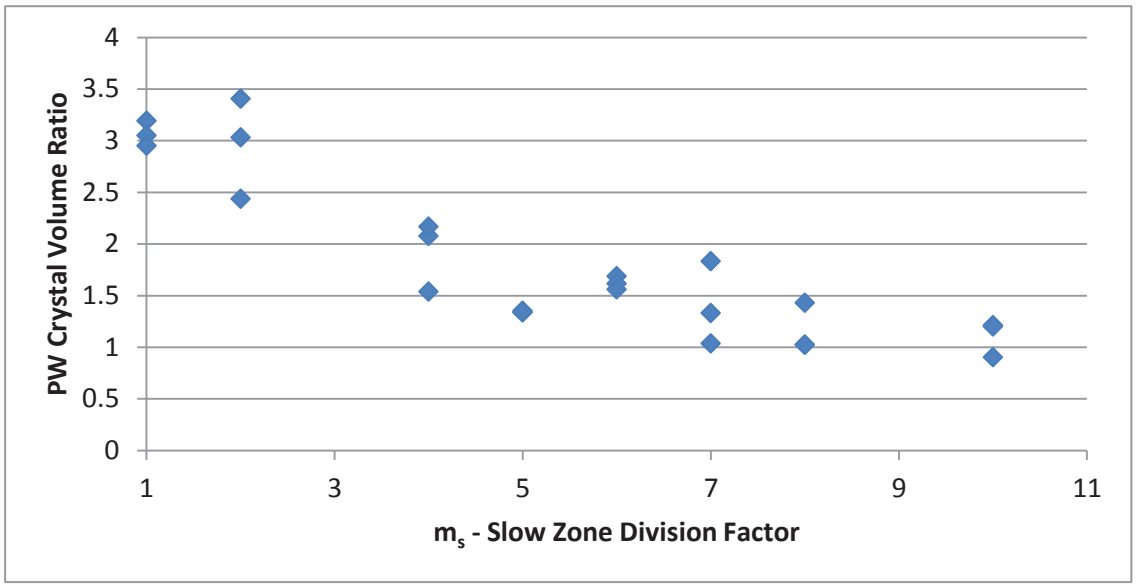


Figure 129 PW crystal volume ratio versus slow zone division factor for $R_l$=18 mm

Increasing $m_f$ and $m_s$ when $R_l$ is constant increases the product and waste span; as shown in Figure 130. This is due to the decreasing $d_{10}$ and $d_{50}$, and increasing $d_{90}$. When the $d_{50}$ starts to increase again the span starts to decrease. The experimental product span is matched at around $m_s$=5.5 and the waste span at around $m_s$=6. All model predictions are based on the span for crystals collected over the entire model solution time of 16 hours, and it could be argued that only product crystals within the last hour of model solution should be used because experimental results presented are from this time. While this may be achievable with the waste stream, the span calculations for the product stream are based on a fewer number of particles than the waste stream, and there is a random element to encountering large product particles due to the model conditions previously discussed. A large product crystal

sample size from the entire simulation time better represents model predictions. This is a limitation to monitoring individual particles; the correct particle amount to what occurs in practice cannot be monitored without very long simulation times.

The theoretical model results of a combined column with $m_f$=5.5 and $R_l$=18 mm closely represent the experimental CSC product results. The waste stream PSD and PW crystal volume ratio conditions are not met.

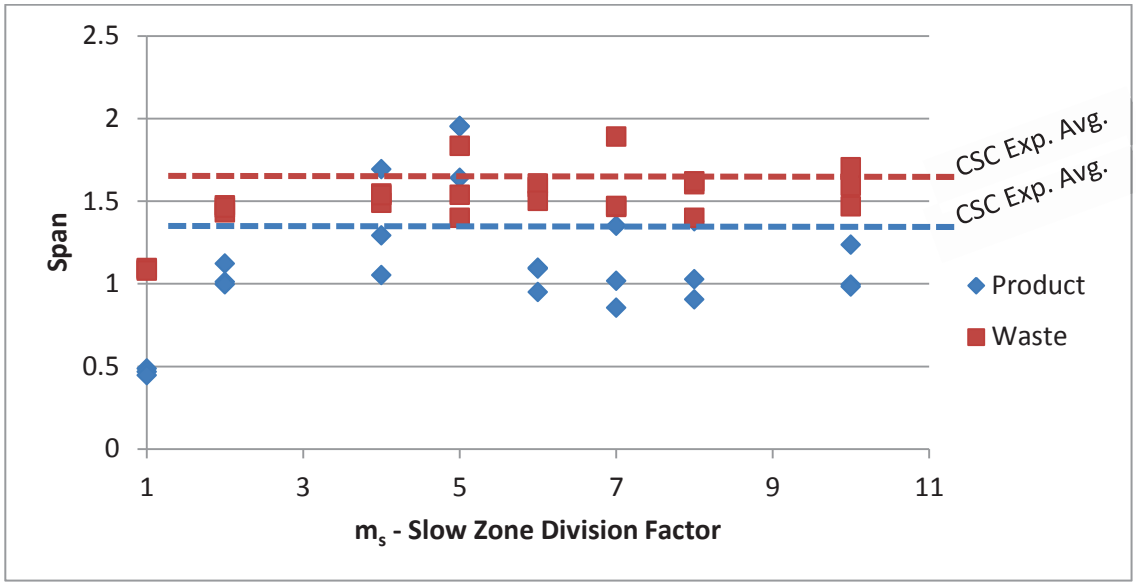


Figure 130 Span versus slow zone division factor for $R_l$=18 mm

The agglomeration term is a limiting factor. Column agglomeration mechanisms are unknown, and an approximate approach was taken (Section 8.2); if the two particles met the height and radius interaction criteria, they will agglomerate. This does not take into account interaction kinetics. Removing the agglomeration term will modify the results, as can be seen Table 26 with agglomeration criteria 2 (AGG2) and without agglomeration (AGG0).

| Stream | $d_{10}$ (µm) | $d_{50}$ (µm) | $d_{90}$ (µm) | Span | AGG% | PW |
|---|---|---|---|---|---|---|
| **AGG2, t=16 hr, Δt=5 s,$P_N$=10, 18$R_l$, 5$m_s$,** | | | | | | |
| Product | 25.9±0.6 | 65.0±6.8 | 95.5±9.4 | 1.07±0.06 | 56.1±2.4 | 1.7±0.2 |
| Waste | 7.3±0.1 | 19.6±0.3 | 37.0±0.9 | 1.51±0.07 | 0.1±0.0 | |
| **AGG2, t=16 hr, Δt=5 s,$P_N$=10, 18$R_l$, 7$m_s$,** | | | | | | |
| Product | 23.6±0.1 | 67.6±2.3 | 92.0±3.0 | 1.07±0.06 | 57.7±3.2 | 1.3±0.1 |
| Waste | 7.3±0.1 | 20.1±0.6 | 38.3±2.9 | 1.55±0.11 | 0.1±0.0 | |
| **AGG0, t=16 hr, Δt=5 s,$P_N$=10, 18$R_l$, 5$m_s$,** | | | | | | |
| Product | 27.7±0.7 | 57.3±14.3 | 87.9±10.8 | 1.07±0.10 | - | 2.6±0.5 |
| Waste | 7.4±0.1 | 19.9±0.9 | 37.5±3.8 | 1.52±0.24 | - | |
| **AGG0, t=16 hr, Δt=5 s,$P_N$=10, 18$R_l$, 7$m_s$,** | | | | | | |
| Product | 24.9±1.5 | 66.1±11.0 | 90.2±5.5 | 1.00±0.12 | - | 2.1±0.8 |
| Waste | 7.3±0.3 | 20.9±1.3 | 39.8±2.9 | 1.55±0.03 | - | |

Table 26 Comparison of combined column conditions with (AGG2) and without (AGG0) agglomeration

The most noticeable effect of removing the agglomeration term for the combined column model is to increase the PW crystal volume ratio, and increase the $d_{10}$ product particle size. The other particle sizes and spans remain approximately the same when taking into account the standard error. The effect of an agglomeration term acts to join crystals and settle them from the column faster than what would happen if allowed to individually grow normally to their terminal settling diameter. At $R_l$=18 mm and $m_s$=5 with no agglomeration, the number of product crystals was 405±7, whereas with agglomeration it was 310±15; this explains the drop in the theoretical model product $d_{10}$ with agglomeration.

### *8.5.3 Waste Stream*

The experimental CSC waste stream has a larger PSD and lower volume percent than the theoretical combined column predictions; potential explanations for these differences are discussed below:

- Fewer small particles reaching the top of the column may have been due to Oswald ripening, which reduces small particles. However, this is unlikely to occur in the column because the supersaturation is high. There is the potential for Oswald ripening to occur in the pre-nucleated dilute feed stream, as this is held at a low supersaturation; although, any reduction in the number of feed nuclei will affect the product and waste crystal concentrations equally.
- Random mixing on filling could be causing larger particles to reach the top, but as laminar column flow prevails, laminar particle settling should occur with run time.
- It is possible there was unaccounted agglomeration of small crystals or surface crystal attachment.
- Due to the uneven surface of the waste cone there may be column re-entrainment of waste-stream particles, column radius position rearrangement, longer growth time, more agglomerates, and larger particles exiting with the waste stream. However laminar flow conditions should mean eddies do not occur, and the comments in the previous statement would be unlikely.
- The Malvern MasterSizer measurements may have been inaccurate due to the very low waste stream crystal volume concentration. Consequently particles sizes less than a few microns may have been omitted from measurements and the Malvern MasterSizer reported a larger particle size than what was occurring in practice.
- Experimental CSC waste PSD was best predicted by normal parabolic column flow, indicating a transition from combined column channelled flow back to ideal laminar flow occurs; this is discussed in the next section.

### 8.5.4 Transition Back to Ideal Flow

The combined column model flow pattern was applied to the entire column height, which is unlikely to occur in practice. Feed concentration and temperature differences, attributed to channelling, will even out and decrease with height. There will be a gradual transformation to true laminar flow conditions, which may or may not be reached by the top of the column. The theoretical models tested predict a waste stream with smaller particle sizes as well as a larger volume percent than what occurs in practice. The initial laminar flow theoretical CSC column model waste stream results differed by less than 5 microns at the $d_{90}$, and the $d_{10}$ and $d_{50}$ were within the error bounds. The combined column CSC model waste stream results have a smaller $d_{10}$ and $d_{50}$. This is further evidence that a constant combined column profile is unlikely to occur all the way up the CSC column, and a transition to ideal laminar flow occurs.

The experimental CSC PW crystal volume ratio ranges from 7 to 15, theoretical CSC laminar flow model PW is 3.3 (product PSD doesn't match), and theoretical CSC combined column model when $m_s$=5 to 7 PW is 1.3 to 1.7 (waste $d_{10}$ lower). Any combined column model flow transition will alter predictions closer to the laminar flow CSC theoretical model PW crystal volume ratio prediction of 3.3. PW crystal volume ratio was found to increase by changing the following model factors: Increasing column height (Z>10% and PW>5%), increasing growth rate constant ($k_g$>10% and PW>20%), decreasing flow rate ($Q_f$<10% and PW>25%), and removing agglomeration.

In the transition to ideal laminar flow, the potential for radial particle movement occurs. The fast zone velocity decreases with height and the slow zone velocity increases. There will be a net radial velocity component from the difference in velocities with height, which will cause radial particle movement; as calculated by Equation 97.

$$\Delta r = (u_{f,2} - u_{f,1})\Delta t$$

**Equation 97 Transition flow net Particle radial movement**

If the combined column channelling flow transitions back to laminar conditions, there will be an increased chance for the fast zone crystals to grow larger and oppose the flow before exiting into the waste stream. There will always be a high velocity to overcome to enter the product stream, so the same sized crystals will be present in the product stream at any given fast zone radius. Overall, it is expected an increased number of large crystals will occur in the product and waste streams. The slow zone will produce larger crystals for the product stream as the terminal settling velocity to overcome increases with height. Consequently, the PSD is expected to increase, and the experimental product $d_{10}$ target will be hard to meet. To allow

for this, the slow and fast zones can be assumed relatively constant for a certain height; after this constant height zone the majority of slow zone particles will have settled. In the slow zone at $m_s$=5, no particles pass a column height of 2 m, therefore all particles in this zone settle out. After the constant flow zone, a transition to laminar flow can occur which affects only the fast zone, with the chance of producing larger waste particles. Table 27 shows predictions for the CSC combined column model with transition to laminar flow and for comparison a combined column solved with 50% faster growth rates (1.5$K_g$). Figure 131 shows the column height transition relationship used for $m_s$ and $m_f$, starting at a column transition height, $Z_t$ (m), equal to 2 m, where $m_s$=37.5e(-Z*0.84); the equation is fitted to give $m_s$=7 at $Z_t$ and decrease to $m_s$=2 at Z=3.5 m, $m_s$=1 would be ideal laminar flow, $m_f$ was calculated using Equation 96.

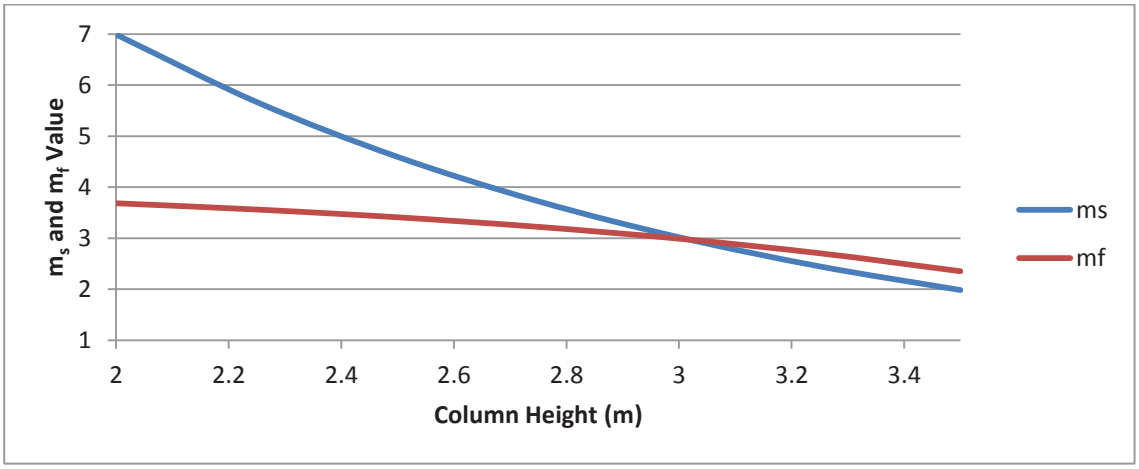


Figure 131 $m_S$ and $m_f$ height transition, $Z_t$=2, $m_s$=37.5e(-Z*0.84), starting with $m_s$=7

| Stream | $d_{10}$ (µm) | $d_{50}$ (µm) | $d_{90}$ (µm) | Span | AGG% | PW |
|---|---|---|---|---|---|---|
| **CSC Experimental values 200M-1, t=16-18 hr** | | | | | | |
| Product | 22.5±0.6 | 53.8±1.6 | 98.2±3.0 | 1.41±0.02 | - | 11.3±4.3 |
| Waste | 10.7±1.0 | 23.0±1.5 | 46.6±3.4 | 1.56±0.12 | - | |
| **AGG2, t=16 hr, Δt=5 s, $P_N$=10, Ckg.CR, 18$R_I$, 7$m_s$,** | | | | | | |
| Product | 23.6±0.1 | 67.6±2.3 | 92.0±3.0 | 1.07±0.06 | 57.7±3.2 | 1.3±0.1 |
| Waste | 7.3±0.1 | 20.1±0.6 | 38.3±2.9 | 1.55±0.11 | 0.1±0.0 | |
| **AGG2, t=16 hr, Δt=5 s, $P_N$=10, 1.5$k_g$, 18$R_I$, 7$m_s$,** | | | | | | |
| Product | 26.7±1.2 | 80.8±3.7 | 109.3±3.8 | 1.02±0.05 | 54.0±1.2 | 1.8±0.4 |
| Waste | 9.5±0.4 | 24.9±1.1 | 43.8±3.3 | 1.38±0.06 | 0.2±0.0 | |
| **AGG2, t=16 hr, Δt=5 s, $P_N$=10, 18$R_I$, 7$m_s$, $Z_t$=0.5 m, $m_s$=8.6e(-Z*0.42)** | | | | | | |
| Product | 24.0±0.8 | 67.7±2.2 | 89.6±7.1 | 0.97±0.06 | 58.8±2.9 | 1.2±0.2 |
| Waste | 7.7±0.1 | 20.2±1.0 | 38.4±3.3 | 1.52±0.11 | 0.1±0.0 | |
| **AGG2, t=16 hr, Δt=5 s, $P_N$=10, 18$R_I$, 7$m_s$, $Z_t$=2 m, $m_s$=37.5e(-Z*0.84)** | | | | | | |
| Product | 25.4±0.7 | 79.6±9.2 | 103.9±7.1 | 1.00±0.17 | 57.6±1.1 | 1.9±0.5 |
| Waste | 7.5±0.2 | 20.0±1.4 | 36.2±3.1 | 1.43±0.07 | 0.1±0.0 | |

Table 27 Theoretical combined column with agglomeration transition results

The flow conditions incorporating a transition back to laminar flow show minor increases in waste $d_{10}$ and no effect on $d_{50}$ and $d_{90}$ particle size. The $Z_t$=2 m transitioned flow also increases the PSD of the product stream, such that the $d_{50}$ is larger than what is experimentally measured. The PW crystal volume ratio increased for $Z_t$=2 m, although still less than normal CSC parabolic flow model predictions and experimental CSC results. Radial movement was predicted to be small, for a $Z_t$=0.5 m transition, maximum 0.33 mm movement occurred with a column average less than 0.01 mm. These predictions suggest a more complex transition flow pattern may exist than what is currently modelled.

## 8.6 CSC versus an Optimised Batch Crystallizer

There are marginal span improvements using the CSC than using the batch bottle roll control, resulting in a higher span than what was initially predicted which has been attributed to channelling. The batch bottle roll controls were 100 mL Duran bottle samples of the CSC feed stream collected at the beginning of the run, and rolled at approximately 5 rpm for a pre-specified growth time. The CSC experiments using IGL-1 lactose had a 6 hr batch bottle roll control span and $d_{50}$ of 1.74±0.17 and 53.7±4.7 µm, with a CSC product span and $d_{50}$ of 1.49±0.04 and 69.1±2.4 µm. The 200M-1 lactose had a 6 hr batch bottle roll control span and $d_{50}$ of 1.49±0.10 and 31.9±2.0 µm, with a CSC product span and $d_{50}$ of 1.41±0.02 and 53.8±1.6 µm. Although span initially increases with time for the 4 to 6 hour bottle roll controls, a stabilisation or relative growth appears to occur for the 6 to 16 hour bottle roll controls (Table 10 and Table 11), conforming with the Common Seed History concept proposed by Butler (1998).

Microscope images of the bottle roll controls after 6 hours of growth showed that they also contained agglomerates. This is not surprising since the low Reynolds suspension method used was designed to represent the growth conditions occurring in the CSC without settling. Through intensive mixing agglomerates could be reduced during growth (7.4.3 Agglomerates), but potentially at the expense of additional secondary nucleation. Reduction of agglomerates was shown not to significantly decrease the span; although a reduced number of agglomerates will likely be important for inhaler grade lactose particle characteristics, such as flowability.

The investigation into an online product stream hydrocyclone (Section 7.4), demonstrates it would be theoretically possible to concentrate the batch bottle roll controls along with the CSC product stream to a span of 1. It is important to note that less product crystal is retained when carrying out a hydrocyclone cut on a stream with a higher starting span than a lower starting

span; so the lowest possible starting span is desired when carrying out a hydrocyclone cut. A potential hydrocyclone CSC column setup is shown in Figure 132.

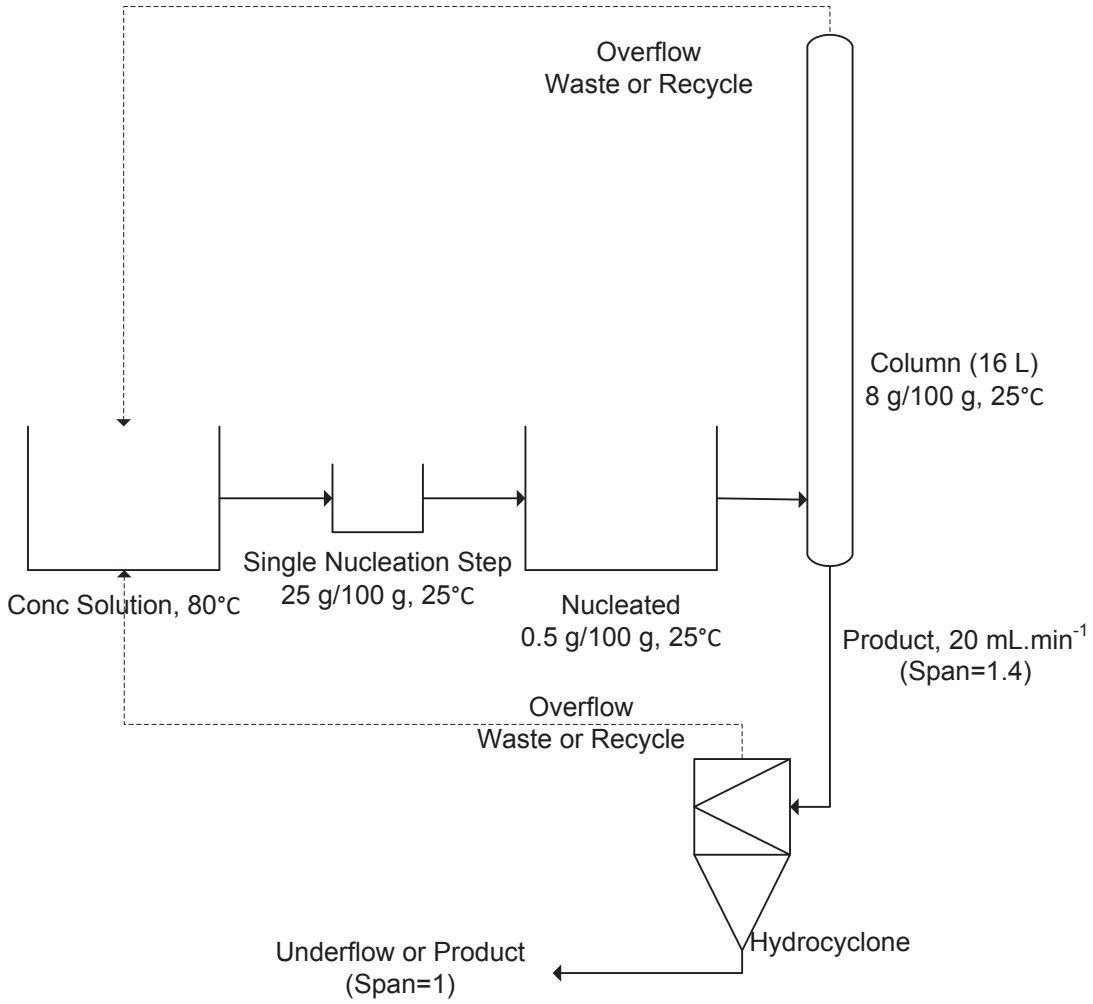


**Figure 132 Generalised CSC setup with a hydrocyclone**

The CSC setup which produced the bottle roll controls contained these key elements:

- single nucleation step; solution cooled to supersaturation, nucleation initiated and subsequently quenched
- Concentration step; concentrating nuclei stream to growth concentration
- Growth and settling; to obtain a desired $d_{50}$

The settling in the column was designed to achieve a single or narrow PSD, and in addition to the single nucleation step, the final growth concentration was chosen to reduce fines and secondary nucleation. However, as previously explained, these span improving aspects were counteracted by the proposed channelling occurring in the column.

If precise feed concentration and temperature control cannot be achieved to maintain laminar CSC conditions, it is proposed a fully mixed tank setup be used instead, with a subsequent

hydrocyclone step to remove fines. If a semi-continuous batch setup can be designed to produce crystals with a span of 1.4 or less, this would allow for smaller and faster setup times compared to the CSC column, while achieving similar or better yields, assuming most CSC overflow waste is recycled.

If the 3.5 m high 16 L CSC ran for 24 hours with a 20 $mL.min^{-1}$ product stream, and it takes approximately 10 hours for the column to fill and reach steady state, then 14 hours of production would correspond to 17 L of product. The relative efficiency of the CSC column could be improved by the following:

- decreasing the height; a fraction of slow growers would be lost, but a trade-off point would be reached
- increasing nuclei being fed into the column; hindered settling and agglomeration issues would likely increase

Alternatively, if an equivalent 16 L agitated batch vessel was set up to match the CSC span, it is predicted 12 hours would be needed to grow to a $d_{50}$ size of 60 µm, based on a 200M-1 6 hr bottle roll control $d_{50}$ size of 30 µm (time depends on inherent crystal growth rate). Two batches could be grown in 24 hours which corresponds to 32 L of product. If additional nucleation can be prevented in the batch case via correct growth concentration and agglomeration reduced via mixing, it may be possible to reliably produce a product stream with a similar PSD to the CSC. The advantage of the batch case, beyond additional yield, would be "easier" control conditions. The CSC is based on laminar settling so temperatures, flow rates and stream concentrations need precision control otherwise disruption to the column occurs, which also makes stream recycle difficult. In a mixed vessel these tight control conditions would not be a significant problem.

The concept for the CSC was developed from the ability of vertical inclined settlers processing batch grown stream to achieve a span less than 1. However, the agglomeration and crystal attaching to surfaces, seen in practice with the CSC, will likely increase this span. A well-mixed batch or continuously grown solution is possibly unavoidable, but exiting streams could undergo settling to remove very large particles and be passed through a hydrocyclone to separate smaller particles, see Figure 133. The focus would then be on optimising batch growth.

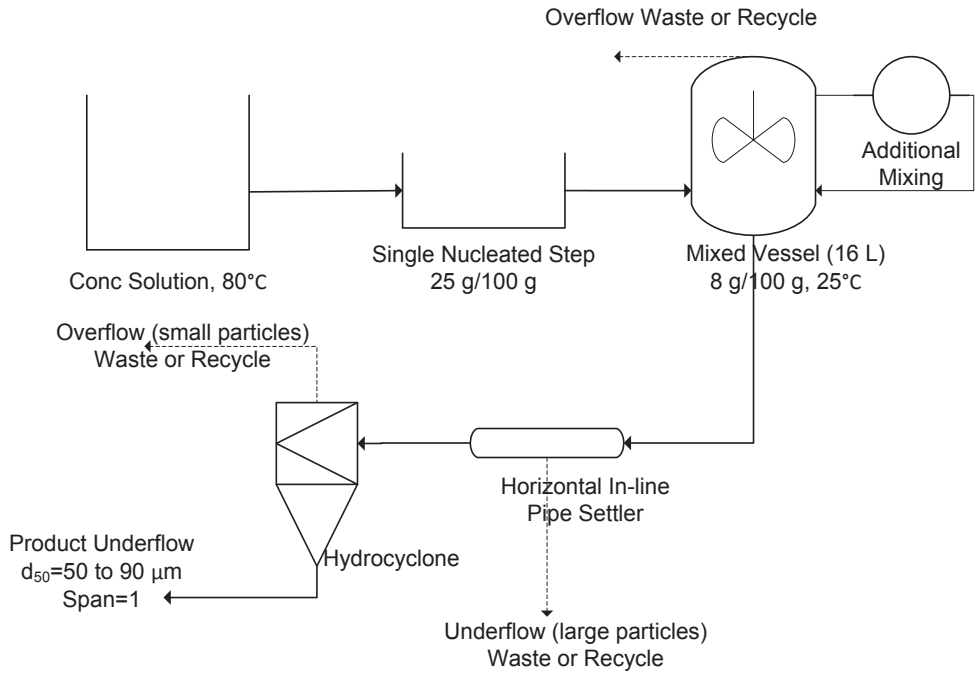


Figure 133 Generalised agitated batch setup with settling and hydrocyclone

### *8.6.1 Developing a Narrow PSD Batch Method*

For a typical industry batch crystallization method, solution is concentrated in a vacuum evaporator over a period of hours while being transferred to a growth vessel, seeds are added and a vessel cooling profile applied, as shown in Figure 134. Nucleation and growth occur during this cooling time. Because the product has a large span, additional washing and centrifuging is needed to remove entrained mother liquor.

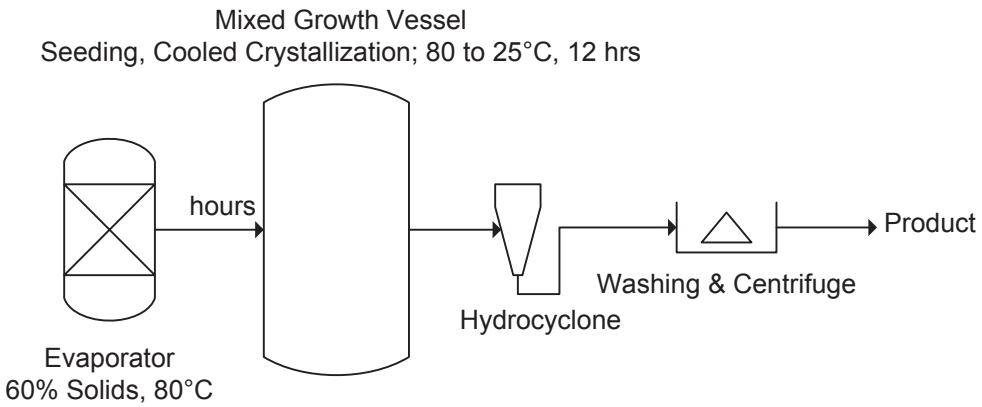


Figure 134 Typical industrial batch growth setup

Interpretation of Hartel's Patent (Application number: 11/284,531, Publication number: US 2006/0128953 A1, Filing date: Nov 21, 2005) controlled batch crystallization method is presented in Figure 135; developed to produce large crystals with the majority above 250 µm.

The nucleation step is distinctly separate from the growth stage, and therefore any secondary nucleation is said to be limited. Looking at the claims given, it is estimated spans in the region of 0.57 (450 µm - 250 µm / 350µm) can be achieved from this method. Product crystals are said to be more easily recovered as less mother liquor is trapped amongst large non-aggregated crystals. It is predicted a small span can be easily achieved for large crystal populations, due to a large $d_{50}$ influence on span calculations, for example a $d_{50}$ of 350 µm to a achieve a span of one can have a $d_{10}$ and $d_{90}$ variation of ±175 µm, whereas a $d_{50}$ of 60 µm can only have $d_{10}$ and $d_{90}$ variation of ±30 µm.

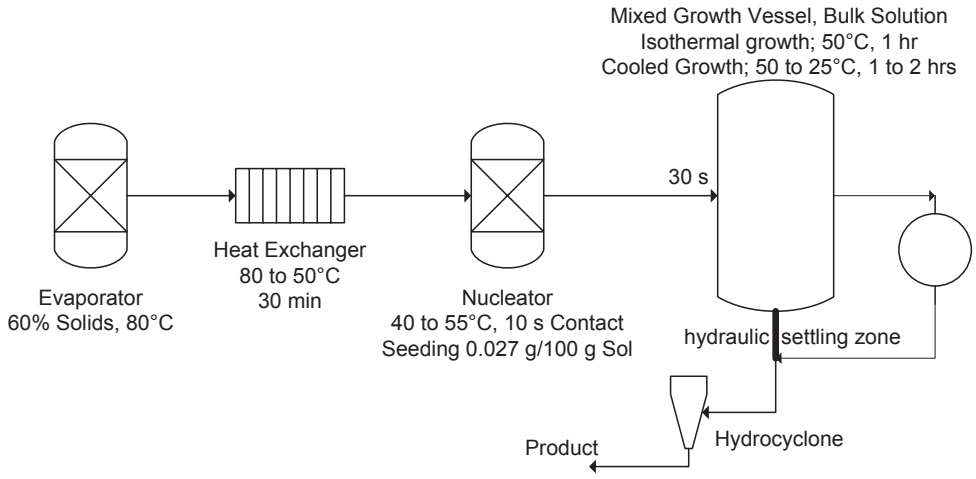


**Figure 135 Hartel controlled growth crystallization setup**

A recommended batch experimental test method is shown in Figure 136. Bulk solution growth concentration and time needs to be altered to grow to the desired $d_{50}$ size range of 50 to 90 µm. A product span of 1.4 or less is desired, with yield significantly greater than the CSC; subsequent to which it would be assumed a hydrocyclone cut could be used to achieve a span of 1, and recycle waste stream back to the start.

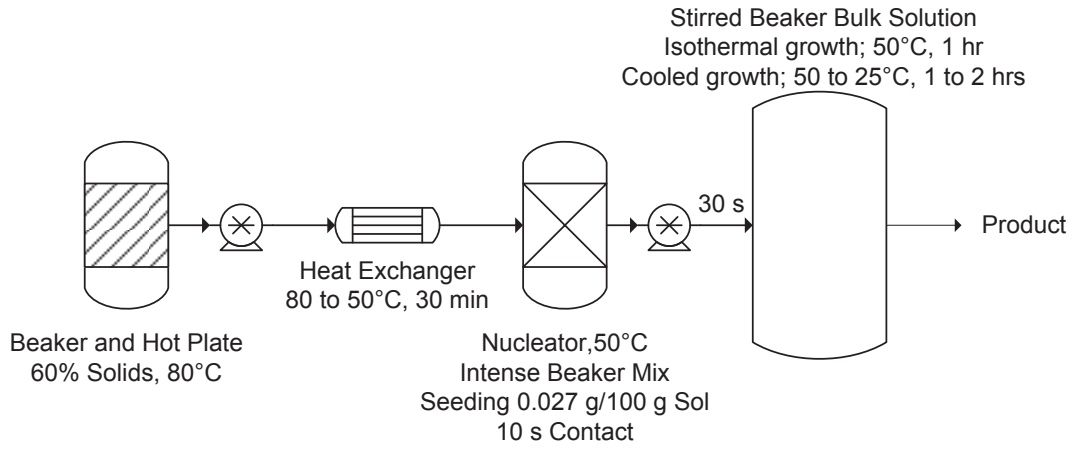


**Figure 136 Recommended small scale batch crystallization setup**

## 8.7 Conclusions

An agglomeration term was added to the standard laminar flow continuous settling crystallizer theoretical model. The agglomerates formed still conform to fluid velocities acting across the column radius, resulting in no significant PSD prediction changes. The agglomeration term was retained because agglomeration did occur in practice.

The laminar flow theoretical continuous settling crystallizer model, over predicted product particle $d_{10}$ and $d_{50}$ and under predicted span. Analysing potential flow conditions, it was determined that channelling, a region of high flow and a subsequent area of low flow, explained the $d_{50}$ and span deviation well. Experimental continuous settling crystallizer waste stream crystals are predicted well using the initial laminar flow model, so a column transition from channelling back to ideal laminar flow is likely.

Due to the difficult continuous settling crystallizer control conditions, it is recommended a single nucleation semi-continuous batch method be developed with a subsequent hydrocyclone cut. It was predicted that the highest inhaler grade lactose yields could be achieved through this process.

# Chapter 9 – Overall Conclusions and Recommendations

This work investigated processes to produce inhaler grade lactose (IGL) directly by crystallization. The key objectives to be met were a $d_{50}$ particle size in the range of 50 to 90 μm, a span less than 1 and no contaminants. Due to growth rate dispersion, typical industrial crystallization processes produce lactose crystals with wide particle size distributions, $d_{50}$ ranging from 200 to 500 μm, and a span from 2 to 2.5. Crystallized pharmaceutical grade lactose commonly undergoes additional processing in the form of milling and sieving to achieve the properties required for IGL. Successive nucleation events increase the particle size distribution and the use of a single nucleation event with subsequent controlled growth conditions will be core to any new narrow particle size crystallizer design.

Three potential methods for producing a narrow particle size distribution were studied in detail: droplet growth (crystallization), hydrocyclone (separation) and inclined settler (separation). Droplet growth counteracts growth rate dispersion by controlling the maximum size a crystal within the drop can reach. This process is ideal for tailoring a narrow particle size distribution; however issues arise with scalability and producing drops without contamination.

A hydrocyclone separates fines from large particles via centrifugal force, while an inclined settler uses gravitational force. Both methods, in theory, are capable of processing a post-crystallized lactose stream to a span less than one, with the inclined settler predicted to be slightly more efficient.

These methods were considered to be additional processing steps; therefore the novel method of a continuous settling crystallizer (CSC) was proposed. The CSC process involves feeding a pre-nucleated stream, from a single nucleation event, near the bottom of a vertical column under laminar conditions. Growth of the nuclei and settling of large crystals occur inside the column. The column has an average fluid velocity and once the nuclei have grown to a large enough crystal size, where the terminal particle settling velocity opposes the fluid velocity, it will settle out from the column. An inherently slow growing crystal travels further up the column before growing to the terminal particle diameter than an inherently fast growing crystal. Crystals with different inherent growth rates settle out from the column at the same final particle size, counteracting growth rate dispersion.

Experiments were conducted with tomahawk shaped alpha-lactose crystals to measure their physical characteristics and settling parameters for use in the theoretical development of the CSC. A Stokes height factor, $B_{St}$, defined as the ratio of the Stokes settling diameter of a crystal to its height, was determined to be 0.595±0.007 and 0.643±0.008 for gel-grown and plant-

grown crystals respectively. Elongation ratios, height B divided by width A, for the gel-grown crystals were 1.44±0.07 and for plant grown crystals 1.37±0.06 where *0.3 mm ≤ B ≤ 1.7 mm*. The Stokes shape factor was measured for gel-grown crystals to be 0.99. Lactose crystal settling velocity can thus be estimated directly from knowledge of crystal height, crystal width, or crystal volume.

Controlled single nucleation methods that could be used in producing a pre-nucleated feed stream for the CSC were investigated. The first technique was continuous orifice nucleation, where orifice Reynolds number and supersaturation wait time prior to the orifice was altered. An apparent effect on crystal numbers was not observed for the wait time and Reynolds number conditions tested. But a wait time and increased orifice Reynolds number lead to an increased particle size for the continuous orifice nucleation of lactose, suggesting that these conditions produced faster growing crystals. Resulting spans obtained were significantly lower for higher Reynolds orifice flow and with the addition of a wait time. The current CSC low feed flow rate, less than 50 $mL.min^{-1}$, and hence small orifice setup, was found to be unreliable to operate on a continuous (16+hour) basis due to pressure limitations and blockages occurring. Without better equipment, a robust alternative single nucleation event utilising impeller mixing followed by dilution and storage was developed for use with the CSC setup.

A theoretical model for the CSC, predicting the theoretical particle size distribution and span from the process was developed. The initial CSC theoretical model used a plug flow profile, which was later modified to a more realistic parabolic velocity profile. Using a parabolic profile increased the product span from near 0 to 0.47±0.01. This meets the crystallizer design criterion of a span less than 1. Changing the base model conditions, crystallizer growth concentration, height and flow rate, had minor effects on the span. The base model conditions also resulted in a $d_{50}$ of 73.2±0.9 µm which is within the crystallizer design objective product $d_{50}$ size of 50 to 90 µm. Changing the theoretical crystallizer concentration and flow rate had the greatest effect on product particle size. Product crystal concentration was shown to increase with growth concentration and crystal growth rates.

The theoretical model investigation into the CSC led to the development of a reliable CSC lab scale setup; consisting of 3.5 m high column, 74 mm internal diameter and a net vertical flow rate of around 30 $mL.min^{-1}$. Only lactose and water were used, complying with the low contaminants criterion. Different batches of lactose (IGL-1, 200M-1 and 200M-2) were used in the CSC experiments and found to have statistically different inherent growth rates, calculated through the bottle roll controls. For the CSC run conditions of a net 28 $mL.min^{-1}$ column flow and absolute alpha supersaturation of 8.2 g/100 g, IGL-1 had a product span of 1.49±0.04 and

$d_{50}$ of 69.1±2.4 µm, 200M-1 had a product span of 1.41±0.02 and $d_{50}$ of 53.8±1.6 µm, and 200M-2 had a product span of 1.54±0.02 and $d_{50}$ of 78.2±2.9 µm. The desired IGL production objectives were not met as the span was greater than 1.

The standard CSC theoretical model, over predicted product particle $d_{10}$ and $d_{50}$ and under predicted span when compared to the experimental results. Agglomeration was proposed as the main point of difference with the theoretical model; potentially causing the increased product span and an agglomeration term was added to the standard CSC theoretical model. The agglomerates formed still conformed to the fluid velocities acting across the column radius, resulting in no significant PSD prediction changes. The agglomeration term was retained because agglomeration was found to occur in practice.

Analysing potential flow conditions, it was determined channelling, a region of high flow and a subsequent area of low flow, explained the $d_{50}$ and span deviation well. The CSC theoretical model was modified to include a channelling effect and, depending on the model condition, predicted theoretical product spans from 0.5 to 2; encompassing the experimental product span result. Theoretical CSC waste stream crystals were predicted well using ideal laminar flow, so a column transition back to laminar flow was also deemed likely to be occurring.

Due to the difficult CSC control conditions, unlikely to be achieved at an industrial scale, it is recommended a single nucleation semi-continuous batch method be developed with a subsequent hydrocyclone cut. It was predicted by mathematical modelling that the highest IGL yields could be achieved through such a process, but this has not been confirmed by experiment.

## Nomenclature

| Abbreviations | |
|---|---|
| BCF | Burton-Cabrera-Frank |
| CCG | Constant crystal growth |
| CSC | Continuous settling crystallizer |
| IGL | Inhaler grade lactose |
| RI | Refractive index |
| PSD | Particle size distribution |

| Symbol | Description | Unit |
|---|---|---|
| $*$ | At equilibrium or saturation | - |
| $a$ | Activity constant | - |
| $a_1$ | Exponential factor/constant | #.m$^{-3}$.s$^{-1}$ |
| $a_2$ | Constant | - |
| $\Delta a_w$ | Differential water activity after and prior to crystallization | - |
| $A$ | Tomahawk crystal width | m |
| $A_c$ | Tube cross sectional area | m$^2$ |
| $A_f$ | Fast zone column cross-sectional area | m$^2$ |
| $A_I$ | Column area at fast/slow interaction boundary | m$^2$ |
| $A_m$ | Cross-sectional area of crystallizer relative to Z=0 | m$^2$ |
| $A_s$ | Slow zone column cross-sectional area | m$^2$ |
| $A_T$ | Total column cross-sectional area | m$^2$ |
| $b_1$ | Pre-exponential factor/constant | - |
| $B$ | Tomahawk crystal height | m |
| $B_{St}$ | Stokes height factor | - |
| $c$ | Concentration | g solute/100 g solvent |
| $C$ | Concentration of crystals in solution | #.m$^{-3}$ |
| $\Delta C$ | Supersaturation or concentration driving force | g lactose/100 g water |
| $C_\alpha$ | Alpha lactose concentration | g lactose/100 g water |
| $C_{\alpha s}$ | Solubility (equilibrium) alpha lactose concentration | g lactose/100 g water |
| $C_\beta$ | Beta lactose concentration | g lactose/100 g water |
| $C_{\beta s}$ | Solubility (equilibrium) beta lactose concentration | g lactose/100 g water |
| $C(d)$ | Classification function | - |
| $C_m$ | Alpha lactose concentration of fluid section m | g lactose/100 g water |
| $C_n$ | Temperature related constant for calculating density | - |
| $C_p$ | Fluid specific heat capacity | kJ.kg$^{-1}$°C |
| $C_s$ | Solubility (equilibrium) lactose concentration | g lactose/100 g water |
| $C_T$ | Total (bulk) lactose concentration | g lactose/100 g water |
| $C_V^P$ | Percent solids feed by volume | % |
| $CV$ | Coefficient of variation | - |
| $d$ | Particle diameter | m |
| $d_i$ | Theoretical model particle diameter input | m |
| $d_n$ | Lactose tomahawk crystal diameter based on longest length | µm |
| $d_v$ | Equivalent volume diameter | m |
| $d_{St}$ | Stokes diameter | m |
| $d_{10,50,90}$ | On a cumulative (volume basis) is the particle size at 10%, 50%, and 90% respectively | µm |

| | | |
|---|---|---|
| $d_{25,75}$ | Size of particle having a 25% and 75% probability reporting in the underflow | µm |
| $d_{50c}$ | Corrected cut/classification size | m |
| $D_c$ | Cyclone diameter | m |
| $D_G$ | Growth rate diffusivity parameter | $\mu m^2.min^{-1}$ |
| $D_i$ | Diameter of cyclone inlet | m |
| $D_o$ | Diameter of cyclone vortex finder | m |
| $D_u$ | Diameter of cyclone spigot | m |
| $E$ | Elongation ratio | - |
| $E_a$ | Activation energy | $kcal.mol^{-1}$ |
| $f_1$ | Temperature dependent factor for the solubility depression of α-lactose by β-lactose | - |
| $F$ | Feed stream | - |
| $F(d)$ | Feed PSD | - |
| $F_r$ | Mass fraction | - |
| $F_s$ | BCF model constant | $\mu m.min^{-1}$ |
| $F_1 - F_4$ | Calibration parameters | - |
| $g$ | Gravity | $m.s^{-2}$ |
| $g_1$ | Growth parameter for size dependent growth | - |
| $g_2$ | Growth parameter for size dependent growth | $m^{-1}$ |
| $g_3$ | Growth parameter for size dependent growth | - |
| $G$ | Growth rate of α-lactose monohydrate crystals, related by supersaturation | $\mu m.min^{-1}$ |
| $\bar{G}$ | Mean time averaged crystal growth rate | $\mu m.min^{-1}$ |
| $G_B$ | Birth and spread growth | $\mu m.min^{-1}$ |
| $G_m$ | Mononuclear growth | $\mu m.min^{-1}$ |
| $G_n$ | Growth rate of α-lactose monohydrate crystals in terms of longest length, related by supersaturation | $\mu m.min^{-1}$ |
| $G_p$ | Polynuclear growth | $\mu m.min^{-1}$ |
| $G_s$ | Spiral growth | $\mu m.min^{-1}$ |
| $h$ | Cyclone free vortex height | m |
| $h_s$ | Birth and spread model step height | m |
| $J_{Het}$ | Heterogeneous nucleation rate | $\#.m^{-3}.s^{-1}$ |
| $J_{Hom}$ | Homogenous nucleation rate | $\#.m^{-3}.s^{-1}$ |
| $J_T$ | Total nucleation rate | $\#.m^{-3}.s^{-1}$ |
| $k$ | Boltzmann constant | $J.K^{-1}$ |
| $k_1$ | Correction factor for settling velocity | - |
| $k_2$ | Exponent for the effect of solids density on the corrected cut size | - |
| $k_g$ | Growth rate constant (crystal specific) | $\mu m.min^{-1}$ |
| $k_{gs}$ | Growth rate constant using supersaturation | $\mu m.min^{-1}$.100 g water/g lactose |
| $k_0$ | Frequency factor | $\mu m^2.min^{-2}$ |
| $k_{St}$ | Stokes shape factor | - |
| $K$ | Equilibrium ratio of β-lactose to α-lactose | - |
| $k_D$ | System specific parameter | $\mu m^2.min^{-1}$ |
| $\overline{k_G}$ | Mean growth kinetic constant | $\mu m.min^{-1}$ |
| $K_S$ | Solubility temperature effect constant | - |
| $lc_m$ | Crystal mass in section m | kg |
| $lc_n$ | Individual crystal mass | kg |

| | | |
|---|---|---|
| $ls_m$ | Soluble lactose in section m | kg |
| $\Delta ls_n$ | Soluble lactose used by crystal growth | kg |
| $lwc_n$ | Individual crystal water mass | kg |
| $\Delta lwc_n$ | Water used by crystal growth | kg |
| $L$ | Channel height/length | m |
| $\Delta L$ | Increase in crystal size (McCabe's Law) | m |
| $\Delta L_m$ | Amount of α-lactose monohydrate crystal | g lactose/100 g water |
| $Lc_F$ | Total feed solid crystal (lactose) flow rate | $kg.s^{-1}$ |
| $Lc_{Fr}$ | Feed solid crystal non-recycled component | $kg.s^{-1}$ |
| $Lc_{Or}$ | Feed solid crystal recycled from overflow component | $kg.s^{-1}$ |
| $Ls_F$ | Total feed soluble lactose flow rate | $kg.s^{-1}$ |
| $Ls_{Fr}$ | Feed soluble lactose non-recycled component | $kg.s^{-1}$ |
| $Ls_{Or}$ | Feed soluble lactose recycled from overflow component | $kg.s^{-1}$ |
| $m$ | As a subscript: fluid section number in crystallizer | - |
| $m_c$ | Classification index | - |
| $m_f$ | Fast zone multiplication factor | - |
| $m_s$ | Slow zone division factor | - |
| $m_{Q_f}$ | Feed mass flow rate | $kg.s^{-1}$ |
| $n_c$ | Number of molecules in a critical nucleus | # |
| $n_1$ | System specific parameter | - |
| $n_L$ | Exponent in Richardson and Zaki equation | - |
| $N_N$ | Number of particles per unit volume | $\#.m^{-3}$ |
| $NW$ | No wait time; prior to orifice flow | - |
| $O$ | Overflow stream | - |
| $O(d)$ | Overflow PSD | - |
| $P$ | Crystal Product stream | - |
| $PW$ | Product by waste, crystal volume ratio | - |
| $P_3$ | Downstream pressure | Pa |
| $P_c$ | Cyclone inlet pressure | Pa |
| $P_f(v)$ | Feed normalised probability size density function | $s.m^{-1}$ |
| $P_i$ | Individual particle properties | - |
| $P_N$ | Number of unique particles inputted per $\Delta$t | # |
| $P_o(v)$ | Overflow normalised probability size density function | $s.m^{-1}$ |
| $\Delta P$ | Pressure drop | Pa |
| $P_u(v)$ | Underflow normalised probability size density function | $s.m^{-1}$ |
| $P_v$ | Water vapour pressure | Pa |
| $q_1$ | Factor to account for interfacial energy reduction | - |
| $q$ | Energy | kW |
| $Q$ | Volumetric flow rate | $m^3.s^{-1}$ |
| $Q_f$ | Feed volumetric flow rate | $m^3.s^{-1}$ |
| $Q_F$ | Fast column volumetric flow rate | $m^3.s^{-1}$ |
| $Q_o$ | Overflow volumetric flow rate | $m^3.s^{-1}$ |
| $Q_u$ | Underflow volumetric flow rate | $m^3.s^{-1}$ |
| $Q_S$ | Slow column volumetric flow rate | $m^3.s^{-1}$ |
| $Q_T$ | Combined fast and slow zone flow rate | $m^3.s^{-1}$ |
| $r$ | Column radius position relative to $R_T$=0 | m |
| $R$ | Universal gas constant | $J.gmol^{-1}.°K^{-1}$ |
| $R_D$ | Correction factor for alpha lactose depression | - |
| $Re$ | Reynolds number | - |

| | | |
|---|---|---|
| $Re_p$ | Particle Reynolds number | - |
| $R_f$ | Recovery of water to underflow | - |
| $R_F$ | Combined column modified outer radius | m |
| $R_I$ | Combined column fast/slow zone boundary radius | m |
| $R_G$ | Mass growth rate | $g.\mu m^{-2}.min^{-1}$ |
| $R_T$ | Column radius | m |
| $s$ | Supersaturation ratio – see Equation 13 | - |
| $S$ | Volumetric flow split (U/O) | - |
| $SI$ | Sharpness Index | - |
| $S_\alpha$ | Absolute α-lactose supersaturation ($C_\alpha$-$C_{\alpha s}$) | g lactose/100 g water |
| $S(d)$ | Selectivity function | - |
| $SD$ | Standard deviation | - |
| $S_L$ | Large particles volumetric down flow | $m^3.s^{-1}$ |
| $S_R$ | Supersaturation Ratio | $C/C^*$ |
| $S_S$ | Small particles volumetric down flow | $m^3.s^{-1}$ |
| $S(v)$ | Volumetric inclined settling rate | $m^3.s^{-1}$ |
| $t$ | Total simulation time | hr |
| $\Delta t$ | Pre-defined time step | s |
| $t_N$ | Time to detect an appreciable amount of nuclei | s |
| $T/T_K$ | Absolute Solution Temperature | K |
| $Tc$ | Solution Temperature | °C |
| $\Delta T$ | Temperature increase | °C |
| $u$ | Settling velocity | $m.s^{-1}$ |
| $u_c$ | Cut off settling velocity for overflow | $m.s^{-1}$ |
| $u_f$ | Average fluid velocity | $m.s^{-1}$ |
| $u_{ff}$ | Average fast zone column velocity | $m.s^{-1}$ |
| $u_{fl}$ | Fluid section velocity at column height relative to Z=0 | $m.s^{-1}$ |
| $u_{fs}$ | Average slow zone column velocity | $m.s^{-1}$ |
| $u_i$ | Upward interstitial liquid velocity | $m.s^{-1}$ |
| $u_o$ | Average liquid velocity at orifice | $m.s^{-1}$ |
| $u_r$ | Parabolic laminar flow profile across a cylinder radius | $m.s^{-1}$ |
| $u_{r,f}$ | Fast zone modified parabolic laminar flow profile | $m.s^{-1}$ |
| $u_{r,s}$ | Slow zone modified parabolic laminar flow profile | $m.s^{-1}$ |
| $u_t$ | Crystal terminal settling velocity | $m.s^{-1}$ |
| $u_{tv}$ | Terminal settling velocity of a spherical equivalent particle with same density and volume | $m.s^{-1}$ |
| $u_z$ | Net particle velocity | $m.s^{-1}$ |
| $U(d)$ | Underflow PSD | - |
| $v_L$ | Large particle fall velocity | $m.s^{-1}$ |
| $v_{L\infty}$ | Terminal fall velocity of a single isolated particle | $m.s^{-1}$ |
| $v_S$ | Small particle fall velocity | $m.s^{-1}$ |
| $V_d$ | Drop volume | $m^3$ |
| $V_e$ | Effective specific volume | $m^3.kg^{-1}$ |
| $V_{fm}$ | Volume of CSC fluid section m | $m^3$ |
| $V_m$ | Molecular volume | $m^3$ |
| $V_P$ | Crystal volume | $m^3$ |
| $V_{St}$ | Stokes equivalent volume | $m^3$ |
| $w$ | Channel width | m |
| $w_m$ | Water mass in section m | kg |

| | | |
|---|---|---|
| $w_p$ | Perpendicular channel spacing | m |
| $W$ | Wait time; prior to orifice flow | - |
| $W_F$ | Total feed water mass flow rate | $kg.s^{-1}$ |
| $W_{Fr}$ | Feed water non-recycled component | $kg.s^{-1}$ |
| $W_{Or}$ | Feed water recycled from overflow component | $kg.s^{-1}$ |
| $x_s$ | Mean distance travelled by absorbing molecule before desorbs | m |
| $\bar{x}$ | Mean | (-) |
| $z$ | Height within the CSC column | m |
| $z_m$ | Height of fluid section m within the column relative to Z=0 | m |
| $z_{l,m}$ | Vertical length of an individual fluid section m | m |
| $z_n$ | Height or position of an individual crystal relative to Z=0 | m |
| $z_t$ | Transition height relative to Z=0 | m |
| $Z$ | Total CSC column height | m |

**Greek Symbols**

| Symbol | Description | Unit |
|---|---|---|
| $\alpha_d$ | Distance between incorporated growth units | µm |
| $\alpha_h$ | Total particle hold up | - |
| $\alpha_1$ | Exponential factor in growth equation, 1.31 | - |
| $\alpha_{hL}$ | Large particles total hold up | - |
| $\alpha_{hS}$ | Small particles total hold up | - |
| $\alpha_v$ | Lactose tomahawk crystal shape factor | - |
| $\beta$ | Solid cylinder height fraction | - |
| $\gamma$ | Activity coefficient | - |
| $\gamma_i$ | Edge free energy of growth unit in a step | J |
| $\gamma_e$ | Edge free energy | $J.m^{-2}$ |
| $\varepsilon_s$ | The number of incorporating spirals | # |
| $\in$ | Screw dislocation activity | - |
| $\eta$ | Segregation efficiency | - |
| $\theta$ | Cylinder cone angle/channel angle of inclination | ° |
| $\mu$ | Chemical potential of supersaturated solution | $J.gmol^{-1}$ |
| $\mu_o$ | Solvent viscosity | Pa.s |
| $\mu_v$ | Fluid viscosity | Pa.s |
| $\pi$ | Pi | - |
| $\rho_f$ | Fluid density | $kg.m^{-3}$ |
| $\rho_{lc}$ | α-lactose monohydrate crystal density | $kg.m^{-3}$ |
| $\rho_p$ | Feed pulp density | $kg.m^{-3}$ |
| $\rho_s$ | Solid (crystal/particle) density | $kg.m^{-3}$ |
| $\rho_w$ | Water density | $kg.m^{-3}$ |
| $\sigma$ | Relative supersaturation – see Equation 14 | - |
| $\sigma_c$ | Cavitation number | # |
| $\sigma_G^2$ | Variance of crystal growth rate | $µm^2.min^{-2}$ |
| $\sigma_i$ | Interfacial energy | $J.m^{-2}$ |
| $\sigma_1$ | BCF system dependent parameter | - |
| $\sigma_{kg}^2$ | Variance distribution parameter | $µm^2.min^{-2}$ |
| $\emptyset$ | Effective volume fraction | - |
| $\emptyset_b$ | Bond energy | J |

## References


Aamir, E., Nagy, Z. K., & Rielly, C. D. (2010). Evaluation of the Effect of Seed Preparation Method on the Product Crystal Size Distribution for Batch Cooling Crystallization Processes. *Crystal Growth & Design, 10*(11), 4728-4740.

Abu Bakar, M. R., Nagy, Z. K., Saleemi, A. N., & Rielly, C. D. (2009). The Impact of Direct Nucleation Control on Crystal Size Distribution in Pharmaceutical Crystallization Processes. *Crystal Growth & Design, 9*(3), 1378-1384.

Achilles, W. (1997). In vitro crystallisation systems for the study of urinary stone formation. *World Journal of Urology*(244-251).

Agrawal, S. G. (2012). *Evaporative Crystallization of Alpha-lactose Monohydrate.* Unpublished PHD, Massey University, Palmerston North.

Allen, K., Davey, R. J., Ferrari, E., Towler, C., Tiddy, G. J., Jones, M. O., et al. (2002). The Crystallization of Glycine Polymorphs from Emulsions, Microemulsions, and Lamellar Phases. *Crystal Growth & Design, 2*(6), 523-527.

Arndt, R. E. A. (1981). Cavitation in Fluid Machinery and Hydraulic Structures. *Annual Review of Fluid Mechanics, 13*(1), 273-326.

Barrero, A., & Loscertales, I. G. (2007). Micro- and Nanoparticles via Capillary Flows. *Annual Review of Fluid Mechanics, 39*(1), 89-106.

Bennett, R. C., Fiedelma.H, & Randolph, A. D. (1973). Crystallizer Influenced Nucleation. *Chemical Engineering Progress, 69*(7), 86-93.

Berkland, C., Kim, K., & Pack, D. W. (2001). Fabrication of PLG microspheres with precisely controlled and monodisperse size distributions. *Journal of Controlled Release, 73*(1), 59-74.

Bhandari, B., & Burel, B. (2007). Prediction of lactose crystals present in supersaturated lactose and whey solutions by measuring the water activity. *International Journal of Food Properties, 10*(1), 163-171.

Bhargava, A., & Jelen, P. (1996). Lactose Solubility and Crystal Growth as Affected by Mineral Impurities. *Journal of Food Science, 61*(1), 180-184.

Biddulph, M. W. (1983). Separating Efficiency Of A Water Elutriator. *AIChE Journal, 29*(6), 956-961.

Biddulph, M. W. (1986). Some Aspects Of The Performance Of Water Elutriators. *Conservation & Recycling, 9*(2), 211-221.

Bouwman, A. M., Bosma, J. C., Vonk, P., Wesselingh, J. A., & Frijlink, H. W. (2004). Which shape factor(s) best describe granules? *Powder Technology, 146*(1-2), 66-72.

Bund, R. K., & Pandit, A. B. (2007a). Rapid lactose recovery from buffalo whey by use of 'anti-solvent, ethanol'. *Journal of Food Engineering, 82*(3), 333-341.

Bund, R. K., & Pandit, A. B. (2007b). *Rapid lactose recovery from paneer whey using sonocrystallization: A process optimization.* Paper presented at the European Process Intensification Conference, Copenhagen, Denmark.

Bund, R. K., & Pandit, A. B. (2007c). Sonocrystallization: Effect on lactose recovery and crystal habit. *Ultrasonics Sonochemistry, 14*(2), 143-152.

Butler, B. (1998). *Modelling Industrial Lactose Crystallisation.* Unpublished PhD, University of Queensland, Queensland, Australia.

Çengel, Y. A., & Cimbala, J. M. (2006). *Fluid mechanics: fundamentals and applications*: McGraw-HillHigher Education.

Chew, J. W., Black, S. N., Chow, P. S., & Tan, R. B. H. (2007). Comparison between Open-Loop Temperature Control and Closed-Loop Supersaturation Control for Cooling Crystallization of Glycine. *Industrial & Engineering Chemistry Research, 46*(3), 830-838.

Chow, A. H. L., Tong, H. H. Y., Chattopadhyay, P., & Shekunov, B. Y. (2007). Particle engineering for pulmonary drug delivery. [Review]. *Pharmaceutical Research, 24*(3), 411-437.

Chu, L.-Y., Yu, W., Wang, G.-J., Zhou, X.-T., Chen, W.-M., & Dai, G.-Q. (2004). Enhancement of hydrocyclone separation performance by eliminating the air core. *Chemical Engineering and Processing, 43*(12), 1441-1448.

Cilliers, J. J., Diaz-Anadon, L., & Wee, F. S. (2004). Temperature, classification and dewatering in 10 mm hydrocyclones. *Minerals Engineering, 17*(5), 591-597.

Darcy, P. A., & Buckton, G. (1998). Crystallization of bulk samples of partially amorphous spray-dried lactose. *Pharmaceutical development and technology, 3*(4), 503-507.

Darcy, P. A., & Wiencek, J. M. (1998). Estimating Lysozyme Crystallization Growth Rates and Solubility from Isothermal Microcalorimetry. *Acta Crystallographica, D54*, 1387-1394.

Davey, R. J., Hilton, A. M., & Garside, J. (1996). *Crystallization from oil in water emulsions: Particle synthesis and purification of molecular materials.* Paper presented at the 13th Symposium on Industrial Crystallization, Toulouse, France.

Davies, C., & Graham, K. (1988). *Pressure Drop Reduction by Wall Baffles in Vertical Pneumatic Conveying Tubes*. Paper presented at the Chemeca 88 (16th : 1988 : Sydney, N.S.W.).

Davies, C., & O'Hagan, T. (1988). *The Use of Wall Baffles to Increase the Separation: Efficiency of an Air Elutriator*. Paper presented at the Chemeca 88 (16th : 1988 : Sydney, N.S.W.).

Davis, R. H., & Gecol, H. (1996). Classification of concentrated suspensions using inclined settlers. *International Journal of Multiphase Flow, 22*(3), 563-574.

Davis, R. H., Zhang, X., & Agarwala, J. P. (1989). Particle classification for dilute suspensions using an inclined settler. *Industrial & Engineering Chemistry Research, 28*(6), 785-793.

Dhumal, R. S., Biradar, S. V., Paradkar, A. R., & York, P. (2008). Ultrasound Assisted Engineering of Lactose Crystals. *Pharmaceutical Research, 25*(12), 2835-2844.

Dhumal, R. S., Biradar, S. V., Paradkar, A. R., & York, P. (2009). Particle engineering using sonocrystallization: Salbutamol sulphate for pulmonary delivery. *International Journal of Pharmaceutics, 368*(1-2), 129-137.

Dincer, T. D. (2000). *Mechanisms of Lactose Crystallisation.* Unpublished PHD, Curtin University of Technology.

Dincer, T. D., Ogden, M. I., & Parkinson, G. M. (2009a). Crystal growth mechanisms of the (0 1 0) face of [alpha]-lactose monohydrate crystals. *Journal of Crystal Growth, 311*(8), 2427-2432.

Dincer, T. D., Ogden, M. I., & Parkinson, G. M. (2009b). In situ investigation of growth rates and growth rate dispersion of [alpha]-lactose monohydrate crystals. *Journal of Crystal Growth, 311*(5), 1352-1358.

Dincer, T. D., Parkinson, G. M., Rohl, A. L., & Ogden, M. I. (1999). Crystallisation of [alpha]-lactose monohydrate from dimethyl sulfoxide (DMSO) solutions: influence of [beta]-lactose. *Journal of Crystal Growth, 205*(3), 368-374.

Doki, N., Kubota, N., Sato, A., & Yokota, M. (2001). Effect of cooling mode on product crystal size in seeded batch crystallization of potassium alum. *Chemical Engineering Journal, 81*(1-3), 313-316.

Dombrowski, N., Foumeny, E. A., Ookawara, S., & Riza, A. (1993). The influence of Reynolds-number on the entry length and pressure-drop for laminar pipe-flow. *Canadian Journal of Chemical Engineering, 71*(3), 472-476.

Dombrowski, R. D., Litster, J. D., Wagner, N. J., & He, Y. (2007). Crystallization of alpha-lactose monohydrate in a drop-based microfluidic crystallizer. *Chemical Engineering Science, 62*(17), 4802-4810.

Doroodchi, E., Fletcher, D. F., & Galvin, K. P. (2004). Influence of inclined plates on the expansion behaviour of particulate suspensions in a liquid fluidised bed. *Chemical Engineering Science, 59*(17), 3559-3567.

Doroodchi, E., Galvin, K. P., & Fletcher, D. F. (2005). The influence of inclined plates on expansion behaviour of solid suspensions in a liquid fluidised bed -- A computational fluid dynamics study. *Powder Technology, 160*(1), 20-26.

Doroodchi, E., Zhou, J., Fletcher, D. F., & Galvin, K. P. (2006). Particle size classification in a fluidized bed containing parallel inclined plates. *Minerals Engineering, 19*(2), 162-171.

Elwell, M. W., Roberts, R. F., & Coupland, J. N. (2004). Effect of homogenization and surfactant type on the exchange of oil between emulsion droplets. *Food Hydrocolloids, 18*(3), 413-418.

Erdemir, D., Lee, A. Y., & Myerson, A. S. (2009). Nucleation of Crystals from Solution: Classical and Two-Step Models. [Review]. *Accounts of Chemical Research, 42*(5), 621-629.

Farhadi, F., & Babaheidary, M. B. (2002). Mechanism and estimation of $Al(OH)_3$ crystal growth. *Journal of Crystal Growth, 234*, 721-730.

Flintoff, B. C., Plitt, L. R., & Turak, A. A. (1987). Cyclone Modelling: A Review Of Present Technology. *CIM Bulletin, 80*(905), 39-50.

Foster, N., Mammucari, R., Dehghani, F., Barrett, A., Bezanehtak, K., Coen, E., et al. (2003). Processing pharmaceutical compounds using dense gas technology. [Review]. *Industrial & Engineering Chemistry Research, 42*(25), 6476-6493.

Friedman, M., Gillis, J., & Liron, N. (1968). Laminar flow in a pipe at low and moderate Reynolds numbers. [Article]. *Applied Scientific Research, 19*(6), 426-&.

Frontana-Uribe, B. A., & Moreno, A. (2008). *On Electrochemically Assisted Protein Crystallization and Related Methods.* Paper presented at the 12th International Conference on Crystalization of Biological Macromolecules, Cancun City, MEXICO.

Galvin, K., & Nguyentranlam, G. (2002). Influence of parallel inclined plates in a liquid fluidized bed system. *Chemical Engineering Science, 57*(7), 1231-1234.

Gerhart, C. (2001). *Untersuchungen zum Trennverhalten von Hydrozyklonen niedriger Trennkorngrößen*: Logos Verlag Berlin.

Gillis, J. (1920). Solubilite du sucre de lait. *Rec. trav. chim.,, 39*, 88-125.

Green, D. W., & Perry, R. H. (2008). *Perry's Chemical Engineers' Handbook* (8th ed.): McGraw-Hill.

Haase, G., & Nickerson, T. A. (1966). Kinetic reactions of alpha and beta lactose. II. Crystallization. *Journal of Dairy Science, 49*(7), 757-761.

Herrington, B. L. (1934). Some physico-chemical properties of lactose: I. The spontaneous crystallization of super-saturated solutions of lactose. *Journal of Dairy Science, 17*(11), 501-519.

Hickey, A. J., Mansour, H. M., Telko, M. J., Xu, Z., Smyth, H. D. C., Mulder, T., et al. (2007). Physical characterization of component particles included in dry powder inhalers. I. Strategy review and static characteristics. [Review]. *Journal of Pharmaceutical Sciences, 96*(5), 1282-1301.

Hudson, C. S. (1904). The hydration of milk-sugar in solution. *Journal of American Chemical Society, 26*, 1065-1082.

Hudson, C. S. (1908). Further studies on the forms of milk-sugar. *Journal of American Chemical Society, 30*, 1767-1783.

Hwang, K.-J., Lyu, S.-Y., & Nagase, Y. (2009). Particle separation efficiency in two 10-mm hydrocyclones in series. *Journal of the Taiwan Institute of Chemical Engineers, 40*(3), 313-319.

Jarzebski, A. B., & Malinowski, J. J. (1995). Potentials And Prospects For Application Of Supercritical-Fluid Technology In Bioprocessing. *Process Biochemistry, 30*(4), 343-352.

Jelen, P., & Coulter, S. T. (1973). Effect of Supersaturation and Temperature on the Growth of Lactose Crystals. *Journal of Food Science, 38*, 1182-1185.

Ju, J. X., Zeng, C. F., Zhang, L. X., & Xu, N. P. (2006). Continuous synthesis of zeolite NaA in a microchannel reactor. *Chemical Engineering Journal, 116*(2), 115-121.

Kalbasenka, A. N., Spierings, L. C. P., Huesman, A. E. M., & Kramer, H. J. M. (2007). Application of seeding as a process actuator in a model predictive control framework for fed-batch crystallization of ammonium sulphate. *Particle & Particle Systems Characterization, 24*(1), 40-48.

Kashchiev, D. (2000). *Nucleation : Basic theory with applications*: Elsevier Science.

Kashchiev, D., & van Rosmalen, G. M. (2003). Review: Nucleation in Solutions Revisited. *Crystal Research Technology, 38*(7-8), 555-574.

Kendrew, J. C., & Moelwyn-Hughes, E. A. (1940). The kinetics of mutarotation of alpha lactose monohydrate *Proceedings of the Royal Society of London., Series A 176*(966), 352-367.

Kerkhoff, T. (1997). *Feinkornklassierung in einem luftkernlosen Hydrozyklon*: vl. nákl.

Kim, S., Lotz, B., Lindrud, M., Girard, K., Moore, T., Nagarajan, K., et al. (2005). Control of the particle properties of a drug substance by crystallization engineering and the effect on drug product formulation. *Organic Process Research & Development, 9*(6), 894-901.

Kirk, J. H., Dann, S. E., & Blatchford, C. G. (2007). Lactose: A definitive guide to polymorph determination. *International Journal of Pharmaceutics, 334*(1-2), 103-114.

Knezic, D., Zaccaro, J., & Myerson, A. S. (2004). Nucleation induction time in levitated droplets. *Journal of Physical Chemistry B, 108*(30), 10672-10677.

Kobayashi, I., Mukataka, S., & Nakajima, M. (2005). Production of monodisperse oil-in-water emulsions using a large silicon straight-through microchannel plate. *Industrial & Engineering Chemistry Research, 44*(15), 5852-5856.

Kougoulos, E., Marziano, I., & Miller, P. R. (2010). Lactose particle engineering: Influence of ultrasound and anti-solvent on crystal habit and particle size. *Journal of Crystal Growth, 312*(23), 3509-3520.

Kraipech, W., Chen, W., Parma, F. J., & Dyakowski, T. (2002). Modelling the fish-hook effect of the flow within hydrocyclones. [Article]. *International Journal of Mineral Processing, 66*(1-4), 49-65.

Kubota, N., Doki, N., Yokota, M., & Sato, A. (2001). Seeding policy in batch cooling crystallization. *Powder Technology, 121*(1), 31-38.

Larhrib, H., Martin, G. P., Marriott, C., & Prime, D. (2003). The influence of carrier and drug morphology on drug delivery from dry powder formulations. *International Journal of Pharmaceutics, 257*(1-2), 283-296.

Laskovski, D., Duncan, P., Stevenson, P., Zhou, J., & Galvin, K. P. (2006). Segregation of hydraulically suspended particles in inclined channels. *Chemical Engineering Science, 61*(22), 7269-7278.

Lefort, R., Caron, V., Willart, J. F., & Descamps, M. (2006). Mutarotational kinetics and glass transition of lactose. *Solid State Communications, 140*(7-8), 329-334.

Leng, J., & Salmon, J. B. (2009). Microfluidic crystallization. *Lab on a Chip, 9*(1), 24-34.

Leung, W. F., & Probstein, R. F. (1983). Lamella and tube settlers. 1. Model and operation. *Industrial & Engineering Chemistry Process Design and Development, 22*(1), 58-67.

Liang, B. M., Hartel, R. W., & Berglund, K. A. (1987). Growth-Rate Dispersion In Seeded Batch Sucrose Crystallization. *AIChE Journal, 33*(12), 2077-2079.

Liotta, V., & Sabesan, V. (2004). Monitoring and Feedback Control of Supersaturation Using ATR-FTIR to Produce an Active Pharmaceutical Ingredient of a Desired Crystal Size. *Organic Process Research & Development, 8*(3), 488-494.

Liu, P. K., Chu, L. Y., Wang, J., & Yul, Y. F. (2008). Enhancement of hydrocyclone classification efficiency for fine particles by introducing a volute chamber with a pre-sedimentation function. *Chemical Engineering & Technology, 31*(3), 474-478.

Lockett, M. J., & Al-Habbooby, H. M. (1973). Differential Settling By Size Of 2 Particle Species In A Liquid. *Transactions of the Institution of Chemical Engineers, 51*(4), 281-292.

Loffelmann, M., & Mersmann, A. (2002). How to measure supersaturation? *Chemical Engineering Science, 57*, 4301-4310.

Lorber, B., & Giege, R. (1995, Nov 12-17). *Containerless protein crystallization in floating drops: Application to crystal growth monitoring under reduced nucleation conditions.* Paper presented at the 6th International Conference on Crystallization of Biological Macromolecules, Hiroshima, Japan.

Mazo, R. (2002). *Brownian motion: fluctuations, dynamics, and applications*: Oxford University Press.

McCabe, W. L. (1929). Crystal Growth in Aqueous Solutions: I -Theory. *Industrial and Engineering Chemistry, 21*(1), 30-33.

McLeod, J. S. (2007). *Nucleation and growth of alpha lactose monohydrate.* Unpublished PhD, Massey University, Palmerston North, New Zealand.

McLeod, J. S., Paterson, A. H. J., Bronlund, J. E., & Jones, J. R. (2010). Nucleation of Alpha lactose monohydrate induced using flow through a venturi orifice. *Journal of Crystal Growth, 312*(6), 800-807.

Michaels, A. S., & van Krevald, A. (1966). Influences of Additives on Growth Rates in Lactose Crystals. *The Netherlands Milk and Dairy Journal, 20*(3), 163-181.

Mimouni, A., Schuck, P., & Bouhallab, S. (2005). Kinetics of lactose crystallization and crystal size as monitored by refractometry and laser light scattering: effect of proteins. *Le Lait, 85*(4-5), 253-260.

Moir, D. N. (1985). Selection and use of hydrocyclones. *Chemical Engineer (London)*(410), 20-25, 27.

Montenegro, R., Antonietti, M., Mastai, Y., & Landfester, K. (2003). Crystallization in miniemulsion droplets. *Journal of Physical Chemistry B, 107*(21), 5088-5094.

Murphy, B. M., Prescott, S. W., & Larson, I. (2005). Measurement of lactose crystallinity using Raman spectroscopy. *Journal of Pharmaceutical and Biomedical Analysis, 38*(1), 186-190.

Myerson, A. S. (2002). *Handbook of Industrial Crystallisation* (Second ed.). United States of America: Butterworth Heinemann.

Neesse, T., Dueck, J., & Minkov, L. (2003, Sep). *Separation of finest particles in hydrocyclones.* Paper presented at the Hydrocyclones 2003 Meeting, Cape Town, South Africa.

Nguyentranlam, G., & Galvin, K. P. (2001). Particle classification in the reflux classifier. *Minerals Engineering, 14*(9), 1081-1091.

Nickerson, T. A., & Moore, E. E. (1974). Factors Influencing Lactose Crystallization. *Journal of Dairy Science, 57*(11), 1315-1319.

Palakodaty, S., York, P., & Pritchard, J. (1998). Supercritical fluid processing of materials from aqueous solutions: The application of SEDS to lactose as a model substance. *Pharmaceutical Research, 15*(12), 1835-1843.

Patel, B. K., Ramirez, W. F., & Galvin, K. P. (2008). A generalized segregation and dispersion model for liquid-fluidized beds. *Chemical Engineering Science, 63*(6), 1415-1427.

Patel, S. R., & Murthy, Z. V. P. (2009). Ultrasound assisted crystallization for the recovery of lactose in an anti-solvent acetone. *Crystal Research and Technology, 44*(8), 889-896.

Patel, S. R., & Murthy, Z. V. P. (2011). Effect of process parameters on crystal size and morphology of lactose in ultrasound-assisted crystallization. *Crystal Research and Technology, 46*(3), 243-248.

Pettyjohn, E. S., & Christiansen, E. B. (1948). Effect of particle shape on free settling rates of isometric particles. *Chemical Engineering Progress, 44*(2), 157-172.

Pilcer, G., Wauthoz, N., & Amighi, K. (2012). Lactose characteristics and the generation of the aerosol. *Advanced Drug Delivery Reviews, 64*(3), 233-256.

Plitt, L. R. (1971). Analysis Of Solid-Solid Separaors In Classifiers. *Canadian Mining and Metallurgical Bulletin, 64*(708), 42-&.

Raghavan, S. L., Ristic, R. I., Sheen, D. B., & Sherwood, J. N. (2001). The bulk crystallization of alpha-lactose monohydrate from aqueous solution. *Journal of Pharmaceutical Sciences, 90*(7), 823-832.

Rhodes, M. J. (2008). *Introduction to particle technology* (2 ed.). Chichester, England: John Wiley.

Richardson, J. F., & Zaki, W. N. (1997). Sedimentation and fluidisation: Part I. *Chemical Engineering Research and Design, 75, Supplement*(0), S82-S100.

Roelfsema, W. A., Kuster, B. F. M., Heslinga, M. C., Pluim, H., & Verhage, M. (Eds.). (2002) Ullmann's Encyclopedia of Industrial Chemistry (6th ed.,). Weinheim, Germany: John Wiley & Sons.

Roetman, K. (1972). Crystallisation of Lactose. *Voedings Middelen Technologie, 3*(43), 230-239.

Roetman, K., & Buma, T. J. (1974). Temperature dependence of the equilibrium $\beta/\alpha$ ratio of lactose in aqueous solution. *Netherlands Milk and Dairy Journal, 28*, 155-165.

Roldanvillasana, E. J., Williams, R. A., & Dyakowski, T. (1993). The Origin Of The Fish-Hook Effect In Hydrocyclone Separators. *Powder Technology, 77*(3), 243-250.

Schiavone, H., Palakodaty, S., Clark, A., York, P., & Tzannis, S. T. (2004). Evaluation of SCF-engineered particle-based lactose blends in passive dry powder inhalers. *International Journal of Pharmaceutics, 281*(1-2), 55-66.

Shaffer, K., Paterson, A. H. J., Davies, C. E., & Hebbink, G. (2011). Stokes shape factor for lactose crystals. *Advanced Powder Technology, 22*(4), 454-457.

Shi, Y., Hartel, R. W., & Liang, B. (1989). Formation and Growth Phenomena of Lactose Nuclei Under Contact Nuclei Conditions. *Journal of Dairy Science, 72*, 2906-2915.

Shi, Y., Liang, B., & Hartel, R. W. (1990). Crystallization Kinetics of Alpha-Lactose Monohydrate in a Continuous Cooling Crystallizer. *Journal of Food Science, 55*(3), 817-820.

Srisa-nga, S., Flood, A. E., & White, E. T. (2006). The secondary nucleation threshold and crystal growth of alpha-glucose monohydrate in aqueous solution. *Crystal Growth & Design, 6*(3), 795-801.

Synowiec, P., Jones, A. G., & Shamlou, P. A. (1993). Crystal Break-Up In Dilute Turbulently Agitated Suspensions. *Chemical Engineering Science, 48*(20), 3485-3495.

Thielmann, F., Burnett, D. J., & Heng, J. Y. Y. (2007). Determination of the surface energy distributions of different processed lactose. *Drug Development and Industrial Pharmacy, 33*(11), 1240-1253.

Thurlby, J. A. (1976). Crystallization Kinetics of Alpha Lactose. *Journal of Food Science, 41*, 38-42.

Ting, H. H., & McCabe, W. L. (1934). Supersaturation and crystal formation in seeded solutions. *Industrial and Engineering Chemistry, 26*, 1201-1207.

Twieg, W. C., & Nickerson, T. A. (1968). Kinetics of Lactose Crystallization. *Journal of Dairy Science, 51*(11), 1720-1724.

Vallevega, P., & Nickerson, T. A. (1977). Measurement of Lactose Crystal-growth by Image Analyzer. *Journal of Food Science, 42*(4), 1069-1072.

van Kreveld, A., & Michaels, A. S. (1965). Measurement of Crystal Growth of á-Lactose. *Journal of Dairy Science, 48*, 259-265.

Visser, R. A. (1982). Supersaturation of α-lactose in aqueous solutions in mutarotation equilibrium. *Netherlands Milk and Dairy Journal, 36*, 89-101.

Walstra, P., Jenness, R., & Badings, H. (1984). *Dairy chemistry and physics*: Wiley.

Werner, S. R. L., Tretiakov, A., Paterson, T., & McLeod, J. S. (2002). *Modelling Lactose Crystallisation: Final Report*. Palmerston North: Massey University.

Whittier, E. O., & Gould, S. P. (1931). Speed of crystallization of lactose, galactose, glucose, and sucrose from pure solution. *Industrial and Engineering Chemistry, 23*, 670-673.

Williams, A. M., Jones, J. R., Paterson, A. H. J., & Pearce, D. L. (2009). Effect of fines on agglomeration in spray dryers: An experimental study. *International Journal of Food Engineering, 5*(2).

Williams, P. A., & Phillips, G. O. (2000). *Handbook of Hydrocolloids*. Cambridge, England: Woodhead Publishing Limited.

Xie, H. Y., & Zhang, D. W. (2001). Stokes shape factor and its application in the measurement of spherity of non-spherical particles. *Powder Technology, 114*(1-3), 102-105.

Xu, S. Q., Nie, Z. H., Seo, M., Lewis, P., Kumacheva, E., Stone, H. A., et al. (2005). Generation of monodisperse particles by using microfluidics: Control over size, shape, and composition. *Angewandte Chemie-International Edition, 44*(5), 724-728.

Yan, Y., & Thorpe, R. B. (1990). Flow regime transitions due to cavitation in the flow through an orifice. *International Journal of Multiphase Flow, 16*(6), 1023-1045.

Yano, J., Furedi-Milhofer, H., Wachtel, E., & Garti, N. (2000). Crystallization of Organic Compounds in Reversed Micelles. I. Solubilization of Amino Acids in Water−Isooctane−AOT Microemulsions. *Langmuir, 16*(26), 9996-10004.

Yu, Z. Q., Chow, P. S., & Tan, R. B. H. (2006). Seeding and constant-supersaturation control by ATR-FTIR in anti-solvent crystallization. *Organic Process Research & Development, 10*(4), 717-722.

Yuyama, H., Watanabe, T., Ma, G. H., Nagai, M., & Omi, S. (2000). Preparation and analysis of uniform emulsion droplets using SPG membrane emulsification technique. *Colloids and Surfaces a-Physicochemical and Engineering Aspects, 168*(2), 159-174.

Zeng, X. M., Martin, G. P., Marriott, C., & Pritchard, J. (2000). Crystallization of lactose from Carbopol gels. *Pharmaceutical Research, 17*(7), 879-886.

Zhang, X., & Davis, R. H. (2002). Particle classification using inclined settlers in series and with underflow recycle. *Industrial & Engineering Chemistry Research, 29*(9), 1894-1900.

Zhou, J., Walton, K., Laskovski, D., Duncan, P., & Galvin, K. P. (2006). Enhanced separation of mineral sands using the Reflux Classifier. *Minerals Engineering, 19*(15), 1573-1579.

Zumstein, R. C., & Rousseau, R. W. (1987). Growth rate Dispersion in Batch Crystallization with Transient Conditions. *AIChE Journal, 33*(11), 1921-1925.

# Appendix

## A.1 Lactose Physical Properties

Reference from page 5.

| Properties | $\alpha$-Lactose monohydrate | $\beta$-Lactose |
|---|---|---|
| *mp*, °C | 201 – 202 (decomp.) | 253 (decomp.) |
| Specific rotation $[\alpha]_D^{20}$, $10^{-2}$ ° · $cm^2/g$ | +89.4 | +34.3 |
| equilibrium value | +52.5 | +52.5 |
| Crystalline form | sphenoidal monoclinic ''tomahawk'''' (Fig. 1) | monoclinic ''uneven-sided diamond'' |
| *a*, nm | 0.7982 | 1.081 |
| *b*, nm | 2.1652 | 1.334 |
| *c*, nm | 0.4824 | 0.484 |
| $\beta$, ° | 109.78 | 91.15 |
| Density (293 K), $g/cm^3$ | 1.54 | 1.59 |
| Bulk density, $g/cm^3$ | | |
| poured | 0.5 – 0.9 | |
| tapped | 0.75 – 1.1 | |
| Enthalpy of dissolution, J/g | – 50.24 | – 9.62 |
| Enthalpy of combustion, J/g | – 16.1 | – 16.5 |
| Specific heat (298 K), $J\,K^{-1}\,g^{-1}$ | 1.251 | 1.193 |
| Entropy (298 K), $J\,K^{-1}\,mol^{-1}$ | 415 | 386 |
| Entropy of formation (298 K), $J\,K^{-1}\,mol^{-1}$ | – 2453 | – 2248 |
| Enthalpy of formation (298 K), kJ/mol | – 2481 | – 2233 |
| Gibbs free energy (298 K), kJ/mol | – 1750 | – 1564 |
| Solubility, g/100 g | | |
| in $H_2O$ | *see* Fig. 2 | *see* Fig. 2 |
| in DMSO | 59 (20 °C) | 30 (20 °C) |
| | 73 (80 °C) | 43 (80 °C) |
| $pK_a$ at 3 – 5 °C | 13.8 | 13.5 |
| Diffusion constant in $H_2O$, $m^2/s$ | $43 \times 10^{-11}$ | |

**Table A.1 Lactose physical properties (Roelfsema, *et al.*, 2002)**

## A.2 Radial Particle Movement Calculations

Reference from page 81.

Assuming a crystal diameter and parabolic fluid flow the pressure differential acting across the crystal can be calculated:

$$u(r) = 2u_{av}(1 - r^2/R^2)$$

$$\Delta P = P_1 - P_2 = 0.5\rho_f(u(1)^2 - u(2)^2)$$

The force acting over the area of crystal can then be calculated:

$$F = \Delta PA = FD \; at \; u_t$$

$$FD = 3\pi d\mu_v u_t$$

$$rerranged \; to: u_t = FD/(3\pi d\mu_v)$$

where $u_{av}$=1.06x10$^{-4}$m.s$^{-1}$, $R$=0.0375m, $\rho_f$=1140kg.m$^{-3}$, $\mu_v$=0.003Pa.s.

Distance moved = $u_t$ x run time.

In 16 hours of run time, movement of 0.032mm was calculated to occur at r=20mm and d=140µm for $Q_F$=28mL.min$^{-1}$, if $Q_F$=280mL.min$^{-1}$ (10xvelocity) then 3.2mm movement occurs.

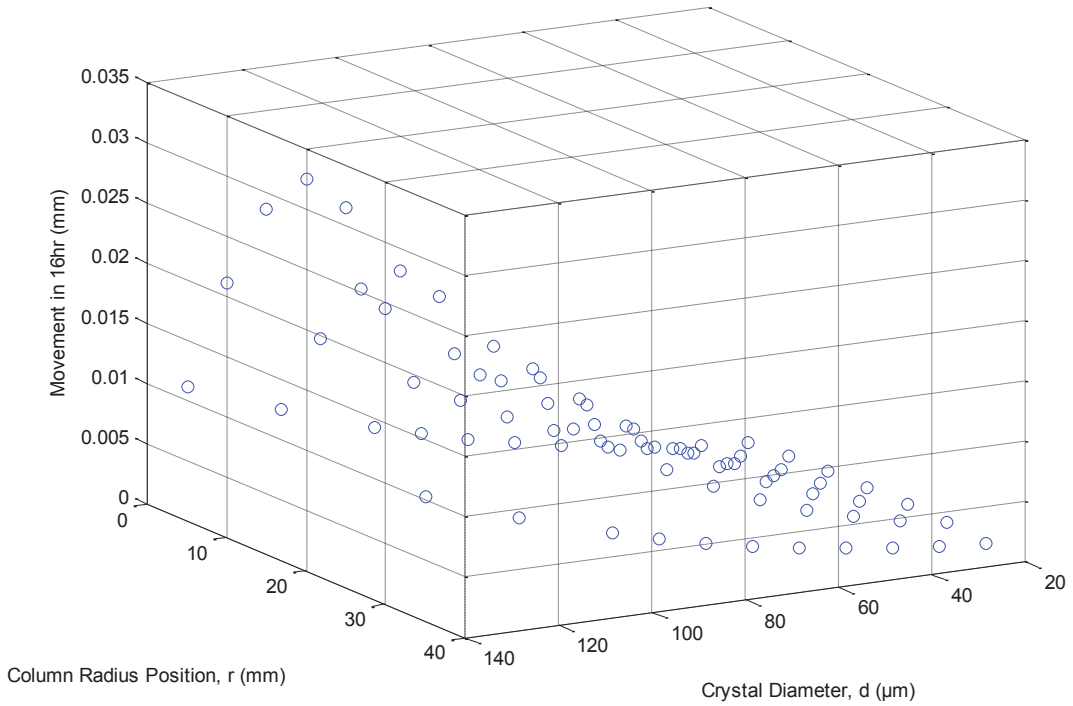


**Figure A.2 Crystal movement after 16 hours assuming a constant pressure differential (constant column radius position and crystal diameter and $Q_F$=28mL.min$^{-1}$)**

## A.3 CSC Column Insulation Calculations

Reference from page 107.

**Heat transfer for column without insulation**

$$\frac{1}{U} = \frac{1}{h_{air}} + \frac{1}{h_{fluid}} + \frac{x_{wall}}{k_{wall}}$$

where $h_{air}$=50W.m$^{-2}$.K$^{-1}$, $h_{fluid}$=500W.m$^{-2}$.K$^{-1}$, $x_{wall}$=0.003m, and $k_{wall}$=0.2 W.m$^{-1}$.K$^{-1}$.

$U$ =27.0 W.m$^{-2}$.K$^{-1}$

Rate, assuming a 1K temperature differential:

$q = UA\Delta T$ where A=(π *0.08m*3.5m)=0.88m$^2$, $q$=23.7W.

Increase in column fluid temperature:

Assuming no fluid movement for 10 minute period, two extreme scenarios are proposed; entire fluid mass to heat, and thin wall layer of fluid with no heat transfer (although in reality energy dissipates quickly).

Mass of entire column fluid = (3.5m*0.074m^2*π/4*1127kg.m$^{-3}$) = 17.0kg

Mass of thin 1mm outer fluid layer = 0.9kg

$\Delta T = q/(mC_P)$ where Cp=4.2kJ.kg$^{-1}$.K$^{-1}$.

$\Delta T_{column}$=0.0003K.s$^{-1}$, which = 0.2°C increase after 10 minutes

$\Delta T_{layer}$=0.006K.s$^{-1}$, which = 3.7°C increase after 10 minutes

**Heat transfer for column with insulation (calculation for final thickness shown):**

$$\frac{1}{U} = \frac{1}{h_{air}} + \frac{1}{h_{fluid}} + \frac{x_{wall}}{k_{wall}} + \frac{x_{ins}}{k_{ins}}$$

where $\boldsymbol{x_{ins}}$**=0.026m**, and $k_{ins}$=0.042 W.m$^{-1}$.K$^{-1}$.

$U_{ins}$=1.52 W.m$^{-2}$.K$^{-1}$

Rate, assuming a 1K temperature differential: $q$=1.3W

$\Delta T_{column}$=0.00002K.s$^{-1}$, which = 0.01°C increase after 10 minutes

$\Delta T_{layer}$=0.0003K.s$^{-1}$, which = 0.2°C increase after 10 minutes

26mm column insulation is acceptable to reduce convection effects.

## A.4 Fluid Movement Due to Density Differences

Reference from page 110.

Using Stokes law, calculated for drops of different density and fluid volume in bulk fluid of constant density:

$$u_t = \frac{d^2 g(\Delta\rho_f)}{18\mu}$$

where g=9.81m$^2$.s$^{-1}$, $\mu$=0.0028Pa.s

| **% increase compared to $u_{av}$** | d=0.1mm | d=0.5mm | d=1mm |
|---|---|---|---|
| $\Delta\rho_f$=0.1kg.m$^{-3}$ | 0.2 | 4 | 18 |
| $\Delta\rho_f$=0.5kg.m$^{-3}$ | 0.9 | 22 | 90 |
| $\Delta\rho_f$=1kg.m$^{-3}$ | 1.8 | 45 | 179 |

Large “fluid drops” with only minor density differences compared to the bulk, will have a significant velocity increase compared to average column velocity of $u_{av}$=0.1mm.s$^{-1}$.

## A.5 CSC Baffle Pressure Drop Calculations

Reference from page 113.Two designs were built: a minimal baffle design consisting of 200mm long baffles splitting flow 4-ways, and a maximal baffle design of fully packed column of 12mm diameter straws, approximately 39 straws per column cross-section area.

The increased pressure loss for a baffled system can be calculated as follows:

Head loss, $h_l = f\frac{Lu^2}{2Dg}$

Friction factor, f=64/Re

Pressure loss, $P_l = \rho g h_l$

Where $L$=3.5m, $\rho$=1140kg.m$^{-3}$, $\mu_v$=0.003Pa.s, $Q_F$=28mL.min$^{-1}$

| | Column D=75mm | 4-way Baffle D=37.5mm | Straws D=12mm | Hypothetical D=1mm |
|---|---|---|---|---|
| Pipe Re | 3.0 | 1.5 | 0.5 | 0.04 |
| f | 21 | 43 | 133 | 1594 |
| $h_l$ | 5.6*10$^{-7}$ | 2.3*10$^{-6}$ | 2.2*10$^{-5}$ | 3.2*10$^{-3}$ |
| $P_l$ (Pa) | 0.0063 | 0.025 | 0.24 | 36 |
| $P_l$ Ratio | - | 4 | 39 | 5625 |

The relative increase in pressure loss is good for the 12mm straws, however this still is a very minor pressure loss of 0.24 Pa, even with 1mm diameter the pressure loss is 36 Pa. More surface area from baffles in a crystallization setup will correspond to increased crystal build up.

## A.6 Targeting Fines Dissolution

Reference from page 128. 10% dissolution of product crystals, ideally fines, was the target. Normal CSC product dilution, 20mL product (increases to ~21mL with pressure head) + 13mL water, RI= ~1.3630 at 25°C, above the absolute supersaturation limit. The pumps can be controlled to within ~0.3mL.

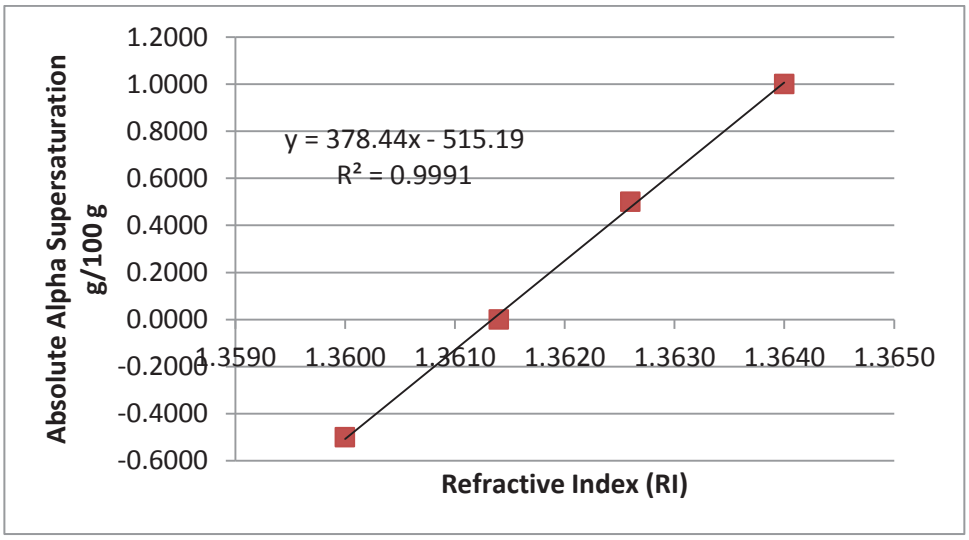


**Figure A.6 Correlation of measured refractive index and calculated absolute alpha supersaturation**

From calculations (on the attached CD) 21 mL product plus 15.4 mL water represented an absolute supersaturation=0 g/100 g and total lactose concentration=21.83 g/100 g, 15.7 mL (minimal 0.3 mL increase) of water had an absolute supersaturation=-0.16 g/100 g and total concentration=21.59 g/100 g. However the concentration of product stream was too low such that all product crystal would dissolve with the pump flow rate change available.

Product stream crystal content =~0.025%/(20/33) =0.042% =0.042%/100*(100 g solution) =0.042 g/100 g

Which is less than the concentration change back to 0 absolute supersaturation, 21.83g/100 g-21.59 g/100 g =0.24 g/100 g. The product stream requires concentration (or more CSC nucleation) before fines targeting can occur.

## A.7 Large Particle Effect on Volumetric Span

Reference from page 139. The previous CSC 16hr, CCG, cross-section area input, AGG0 model simulation had a product $d_{10}$=40 µm, $d_{50}$=67 µm, $d_{90}$=84 µm and span=0.67. 0.5% on a numbers basis of crystals was added ranging in size from 99-175µm, and changed the theoretical predictions to $d_{10}$=41 µm, $d_{50}$=71 µm, $d_{90}$=135 µm and span=1.33, doubling the span.

## A.8 CSC Experiment Reference Table

| Key | Date | Column Flow | Product Flow | Lactose | Feed Conc | Insulation | Baffle | Septum | Problems/Changes/Additional product processing |
|---|---|---|---|---|---|---|---|---|---|
| 1 | 13.10.11 | 23 | 20 | IGL-1 | 37 | no | no | no | |
| 2 | 21.10.11 | 23 | 20 | IGL-1 | 42 | no | no | no | |
| 3 | 27.10.11 | 23 | 20 | IGL-1 | 42 | no | no | no | Conc tank heat stop |
| 4 | 4.11.11 | 23 | 20 | IGL-1 | 42 | no | no | no | New Conc Tank and HT Tubing, No Nuclei |
| 5 | 7.11.11 | 23 | 20 | IGL-1 | 42 | no | no | no | New nucleation dilution method |
| 6 | 10.11.11 | 23 | 20 | IGL-1 | 42 | no | no | no | Cone vibrator added |
| 7 | 17.11.11 | 28 | 20 | IGL-1 | 42 | no | no | no | |
| 8 | 24.11.11 | 28 | 20 | IGL-1 | 42 | yes | no | no | |
| 9 | 2.12.11 | 28 | 20 | IGL-1 | 42 | yes | no | no | |
| 10 | 9.12.11 | 33 | 20 | IGL-1 | 42 | yes | no | no | |
| 11 | 11.1.12 | 28 | 20 | 200M-1 | 42 | yes | no | yes | |
| 12 | 2.2.12 | 28 | 20 | 200M-1 | 42 | yes | no | yes | Agglomerate Imaging |
| 13 | 7.2.12 | 28 | 20 | IGL-2 | 42 | yes | no | yes | Product steam blocked during 6-16hr |
| 14 | 9.2.12 | 28 | 20 | 200M-1 | 42 | yes | no | yes | nucleation container room temp |
| 15 | 21.2.12 | 28 | 20 | 200M-1 | 42 | yes | no | yes | nucleation 7.30min at 600rpm |
| 16 | 20.3.12 | 30 | 20 | 200M-1 | 42 | yes | yes | yes | |
| 17 | 23.3.12 | 36 | 20 | 200M-1 | 42 | yes | yes | yes | Ultrasound + dilution |
| 18 | 30.3.12 | 28 | 20 | 200M-1 | 42 | yes | yes | yes | Ultrasound + dilution + filter |
| 19 | 7.4.12 | 28 | 20 | 200M-1 | 42 | yes | yes | yes | Ultrasound + dilution + filter |
| 20 | 13.4.12 | 28 | 20 | 200M-1 | 42 | yes | yes | yes | Ultrasound + dilution + centrifuge |
| 21 | 9.5.12 | 28 | 20 | 200M-1 | 42 | yes | yes | yes | Magnetic flea product recycle |
| 22 | 16.5.12 | 28 | 20 | 200M-1 | 42 | yes | yes | yes | straws added above feed normal |
| 23 | 20.5.12 | 28 | 20 | 200M-2 | 42 | yes | yes | yes | test new 200M lactose |
| 24 | 23.5.12 | 28** | 20 | 200M-2 | 42 | yes | yes | yes | Impeller mix 2-pump recycle |
| 25 | 30.5.12 | 28 | 20 | 200M-2 | 42 | yes | yes | yes | Normal tested agglomerate breakdown |
| 26 | 1.10.12 | 28 | 20 | 200M-2 | 42 | yes | yes | no | full straw - product blocked |
| 27 | 1.11.12 | 28 | 20 | 200M-2 | 42 | yes | yes | no | full straw - no product nuclei |
| 28 | 7.11.12 | 28 | 20 | 200M-2 | 42 | yes | yes | no | full straw - no product nuclei |
| 29 | 12.11.12 | 28 | 20 | 200M-2 | 43 | yes | yes | no | full straw - max nucleation |

**Table A.8 Labelling in report is shown as Key.Run Time(hrs:min)**

**All lactose used was provided by DFE Pharma (previously known as DMV-Fonterra-Excipients).**

**IGL-1 Label Description:**

Wynhale™ Inhalation Lactose

GSK Item Code:10000000059577, GSK Description: Lactose MHDT ex LNZ Grade 5, Order #: 4500628679, LNZ Item code: 105510, Batch #: J1011, MANU: 12-05-2010, EXP: 10-05-2012,

**200M-1 Label Description:**

Pharmatose® 200M Milled Lactose

HV040017 A6081, MANU: 04/03/11, EXP: 02/03/14

**200M-2 Label Description:**

Pharmatose® 200M Milled Lactose

FW030017 A4487, MANU: 3/1/12, EXP: 1/1/15

## A.9 CD

The CD contains the following:

Matlab models:

- Drop growth model
- Batch growth model
- Laminar flow CSC model
- Combined column CSC model

Summarised Malvern MasterSizer experimental data.

Raw data used in the calculation of statistics and graphs.

Inclined settler process flow diagram Figure 24 with stream values.

Hydrocyclone calculations for the results presented in Chapter 7.